Towards the identification and functional characterization of molecular components involved in PEN2-mediated entry control of non-adapted powdery mildews in *Arabidopsis*

Dissertation

zur Erlangung des mathematisch-naturwissenschaftlichen Doktorgrades

"Doctor rerum naturalium"

der Georg-August-Universität Göttingen

im Promotionsprogramm Biologie

der Georg-August University School of Science (GAUSS)

vorgelegt von

Lena Wagenknecht

aus Marburg an der Lahn

Göttingen, 2021

Betreuungsausschuss

1. Betreuer: **Prof. Dr. Volker Lipka**
Zellbiologie der Pflanze
Albrecht-von-Haller Institut für Pflanzenwissenschaften

2. Betreuer: **Prof. Dr. Ivo Feußner**
Biochemie der Pflanze
Albrecht-von-Haller Institut für Pflanzenwissenschaften

3. Betreuer: **PD Dr. Thomas Teichmann**
Zellbiologie der Pflanze
Albrecht-von-Haller Institut für Pflanzenwissenschaften

Anleiter: **Prof. Dr. Volker Lipka**
Zellbiologie der Pflanze
Albrecht-von-Haller Institut für Pflanzenwissenschaften

Mitglieder der Prüfungskommission

Referent: **Prof. Dr. Volker Lipka**
Zellbiologie der Pflanze
Albrecht-von-Haller Institut für Pflanzenwissenschaften

Korreferent: **Prof. Dr. Ivo Feußner**
Biochemie der Pflanze
Albrecht-von-Haller Institut für Pflanzenwissenschaften

Weitere Mitglieder der Prüfungskommission

Prof. Dr. Andrea Polle
Forstbotanik und Baumphysiologie
Fakultät für Forstwissenschaften und Waldökologie

PD Dr. Till Ischebeck
Biochemie der Pflanze
Albrecht-von-Haller Institut für Pflanzenwissenschaften

PD Dr. Thomas Teichmann
Zellbiologie der Pflanze,
Albrecht-von-Haller Institut für Pflanzenwissenschaften

PD Dr. Marcel Wiermer
Molekularbiologie der Pflanze-Mikroben Interaktionen
Albrecht-von-Haller Institut für Pflanzenwissenschaften

Tag der mündlichen Prüfung: 15.07.2021

Promovierenden-Erklärung

der Georg-August-Universität Göttingen

Die Gelegenheit zum vorliegenden Promotionsvorhaben ist mir nicht kommerziell vermittelt worden. Insbesondere habe ich keine Organisation eingeschaltet, die gegen Entgelt Betreuerinnen und Betreuer für die Anfertigung von Dissertationen sucht oder die mir obliegenden Pflichten hinsichtlich der Prüfungsleistungen für mich ganz oder teilweise erledigt.

Hilfe Dritter wurde bis jetzt und wird auch künftig nur in wissenschaftlich vertretbarem und prüfungsrechtlich zulässigem Ausmaß in Anspruch genommen. Insbesondere werden alle Teile der Dissertation selbst angefertigt; unzulässige fremde Hilfe habe ich dazu weder unentgeltlich noch entgeltlich entgegengenommen und werde dies auch zukünftig so halten.
Die Ordnung zur Sicherung der guten wissenschaftlichen Praxis an der Universität Göttingen wurde von mir beachtet.

Eine entsprechende Promotion wurde an keiner anderen Hochschule im In- oder Ausland beantragt; die eingereichte Dissertation oder Teile von ihr wurden nicht für ein anderes Promotionsvorhaben verwendet.

Mir ist bekannt, dass unrichtige Angaben die Zulassung zur Promotion ausschließen bzw. später zum Verfahrensabbruch oder zur Rücknahme des erlangten Grades führen.

Lena Wagenknecht Göttingen, den 07.06.2021

Abstract

The *Arabidopsis thaliana* cytochrome P450 monooxygenase CYP81F2 and the myrosinase PENETRATION2 (PEN2) are important components for broad-spectrum pre-invasion defense against filamentous plant pathogens, including non-adapted powdery mildews (Lipka et al., 2005; Bednarek et al., 2009; Clay et al., 2009; Fuchs et al., 2016). PEN2 is a tail-anchored protein, which is targeted to both peroxisomes and mitochondria. Pathogen-triggered recruitment and accumulation of mitochondrial subpopulations were observed at sites of attempted fungal penetration. Moreover, mitochondrial immobilization is accompanied by aggregate formation of PEN2 on the outer mitochondrial membrane on clustered and immobilized mitochondria (Fuchs et al., 2016). PEN2 was shown to form pathogen-triggered oligomers and dimers of higher order in the periphery of arrested mitochondria (Fuchs et al., 2016). The ER-localized CYP81F2 accumulates in infected cells. Upon pathogen attack, the ER reorganizes in proximity to the arrested mitochondria (Fuchs et al., 2016). CYP81F2 functions in the pathogen-induced biosynthesis of 4MI3G (4-methoxyindol-3-ylmethyl glucosinolate), which is a substrate of the PEN2 myrosinase. PEN2 catalyzes the hydrolyzation of 4MI3G, resulting in the formation of toxic hydrolysis products (Bednarek et al., 2009; Clay et al., 2009). The ABC transporter PENETRATION3 (PEN3) is proposed to secrete these biologically active indole glucosinolates (IG)-metabolism products across the plasma membrane and into the apoplast to terminate attempted pathogen entry at the cell periphery (Stein et al., 2006; Matern et al., 2019).

These pathogen-induced and cell-autonomous defense mechanisms at the site of attempted fungal invasion very likely require sensing of the potential intruder by the plant. To study the connection between pathogen recognition and PEN2-mediated defense, the first part of the presented study focused on the role of microbe-associated molecular pattern (MAMP)-dependent signaling for CYP81F2 accumulation, ER rearrangement, mitochondrial arrest and PEN2 aggregate formation. CYP81F2-RFP accumulated in the ER and nuclear envelope after flagellin and chitin infiltration. Moreover, mitochondrial arrest and PEN2-aggregate formation was induced upon the perception of MAMPs, similar to powdery mildew infection. Additionally, MAMP-induced PEN2-GFP-TA_{PEN2} aggregates with increased fluorescence on single, mobile mitochondria.

The second part of this project focused on the identification and characterization of novel molecular components contributing to PEN2-mediated pathogen entry control. For this purpose, a homozygous double transgenic line expressing both PEN2-GFP-TA_{PEN2} and CYP81F2-mKate2 from a single cassette was generated and characterized. The T-DNA insertion disrupts no coding sequence. CLSM of GFP-tagged PEN2 and mKate2-tagged CYP81F2 showed expected localization and accumulation patterns unchallenged and 20 hpi with *Blumeria graminis f.sp. hordei* (*Bgh*). The selected line might be used

for a CLSM-based forward genetic screen to identify novel molecular components required for CYP81F2/PEN2-mediated disease resistance.

The Glutathione-S-transferase class-tau member 13 (GSTU13) is an important molecular component of the PEN2 defense pathway for IG metabolism. It is suggested that GSTU13 mediates the conjugation of the unstable I3G-ITC (indol-3-ylmethyl-isothiocyanate)/4MI3G-ITC (4-methoxyindol-3-ylmethyl-isothiocyanate) with glutathione. GSTU13 was shown to be required for the formation of the end products indol-3-ylmethyl amine (I3A), raphanusamic acid (RA) and 4-O-β-d-glucosyl-indol-3-yl formamide (4OGlcI3F) of the PEN2 pathway (Piślewska-Bednarek et al., 2018). This study showed that N- and C-terminally RFP-tagged GSTU13 is localized to the cytosol, the nucleus and punctate structures, which showed no co-localization with PEN2. Upon powdery mildew attack, the cytoplasm relocalized to the site of attempted *Bgh* invasion, which was accompanied by elevated GSTU13-RFP fluorescence intensities.

Several molecular components involved in pre-invasive non-host resistance were previously shown to be co-regulated with PEN2 and PEN3 in *Arabidopsis* (Humphry et al., 2010). To identify additional compounds required for PEN2-mediated resistance, two co-expressed genes, *AT1G08930* (*Early response to dehydration* 6 (*ERD6*)) and AT1G55450 (*S-adenosyl-L-methionine-dependent methyltransferase;* named SAM-MT) were selected for further analysis in this study.

ERD6 was shown to be required for penetration resistance against *Erysiphe pisi* at 72 hpi but does not contribute to defense against *Bgh* and *Golovinomyces orontii*. It was demonstrated that the transporter localizes to multivesicular bodies/late endosomes (MVBs/LEs) and the lumen of the vacuole in unchallenged leaf epidermal cells. Upon infection, ERD6 positive vesicles were shown to accumulate at powdery mildew contact sites and in proximity to clustered and immobilized mitochondria decorated with aggregates of PEN2. An untargeted metabolomic approach revealed that the PEN2/CYP81F2 substrate I3G, the IGMT1 and IGMT2 substrate 4OHI3G, the PEN2 substrate 4MI3G and glycosylated dihydroascorbigen accumulated in *erd6* mutants, suggesting that ERD6 might be required for the transport of these substances.

The regulatory pathways that coordinate the accumulation and immobilization of mitochondrial subpopulations and PEN2-aggregate formation are unknown. To gain new insights into the molecular mechanisms of PEN2-mediated pathogen entry control, IP-MS experiments were performed to identify potential PEN2 interactors. This analysis identified the Guanylate-binding family protein-like 3 (GBPL3) as a potential PEN2 interaction partner. Guanylate binding proteins function in cell-autonomous immunity against a broad spectrum of intracellular pathogens in mammals (Kim et al., 2012; Tretina et al., 2019). In this study, no homozygous *gbpl3* mutants were found, suggesting em-

bryo-lethality and a potential defect in seed development. Heterozygous *gbpl3* mutants showed wild-type-like *Bgh* invasion frequencies.

Zusammenfassung

Die Cytochrome P450 Monooxygenase CYP81F2 und die atypische Myrosinase PENETRATION2 (PEN2) sind bedeutende Komponenten der präinvasiven Resistenz von *Arabidopsis thaliana* gegen filamentöse Pathogene (Lipka et al., 2005; Bednarek et al., 2009; Clay et al., 2009; Fuchs et al., 2016). PEN2 ist ein C-terminal verankertes Membranprotein und ist in der Peripherie von Mitochondrien und Peroxisomen lokalisiert (Lipka et al., 2005; Fuchs et al., 2016). Infektionsexperimente mit dem nicht-adaptierten Mehltaupilz *Blumeria graminis f.sp hordei* (*Bgh*) zeigten eine Akkumulation und Immobilisierung von mitochondrialen Subpopulationen an der Interaktionsstelle. Des Weiteren, bildeten sich PEN2-Aggregate an der äußeren Mitochondrienmembran von immobilisierten Mitochondrien, direkt unter der versuchten Invasionsstelle des Mehltaupilzes (Fuchs et al., 2016). Fuchs *et al*., 2016 zeigten, dass PEN2 nach Mehltauinfektion detergenz-resistente Oligomere und Dimere ausbildete. Die Cytochrome P450 Monooxygenase CYP81F2 ist am Endoplasmatischen Retikulum (ER) lokalisiert und akkumuliert in infizierten Zellen. Nach Pilzinokulation reorganisierte sich das ER in direkter Nähe der immobilisierten Mitochondrien an Stellen der versuchten Invasion (Fuchs et al., 2016). CYP81F2 ist an der Synthese von 4MI3G beteiligt, welches das Substrat der Myrosinase PEN2 ist und für die präinvasive Resistenz der Pflanze benötigt wird. PEN2 katalysiert die Hydrolyse von 4MI3G (Bednarek et al., 2009; Clay et al., 2009). Die Hydrolyse von 4MI3G führt zu der Bildung von toxischen Sekundärmetaboliten, die von dem ABC-Transporter PEN3 in den Apoplasten transportiert werden, um die versuchte Invasion des Pilzes abzuwehren (Stein et al., 2006; Matern et al., 2019).

Die Pathogen-induzierte und zellautonome Abwehrmechanismen basieren vermutlich auf der Perzeption des potentiellen Pathogenes. Um die Verbindung zwischen der Erkennung des Pathogens und der PEN2-vermittelten präinvasiven Resistenz genauer zu untersuchen, konzentriert sich der erste Teil dieser Studie auf die Analyse der MAMP-abhängigen CYP81F2 Akkumulation, ER Reorganisation, Akkumulation von Mitochondrien, sowie der PEN2 Aggregatbildung. CYP81F2 akkumulierte am ER und an der Zellkernhülle nach Chitin- und Flagellin-Infiltration. Ähnlich wie bei Mehltaupilzen rufen MAMPs die Akkumulierung von Mitochondrien, sowie die PEN2-Aggregatbildung an immobilisierten Mitochondrien hervor. Darüber hinaus wurden nach MAMP-Behandlung auch einzelne, mobile Mitochondrien mit stark fluoreszierenden PEN2-Aggregaten beobachtet. Immobilisierung oder PEN2-Aggregatbildung an Peroxisomen trat nach MAMP-Behandlung nicht auf.

Der Zweite Teil dieser Arbeit beschäftigte sich mit der Identifizierung und Charakterisierung von weiteren molekularen Komponenten die an der PEN2-vermittelten präinvasiven Resistenz beteiligt sind. Um solche Komponenten zu identifizieren wurde eine homozygote transgene Linie generiert, die *PEN2-GFP-TA*$_{PEN2}$ and *CYP81F2-mKate2* von einer Kassette exprimiert. Die T-DNA Insertion befindet

sich in keiner kodierenden Sequenz. Konfokale Laserscanningmikroskopie Analysen zeigten die erwartete subzelluläre Lokalisation von GFP-markiertem PEN2 und mKate2-markiertem CYP81F2 nach Pilzinfektion. Die selektierte Linie kann in weiteren Studien für einen vorwärtsgerichteten-genetischen und Konfokalmikroskopie-basierten Screen verwendet werden, um weitere Komponenten der CYP81F2/PEN2- vermittelten präinvasiven Resistenz zu identifizieren.

Die Glutathione-S-transferase class-tau member 13 (GSTU13) wurde als weitere wichtige Komponente der präinvasiven Resistenz von *Arabidopsis* identifiziert (Piślewska-Bednarek et al., 2018). Es wird angenommen, dass die Glutathiontransferase das Indol-3-ylmethyl-isothiocyanat (I3G-ITC) und das 4-Methoxyindol-3-ylmethyl-isothiocyanat (4MI3G-ITC) mit Glutathion konjugiert und an der Biosynthese von Indol-3-ylmethyl amin (I3A), Raphanusamsäure (RA) und 4-O-β-d-glucosyl-indol-3-yl formamid (4OGlcI3F), welche mögliche Endprodukte der PEN2-vermittelten präinvasiven Immunantwort sind, beteiligt ist (Piślewska-Bednarek et al., 2018). Konfokalmikroskopische Analysen zeigten, dass N-und C-terminal RFP-markiertes GSTU13 im Zytosol, Zellkern und in runden Strukturen lokalisiert ist. Diese runden Strukturen zeigten keine Kolokalisation mit PEN2-GFP-TA_{PEN2}-positiven Membrankompartimenten. Nach Pilzinfektion akkumulierte nicht nur das Zytoplasma an der Interaktionsstelle, sondern es zeigte sich eine erhöhte GSTU13-RFP Fluoreszenz unterhalb der versuchten Penetrationstelle.

Es wurde gezeigt, dass molekulare Komponenten, der präinvasiven Resistenz von *Arabidopsis* mit PEN2 und PEN3 koexprimiert sind (Humphry et al., 2010). Um weitere molekulare Komponenten zu identifizieren, die an der PEN2-vermittelten präinvasiven Resistenz beteiligt sind, wurden in dieser Arbeit, zwei koexprimierte Gene, *AT1G08930* (*Early response to dehydration* 6 (*ERD6*)) und *AT1G55450* (*S-adenosyl-L-methionine-dependent methyltransferase;* genannt SAM-MT) für weitere Analysen ausgewählt.

Der vorhergesagte Saccharose-Transporter ERD6 ist an der präinvasiven Resistenz gegen den nicht-adaptierten Mehltaupilz *Erysiphe pisi* beteiligt, trägt jedoch nicht zur Abwehr gegen *Bgh* und *Golovinomyces orontii* bei. Konfokalmikroskopische Analysen von unbehandelten Epidermiszellen zeigten das mTurquoise2-markiertes ERD6 mit multiversikularen Körpern assoziiert ist und auch in der Vakuole lokalisiert. Nach *E. pisi* Infektion akkumulierten ERD6-positive Vesikel an dem Ort der versuchten Invasion und in der Nähe von immobilisierten Mitochondrien, die mit PEN2-Aggregaten assoziiert sind. Eine ungerichtete Metaboliten-Analyse zeigte eine Akkumulation des PEN2/CYP81F2 Substrats I3G, des IGMT1/IGMT2-Substrats 4OHI3G, und des PEN2-Substrats 4MI3G, sowie der glykosylierten Form von Dihydroascorbigen in der *erd6* Mutante, was auf einem möglichen ERD6-abhängigen Transport dieser Sekundärmetaboliten hindeutet.

Die genauen Mechanismen, welche die Akkumulation und Immobilisierung von Mitochondrien, sowie die PEN2-Aggregatbildung regulieren und koordinieren sind unbekannt. Um neue Erkenntnisse in

diesem Bereich der präsinvasiven Resistenz zu bekommen wurden Immunoprezipitationsanalysen und anschließende massenspektrometrische Analysen durchgeführt. Diese Analysen identifizierten das Guanylate-binding family protein-like 3 (GBPL3) als einen potentiellen Interaktionspartner von PEN2. Guanylat-bindende Proteine sind in Säugetieren an der Zell-autonomen Resistenz gegen eine Vielzahl von intrazellulären Pathogenen beteiligt (Kim et al., 2012; Tretina et al., 2019). In dieser Arbeit wurden *gbpl3* Mutaten untersucht, es konnten jedoch keine homozygoten Pflanzen isoliert werden. Dies deutet daraf hin, dass GBPL3 eine essentielle Funktion in der Embryo- und Samenentwicklung hat. Herozygote *gbpl3* mutanten zeigten eine mit dem Wildtyp verleichbare *Bgh*-Invasionsrate.

List of abbreviations

α	anti/ alpha
°C	degree Celsius
4MI3G	4-methoxyindol-3-ylmethyl glucosinolate
4MI3G-ITC	4-methoxyindol-3-ylmethyl-isothiocyanate
4MI3G-ITC-GSH	4-methoxyindol-3-ylmethyl-isothiocyanate-glutathione
4MOI3Cys	S-(4-Methoxyindol-3-ylmethyl)cysteine
4MOI3M	4-methoxyindol-3-methanol
4MTB	4-methylthiobutyl glucosinolate
4OGlcI3F	4-O-β-d-glucosyl-indol-3-yl formamide
4OHI3G	4-hydroxy-indol-3-yl-methyl glucosinolate
ABC	ATP-binding cassette
ADP	adenosindiphosphat
AG	aliphatic glucosinolates
AP	alkaline phosphatase
Ap	appressoria
APS	ammonium persulfate
ATP	adenosintriphosphat
Avr	avirulence
BAK1	BRI1-ASSOCIATED KINASE 1
Bgh	*Blumeria graminis f.sp. hordei*
BIK1	BOTRYTIS-INDUCED KI-NASE 1
bp	base pair
BSA	bovine serum albumin
bZIP	BASIC LEUCINE-ZIPPER
C-terminus	carboxy-terminus
Ca^{2+}	Calcium
CC	coiled-coil
cDNA	complementary DNA
CERK1	CHITIN ELICITOR RECEPTOR KINASE1
CLSM	Confocal laser scanning microscopy
Col-0	Columbia-0

ConcA	ConcanamycinA
CRISPR	clustered regularly interspaced short palindromic repeats
Cw	cell wall;
CYP	CYTOCHROME P450 MONOOXYGENASE
DAMP	damage-associated molecular pattern
ddH20	double-distilled water
DeHydroAsc Hex	dehydroascorbic acid hexoside
DMSO	dimethylsulfoxid
DNA	desoxyribonucleic acid
dNTP	desoxyribonucleotidetriphosphate
dpi	day post infection/ infiltration
Dpi	days post infection
DTT	dithiothreitol
DYT	double yeast tryptone
E. coli	Escherichia coli
E. pisi	*Erysiphe pisi*
eATP	extracellular ATP
EDS	ENHANCED DISEASE SUSCEPTIBILITY
EDS1	ENHANCED DISEASE SUS-CEPTIBILITY 1
EDTA	ethylenediaminetetraacetic acid
EE	early endosome
EMS	ethyl methane sulfonate
ER	Endoplasmic reticulum
ERD6	EARLY RESPONSE TO DEHYDRATION 6
ERF6	ETHYLENE RESPONSE FACTOR6
ESCRT	ENDOSOMAL SORTING COMPLEX REQUIRED FOR TRANSPORT
ESL1	ERD SIX-LIKE 1
ET	ethylene
et al.	et alii; and others
ETI	effector-triggered immunity
EtOH	ethanol
ETS	effector-triggered susceptibility
f.sp.	forma specialis
flg22	flagellin (22 amino acid peptide)

FLS2	FLAGELLIN SENSING 2
g	gram or gravitation
G. orontii	*Golovinomyces orontii*
GBPL3	GUANYLATE-BINDING FAMILY PROTEIN-LIKE 3
gDNA	genomic DNA
GFP	green fluorescence protein
GLS	glucosinolates
GLUT	glucose transporter
GSH	glutathione
GST	glutathione S-transferase
GTPase	guanosine triphosphatases
GTR	Glucosinolate Transporter
H	hyphae
h	hour(s)
H_2O_2	hydrogen peroxide
Ha	haustorium
HCl	hydrochloric acid
hpi	hours post infection/ infiltration
HR	hypersensitive response
I3A	indol-3-ylmethyl amine
I3G	indol-3-ylmethyl glucosinolate
I3G-ITC	indol-3-ylmethyl-isothiocyanate
I3G-ITC-GSH	indol-3-ylmethyl-isothiocyanate-glutathione
IAA	indole acetic acid
IAM	iodoacetamide
IG	indole glucosinolate
IGMT1/2	INDOLE GLUCOSINOLATE O-METHYLTRANSFERASE 1/2
ILV	intraluminal vesicle
IP	immunoprecipitation
ITC	isothiocyanates
JA	jasmonic acid
kDa	kilo Dalton
l	liter
LC	liquid chromatography

LE	late endosome
LRR	leucine-rich repeat
LYK	LYSM RECEPTOR-LIKE KI-NASE
LYM	LYSM RECEPTOR-LIKE PRO-TEIN
LysM	lysin motifs
m	meter
M	molar
MAMP	microbe associated molecular pattern
MAPK	mitogen-activated protein kinase
MES	2-(N-morpholino)ethanesulfonic acid
min	minute
MIT/PTI	MAMP/PAMP-triggered immunity
ml	milliliter
mm	millimeter
mM	millimolar
MOPS	3-(N-morpholino)propanesulfonic acid
MS	mass spectrometry
MS	Murashige-Skoog
MVBs	multivesicular bodies
N-terminus	amino-terminus
N. benthamiana	*Nicotiana benthamiana*
NASC	Nottingham Arabidopsis Stock Center
NB	nucleotide binding
NHR	nonhost resistance
NLR	nucleotide-binding leucine-rich repeat
nm	nanometer
nM	nanomolar
OGs	oligogalacturonides
P. infestans	*Phytophthora infestans*
P. syringae	*Pseudomonas syrinagae*
Pa	papilla;
PAD3	PHYTOALEXIN DEFICIENT 3
PAD4	PHYTOALEXIN-DEFICIENT 4
PAMP	pathogen-associated molecular pattern

PCR	polymerase chain reaction
PCS1	PHYTOCHELATIN SYNTHASE 1
PCWDEs	plant cell wall-degrading enzymes
PD	plasmodesma(ta)
PDR	pleiotropic drug resistance
PEN	PENETRATION
Pep	plant elicitor peptides
PEPR	Pep receptor
PGN	peptidoglycan
pH	negative decimal logarithm of the H+ concentration
PIC	Protease Inhibitor Cocktail
PM	plasma membrane
PMS	Peptide Spectrum Matches
PR	PATHOGENESIS RELATED
PRR	pattern recognition receptor
PTI	pattern-triggered immunity
pv.	pathovar
PVDF	polyvinylidene fluoride
R	resistance
RA	raphanusamic acid
RFP	red fluorescent protein
RLCK	receptor-like cytoplasmic kinase
RLK	receptor-like kinase
RLP	receptor-like proteins
RNA	ribonucleic acid
ROS	reactive oxidative species
rpm	rounds per minute
RT	room temperature
s	second(s)
SA	salicylic acid
SAG	salicylic acid glucoside
SAG101	SENESCENCEASSOCIATED GENE 101
SAM-MT	S-adenosyl-L-methionine-dependent methyltransferase
SAR	systemic acquired resistance

SDS	sodium dodecyl sulfate
SDS-PAGE	sodium dodecyl sulfate poly-acrylamide gel electrophoresis
SID2	SA-DEFICIENT MUTANT 2
SNAP33	SYNAPTOSOME-ASSOCIATED PROTEIN 33
SNARE	SOLUBLE N-ETHYLMALEIMIDE-SENSITIVE FACTOR ATTACHMENT RECEPTOR
Sp	Spore
SUR1	SUPERROOT1
SYP121	syntaxin of plants 121
t	time
T-DNA	transfer-DNA
TA	tail-anchor
TAE	Tris-acetic acid EDTA
TAIR	The Arabidopsis Information Resource
Taq	*Thermus aquaticus*
TBS-T	Tris buffered saline - Tween-20
TCH3	TOUCH3
TEMED	Tetramethylethylenediamine
TFA	trifluoroacetic acid
TGG	thioglucosidase
TGN	trans-Golgi network
TMD	transmembrane domain
U	unit
UV	ultraviolet
V	volt
VAMP722	VESICLE-ASSOCIATED MEMBRANE PROTEIN 722
Wm	Wortmanin
ZAR1	HOPZ-ACTIVATED RESIS-TANCE 1
µg	microgramm
µl	microliter
µm	micrometer
µM	micromolar
Δ	delta (Deletion)

Table of contents

1 Introduction

1.1 Plant innate immunity

Plants are permanently challenged by a wide range of potentially pathogenic microorganisms including bacteria, viruses, fungi and oomycetes. These microbial pathogens exhibit different lifestyles and infection strategies. Necrotrophic pathogens secrete enzymes and toxins to actively kill host cells and to acquire nutrients from dead plant tissue. Biotrophs require living plant tissue to obtain nutrients, whereas hemibiotrophic pathogens combine an early biotrophic phase followed by a necrotrophic phase to complete their life cycle (Horbach et al., 2011). However, successful microbial colonization resulting in disease is an exception due to a complex and multi-layered defense machinery of plants. (Jones and Dangl, 2006; Dodds and Rathjen, 2010). In a compatible plant-pathogen interaction, the pathogen can circumvent or suppress the plant immune system (host susceptibility). In an incompatible interaction, the pathogen is directly or indirectly recognized by the plant. This triggers defense responses and stops pathogen colonization (host resistance) (Lamb et al., 1992). In contrast to mammals, plants lack a somatic adaptive immune system including mobile immune cells. In response to invasion and colonization by phytopathogens, plants use an innate immune system comprised of various constitutive defense mechanisms and inducible responses (Dodds and Rathjen, 2010). The epidermal cuticle and the plant cell wall layer are the first physiological barriers encountered by the potential intruder attempting to colonize plant tissue (Tucker and Talbot, 2001). For the establishment of a chemical barrier, plants constitutively accumulate a variety of antimicrobial compounds (phytoanticipins). These preformed secondary metabolites are potentially toxic and inhibitory for the invading microbe (VanEtten et al., 1994). To overcome physical barriers, pathogens evolved complex strategies for plant invasion such as entering through stomata or wounds, formation of specialized penetration structures that develop a high turgor pressure and/or secretion of plant cell wall-degrading enzymes (PCWDEs) (Tucker and Talbot, 2001; Chisholm et al., 2006). Pathogens that have breached the plant cuticle and cell wall, face the plasma membrane (PM) and are exposed to the plant immune system. The plant immune system can be divided into cell-surface and intracellular immunity (Wang et al., 2020). Cell-surface immunity relies on pattern recognition receptors (PRRs) recognizing highly conserved non-self ligands known as microbe/pathogen-associated molecular patterns (MAMPs/PAMPs). Many types of MAMPs/PAMPs have been identified, such as microbial carbohydrates (bacterial lipopolysaccharide, peptidoglycan, fungal chitin) or microbial proteins and peptides (bacterial elongation factor-Tu (EF-Tu), its derived peptide elf18, the flg22 peptide derived from bacterial flagellin, peptides derived from secreted necrosis- and ethylene-inducing-like proteins (nlp20/nlp24)) (Kunze et al., 2004; Boller and Felix, 2009; Dodds and Rathjen, 2010; Thomma et al.,

2011; Oome et al., 2014; Oome and Van den Ackerveken, 2014; Kanyuka and Rudd, 2019). Additionally, PRRs sense plant-derived ligands such as damage-associated molecular patterns (DAMPs). Known recognized plant-elicitors are peptides (plant elicitor peptides (Peps) derived from precursor peptides (PROPEPs)), extracellular ATP (eATP), host cell wall-derived degradation products (α-1,4-linked galacturonic acid (OGs), cellulose-derived oligomers)), which might be released after plant tissue penetration and/or host cell damage by the invading pathogen. (Chisholm et al., 2006; Huffaker et al., 2006; Boller and Felix, 2009; Postel and Kemmerling, 2009; Ferrari et al., 2013; Choi and Klessig, 2016; Souza et al., 2017). MAMP or DAMP recognizing PRRs are localized at the PM and are categorized as receptor-like-kinases (RLKs) and receptor-like proteins (RLP) depending on the presence or absence of an intracellular kinase domain (Boller and Felix, 2009). PRRs sensing carbohydrate-derived ligands may contain extracellular lysin motifs (LysM), epidermal growth factor (EGF)-like domains or lectin motifs, while PRRs perceiving proteins or peptides typically contain leucine-rich repeat (LRR) domains (Macho and Zipfel, 2015; Tang et al., 2017). Additionally, PRRs are mostly dependent on specialized co-receptors for signal transduction leading to immune responses (Macho and Zipfel, 2014; Wan et al., 2019).

For example, the best-studied *Arabidopsis* lysin-motif (LysM)-RLK CHITIN ELICITOR RECEPTOR KINASE1 (CERK1) perceives the fungal cell wall-derived carbohydrate chitin, which is composed of β-1,4-linked N-acetylglucosamine. The binding of polymeric chitin or chitin octamers induces homodimerization of CERK1 and subsequent auto-phosphorylation which is needed for signal transduction and activation of immune responses (Petutschnig et al., 2010; Liu et al., 2012). Besides CERK1, the kinase-dead LysM-RLKs LYK4 and LYK5 were demonstrated to bind chitin (Cao et al., 2014). CERK1 forms a receptor complex with LYK4 and LYK5, which is required for efficient downstream signaling and activation of defense (Petutschnig et al., 2010; Wan et al., 2012; Cao et al., 2014; Erwig et al., 2017)

In *Arabidopsis,* the two LysM RLP LysM-CONTAINING RECEPTOR-LIKE PROTEIN1 (LYM1) and LYM3 were shown to act in the perception of the bacterial cell wall component PNG (Willmann et al., 2011). LYM2, which is closely related to LYM1 and LYM3, was shown to perceive chitin. However, LYM2 is not required for activation of chitin-induced defense responses but regulates plasmodesmata flux by callose deposition in response to chitin (Faulkner et al., 2013; Cheval et al., 2020).

Oligogalacturonides (OGs) function as carbohydrate DAMP. These α-1,4-linked galacturonic acid fragments are suggested to be derived from the hydrolysis of plant cell wall component homogalacturonan by microbial polygalacturonases and are sensed by the RLK WALL-ASSOCIATED KINASE1 (WAK1) (Cabrera et al., 2008; Ferrari et al., 2013).

Recently, β-1,3-glucan oligosaccharides were shown to trigger immune responses in a CERK1-dependent manner. β-1,3-glucan oligosaccharides are present in the form of callose in the plant but are also abundant in the cell wall of fungi. However, the corresponding receptor involved in the perception of β-1,3-glucan oligosaccharides remains elusive (Mélida et al., 2018).

The *Arabidopsis* flagellin sensing 2 (FLS2) PRR is a well-characterized leucine-rich-repeat (LRR)-RLK which recognizes the proteinaceous PAMP flg22, an N-terminal 22 amino acid epitope of flagellin (Gómez-Gómez und Boller 2000; Chinchilla et al., 2006; Robatzek et al., 2007). Another important LRR-RLK is the ELONGATION FACTOR THERMO UNSTABLE RECEPTOR (EFR), which perceives the bacterial EF-Tu and its derived N-terminal peptide elf18 (Kunze et al., 2004; Zipfel et al., 2006). The kinase active BRI1-ASSOCIATED RECEPTOR KINASE 1 (BAK1) is a LRR-RLK and functions as a co-receptor for many LRR-RLK. Upon ligand perception, BAK1 forms a heteromeric complex with either FLS2 or ERF, which leads to transphosphorylation events at the intracellular kinase domain (Chinchilla et al., 2007; Heese et al., 2007; Schulze et al., 2010; Roux et al., 2011). Furthermore, the receptor-like cytoplasmic kinase (RLCK) BOTRYTIS-INDUCED KINASE 1 (BIK1) is also present in this receptor complex. Transpohosphorylation events between the respective LRR-RLK, BAK1 and BIK1 lead to the release of BIK1 from the receptor complex and activation of downstream immune signaling (Lu et al., 2010; Zhang et al., 2010).

RLPs, such as RLP23 sense a peptide of 20 amino acids from the NECROSISAND ETHYLENE INDUCING PEPTIDE1 (NEP1)-LIKE PROTEINs (NLPs; nlp20). Since RLP23 lacks an intracellular kinase domain, it requires the adaptor LRR-RLK SUPPRESSOR OF BIR1-1 (SOBIR1) and the co-receptor BAK1 for downstream signal transduction (Bi et al., 2014; Albert et al., 2015).

In *Arabidopsis*, the most prominent receptors of peptide DAMPs are the LRR-RLKs PLANT ELICITOR PEPTIDE RECEPTOR1 (PEPR1) and PEPR2. Both receptors perceive Peps, which are derived from the precursor PROPEPs, small proteins of about 100 amino acids (Huffaker et al., 2006; Bartels and Boller, 2015). Upon DAMP perception, PEPR1 and PEPR2 associate with BAK1 and BIK1, leading to phosphorylation events and intracellular signal transduction (Liu et al., 2013; Yamada et al., 2016).

Perception of extracellular MAMPs and DAMPs by PRRs results in MAMP/PAMP-triggered immunity (MTI/PTI), which can attenuate or stop colonization of most pathogens (Figure 1, 1) (Jones and Dangl, 2006; Boller and Felix, 2009; Thomma et al., 2011). Plant defense responses associated with MTI/PTI include enhanced intracellular Ca^{2+} levels, production of reactive oxidative species (ROS) in the apoplast via NADPH oxidases, activation of mitogen-activated protein (MAP) kinase cascades, leading to phosphorylation of proteins and signal transduction, accumulation of antimicrobial defense molecules, callose deposition and expression of defense-related genes (Boller and Felix 2009; Dodds and Rathjen 2010; Macho and Zipfel 2014). However, adapted pathogens have developed special mecha-

nisms to overcome MTI/PTI by secretion and/or delivery of effector proteins into the host plant to actively suppress plant immunity, manipulate the hosts metabolism, facilitate nutrition and regulation of the infection process (Figure 1, 2) (Birch et al., 2006; Block et al., 2008). These effectors are contributing to pathogen virulence resulting in effector-triggered susceptibility (ETS) of the plant(Figure 1, 3) (Jones and Dangl, 2006; Thordal-Christensen, 2020). Pathogenic gram-negative bacteria utilize a Type III secretion system for direct injection of virulence effector proteins into the plant cell (Cornelis and Van Gijsegem, 2000). For effector secretion, fungal pathogens use internal hyphae or specialized feeding structures, the haustoria (Selin et al., 2016). Virulence effectors of fungi and oomycetes are grouped into apoplastic and cytoplasmic molecules. Apoplastic effectors stay and act in the interaction zone between the fungal hyphae and the plant PM, while cytoplasmic effectors are taken up and exert their function inside the plant cell. However, the molecular mechanisms of the underlying delivery process of effector proteins from eukaryotic pathogens into the plant cell remain poorly understood (Win et al., 2012; Petre and Kamoun, 2014).

Plants can sense cytoplasmic effectors directly or indirectly, activating effector-triggered immunity (ETI), also known as intracellular immunity. The recognition of host-adapted microbes is mediated by an intracellular plant receptor, upon sensing of an intracellular effector protein or effector modifications on host molecules (Figure 1, 8) (Jones and Dangl, 2006; Wang et al., 2020). Previously, the underlying genetic mechanisms of ETI were called “gene-for-gene resistance” describing recognition of effectors encoded by pathogen avirulence (AVR) genes by specialized resistance (R) proteins of the host (Flor, 1971). PTI and ETI were commonly considered as two distinct immune signaling pathways and have been thought to developed sequentially (Jones and Dangl, 2006). ETI is often resulting in disease resistance associated with the induction of a hypersensitive response (HR), also known as local programmed cell death to limit further spreading of biotrophic pathogens inside the plant tissue (Chisholm et al., 2006; Jones and Dangl, 2006). Interestingly, increasing knowledge of cell-surface and intracellular-mediated immunity indicates no clear borders between PTI and ETI. Recent studies revealed overlapping and synergistically working immune mechanisms and common downstream signaling pathways necessary to induce a robust disease resistance (Ngou et al., 2020; Pruitt et al., 2020; Yuan et al., 2020). In *Arabidopsis,* two PRR/co-receptor triple mutants *fls2/efr/cerk1* and *bak1/bkk1/cerk1* failed to induce ETI when challenged with *Pseudomonas syrinagae* bacteria. ROS production was shown to be an important early signaling event connecting PRR and ETI signaling cascades (Yuan et al., 2020). Furthermore, intracellular receptors were demonstrated to be required for both ETI and PTI (Pruitt et al., 2020).

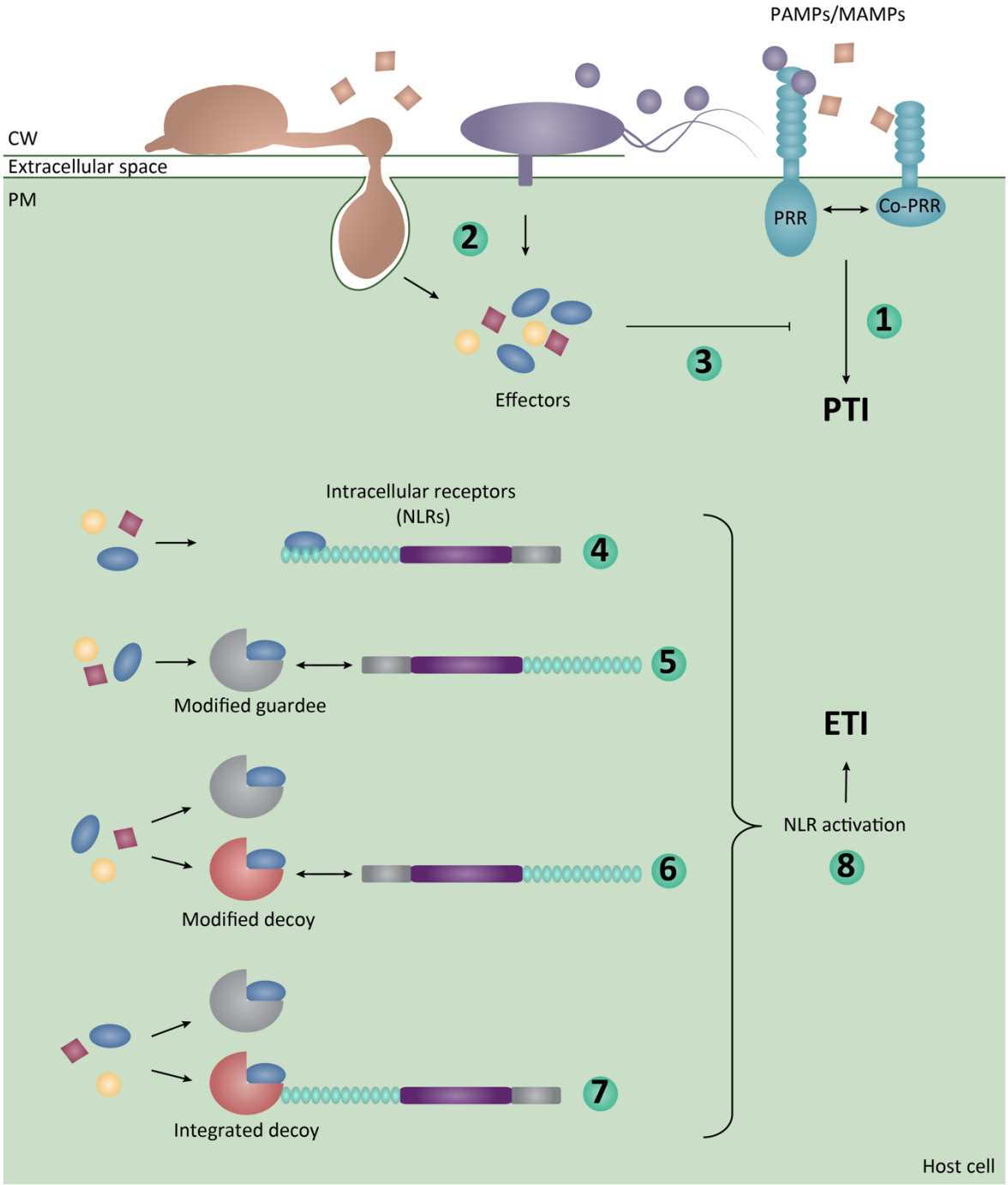

Figure 1. Schematic representation of cell-surface and intracellular plant immunity. Perception of extracellular MAMPS/DAMPs via pattern recognition receptors (PRRs), which typically interact with co-receptors (Co-PRRs) for signal transduction to initiate PAMP/MAMP triggered immunity (PTI/MTI) **(1)**. Adapted pathogens secrete and deliver effector molecules into the plant cell **(2)** to actively suppress PTI signaling **(3).** Intracellular immunity is mediated by nucleotide-binding leucine-rich repeat (NLR) proteins directly recognizing effector proteins by physical binding **(4)** or indirectly by sensing and monitoring functional target proteins of effectors **(5)** or decoys of effector targets **(6)**. NLRs often contain integrated domains that mimic an effector target, allowing sensing of effectors through direct binding **(7)**. Effector perception induces NLR activation and effector-triggered immunity (ETI) **(8)**. Figure modified from Cesari *et al.*, 2018 and Bentham *et al.*, 2020.

Intracellular immunity is mediated and transduced by intracellular receptors, typically nucleotide-binding, leucine-rich repeat receptor proteins (NB-LRR or NLRs) (Takken and Tameling, 2009). These immune receptors are characterized by a LRR domain at the C-terminus and a central nucleotide-binding ARC domain (NB-ARC, nucleotide-binding domain shared by APAF1, R gene products and CED4) (Sukarta et al., 2016; Bentham et al., 2017). At the N-terminus, the receptors may contain either a coiled-coil (CC) domain, an RPW8 (resistance to powdery mildew 8)-like CC domain (CC-RPW8) or a Toll/Interleukin-1-receptor (TIR) region (Duxbury et al., 2016; Jones et al., 2016). The LRR domain is implicated in protein-protein interaction, effector recognition and was proposed to be important for autoinhibition of the immune receptor activity (Dodds et al., 2004; Faustin et al., 2007; Bentham et al., 2017). The central NB domain serves as a molecular switch regulated by nucleotide-binding upon pathogen effector recognition. Effector molecule perception is transduced through this domain by switching from the inactive ADP-bound “off-state” to the active ATP-bound “on-state” (Takken and Tameling, 2009). The N-terminal domains mediate immune signaling, classifying the immune receptors into TIR-type NLRs (TNLs), CC-type NLRs (CNLs) and RPW8-NLRs (RNLs) (Shao et al., 2016). However, the direct functions of CC and TIR domains are currently unknown. In transient expression experiments, these N-terminal domains activate cell-death responses in the absence of an effector molecule revealing a role in cell death execution (Zhang et al., 2017a).

Recognition of the pathogen effector by NLRs can be either direct or indirect. Different models describe the detection of effectors by intracellular receptors. Direct binding is based on the physical binding of the effector molecule to the NLR leading to receptor activation (Figure 1, 4) (Dodds et al., 2006; Cui et al., 2015). For the indirect perception of effectors, the guard hypothesis predicts that NLR proteins monitor target proteins of effectors. Effector modifications on these host targets are perceived by the NLR, resulting in the induction of immune responses (Figure 1, 5). In contrast to the guard hypothesis, the decoy model proposes that during evolution plants developed gene duplications that mimic a target of a pathogen effector (Figure 1, 6) (Hoorn and Kamoun, 2008). The integrated domain (ID)-model is an evolutionary innovation (Figure 1,7). In addition to their conserved NLR domain architecture, some NLRs contain unconventional domains (Cesari et al., 2014). These IDs mimic decoys of effector targets, allowing physical interaction and recognition of the corresponding effector molecule (Maqbool et al., 2015; Ortiz et al., 2017). Perception of the effector molecules induces NLR activation leading to conformational changes such as domain rearrangements and/or oligomerization of the immune receptor, downstream signaling and defense responses. One example is the *Arabidopsis* sensor CNL HopZ-activated resistance 1 (ZAR1). In an inactive state, ZAR1 interacts with receptor-like cytoplasmic kinases (RLCKs) (Wang et al., 2019b, 2019a). Effector-modified decoy proteins can bind to the ZAR1-RLCK dimer. This induces conformational changes of ZAR1, causing

nucleotide exchange of ADP by ATP. Upon ATP binding, the active ZAR1 forms a pentameric complex, called the resistosome, which is structurally similar to the mammalian inflammasome. This pentameric complex is integrated into membranes via the N-terminal CC domains causing pore formation and initiation of a cell death response, putatively through perturbation of the membrane or ion efflux (Burdett et al., 2019; Dangl and Jones, 2019; Wang et al., 2019b, 2019a). Recent studies revealed that NLRs can function as singletons, receptor pairs or tightly connected NLR networks. NLR singletons are considered to represent an evolutionary ancient mechanism and that NLR pairs or networks evolved during evolutionary processes due to diversification and functional specialization (Wu et al., 2018; Adachi et al., 2019; Jubic et al., 2019). NLR singleton receptors such as ZAR1 function autonomously by combining both detection of the pathogen and inducing an immune response (Adachi et al., 2019). Functional specialization resulted in NLR pairs, divided into sensor NLRs that directly interact or sense effector target modifications and helper NLRs that are required for effective downstream signaling (Adachi et al., 2019; Jubic et al., 2019). Recent studies revealed that signaling functions of connected helper NLR networks are essential for a majority of sensor NLRs. For instance, the two distinct helper NLR classes ACTIVATED DISEASE RESISTANCE1 (ADR1) and N REQUIREMENT GENE1 (NRG1) are required for downstream signaling of a large number of sensor NLRs after pathogen perception (Jubic et al., 2019; Wu et al., 2019). In addition to helper NLRs, downstream ETI signaling of TNLs and some CNLs rely on the function of the lipase-like protein ENHANCED DISEASE SUSCEPTIBILITY1 (EDS1), whereas the majority of CNLs require NON-RACE-SPECIFIC DISEASE RESISTANCE 1 (NDR1) for signaling (Wiermer et al., 2005; Xiao et al., 2005; Wagner et al., 2013). EDS1 forms heterodimers with two related defense-regulators PHYTOALEXIN DEFICIENT 4 (PAD4) or SENESCENCE ASSOCIATED GENE 101 (SAG101). EDS1-PAD4 complexes are located in the cytosol as well as the nucleus, whereas exclusively nuclear complexes are formed by EDS1-SAG101 (Feys et al., 2005). It is proposed that TNL resistance signaling requires EDS1-helper NLR complexes. EDS1-PAD4-ADR1 signaling mediates transcriptional changes leading to restriction of pathogen growth, whereas EDS1-SAG101-NRG1 are suggested to be required for induction of HR signaling (Cui et al., 2015; Castel et al., 2019; Lapin et al., 2019; Wang et al., 2020). ETI downstream signaling results in disease resistance overlapping with PTI, such as accumulation of ROS, activation of MAPK cascades and transcriptional induction of defense genes (Jones and Dangl, 2006; Cui et al., 2015). Additionally, ETI induces HR at the site of infection and systemic acquired resistance (SAR) in non-infected parts of the plant. SAR, predominantly against biotrophic and hemibiotrophic pathogens, is associated with the accumulation of the phytohormone salicylic acid (SA). SA-mediated signaling leads to the expression of pathogenesis-related (PR) genes and disease resistance to a broad spectrum of pathogens (Durrant and Dong, 2004; Gao et al., 2015).

1.2 Cell polarization in pathogen defense

Upon pathogen recognition, the plant cell undergoes various changes including morphological alterations, transcriptional- and metabolic reprogramming and dynamic rearrangements of cellular components (Schmelzer, 2002). Pathogen-triggered cell polarization, associated with protein translocation and recruitment of organelles to the sites of plant-pathogen interactions is considered to be a general response of monocot and dicot plants (Schmelzer, 2002).

In response to fungal penetration attempts, cell-autonomous and focal accumulation of the cytoplasm, focal accumulation of hydrogen peroxide (H_2O_2), transport of the nucleus, peroxisomes, mitochondria and chloroplasts, rearrangement of the cytoskeleton and the ER was observed in proximity to the invasion sites (Gus-Mayer et al., 1998; Koh et al., 2005; Hardham et al., 2008; Fuchs et al., 2016; Branco et al., 2017; Ding et al., 2019). Moreover, a local mechanical stimulus using a microneedle triggered similar cell polarization processes as observed after a pathogen attack (Gus-Mayer et al., 1998; Koh et al., 2005; Hardham et al., 2008; Branco et al., 2017).

The cytoplasm was shown to move and accumulate at sites of attempted invasion of compatible and incompatible pathogens during the early stages of attack (Takemoto et al., 2003; Koh et al., 2005). Furthermore, cytoplasmic strands appeared oriented towards the plant-pathogen interaction site (Freytag et al., 1994; Kobayashi et al., 1994). Often, cytoplasm aggregation is suggested to be associated with plant resistance and with the deposition of cell wall material and toxins. However, the exact function and mechanisms that control cytoplasm aggregation and streaming remain elusive (Takemoto et al., 2003).

The cytoskeleton plays an important role during cellular defense. Actin filaments start to align and microtubules form radial arrays underneath fungal contact sites (Kobayashi et al., 1992, 1994, 1997). Kobayashi *et al*., 1997 and Takemoto *et al*., 2003 revealed that actin filaments are consistently observed to rearrange in proximity to the pathogen invasion site in incompatible and compatible interactions, whereas the response of microtubules is highly variable in various plant-microbe interactions. Inhibitors were used to analyze polymerization and depolymerization of microtubule- and actin filaments in more detail. Inhibition of actin filaments causes increased fungal penetration in various compatible and incompatible interactions (Tomiyama et al., 1982; Hazen and Bushnell, 1983; Kobayashi et al., 1997; Yun et al., 2003; Jarosch et al., 2005). Furthermore, movement of the nucleus as well as the transport of chloroplasts, peroxisomes, mitochondria, the ER and Golgi stacks were shown to rely on actin filaments (Liebe and Quader, 1994; Van Gestel et al., 2002; Wada and Suetsugu, 2004). In addition, deposition of callose and cell wall material, protein accumulation and cell death responses were compromised by actin inhibition, whereas microtubule inhibitors showed only

minor effects (Kobayashi et al., 1997; Skalamera and Heath, 1998, 1998). *eds1* mutants, compromised in post-invasive resistance, showed breakdown of nonhost resistance (NHR; see 1.3.1) against the incompatible powdery mildew *Blumeria graminis f. sp. tritici* upon actin inhibition (Yun et al., 2003). These results indicate the importance of actin filaments for pre-invasive NHR.

Cytoplasmic aggregation and cytoskeleton rearrangement are accompanied by local accumulation of H_2O_2, which was shown to support the strengthening of the papilla due to cross-linking reactions. In addition, the H_2O_2 can be toxic for the invading pathogen and leads to transcriptional activation of defense-related genes (Levine et al., 1994; Mellersh et al., 2002). Furthermore, H_2O_2 was shown to elicit relocalization of chloroplasts around the nucleus during plant-pathogen interactions in *N. benthamiana* (Ding et al., 2019). Transport of chloroplast towards the nucleus was suggested to be required for chloroplast-nuclear communication through retrograde signaling mechanisms, which transduce developmental and environmental cues to regulate transcriptional changes (Chan et al., 2016). Upon pathogen attack, chloroplasts function as the source of defensive and signaling compounds such as ROS, both phytohormones jasmonic acid (JA), SA and calcium burst in the cytoplasm (Nomura et al., 2012; de Torres Zabala et al., 2015; Pogorelko et al., 2016; Park et al., 2017; Sowden et al., 2018). Chloroplasts were shown to be transported in association with microtubules and are interconnected to the nucleus via actin filaments (Kumar et al., 2018).

Besides the movement of the nucleus to the fungal invasion site, the nucleus undergoes dynamic changes during immune responses. The nucleus in penetrated cells was shown to enlarge due to enhanced transcriptional activation. Approximately, 20 % of the *Arabidopsis* genome was differentially expressed upon pathogen challenge (Maleck et al., 2000; Tao et al., 2003).

Similar to the nucleus, peroxisomes are transported to the plant-microbe interaction sites (Koh et al., 2005; Hardham et al., 2008). These cell organelles are enclosed by a single membrane and are involved in various oxidizing processes such as photorespiration (Liepman and Olsen, 2001, 2003), and phytohormone biosynthesis, including auxin (indole acetic acid, IAA) and JA biosynthesis (Bartel et al., 2001; Zolman et al., 2001; Feussner and Wasternack, 2002; Schneider et al., 2005), mobilization of lipids (Goepfert et al., 2005), signal transduction and detoxification of ROS (del Río et al., 2002; Foyer and Noctor, 2005). Peroxisomes are suggested to be involved in signal transduction and detoxification by the degradation of ROS generated at plant-microbe interaction sites (del Río et al., 2002; Apel and Hirt, 2004; Mittler et al., 2004; Koh et al., 2005; Torres and Dangl, 2005).

Mitochondria are important organelles in defense against pathogens. Upon pathogen perception, mitochondrial function is influenced by cytosolic ROS, calcium and SA, which are derived from different defense pathways (Mur et al., 2008; Colombatti et al., 2014). Cytosolic ROS, SA and calcium were shown to influence the mitochondrial membrane potential resulting in alterations of mitochondrial

respiration. Changes in the mitochondrial respiration lead to the formation of mitochondrial ROS and to alterations of the redox status of the cell, which results in transcriptional reprogramming in the nucleus via retrograde signaling. In order to stop pathogen colonization, mitochondrial ROS induces programmed cell death responses (Colombatti et al., 2014). Mitochondria were shown to accumulate at pathogen invasion sites in the dicot *Arabidopsis* (Fuchs et al., 2016) and the monocot barley (Kunoh, 1972) indicating that this phenomenon is an evolutionally ancient and conserved mechanism. Moreover, accumulation and immobilization of mitochondria are triggered by UV light (Gao et al., 2008), methyl jasmonate (Zhang and Xing, 2008), oxylipin 9-hydroxy-10,12,15-octadecatrienoic acid (Vellosillo et al., 2013) and ROS (Scott and Logan, 2008).

The ER is highly dynamic and rearranges in proximity to attempted fungal invasion sites (Fuchs et al., 2016). Moreover, the ER was shown to reorganize around the haustoria of *Erysiphe pisi* (Leckie et al., 1995). This organelle plays an important role in the storage of Ca^{2+} and is involved in intracellular Ca^{2+} signaling in pathogen defense. Moreover, the ER is required for the production and quality control of proteins destined for the vacuole, apoplast or PM, including defense-related protein such as PRRs (Padmanabhan and Dinesh-Kumar, 2010; Schäfer and Eichmann, 2012).

Besides ER rearrangement and movement of the nucleus, other components of the endomembrane system such as Golgi stacks and multivesicular bodies (MVBs) reorganize upon pathogen attack. Golgi stacks were shown to accumulate and move in close proximity to the penetration site in different *Arabidopsis*-oomycete interactions suggesting a temporary stop at the penetration site. In addition, the accumulation of Golgi stacks at the invasion site changes over time (Takemoto et al., 2003). Koh *et al*., 2005 revealed the accumulation of Golgi stacks near haustorial complexes. Furthermore, Golgi-derived vesicles such as MVBs accumulate at pathogen penetration sites to facilitate various plant defense responses (Ruano and Scheuring, 2020).

1.3 The *Arabidopsis* - powdery mildew pathosystem

1.3.1 Powdery mildews - a biotrophic model system

Powdery mildew disease occurs on a wide variety of plant species and is caused by Ascomycete fungi of the order *Erysiphales.* These include pathogens that infect and cause significant losses to economically important crop species such as wheat, barley, tomato and grapevine (Hückelhoven, 2005; Micali et al., 2008). Powdery mildew fungi are divided into five tribes (*Erysipheae*, *Golovinomycetinae*, *Cystotheceae*, *Phyllactinieae*, *Blumerieae*), comprising approximately 500 known species in total (Micali et al., 2008; Braun, 2011). Powdery mildews are obligate biotrophs that invade and colonize epidermal cells. The life cycle of these fungi includes both asexual and sexual reproduction. In the asexual life cycle, powdery mildew disease is characterized by the formation of white powder-like pus-

tules on infected plant tissue, representing fungal mycelium and conidiophores, a specialized conidiospore-producing hypha (Eichmann and Hückelhoven, 2008; Micali et al., 2008; Kuhn et al., 2016). Powdery mildew conidiospores (asexual spores) are distributed by wind in the environment. Following landing on the plant surface, the spore germinates and forms a short primary germ tube, mediating attachment to the plant surface. Upon sensing of plant surface signals, a second germ tube emerges from the conidiospore which differentiates into a specialized penetration structure, the so-called appressorium (Both et al., 2005; Kuhn et al., 2016). Primary or secondary germ tube formation is dependent on the genera of the invading powdery mildew (Green et al., 2002). For efficient penetration of the plant cuticle and cell wall, appressoria are generating a high turgor pressure to facilitate mechanical entry which is likely aided by the secretion of plant cell wall-degrading enzymes (PCWDE) (Pryce-jones et al., 1999). Successful plant cell wall penetration without disruption of the plasma membrane might lead to the formation of a specialized feeding structure, known as the haustorium. The haustorium is enveloped by a plant-derived extrahaustorial membrane (EHM) generating a plant-fungus interaction zone, suggested of being important for nutrient uptake and effector secretion (O'Connell and Panstruga, 2006; Kuhn et al., 2016). After haustorium formation, epiphytic growth is initiated by the formation of secondary hyphae leading to rapid proliferation and generation of powdery mildew colonies. 3-7 days post infection (dpi), conidiophores are produced which generate and release conidiospores to complete the asexual life cycle (Kuhn et al., 2016). In temperate climates, powdery mildews can switch to sexual reproduction and give rise to cleistothecia (fruiting bodies), which contain ascospores (sexual spore) enclosed in asci. In fall, these structures are visible as dark brown spots on leaves and can persist throughout the winter periods outside of the host plant (Kuhn et al., 2016).

The *Arabidopsis*-Powdery mildew pathosystem is an excellent tool to study and understand molecular processes regulating powdery mildew infection. In a compatible interaction between the dicotyledonous plant *Arabidopsis* and the powdery mildew *Golovinomyces orontii,* the adapted pathogen efficiently suppresses plant immune responses to invade and complete the asexual life cycle. Approximately 70 % of *G. orontii* penetration attempts are successful at 24 hpi (Lipka et al., 2005). However, in the incompatible interaction between *Arabidopsis* and the barley powdery mildew *Blumeria graminis f.sp. hordei* (*Bgh*), the non-adapted powdery mildew fails to invade the majority of attacked epidermal cells and is not able to reproduce on the non-host plant. Similar to *Bgh*, the non-adapted pea powdery mildew *E. pisi* fails to successfully reproduce on *Arabidopsis*. One day after inoculation, approximately 95% and 75% of *Bgh* and *E. pisi* attempted penetration events are restricted (Figure 3) (Lipka et al., 2005, 2010).

Nonhost resistance (NHR) refers to the ability of an entire plant species to withstand all attempts of infection and colonization of a pathogen species. This type of broad-spectrum resistance is considered to be the most robust form of plant immunity (Heath, 2000; Nürnberger and Lipka, 2005; Lipka et al., 2010; Kuhn et al., 2016; Lee et al., 2016). However, NHR is a phenomenological concept rather than a molecular mechanism (Panstruga and Moscou, 2020). NHR is proposed to require the same immunity-related components and similar principles as other types of plant immunity such as intracellular immunity (ETI), systemic acquired resistance (SAR) and basal immunity referred to as the remaining immune responses after a pathogen effectively overcomes plant species-specific defense mechanisms (Panstruga and Moscou, 2020). Pre-invasive NHR relies on preformed constitutive defenses including preformed chemical and physical barriers as well as timely and local inducible defenses (Nürnberger and Lipka, 2005; Lipka et al., 2010). In contrast to preformed barriers, inducible defenses require recognition of a pathogen by cell-surface immune receptors and effective downstream signal transduction (Lipka et al., 2010; Panstruga and Moscou, 2020). Inducible defense responses include cytoskeletal rearrangements, polarized secretion events, organelle movement, accumulation of proteins at the sites of attempted fungal invasion, production and discharge of toxic compounds and focal cell wall remodeling (Nürnberger and Lipka, 2005; Ellis, 2006; Lipka et al., 2010; Panstruga and Moscou, 2020). Both adapted and non-adapted powdery mildews induce the formation of cell wall remodeling including the generation of a small papilla underneath the attempted penetration site (Figure 2A) (Collins et al., 2003; Assaad et al., 2004; Koh et al., 2005). The papilla is enriched with the high molecular weight β-1,3-glucan polymer callose. Besides callose, papillae contain ROS, pectic polysaccharides, phenolic compounds including lignin, peroxidases and cell wall structural proteins. Papillae provide cell wall reinforcement to generate an effective barrier against fungal invasion (Zeyen et al., 2002; Underwood, 2012; Ellinger and Voigt, 2014; Kuhn et al., 2016). However, some pathogens successfully overcome pre-invasive defenses leading to the activation of post-invasive NHR, which is typically associated with callose encasement of haustoria (Figure 2B), local HR-like cell death responses (Figure 2C) and SA-signaling to restrict fungal proliferation and nutrient uptake (Lipka et al., 2005; O'Connell and Panstruga, 2006). Similar to local HR symptoms in NHR, HR-like cell death responses are observed for isolate-specific resistance mediated by intracellular immune receptors indicating potential involvement of cytoplasmic immune receptors and recognition of effectors in NHR (Panstruga and Moscou, 2020).

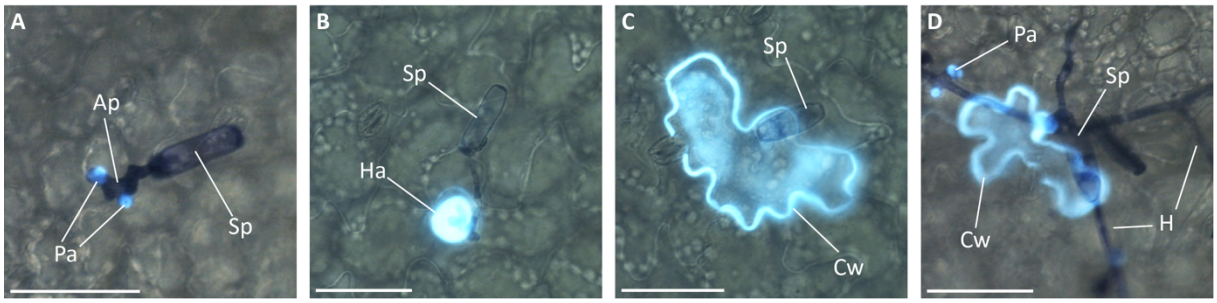

Figure 2. Pre- and post-invasive NHR are involved in defense against non-adapted powdery mildews in *Arabidopsis*. *Arabidopsis* leaf epidermal cells 72 hpi with *E. pisi*. Fungal structures are stained with Coomassie brilliant blue (dark blue) and callose is stained with Aniline blue (light blue). **(A)** Pre-invasive defense mechanisms such as papillae formation prevent effective fungal penetration. In case of fungal entry, post-invasive NHR results in callose encasement of haustoria **(B)** or local HR-like cell death formation on attacked epidermal cells terminating further fungal development **(C, D)**. In rare cases, *E. pisi* develops hyphae on the nonhost plant *Arabidopsis* **(D)**. Ap, appressoria; Pa, papilla; Sp, conidiospore; Ha, haustorium; Cw, cell wall; H, Hyphae. Scale bar 10 µm.

1.3.2 Powdery mildew entry control

A Forward genetic screen for chemically induced *Arabidopsis* mutants, identified four mutants with impaired nonhost interaction upon *Bgh* and *E. pisi* infection. Isolated mutants exhibited enhanced invasion and localized cell death formation indicating an essential role of the affected genes in pre-invasive NHR against non-adapted powdery mildews. The identified molecular components PENETRATION1 (PEN1, 1.5.2), PEN2 (1.6.2), PEN3 (1.6.7) and PEN4 (1.6.6) have a function in polarized secretion, activation and transport of defense molecules to the site of attempted fungal invasion. In addition, PEN proteins focally accumulate in close proximity to the powdery mildew invasion sites (Collins et al., 2003; Assaad et al., 2004; Lipka et al., 2005; Stein et al., 2006; Hématy et al., 2020). Genetic analysis of penetration resistance against *Bgh* revealed that *pen2 pen3* and *pen2 pen4* double mutants showed similar *Bgh* invasion rates as the single mutants. In contrast, the *pen1 pen3* double mutants exhibited enhanced levels of successful *Bgh* penetration attempts (Lipka et al., 2005; Stein et al., 2006; Hématy et al., 2020). These genetic tests suggest that PEN2, PEN3 and PEN4 function in the same pathway, which is distinct from the PEN1-dependent mechanism. In agreement with this notion, metabolite quantification in *pen2* and *pen4* single mutants revealed similar defects in pathogen-triggered biosynthesis of IG-derived defense compounds (Matern et al., 2019; Hématy et al., 2020). Furthermore, *pen2* and *pen3* mutations affect broad-spectrum disease resistance against several and distantly related filamentous pathogens such as the adapted powdery mildews *G. orontii* and *Golovinomyces cichoracearum,* the adapted necrotrophic fungus *Plectosphaerella cucumerina* and the hemibiotrophic non-adapted oomycete *Phytophthora infestans* (Lipka et al., 2005; Stein et al., 2006; Sanchez-Vallet et al., 2010). In contrast, *pen1* mutations exclusively influence penetration resistance against the non-adapted powdery mildews *Bgh* and *E. pisi* (Lipka et al., 2005). Additionally, phylogenetic analysis suggested that *PEN2* is a recent innovation of the *Arabidopsis* genome (Con-

sonni et al., 2006; Lipka et al., 2010), whereas PEN1 is likely an ancient component in powdery mildew entry control (Collins et al., 2003). Taken together, these findings support the concept that PEN1 acts in an independent powdery mildew entry control mechanism, whereas PEN2 operates together with PEN3 and PEN4 (Lipka et al., 2005; Stein et al., 2006; Hématy et al., 2020).

PEN1-mediated pre-invasive resistance relies on vesicle trafficking, whereas PEN2, PEN3 and PEN4 contribute to indole glucosinolate (IG)-mediated penetration resistance. Therefore, the role of vesicle transport and IGs in plant immunity are reported in the next chapters in more detail.

1.4 Vesicle trafficking in plant immunity

1.4.1 Multivesicular bodies/late endosomes in plant immunity

A recent study indicates that the dynamics of the endomembrane system are important for cell-surface and intracellular immunity in plants (Ruano and Scheuring, 2020). This intracellular membrane system is involved in signal transduction and is required for secretion of biomolecules, uptake of substances and transport to intracellular locations. Different endomembrane compartments are connected via the transport of vesicles (Figure 3) (Foresti and Denecke, 2008).

After folding and maturation of newly synthesized PM-localized proteins in the ER, they follow the secretory pathway via Golgi stack for cell-surface localization (Figure 3, 1). Some cell-surface localized proteins, including some PRRs constitutively recycle between the PM and the trans-Golgi network/early endosomes (TGN/EE) (Figure 3, 2). In the endocytosis pathway, extracellular substances or cell-surface localized proteins are internalized into the cell via endocytic vesicles (Figure 3, 3) (Fan et al., 2015). Following the release of endocytic vesicles from the PM, they fuse with the TGN/EEs (Chen et al., 2011; McMahon and Boucrot, 2011). Over time, EEs mature into late endosomes (LEs) (Figure 3, 4) (Chen et al., 2011). Lipid bilayer-enclosed LEs are multivesicular bodies (MVBs) harboring intraluminal vesicles (ILV), which develop from invagination and budding of a portion of the limiting membrane into the lumen of the MVB. The cargoes of ILVs are either degraded by fusion of MVBs with vacuoles and lysosomes or are released as exosomes into the extracellular space upon fusion of the MVB with the PM. In this process, the outer membrane of MVBs is fused with the tonoplast, the membrane of lysosomes or the PM (Li et al., 2018; Ruano and Scheuring, 2020). TGN-derived endosomes transport newly synthesized proteins to either the lumen of the vacuole or the tonoplast (Li et al., 2018). Degradation of MVB cargo in the vacuole or cargo recycling to the PM requires various sorting mechanisms (Ruano and Scheuring, 2020). ILV budding from the limiting membrane was shown to require the ENDOSOMAL SORTING COMPLEX REQUIRED FOR TRANSPORT (ESCRT) machinery (Wollert and Hurley, 2010). The plant ESCRT machinery consists of three ESCRT sub-complexes, including ESCRT-I, -II and -III. The ESCRT complex associates with the endosomal membrane of the

TGN/EEs, where it functions in sorting and clustering of ubiquitinated cargo and subsequent budding of the limiting membrane into the lumen of MVBs (Raiborg and Stenmark, 2009; Otegui, 2018).

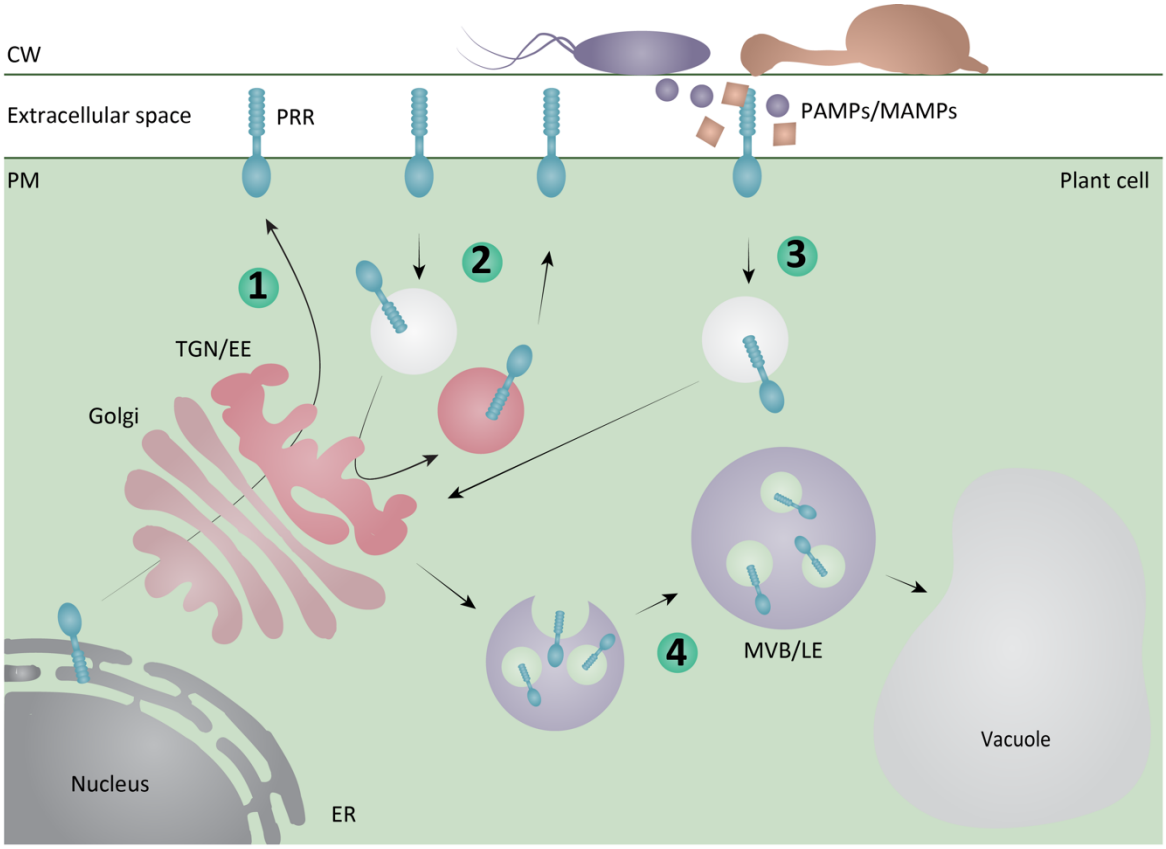

Figure 3. Schematic representation of endocytosis in plants. (1) Newly synthesized and cell-surface destined proteins, including PRRs are folded and mature in the ER. These proteins follow the secretory pathway via Golgi stack for localization to the PM. **(2)** Some cell-surface localized proteins constitutively recycle between the PM and the TGN. **(3)** PRRs monitor the cells environment for potential pathogens. Upon ligand perception (MAMPs/PAMPs), PRRs are internalized into the cell via endocytic vesicles. These vesicles fuse with the TGN/EEs. Over time, EEs mature into MVBs/LEs. MVBs/LEs contain ILVs, which develop from invagination and budding of the limiting membrane into the lumen of the MVB/LE. MVBs/LEs are directed to the vacuole. Upon fusion of MVBs/LEs with the vacuole, the cargoes of ILVs are degraded. Figure modified from Postma et al., 2016.

MVBs perform various functions within the secretory pathway that are important for plant immunity (Li et al., 2018). Besides the transport of vacuolar designated proteins, MVBs are required for the degradation of PRRs from the PM (Robatzek et al., 2006; Geldner et al., 2007; Erwig et al., 2017). FLS2 constitutively cycles between the PM and the TGN/EE (Beck et al., 2012). Upon flg22 perception, FLS2 is internalized from the PM, transported from the TGN/EE to MVBs and followed by subsequent degradation in the vacuole (Robatzek et al., 2006). Moreover, *Arabidopsis* PM localized LYK5 was shown to undergo CERK1-dependent endocytosis (Erwig et al., 2017). Ligand-dependent endocytosis was suggested to be important for immune signaling such as the signal amplitude, duration and specificity of immune responses (Claus et al., 2018). Besides the function of MVBs in the internaliza-

tion of PRRs, MVBs were shown to be important for intracellular NLRs to activate immune responses (Engelhardt et al., 2012; Li et al., 2018). In *Solanum tuberosum*, the cytosolic localized NLR R3a relocalizes to MVBs upon perception of the effector protein Avr3a^{KI} from *Phytophthora infestans*. This relocalization of R3a is required for HR immune signaling (Engelhardt et al., 2012).

In addition, MVBs/LEs were shown to play an important role in PTI. Accumulation of MVBs was observed in proximity to papillae at various plant-fungi contact sites (Chamberland et al., 1989; Collins et al., 2003; An et al., 2006b, 2006a; Böhlenius et al., 2010). MVB-mediated transport of substances and proteins and the release of ILVs to the extracellular space are important for resistance against pathogens at the plant surface. Cargos of ILVs, which are delivered by MVBs to the papillae include defense-related substances such as callose, phytoalexins and ROS (An et al., 2006a, 2006b; Meyer et al., 2009; Böhlenius et al., 2010; Nielsen et al., 2012). In *Arabidopsis*, PEN1-mediated defense mechanisms (1.4.2) are suggested to transport building material for the papillae (Assaad et al., 2004; Meyer et al., 2009; Nielsen et al., 2012). ADP-ribosylation factor (ARF) GTPases function in vesicle budding. In barley, the MVB-localized ARFA1b/1c GTPase was shown to be required for the accumulation of REQUIRED FOR MLO-SPECIFIED RESISTANCE2 (ROR2), the barley homolog of PEN1, to the papillae indicating a functional link between ROR2 and MVBs in penetration defense. In addition, ARFA1b/1c is also required for callose deposition to the papillae (Böhlenius et al., 2010).

Furthermore, the recruitment of PEN1 (1.4.2), SNARE SOLUBLE N-ETHYLMALEIMIDE-SENSITIVE FACTOR ADAPTOR PROTEIN (SNAP33; 1.4.2) and PEN3 (1.5.7) was observed to both the papillae and callose encased haustoria. This process was suggested to require secretion via exosomes derived from MVBs (An et al., 2006b; Meyer et al., 2009). The recruitment of PEN1 and PEN3 to the papillae was shown to be specific for powdery mildews interactions. However, the incorporation into haustorial encasements was observed for various pathogens indicating distinct roles of PEN1 and PEN3 accumulation in pre- and post-invasive NHR (Meyer et al., 2009). The isolation of extracellular vesicles from the *Arabidopsis* leaf extracellular space confirmed that specific components involved in antimicrobial defense (PEN3), immune signaling (SOBIR1) and polarized immune mechanism (PEN1) are cargos of exosomes (Rutter and Innes, 2017).

In eukaryotes, highly conserved Rab5 GTPases are important for the formation and maturation of MVBs and MVB-fusion with target membranes (Carney et al., 2006). Rab5 GTPases were shown to function in the secretion of exosomes (Baietti et al., 2012). *Arabidopsis* contains three Rab5-like GTPases, the two functionally redundant ARABIDOPSIS RAB GTPASE HOMOLOG F2B (ARA7) and ARABIDOPSIS RAB HOMOLOG F2A (RHA1) (Sohn et al., 2003; Lee et al., 2004) and the plant-specific ARA6 (Ueda et al., 2001). The Rab5 GTPases localize to MVBs and are commonly used as MVB markers (Kotzer et al., 2004; Haas et al., 2007; Lee et al., 2016). However, ARA6 did not show a completely

overlapping localization pattern with ARA7 and RHA1 (Ueda et al., 2001). ARA7 and RHA1 were found to be important for the initiation of MVB maturation and the transport of cargo to the vacuole (Sohn et al., 2003), whereas ARA6 was shown to mediate the transport of endosomes to the plasma membrane (Ebine et al., 2011). Rab5 GTPases were shown to accumulate in the extra-haustorial membrane, indicating redirection of MVBs to the plant-pathogen contact sites. In addition, activation of RAB5 GTPases by the endosome-localized VPS9a ARF GTPase guanine-nucleotide exchange factor is important for MVB maturation and MVB fusion with membranes. VPS9a is proposed to function in the organization of cellular endomembrane trafficking. (Nielsen et al., 2017). A Recent study by Nielson *et al*., 2017 provides evidence that VPS9a is required for both pre- and post-invasive NHR against adapted and non-adapted powdery mildew. Additionally, VPS9a was suggested to act in addition to PEN1 and PEN2 (1.5.4)-defense mechanisms.

1.4.2 PEN1

One identified pre-invasion NHR mechanism against non-adapted powdery mildews relies on the activity of the PM-localized syntaxin PEN1 (Figure 4, 1). PEN1, also referred to as SYNTAXIN OF PLANTS 121 (SYP121), contains an *N*-ethylmaleimide–sensitive factor (NSF) attachment protein receptor (SNARE) domain (Collins et al., 2003). A syntaxin forms a SNARE complex with an adaptor SNARE and a vesicular-anchored v-SNARE. This SNARE complex functions in vesicle-associated membrane fusion events and secretion processes, including endo- and exocytosis (1.4.1) (Collins et al., 2003; Lipka et al., 2007). Besides the strong focal accumulation of GFP-PEN1 in plasma membrane microdomains at fungal penetration sites, GFP-PEN1 accumulation is elicited after MAMP treatment, suggesting that PEN1 recruitment is initiated after MAMP perception by PRRs (Assaad et al., 2004; Underwood and Somerville, 2013). Upon pathogen attack, PEN1 forms an SDS-resistant ternary complex with the plasma membrane-associated adaptor SNARE SOLUBLE N-ETHYLMALEIMIDE-SENSITIVE FACTOR ADAPTOR PROTEIN (SNAP33) and either one of the two functionally redundant vesicle-associated v-SNAREs VESICLE-ASSOCIATED MEMBRANE PROTEINS VAMP721 or VAMP722 (Kwon et al., 2008). This complex was suggested to be required for the timely appearance of the papilla and to mediate exosome secretion, possibly releasing cell wall-reinforcing- and antimicrobial cargo into the apoplast at the fungal invasion site (Figure 4, 3) (Assaad et al., 2004; Bhat et al., 2005). Furthermore, GFP-PEN1 and mYFP-SNAP33 were shown to accumulate in both papillae and callose-encased haustoria (Meyer et al., 2009). Meyer *et al*., 2009 proposed transcytosis-mediated transport of PEN1 to the papilla. In transcytosis, endocytosed PM material is transported through the cell to a different part of the PM, where it is released as exosomes into the extracellular space (Meyer et al., 2009). Callose and PEN1 accumulation in the papilla was shown to require the ARF GTPase-guanine nucleo-

tide exchange factor (GEF) GNOM (Figure 4, 2) (Nielsen et al., 2012). It is assumed that upon powdery mildew attack GNOM mediates endocytosis of PEN1 and recycling of plasma membrane material to the papilla (Nielsen et al., 2012; Nielsen and Thordal-Christensen, 2013). The PEN1-transcytosis theory is further supported by the finding that PEN1 cycles between the PM and the TGN and that accumulation of PEN1 in the papilla does not require de novo PEN1 synthesis (Nielsen and Thordal-Christensen, 2013). Nielsen and Thordal-Christenses 2013 proposed that PEN1 functions at the TGN in receiving PM material for papilla formation (Figure 4, 3).

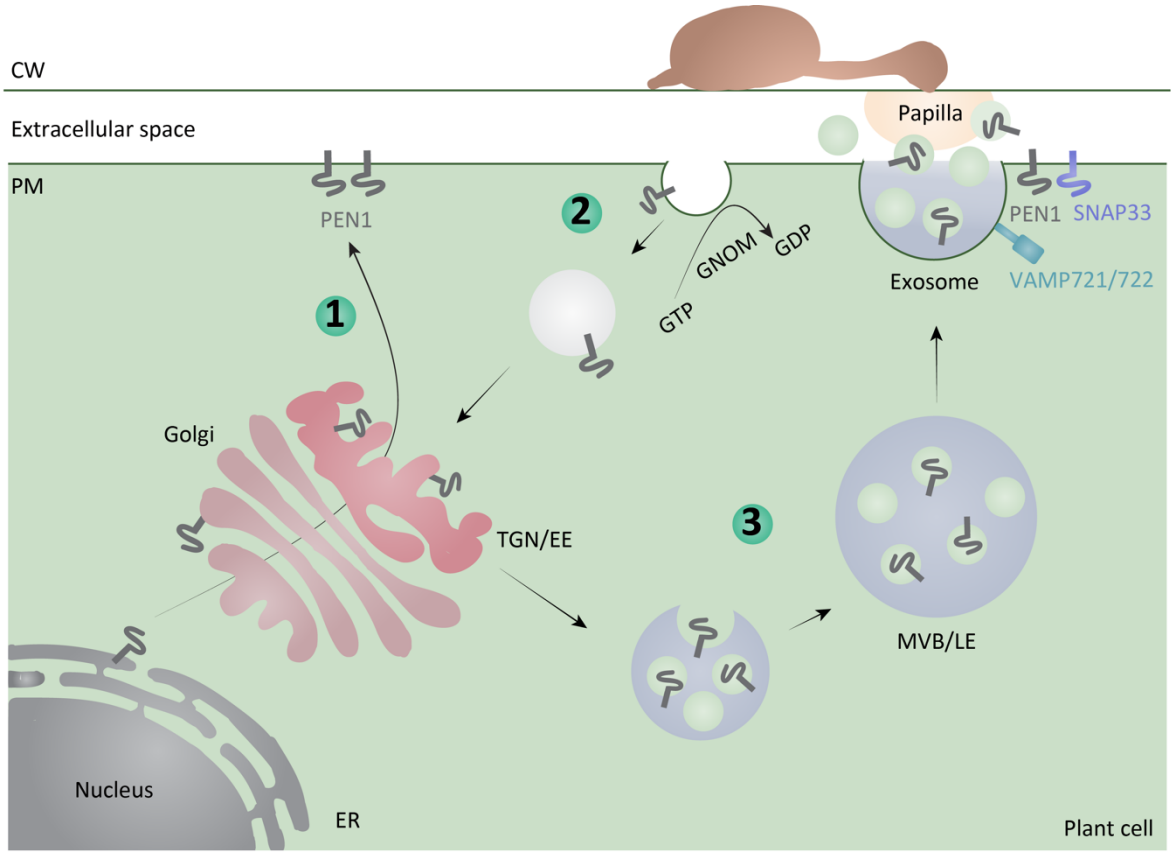

Figure 4. Schematic representation of PEN1 subcellular trafficking pathways. (1) PEN1 follows the secretory route via ER and Golgi stack for localization to the PM. **(2)** Upon powdery mildew attack, GNOM mediates endocytosis of PEN1 and PM material designated for the papilla. **(3)** At the TGN/EE, PEN1 receives PM material and mediates the fusion of vesicles with the TGN/EE. TGN/EE-derived vesicles mature into MVBs/LEs. PEN1 might end up in ILV of MVBs. MVBs transport their cargo to the site of attempted fungal invasion. MVBs fuse with the PM and exosomes are released into the papillary matrix. PEN1, SNAP33 and VAMP721/722 could be involved in the fusion of exosomes with the PM. Figure modified from Hansen and Nielsen, 2017.

The PEN1-induced fusion of vesicles with the TGN mediates the formation of MVBs, which transport building material for the papillae to the site of attempted fungal invasion. Upon fusion of the MVB with the PM, exosomes are released into the papillary matrix. Recently, Rutter and Innes 2017 isolated extracellular vesicles from the *Arabidopsis* leaf apoplast, which contain PEN1 and PEN3 together with other defense- and stress-related proteins. Protease protection experiments showed that PEN1

is sheltered inside the lumen of the secreted exosomes (Rutter and Innes, 2017). However, the biological relevance of PEN1 as cargo of exosomes is currently unknown (Nielsen and Thordal-Christensen, 2013).

1.5 Glucosinolate-mediated pathogen defense

1.5.1 Glucosinolate biosynthesis and transport

Significant advancements have been made in understanding plant innate immune responses. However, relatively little is known about processes and mechanisms that directly contribute to the restriction of pathogen growth. Recent studies suggest that biosynthesis of secondary metabolites, generation of antimicrobial peptides and reinforcement of the cell wall play an important role in restricting pathogen invasion (Bednarek, 2012; Voigt, 2014; Maróti et al., 2011). Low-molecular-weight secondary metabolites comprise a large group of diverse molecules derived from a variety of primary metabolites or biosynthetic intermediates by specialized metabolic enzymes (Weng et al., 2012). Glucosinolates (GLS) are unique nitrogen- and sulfur-containing secondary metabolites generated by plants belonging to the order *Capparales* including Brassicaceae such as cabbage (*Brassica oleracea*), oilseed rape (*Brassica napus*), and the model plant thale cress (*Arabidopsis thaliana*) (Halkier and Gershenzon, 2006). GLS are derived from three different amino acids and can be classified into tryptophan-derived indolic glucosinolates (IGs), methionine-derived aliphatic glucosinolates (AGs) and phenylalanine-derived benzyl glucosinolates. IGs and AGs are the two major GLS accumulating in *Arabidopsis* (Sønderby et al., 2010). These constitutive secondary metabolites are chemically stable and biologically inactive (Halkier and Gershenzon, 2006; Morant et al., 2008). However, glucosinolate hydrolysis products function in herbivore defense and plant innate immune responses against microbial pathogens (Hopkins et al., 2009; Pedras et al., 2011; Piślewska-Bednarek et al., 2018; Halkier and Gershenzon, 2006). The function of glucosinolates relies on the activity of β-thioglycoside glucohydrolases also known as myrosinases. These specialized enzymes catalyze the hydrolysis of GLS resulting in the formation of bioactive and toxic metabolism products such as isothiocyanates (ITCs) (Nakano et al., 2017). Due to the toxicity of IG-derived metabolism products, myrosinases and glucosinolates are separately stored in specialized cells. Myrosinases highly accumulate in guard cells and in the vacuole of myrosin cells, which develop adjacent to the phloem (Kissen et al., 2009; Husebye et al., 2002). Glucosinolates are stored in S-cells (Storage-cells) (Koroleva et al., 2000, 2010). These cells are positioned next to the phloem cells of each vascular bundle and the endodermis (Koroleva et al., 2000). Myrosinase-mediated defense mechanisms against herbivores and necrotrophic pathogens require tissue and cell disruption by chewing insects or necrotrophic pathogen invasion and an immediate mixture of compartmentalized myrosinase and GLS (Halkier and Gershenzon, 2006). It is

suggested that plants require a diversity of GLS, leading to the formation of a variety of toxic hydrolysis products for defense against different herbivore species (Wittstock and Halkier, 2002; Müller et al., 2010). For example, the two redundant myrosinases TGG1 and TGG2 were shown to function in herbivore defense by unspecific hydrolysis of AGs and IGs (Barth and Jander, 2006). In contrast to tissue and cell disruption in herbivore defense, PEN2-mediated IG hydrolysis represents a pathogen-induced and cell-autonomous mechanism required for broad-spectrum antifungal defense in *Arabidopsis* (1.5.3) (Lipka et al., 2005; Stein et al., 2006; Bednarek et al., 2009; Clay et al., 2009). This metabolic pathway functions in living plant cells and leads to the generation of end-products that differ from the metabolism products generated during cell disruption (Bednarek et al., 2009). Besides the function of IG in pathogen defense, AG-derived hydrolysis products were shown to function in defense against the non-adapted *P. syringae* (Fan et al., 2011) and the necrotrophic pathogen *Sclerotonia sclerotiorum* (Stotz et al., 2011).

IG core structure biosynthesis starts with the conversion of the precursor amino acid Trp to indole-3-acetaldoxime (Figure 5). The indole-3-acetaldoxime is suggested to be a metabolic branching point for the biosynthesis of IG, camalexin and the phytohormone auxin (indole acetic acid (IAA)) (Malka and Cheng, 2017). Besides IGs, camalexin is an important tryptophan-derived indolic secondary plant metabolite, which is induced in response to a variety of pathogens (Tsuji et al., 1992; Thomma et al., 1999; Glawischnig, 2007; Stotz et al., 2011). In IG biosynthesis, the reaction from Trp to indole-3-acetaldoxime is catalyzed by two redundant cytochrome P450 monooxygenases CYP79B2 and CYP79B3. Subsequently, the indole-3-acetaldoxime is oxidized by CYP83B1 leading to the formation of a yet uncharacterized intermediate, which is further converted to a thiohydroximate by the glutathione S-transferases 9 (GSTF9) and GSTF10, γ-Glutamyl Peptidase 1 (GGP1) and the C-S lyase Super root 1 (SUR1). SUR1 catalyzes the formation of S-alkyl-thiohydroximate into thiohydroximate. Furthermore, the activity of UDP-glucosyltransferase 74B1 (UGT74B1) and Sulfotransferase 16 (SOT16) and SOT18 is required for the conversion of the thiohydroximate to indol-3-ylmethyl glucosinolate (I3G) (Sønderby et al., 2010).

In the aliphatic GLS biosynthesis, CYP79F1 and CYP79F2 convert Met derivates to aldoximes, which are further oxidized by CYP83A1 (Figure 5). CYP83A1 is specific for aliphatic GLS core structure biosynthesis. GSTF11 and GSTF20 mediate the conjugation of an unidentified intermediate with glutathione (GSH). Following cleavage of the intermediate by GGP1, SUR1 converts the S-alkyl-thiohydroximate into thiohydroximate (Sønderby et al., 2010). GGP1 and SUR1 are required for both indole and aliphatic GLS biosynthesis. Moreover, UGT74B1 and UGT74C1 are suggested to function in glucosylation of Met-derived substances (Gachon et al., 2005). Desulfoglucosinolates are sulfated by SOT16, SOT17 and SOT18 to form aliphatic glucosinolates (Sønderby et al., 2010).

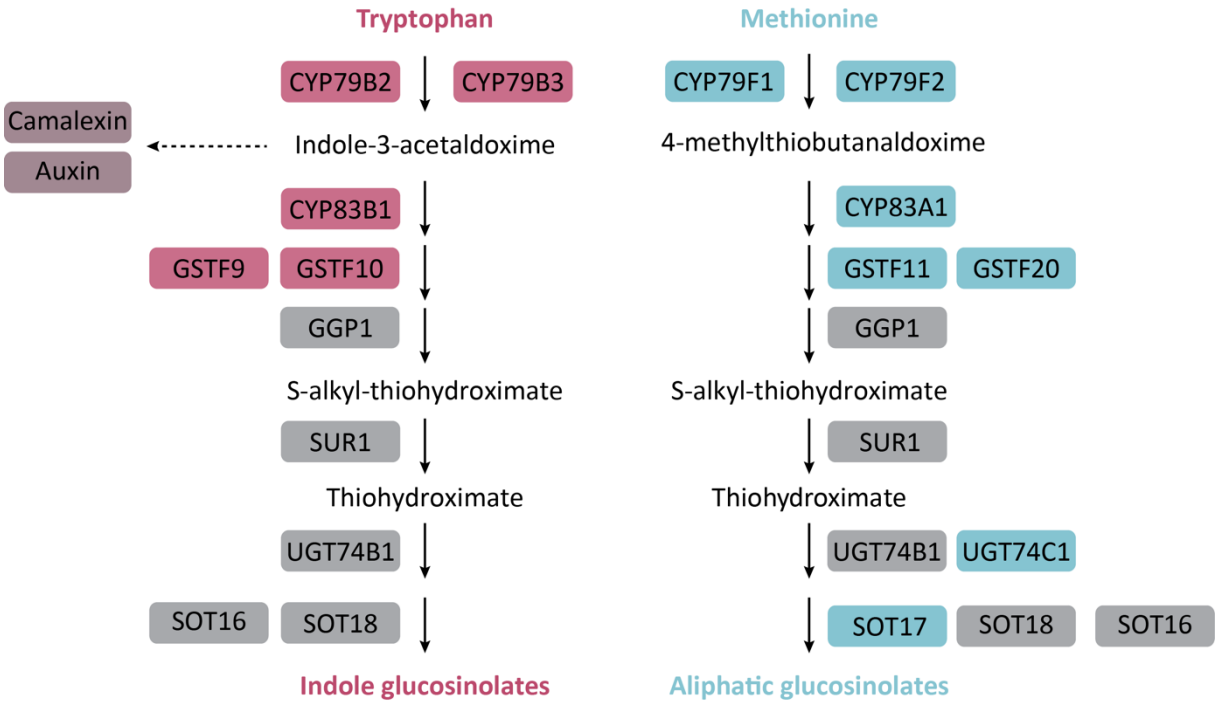

Figure 5. Indole- and aliphatic glucosinolate biosynthesis in *Arabidopsis*. Simplified scheme of indole- and aliphatic glucosinolate biosynthesis. The indole core structure biosynthetic pathway is indicated in red and the aliphatic core structure biosynthetic pathway in blue. Enzymes that function in both pathways are depicted in grey. Black arrows indicate single reactions. CYP79B2, cytochrome P450 monooxygenase 79B2; CYP79B3, cytochrome P450 monooxygenase 79B3; CYP79F1, cytochrome P450 monooxygenase 79F1; CYP79F2, cytochrome P450 monooxygenase 79F2; CYP83B1, cytochrome P450 monooxygenase 83B1; CYP83A1, cytochrome P450 monooxygenase 83A1; GSTF, glutathione S-transferases; GGP1, γ-Glutamyl Peptidase 1; SUR1, superroot1;. UGT74B1, UDP-glucosyltransferase 74B1; UGT74C1, UDP-glucosyltransferase 74C1; SOT, Sulfotransferase. Figure modified from Sønderby *e al*., 2010 and Malka and Cheng, 2017.

The two homologous and non-redundant enzymes CYP83A1 and CYP83B1 are used as markers for AG and IG biosynthesis pathways, respectively (Naur et al., 2003; Nintemann et al., 2018). Recent subcellular localization studies of the endoplasmic reticulum-membrane bound CYP83B1-mVenus and CYP83A1-mVenus revealed localization of both CYP83s to the vasculature. A more detailed analysis observed weak expression of CYP83B1-mVenus in major veins of the vegetative rosette, a stronger signal in smaller vascular bundles in the leaf periphery and the hypocotyl of *Arabidopsis* seedlings. CYP83A1-mVenus showed stronger fluorescence signals in the center of the rosette, along the midrib and major secondary vascular bundles of leaves. Furthermore, CYP83B1-mVenus was identified to localize close to the lateral root primordia. In contrast to CYP81B1-mVenus, no CYP83A1-mVenus fluorescence signal was detected in root tips (Nintemann et al., 2018). Moreover, SUR1 and SOT17 were shown to localize in major vascular bundles, in peripheral veins of leaves and the root apical meristem. (Nintemann et al., 2018). At the cellular level, CYP81A1-mVenus was detected in phloem parenchyma cells and cells surrounding the xylem vessels, whereas CYP81B1 was exclusively found in

phloem parenchyma cells. These localization studies revealed overlapping, but distinct sites of AG and IG biosynthesis, indicating that one or both classes of GLS can be produced in GLS-biosynthetic cells in close proximity to GLS storage cells (Nintemann et al., 2018). However, the localization of enzymes in AG and IG biosynthetic pathways along the vasculature does not correlate with the distribution of GLS within leaves, suggesting that GLS are transported from the vasculature (site of biosynthesis) to epidermal cells for storage (Figure 6) (Li et al., 2011; Madsen et al., 2014; Nintemann et al., 2018).

According to current models, distribution of IGs and AGs within leaves occurs via a combination of symplastic intracellular transport by diffusion through plasmodesmata and import from the apoplast into mesophyll cells mediated by GTRs (Andersen et al., 2013; Madsen et al., 2014; Xu et al., 2017; Nintemann et al., 2018; Hunziker et al., 2019). So far, the plasma-membrane localized Glucosinolate Transporters GTR1/NPF2.10, GTR2/NPF2.11 and GTR3/NPF2.9 belonging to the NRT1/PTR FAMILY (NPF) were identified and characterized (Wang and Tsay, 2011; Nour-Eldin et al., 2012; Jørgensen et al., 2017). GTR1 and GTR2 are expressed in leaf veins, whereas GTR1 is also expressed in mesophyll cells adjacent to leaf veins in *Arabidopsis* (Nour-Eldin et al., 2012). The two proton-dependent glucosinolate importers, GTR1 and GTR2 were shown to transport both the indole glucosinolate I3G and the aliphatic GLS 4-methylthiobutyl glucosinolate (4MTB) into *Xenopus laevis* oocytes, whereas GTR3 specifically transports I3G, but not 4MTB into *Xenopus laevis* oocytes (Jørgensen et al., 2017). *gtr1* and *gtr2* single mutants showed reduced total GLS levels in seeds. Moreover, AGs and IGs were below the detection limit in seeds of *gtr1 gtr2* double mutants, which was complemented by either GTR1 or GTR2. Met-derived GLS highly accumulate in the rosette from wilted *gtr1 gtr2*, indicating that GTRs function in the transport of GLS from source tissue to seeds. Based on these results, Nour-Eldin *et al*., 2012 proposed that GTR1 and GTR2 load apoplasmic GLS into companion cells for long-distance phloem-transport. In contrast to Met-derived GLS, IGs did not accumulate in rosette tissue of wilted *gtr1 gtr2* (Nour-Eldin et al., 2012), suggesting IG turnover and/or a negative feedback mechanism (Bednarek et al., 2009; Nour-Eldin et al., 2012).

In *Arabidopsis*, GTR3 was shown to localize to phloem companion cells in roots (Wang and Tsay, 2011). Furthermore, GTR3 is co-expressed with GTR1 and GTR2 in phloem companion cells in the rosette. Based on IG quantification in roots and shoots of *gtr1*, *gtr2*, and *gtr3* single and multiple mutants it has been proposed that GTR1-3 are required for the distribution of IGs between shoot and root (Jørgensen et al., 2017).

PM-localization of GTRs in mesophyll cells and localization to the vasculature supports the model that GTRs are involved in GLS intra leaf-distribution and long-distance transport to seeds suggesting a

role in phloem loading and xylem retrieval (Nour-Eldin et al., 2012; Andersen et al., 2013; Andersen and Halkier, 2014; Madsen et al., 2014, 2015; Jørgensen et al., 2017; Xu et al., 2017).

Increased concentrations of AG and IG were found in *Arabidopsis* leaf epidermal cells relative to the rest of the leaf. The epidermis accumulates 4- to 5-fold higher I3G concentrations. However, GTR1 and GTR2 are not involved in the transport of AGs and IGs into epidermal cells, suggesting symplastic transport of glucosinolates via plasmodesmata (Madsen et al., 2014).

GLS immunolocalization analysis in *Brassica napus* revealed accumulation of GLS in vacuoles in epidermal cells (Kelly et al., 1998). For the storage of GLS in *Arabidopsis* epidermal leaf cells, GLS are proposed to be transported from the cytosol into the vacuole by an unknown vacuolar importer leading to the accumulation in the outer cell layer (Madsen et al., 2014).

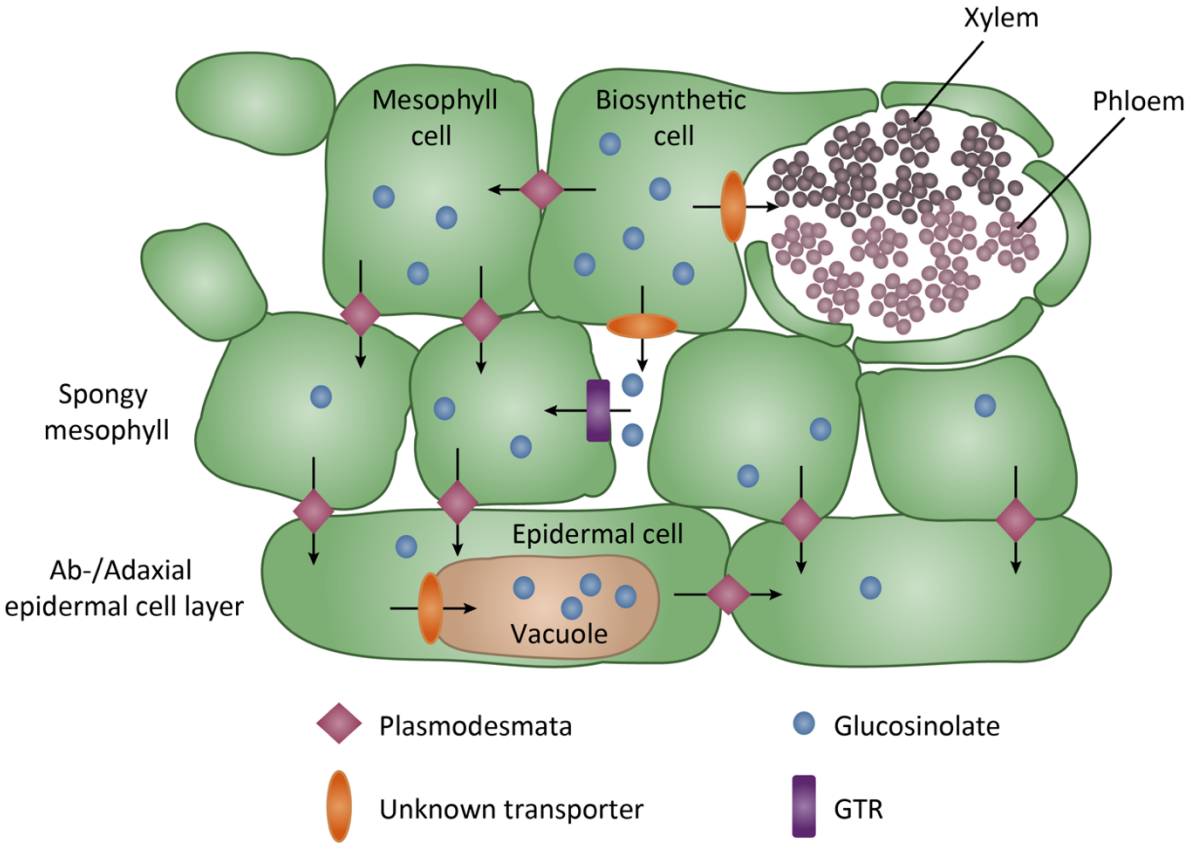

Figure 6. Schematic representation of intra-leaf distribution of glucosinolates. Model of intra-leaf distribution of glucosinolates. Glucosinolates are synthesized in neighboring cells of the vasculature. Following biosynthesis, different transport pathways have been proposed. Glucosinolates are distributed from the biosynthetic cell into the apoplast by an unknown transporter. GTRs mediate the transport of GLS from the apoplast into adjacent mesophyll cells. In addition to the import from the apoplast into cells, GLS might be distributed from cell-to-cell via a symplastic intracellular transport enabled by plasmodesmata. For the storage of GLS in epidermal leaf cells, GLS are proposed to be transported from the cytosol into the vacuole by a yet unidentified vacuolar importer leading to the accumulation in the outer cell layer. Figure modified from Madsen *et al.*, 2014.

Hunziker *et al.*, 2020 showed that biosynthesis of I3G is cell-autonomously induced in the epidermis after pathogen attack. CYP83B1-YFP and CYP83A1-YFP fluorescence signals were undetectable in

unchallenged leaf epidermal cells. However, a strong and cell-autonomous YFP-fluorescence signal of CYP81B1-YFP was observed 24 h and 48 h after inoculation with the non-adapted powdery mildew *Bgh* and the adapted powdery mildew *G. orontii*, while the fluorescence of CYP83A1-YFP was undetectable. Quantification of GLS concentrations revealed increased levels of 4MI3G at both time points upon *Bgh* inoculation, whereas 4MI3G was not induced during attempted *G. orontii* colonization. Moreover, induction of CYP81F2 expression was observed in both incompatible and compatible interactions suggesting that the deficiency of 4MI3G accumulation after *G. orontii* infection results from deficient indole GLS core structure biosynthesis in the epidermal cell layer during a compatible plant-pathogen interaction. In addition, SUR1 was not detected in unchallenged epidermal cells but accumulates upon infection 24 and 48 hpi with *Bgh*. Surprisingly, SUR1 accumulation was deferred during *G. orontii* invasion suggesting SUR1 as the putative target of a powdery mildew effector. Besides GLS core structure biosynthesis, intra-leaf GLS transport mediated by GTRs was shown to be not involved in defense against compatible and incompatible fungal pathogens. Infection experiments revealed no accumulation of GTR1 and GTR2 in attacked cells. Additionally, *gtr1 gtr2* double and *gtr1 gtr2 gtr3* triple mutants exhibited a wild-type-like penetration resistance and sporulation phenotype towards *Bgh* and *G. orontii*, respectively (Hunziker et al., 2020). These findings of Hunziker *et al*., 2020 oppose the hypothesis that IGs with a function in powdery mildew defense need to be transported to attacked cells from surrounding tissue. However, it is unknown whether PEN2-mediated pathogen entry control relies on *de novo* I3G synthesis or remobilization of preformed and stored I3G.

1.5.2 CYP81F2

A second, and PEN1 independent, pre-invasive NHR defense mechanism relies on the activity of the cytochrome P450 monooxygenase CYP81F2, the INDOLE GLUCOSINOLATE O-METHYLTRANSFERASE (IGMT1) and IGMT2 (1.5.3), the atypical myrosinase PEN2 (1.5.4), the Glutathione-S-Transferase class-tau member 13 (GSTU13; 1.5.5) the PHYTOCHELATIN SYNTHASE 1 (PCS1/PEN4; 1.5.6) and the ATP binding cassette transporter PEN3 (1.5.7), which were found to be involved in activation and transport of toxic IG-derived metabolism products (Lipka et al., 2005; Stein et al., 2006; Bednarek et al., 2009; Clay et al., 2009; Pfalz et al., 2009; Fuchs et al., 2016; Piślewska-Bednarek et al., 2018; Hématy et al., 2020).

The cytochrome P450 monooxygenase CYP81F2 was identified to function in the biosynthesis of 4-methoxyindol-3-ylmethylglucosinolate (4MI3G) providing the PEN2 substrate required for pathogen entry control (Bednarek et al., 2009; Clay et al., 2009). Bednarek *et al*., 2009 and Clay *et al*., 2009 revealed that CYP81F2 catalyzes the hydroxylation of the fourth position of the indole ring of I3G

leading to the formation of 4-hydroxy-indol-3-yl-methyl glucosinolate (4OHI3G) (Figure 7) (Bednarek et al., 2009; Pfalz et al., 2011). *cyp81f2* mutants exhibit a decrease in penetration resistance indistinguishable from *pen2*. *pen2 cyp81f2* double mutants show similar *Bgh* invasion frequencies as the *pen2* and *cyp81f2* single mutants indicating that the two enzymes function in the same molecular pathway (Bednarek et al., 2009). Subcellular localization studies using transgenic plants expressing functional RFP-tagged CYP81F2 revealed that CYP81F2 is undetectable in unchallenged leaf epidermal cells. However, CYP81F2-RFP was shown to be cell-autonomously induced in pathogen invaded epidermal cells. For co-localization experiments, CYP81F2-RFP was coexpressed with an ER marker. These analyses revealed that CYP81F2-RFP is localized to the ER (Figure 8), which becomes structurally reorganized in immediate proximity to subpopulations of clustered and immobilized PEN2-labelled mitochondria (see section 1.5.4) (Fuchs et al., 2016). Moreover, CYP81F2 harbors a predicted N-terminal transmembrane domain (Pfalz et al., 2011), which is similar to CYP81B1 that was shown to associate with the ER and potentially expose the catalytic site to the cytoplasm (Nintemann et al., 2018).

Biosynthesis and hydrolysis of IGs are important for flg22-triggered callose deposition (Clay et al., 2009). *pen2* and *cyp81f2* were shown to lack the callose response following flg22 treatment. Therefore, 4MI3G-derived hydrolysis products have been suggested to function as signaling compounds or coactivators for flg22-induced callose deposition (Clay et al., 2009). However, *pen2* mutant plants were shown to recruit callose in response to attempted invasion of various pathogens indicating that PAMP-induced deposition of callose and pre-invasive NHR are not directly linked and might be regulated by different end products of pathogen-triggered IG-hydrolysis (Lipka et al., 2005; Maeda et al., 2009; Hiruma et al., 2010; Bednarek, 2012).

1.5.3 IGMT1/IGMT2

The next step in 4MI3G biosynthesis is suggested to be catalyzed by either INDOLE GLUCOSINOLATE O-METHYLTRANSFERASE (IGMT1) or the closely related IGMT2 which belong to the family 2 of O-methyltransferases (Pfalz et al., 2009). Pfalz *et al*., 2011 identified that following CYP81F2-mediated hydroxylation of I3G, the fourth position of the indole ring is directly methoxylated by IGMT1 or IGMT2 by reconstructing the indole glucosinolate biosynthetic pathway of *Arabidopsis* in *N. benthamiana*. 4-methoxylation of 4OHI3G leads to the formation of 4MI3G (Figure 7).

Recently, mitogen-activated protein kinases 3 (MPK3) and MPK6 together with their substrate ETHYLENE RESPONSE FACTOR6 (ERF6), were shown to facilitate the conversion of I3G to 4MI3G in response to *Botrytis cinerea.* MPK3 and MPK6 signaling through ERF6 is required to control the expres-

sion of the two transcription factors MYB51 and MYB122, which are regulating CYP81B1, CYP79B2, CYP79B3, as well as CYP81F2, IGMT1 and IGMT2 (Xu et al., 2016).

1.5.4 PEN2

The atypical myrosinase PEN2, also known as β-GLYCOSYL HYDROLASES 26 (BGLU26), is a member of the *Arabidopsis* family 1 glycosyl hydrolases (F1GHs) including 47 predicted members (BGLU1-BGLU47) (Xu et al., 2004; Lipka et al., 2005; Fuchs et al., 2016). F1GHs catalyze the hydrolysis of S- or O-glycosidic linkages between a sugar and a non-carbohydrate moiety leading to the release of an aglycone. Indole-derivates are linked to the glucose via an S-glycosidic bond, which is typically hydrolyzed by thioglucosidases (TGGs) also known as myrosinases (Xu et al., 2004). GLS hydrolysis by myrosinases results in the formation of a chemically unstable aglycone, which can be directly decomposed into various end products. These endproducts include nitriles, thiocyanates and the extremely reactive isothiocyanates (ITCs), that are potentially toxic for the invading pathogen (Xu et al., 2004; Piasecka et al., 2015).

Genetic and biochemical analysis revealed that PEN2 catalyzes the hydrolysis of the IGs I3G and 4MI3G (Bednarek et al., 2009). Thus, PEN2 is required for the biosynthesis of different end products such as indol-3-ylmethyl amine (I3A), raphanusamic acid (RA), 4-O-β-d-glucosyl-indol-3-yl formamide (4OGlcI3F), 4-methoxyindol-3-methanol (4MOI3M), S-(4-methoxy-indol-3-yl-methyl) (4MOI3Cys) and additional yet unidentified and potentially toxic substances (Bednarek et al., 2009, 2011; Lu et al., 2015; Matern et al., 2019) (Figure 7). However, RA and I3A accumulation was observed in *cyp81f2* mutants, indicating that these hydrolysis products are not required for pre-invasive NHR against powdery mildews (Bednarek et al., 2009).

Cyanogenic β-glucosidase 1 (CBG1) from *Trifolium repens* was used as a template for structural modeling of PEN2. This analysis revealed the typical F1GH barrel fold structure of PEN2, harboring a catalytic center. Myrosinases contain a glutamine and a glutamate residue within the enzymatic part of the protein (Xu et al., 2004; Sugiyama and Hirai, 2019). However, PEN2 has an uncharacteristic amino acid composition within the catalytic site consisting of two conserved glutamates (E183 and E398) (Lipka et al., 2005), which is typically found for beta-glucosidases and suggested to be important for cleavage of the thioglucoside moiety. *pen2-1* mutants expressing the $PEN2_{E182D}$ mutant variant, which contains an aspartic acid at position 182 instead of glutamate, are not able to complement the reduced pathogen entry defense phenotype of the *pen2* mutant. This result showed the importance of PEN2 catalytic activity for pre-invasive NHR (Lipka et al., 2005). Moreover, in *Arabidopsis* roots, the PYK10/BGLU23 was shown to be the most abundant β-glucosidase in ER-bodies, an organelle found within the order *Brassicales* (Matsushima et al., 2003). Similar to PEN2, PYK10 has myrosinase activi-

ty against I3G and contains two conserved glutamates within its enzymatic part (Nakano et al., 2017). Based on these findings, PEN2 and PYK10 were specified as atypical myrosinase (Lipka et al., 2005; Bednarek et al., 2009; Nakano et al., 2017).

Besides the catalytic center of PEN2, PEN2 contains a unique C-terminal extension consisting of a tail-anchor (TA; 28 amino acids), with a predicted α-helical structure, which is linked to the bulk part via a low complexity region (15 amino acids). The PEN2 C-terminal extension was shown to be required for PEN2-mediated pre-invasive resistance (Lipka et al., 2005). TA proteins typically harbor a hydrophobic transmembrane domain (TMD), necessary for post-translational insertion in intracellular membranes, whereby the C-terminal domain is exposed to the inside of the membrane compartment and the N-terminal domain extends into the cytosol (Abell and Mullen, 2011). The TA of PEN2 was shown to contain a predicted TMD within the C-terminal extension (Fuchs et al., 2016).

To generate a functional protein complementing the increased *Bgh* penetration phenotype of the *pen2* mutant, GFP was inserted between the predicted globular enzymatic part of the PEN2 protein and the C-terminal extension (PEN2-GFP-TA_{PEN2}) (Lipka et al., 2005). CLSM analysis showed that *pPEN2::PEN2-GFP-*TA_{PEN2} is constitutively expressed in leaf epidermal cells. Furthermore, PEN2 is localized to the cytosol and associated with small membrane compartments (Lipka et al., 2005). To analyze the subcellular localization of PEN2 in more detail, co-localization studies were performed, with either the peroxisomal marker RFP-PEROXISOME TARGETING SIGNAL1 (RFP-PTS1) or the mitochondrial marker Saccharomyces cerevisiae CYTOCHROME C OXIDASE IV-RFP (ScCOX4-RFP). These analyzes revealed that PEN2 is dual-targeted to the membrane of peroxisomes and mitochondria (Lipka et al., 2005; Fuchs et al., 2016). Importantly, PEN2-GFP-TA_{PEN2}-labelled mitochondria accumulate and are immobilized at sites of attempted *Bgh* penetration 20 hpi (Figure 8). Mitochondrial arrest is accompanied by the appearance of highly fluorescent punctate PEN2-GFP-TA_{PEN2} signals in the periphery of the mitochondria. In contrast, all peroxisomes in a cell retain their mobility and show unaltered peripheral PEN2 localization patterns. The hyperfluorescent foci of PEN2-GFP-TA_{PEN2} are likely PEN2 aggregates on the outer membrane of immobilized mitochondria (Fuchs et al., 2016). Previous findings revealed that PEN2 orthologs form heteromeric aggregates. Hetero- and homo-oligomers were found to be important for the control of enzymatic activity (Kittur et al., 2007; Yamada et al., 2010). Further analysis confirmed that only full-length PEN2 has the capacity to homodimerize and to form pathogen-induced oligomers and dimers of higher order in planta. The N-terminal enzymatic part (M1-D489) or the C-terminal domain of PEN2 (Q496-N560) alone are not able to interact with full-length PEN2 (Fuchs et al., 2016).

A more detailed analysis of the C-terminal tail-anchor of PEN2 revealed that the GFP-tagged tail-anchor of PEN2 (GFP-TA_{PEN2}) localizes to the outer membrane of either mobile or arrested membrane

compartments at sites of attempted fungal invasion (Fuchs et al., 2016). However, the periphery of immobilized mitochondria was not associated with GFP-TA_{PEN2} aggregates and characteristic hyper-fluorescence. These results indicate that pathogen-induced PEN2 aggregate formation and increased GFP-fluorescence relies on the N-terminal globular enzymatic part and is not an artifact resulting from unspecific GFP-GFP interactions (Fuchs et al., 2016). PEN2 TA functionality was further dissected by the analysis of different TA deletion mutants. Mutants with either deletion of the complete transmembrane domain (PEN2-GFP-$TA_{PEN2\Delta TM}$), or with five amino acids at the end of the C-terminus (PEN2-GFP-$_{PEN2\Delta C5}$), or of an exchange of the positively charged lysine to neutral glycine at the fifth last position of the C-terminus (PEN2-GFP-$_{PEN2\Delta K556G}$) are not able to complement reduced pathogen entry defense of the *pen2* mutant. Furthermore, these mutants showed mistargeted PEN2 with diffuse distribution in the cytosol and potential ER association. In addition, exclusive targeting of PEN2 to the outer mitochondrial membrane by exchanging the PEN2 TA with the TA of *Arabidopsis* TRANSLOCASE OF OUTER MITOCHONDRIAL MEMBRANE 20-4 (TOM20-4) complemented the *pen2* mutant phenotype. These findings confirm the tail-anchor function of the PEN2 C-terminal extension and the importance of PEN2-association with mitochondria at plant-fungal interaction sites (Fuchs et al., 2016).

Fuchs *et al*., 2016 suggested that accumulation of mitochondria at plant-microbe-interaction sites may also supply ATP for pathogen-induced energy-dependent cellular processes such as secretion and transport of antimicrobial compounds by SNARE proteins or ABC-transporters across the PM. Furthermore, mitochondria function in sensing cellular functional imbalances. Redox processes of the mitochondrial respiratory machinery can react and respond sensitively to changing conditions. Altered mitochondrial redox status can trigger retrograde mitochondria-nucleus signaling and transcriptional changes (Schwarzländer and Finkemeier, 2013; Ng et al., 2014). Fuchs *et al*., 2016 used plants expressing the mitochondrial matrix-targeted redox-sensitive GFP2 sensor (mt-roGFP2) (Schwarzländer et al., 2008; Albrecht et al., 2014) to analyze the redox status of mitochondria upon *Bgh* inoculation. mt-roGFP2 allows the measurement of the glutathione redox potential in *Arabidopsis* plants. The mt-roGFP2 sensor contains two engineered cysteine residues, which are able to form disulfide bonds, depending on the redox status in the cellular environment of the protein. Disulfide bridge formation in an oxidizing environment leads to conformational changes of the roGFP2 protein and to changes in the excitation spectrum. To differentiate between reduced and oxidized forms of mt-roGFP2, ratiometric imaging of GFP fluorescence emission is performed at 500 to 540 nm after excitation at the two excitation wavelengths 405 versus 488 nm (Schwarzländer et al., 2008; Albrecht et al., 2014). These analyses revealed that immobilized mitochondria show a pathogen-induced redox imbalance. Arrested subpopulations of mitochondria close to the *Bgh* invasion site showed en-

hanced mt-roGFP2 oxidation in comparison to the rest of the mitochondrial population within a cell. Changes in the glutathione redox status of immobilized mitochondria might be due to the release of ROS such as superoxide or hydrogen peroxide, which could induce retrograde mitochondria-nucleus signaling and transcriptional reprogramming (Fuchs et al., 2016).

Arabidopsis pen mutants are still nonhost plants for non-adapted powdery mildews. In this case, pathogen attack is restricted by post-invasion NHR mechanisms which are associated with callose encased haustoria and single epidermal cell death responses (Lipka et al., 2005; Stein et al., 2006). In both cases, callose can be visualized by Anilin blue staining (Figure 2). Besides the involvement of the functionally redundant lipase like EDS1, PAD4 and SAG101 (1.1) in basal immunity and ETI (Hammond-Kosack and Parker, 2003; Lipka et al., 2005; Wiermer et al., 2005; Stein et al., 2006), these proteins were identified as important molecular components involved in post-invasive NHR (Lipka et al., 2005; Stein et al., 2006). In comparison to the *pen* mutants, *eds1*, *pad4* and *sag101* single mutants showed no enhanced fungal invasion of powdery mildews. However, slightly increased secondary hyphae and microcolony formation were observed for *Bgh* and *E. pisi* due to less frequent HR-like single cell death responses (Lipka et al., 2005; Stein et al., 2006). *pen2 eds1*, *pen2 sag101* and *pen2 pad4* double mutants showed enhanced epiphytic growth of *Bgh* (Lipka et al., 2005). The non-adapted powdery mildew *Bgh* is able to form conidiophores on *pen2 pad4 sag101* triple mutants indicating disruption of NHR. In contrast, the breakdown of NHR resistance against *E. pisi* was already observed on *pen2 eds1* and *pen2 and pad4* double mutants. These results are indicating that NHR against powdery mildews is based on independent and multi-component pre-invasive and post-invasive defense responses sufficient to restrict pathogen colonization (Lipka et al., 2010).

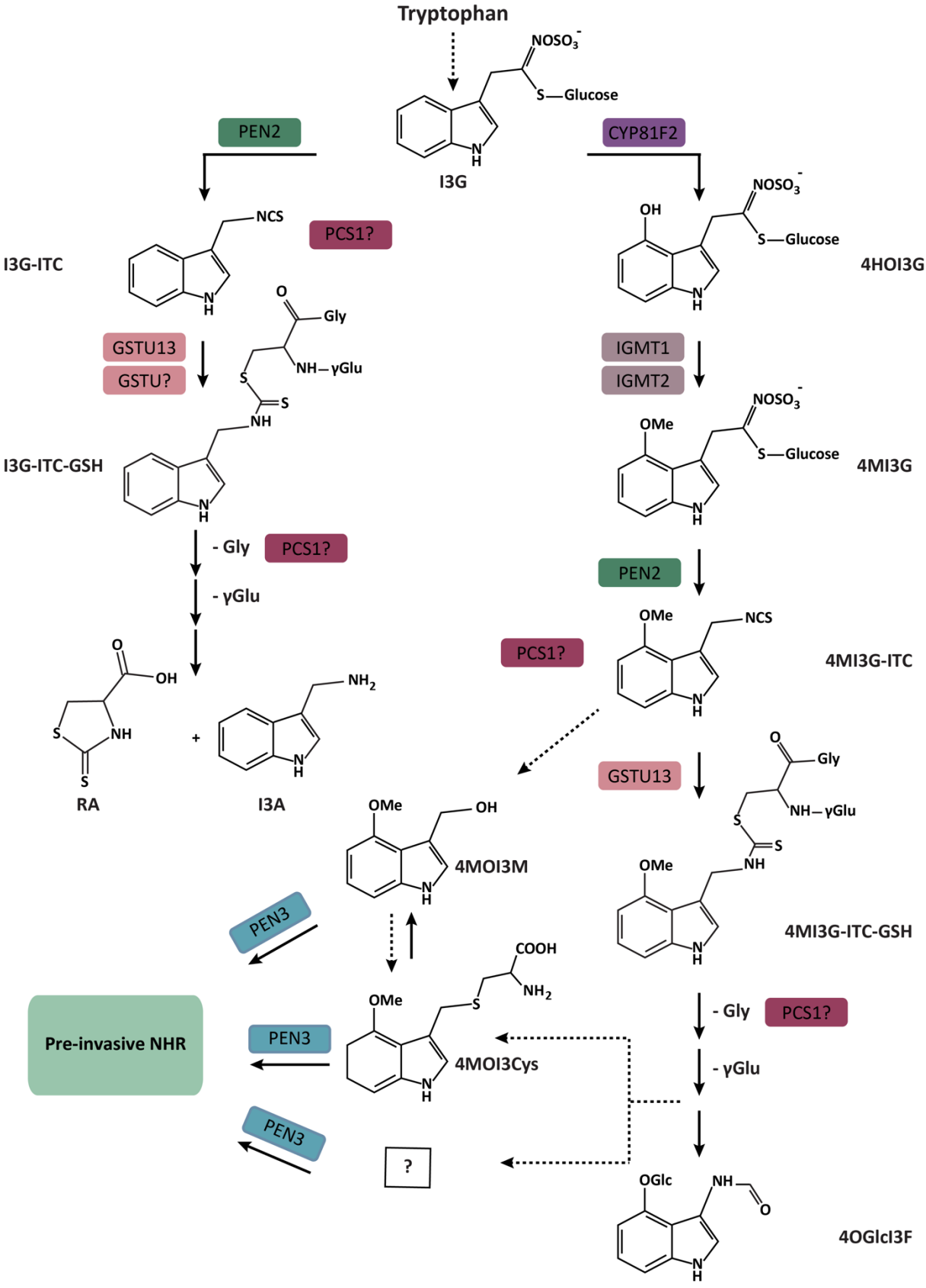

Figure 7. Schematic and simplified illustration of PEN2-mediated indole glucosinolate hydrolysis. Black arrows indicate single reactions; Dashed arrow depicts multiple reactions. Enzymes involved in IG-metabolism are depicted in different colors. I3G, indole-3-ylmethyl glucosinolate; I3G-ITC, indol-3-ylmethyl-isothiocyanate; I3G-

ITC-GSH, indol-3-ylmethyl-isothiocyanate-glutathione; RA, raphanusamic acid; I3A, indol-3-ylmethyl amine; 4OHI3G- 4-hydroxy-indol-3-yl-methyl glucosinolate; 4MI3G, 4-methoxyindol-3-ylmethyl glucosinolate; 4MI3G-ITC, 4-methoxyindol-3-ylmethyl-isothiocyanate; 4MI3G-ITC-GSH, 4-methoxyindol-3-ylmethyl-isothiocyanate-glutathione; 4OGlcI3F, 4-O-β-d-glucosyl-indol-3-yl formamide; 4MOI3M, 4-methoxyindol-3-methanol; 4MOI3Cys, S-(4-Methoxyindol-3-ylmethyl)cysteine; PEN2, PENETRATION1; CYP81F2, CYTOCHROME P450 MONOOXYGENASE; IGMT1, INDOLE GLUCOSINOLATE O-METHYLTRANSFERASE 1; IGMT2, INDOLE GLUCOSINOLATE O-METHYLTRANSFERASE 2; GSTU13, GLUTATHIONE-S-TRANSFERASE CLASS-TAU MEMBER 13; PCS1, PHYTOCHELATIN SYNTHASE 1; PEN3, PENETRATION 3. This figure is based on Bednarek et al., 2009, Clay et al., 2009, Pfalz et al., 2011, Piślewska-Bednarek et al., 2018, Matern et al., 2019 and Hématy et al., 2020.

1.5.5 GSTU13

Glutathione (GSH) transfer to 4-methoxyindol-3-ylmethyl-isothiocyanate (4MI3G-ITC) is suggested to be an important step in pathogen-induced PEN2-mediated IG metabolism. The main points for this hypothesis are the decrease of IG metabolites and the enhanced penetration of fungal pathogens in GSH-deficient mutants (Bednarek et al., 2009; Piślewska-Bednarek et al., 2018). Furthermore, it is suggested that after I3G hydrolysis, the generated I3G-ITC directly reacts with GSH resulting in the formation of a dithiocarbamate-type adduct. This product is further processed to I3A and RA (Bednarek et al., 2009).

The *Arabidopsis* genome contains 47 genes belonging to the glutathione S-transferase (GST) superfamily. GSTs are grouped into the different classes tau, phi, theta and zeta, depending on sequence similarities (Wagner et al., 2002). These diverse and multifunctional enzymes are involved in detoxification of toxic components by catalyzing the conjugation with glutathione (Dixon and Edwards, 2010; Labrou et al., 2015).

Piślewska-Bednarek *et al*., 2018 identified the Glutathione-S-Transferase class-tau member 13 (GSTU13) as an important component in the PEN2-immune mechanism (Figure 7). GSTU13 was shown to be co-expressed with PEN2 and genes encoding enzymes involved in IG core structure biosynthesis such as GSTF9, GSTF10, CYP79B3/B2 and CYP83B1 (Piślewska-Bednarek et al., 2018). Furthermore, *in vitro* enzymatic analysis suggested a high activity of GSTU13 towards benzyl-ITC as substrate (Wagner et al., 2002; Dixon et al., 2009). *gstu13* mutants showed reduced resistance against the non-adapted *E. pisi*, *Colletotrichum gloeosporioides*, and *Plectosphaerella cucumerina* and lack callose deposition after sensing flg22 (Piślewska-Bednarek et al., 2018).

Bgh-infected *gstu13* leaves showed significantly reduced RA and I3A concentrations compared to Col-0. However, in comparison to *pen2-2*, RA and I3A significantly accumulated in *gstu13* during attempted fungal invasion, suggesting that GSTU13 functions redundantly with other and so far unidentified GSTs in the generation of RA and I3A (Piślewska-Bednarek et al., 2018). Moreover, 4OGlcI3F is significantly reduced in *gstu13* upon pathogen attack similar to the *pen2-2* mutant. These results suggest that GSTU13 appears to be the only enzyme required for the pathogen-induced formation of

4OGlcI3F. Furthermore, the function of GSTU13 was shown to be independent of core structure IG biosynthesis (Piślewska-Bednarek et al., 2018).

At present, the subcellular localization of most GSTs involved in IG core structure or IG-derived metabolites in PEN2-mediated pre-invasive resistance is unknown. Only GFP-GSTF6 was shown to localize to the cytosol (Dixon et al., 2009). It needs further investigation whether the function of GSTU13 in the PEN2 mechanism results from its I3G-ITC/4MI3G-ITC substrate specificity (Wagner et al., 2002; Dixon et al., 2009) or requires a specific subcellular localization and/or protein- or organelle remobilization to pathogen invasion sites similar to PEN2, CYP81F2, PEN3 and PEN4 (Lipka et al., 2005; Stein et al., 2006; Fuchs et al., 2016; Hématy et al., 2020).

1.5.6 PCS1/PEN4

Recently, PEN4 was identified as another component of PEN2-mediated entry control against non-adapted pathogens and functions in basal resistance against a broad variety of pathogens (Hématy et al., 2020). *PEN4* encodes the PHYTOCHELATIN SYNTHASE 1 (PCS1) which was shown to be involved in heavy metal tolerance in plants. PCSs function in the biosynthesis of the heavy metal binding polypeptide phytochelatin ((γ-Glu-Cys)$_n$-Gly) from glutathione by the transfer of a glutamylcysteinyl residue to GSH (Beck et al., 2003; Grzam et al., 2006; Blum et al., 2007). Additionally, PCSs are known to have peptidase activity. For the breakdown of GSH, PCSs have been shown to catalyze the cleavage of the Gly residue from GSH (Grill et al., 1989; Howden et al., 1995; Rea, 2006).

Lack of functional *pen4* results in a similar metabolic phenotype as observed for *pen2*. Upon pathogen attack, *pen4* accumulates 4MI3G, but not I3G. In addition, *pen4* showed reduced levels of the I3G hydrolysis products RA and I3A. After pathogen attack, reduced concentrations of the 4MI3G hydrolysis product 4OGlcI3F were observed for *pen4* mutants (Hématy et al., 2020). Matern *et al*., 2019 revealed that *pen4* plants also exhibit increased levels of the PEN3 substrate 4MO3IM and 4MOI3Cys, upon pathogen inoculation. These results suggest that PCS1 might function in the biosynthesis of I3A and RA and the pathogen-induced biosynthesis of 4MI3G (Figure 7). Moreover, PCS1 might be involved in further processing 4MI3G to 4OGlcI3F, 4MO3IM and 4MOI3Cys (Matern et al., 2019; Hématy et al., 2020). Piślewska-Bednarek *et al*., 2018 hypothesized that the formation of end products of the PEN2-pathway might require peptidase activity of PCS1 for cleavage of the Gly residue from I3G-ITC-GSH/4MI3G-ITC-GSH. Currently, it is not known at which step of IG biosynthesis PCS1 modifies the glutathione moiety. PCS1 might function upstream, downstream or in parallel with PEN2 or GSTU13 (Figure 7) (Matern et al., 2019; Hématy et al., 2020).

Subcellular localization analysis revealed that N- and C-terminally GFP-tagged PCS1 is localized to the cytosol in unchallenged leaf epidermal cells (Blum et al., 2010; Hématy et al., 2020). Upon pathogen

attack, the protein is translocated and co-localizes with PEN2 in aggregate structures in the periphery of clustered and arrested mitochondrial subpopulations (Figure 8) (Hématy et al., 2020). CLSM analysis of PCS1 in the *pen2-1* mutant background revealed PCS1 aggregate formation in proximity to the pathogen invasion site (Hématy et al., 2020). Moreover, no physical protein-protein interaction between PEN2 and PCS1 was observed, suggesting that PEN2 is not involved in the translocation of PCS1 to arrested mitochondria (Hématy et al., 2020).

Both PCS1-GFP and GFP-PCS1 complemented the heavy metal sensitivity of the *pen4* mutant. In contrast to N-terminally GFP-tagged PCS1, PCS1-GFP fusion proteins are nonfunctional in 4MI3G-metabolism and pre-invasive defense (Hématy et al., 2020). To test whether the involvement of PCS1 in pre-invasive NHR is independent of PCS1 function in phytochelatin biosynthesis, catalytically inactive PCS1 mutants were analyzed after *Bgh* inoculation. The tested mutants showed fungal penetration frequencies comparable to the wild-type Col-0, indicating that the function of PCS1 in pre-invasive NHR required a PCS1 function or activity that is independent of the synthesis of phytochelatin (Hématy et al., 2020).

1.5.7 PEN3

PEN3/PDR8 encodes a pleiotropic drug resistance (PDR) ATP-binding cassette (ABC) transporter and was identified as a further molecular component involved in pre-invasive NHR against powdery mildews (Stein et al., 2006). Transmembrane localized ABC transporters act in ATP-dependent transport of various substrates across intra- and extracellular membranes (Crouzet et al., 2006).

Subcellular localization studies using transgenic plants expressing functional GFP-tagged PEN3 showed that the transporter is localized to the plasma membrane similar to PEN1 (Figure 8). Upon pathogen attack, PEN3-GFP strongly accumulates in diffuse halos and bubble-like structures beneath the invading fungal appressoria (Stein et al., 2006). Infiltration of PEN3-GFP expressing leaves with either chitin or flagellin triggered focal accumulation of PEN3-GFP. Similarly, upon infiltration of leaves with *E. coli* cells, expressing the fluorophore *Discosoma* red fluorescent protein (dsRED), PEN3-GFP accumulation in ring-like structures was triggered in proximity to *E. coli* clusters (Underwood and Somerville, 2013). CLSM analysis of PEN3-GFP in either the *cerk-1* or *fls2* mutant background revealed no accumulation of PEN3-GFP after chitin or flg22 treatment, respectively. These results indicate that focal accumulation of PEN3 is triggered by sensing of chitin and flagellin by the corresponding PRRs CERK1 and FLS2, respectively. However, MAMP induced accumulation of PEN3 was shown to be independent of the co-receptor BAK1 (Underwood and Somerville, 2013).

In addition, PEN3 was shown to be incorporated into papilla and haustorial encasements of the powdery mildew *G. orontii* (Meyer et al., 2009). A more detailed analysis of PEN3 subcellular behavior

using different pharmacological inhibitors revealed that pathogen- and MAMP-triggered accumulation of PEN3 requires actin filaments and occurs extracellularly within the papillae. In contrast, PEN1 recruitment to the papillae does not rely on actin filaments indicating that PEN1 and PEN3 are recruited through different trafficking mechanisms (Underwood and Somerville, 2013).

The *trans*-Golgi localized lipid flippase P4 ATPase AMINOPHOSPHOLIPID ATPASE 3 (ALA3) is an important component for vesicle formation and was shown to be involved in timely recruitment of PEN3 to sites of pathogen invasion (Underwood et al., 2017). Similar to PEN3, PEN1 is localized to punctate endomembrane components and is delayed in pathogen-triggered focal accumulation in *ala3* indicating that ALA3 also affects trafficking of PEN1. Partial co-localization of PEN1 and PEN3 in *ala3* mutants suggests that both defense proteins continuously cycle through overlapping or similar endomembrane compartments following endocytosis from the plasma membrane. Furthermore, both GFP-PEN1 and PEN3-GFP accumulate in endomembrane compartments after flg22 and chitin treatment (Underwood et al., 2017). In addition, the cytosolic BTB (Broad-Complex, Tramtrack and Bric a brac)/POZ (POxvirus and Zinc finger)-domain protein ENDOPLASMIC RETICULUM-ARRESTED PEN3 (EAP3) was shown to be important for the release of PEN3 from the ER and disease resistance against the root-penetrating fungus *Fusarium oxysporum f. sp. conglutinans* (Mao et al., 2017).

Similar to *pen2*, *cyp81f2*, *gstu13* and *pen4* mutants, *pen3* mutant plants were shown to be impaired in callose deposition in response to flg22-treatment (Stein et al., 2006). In addition, *pen3* mutants showed enhanced penetration rates towards non-adapted powdery mildews (Stein et al., 2006). In contrast to *pen1* and *pen2*, *pen3* mutants exhibit increased basal resistance against adapted powdery mildews. Elevated basal resistance might be explained by hyper-activation of SA-dependent defense signaling pathways due to increased accumulation of toxic PEN2 metabolism products. This hypothesis was further supported by the observation that this phenotype is reduced in the *pen2 pen3* double mutants (Stein et al., 2006).

PEN3 is proposed to transport potentially antimicrobial PEN2 IG-metabolism products across the plasma membrane and into the apoplast to restrict pathogen entry at the cell periphery (Figure 8) (Stein et al., 2006; Johansson et al., 2014; Matern et al., 2019). The transporter exhibits a wide substrate specificity including indole butyric acid and cadmium (Kim et al., 2007; Strader and Bartel, 2009). Lu *et al*., 2015 showed that 4OGlcI3F over-accumulates in *pen3* mutants and is generated in a CYP81F2/PEN2-dependent manner upon pathogen attack (Lu et al., 2015). 4OGlcI3F is suggested to be a detoxification product for antimicrobial IG-derived metabolism products. Therefore, one or several unknown precursor molecules of 4GlcOI3F are suggested to be a substrate of PEN3 involved in pathogen defense (Figure 7) (Lu et al., 2015). Recently, Matern *et al*., 2019 identified *Phytophthora infestans*-induced leaf surface IG-derivates 4MOI3M and 4MOI3Cys in *Arabidopsis*. These compounds

are suggested to be derived from 4MI3G-ITC and synthesized in a PEN2- and PCS1-dependent manner and are secreted by PEN3 into the apoplast (Figure 7). Direct hydrolyzation of 4MI3G-ITC might lead to the formation of 4MOI3M and conversion to 4MeOI3Cys by yet unidentified enzymes. Furthermore, PCS1 might be involved in the biosynthesis of 4MeOI3Cys providing the PEN3 substrate required for pathogen entry control (Matern et al., 2019).

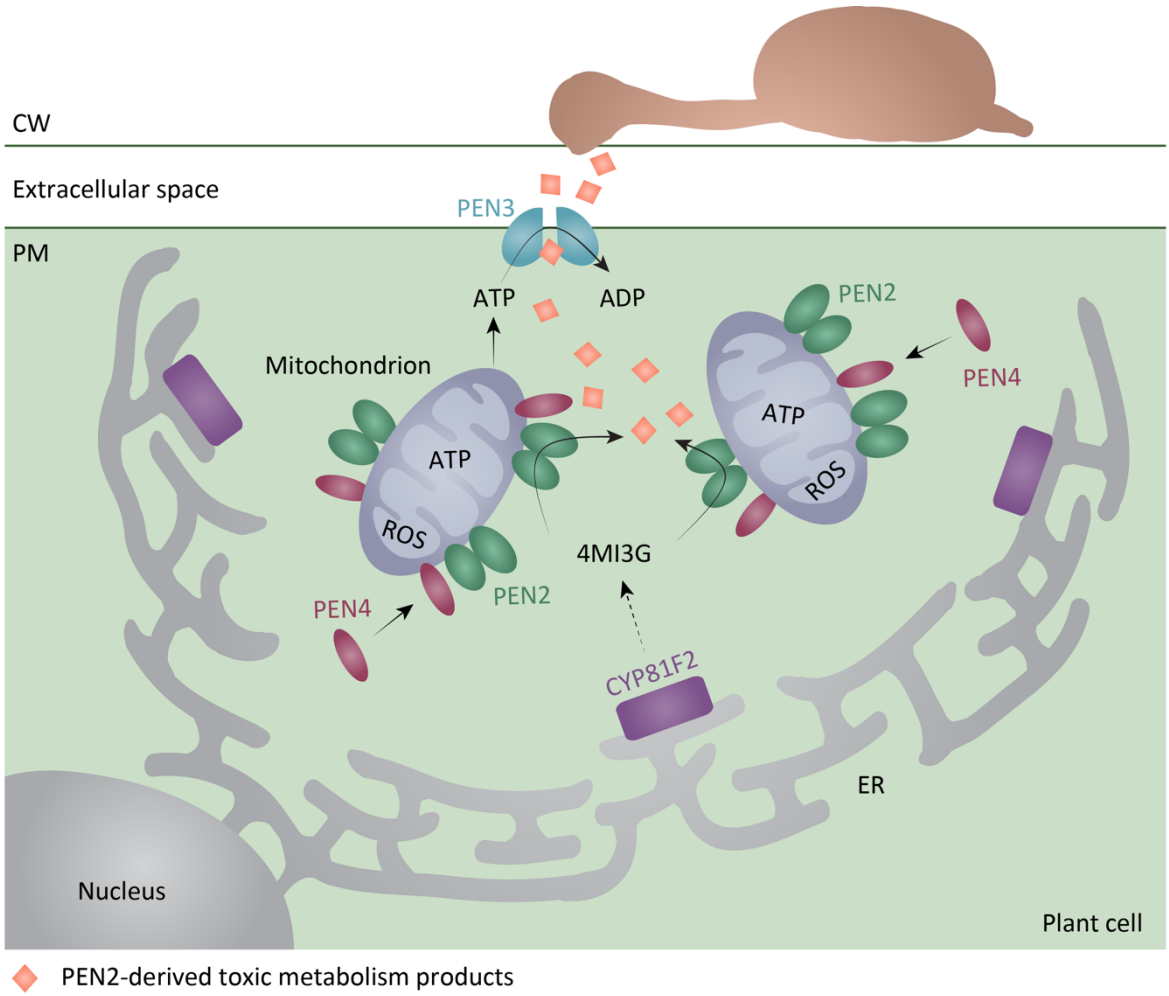

Figure 8. Schematic illustration of indole glucosinolate-mediated defense against powdery mildews. Attempted *Bgh* penetration of the non-host plant *Arabidopsis*. The ER reorganizes and mitochondria accumulate in close proximity to the fungal penetration site. PEN2 is localized to the outer mitochondrial membrane. Mitochondria accumulation and immobilization are associated with PEN2 aggregate formation. PEN4 is translocated and co-localizes with PEN2 in aggregate structures in the periphery of clustered and arrested mitochondrial subpopulations. The ER-localized CYP81F2 is involved in the biosynthesis of the PEN2 substrate 4MI3G. PEN2 catalyzes the hydrolysis of 4MI3G, resulting in the formation of toxic hydrolysis products. PEN3 transports potentially antimicrobial PEN2 IG-metabolism products across the plasma membrane and into the apoplast to restrict pathogen entry at the cell periphery. PEN4/PCS1 relocalizes from the cytoplasm to clustered and immobilized mitochondria. PEN4 might function upstream, downstream or in parallel with GSTU13 and/or PEN2. Immobilized mitochondria show a pathogen-induced redox imbalance, which might be due to the release of ROS. Changes in the mitochondrial redox status might trigger retrograde mitochondria-nucleus signaling and transcriptional changes. Mitochondria may also supply ATP for pathogen-induced energy-dependent cellular processes such as the transport of antimicrobial compounds by PEN3 across the PM. This figure is based on Lipka et al., 2005, Stein et al., 2006, Bednarek et al., 2009, Clay et al., 2009, Fuchs et al., 2016 and Hématy et al., 2020.

1.5.8 ERD6

The putative sugar transporter EARLY RESPONSE TO DEHYDRATION 6 (ERD6) belongs to the ERD6-like family in *Arabidopsis*. The 19 members of the ERD6-like family share 48-95% similarity among each other and are a sub-group of the monosaccharide transporter(-like) gene family in *Arabidopsis* (Kiyosue et al., 1998). These different transporters facilitate the transport of sugars across membranes including the plasma membrane or organellar membranes (Schäfer et al., 1977; Rausch, 1991; Rost et al., 1996; Martinoia et al., 2000). Vacuoles play an important role in the storage of soluble sugars. Several members of the ERD6-like family were identified to localize to the tonoplast in *Arabidopsis* including ERD6-LIKE 6 (ERDL6) (Poschet et al., 2011) and the closest homolog of ERD6, ERD SIX-LIKE 1 (ESL1) (Yamada et al., 2010). ESL1 was demonstrated to be an abiotic stress-induced monosaccharide transporter, which requires an LXXXLL motif in the N-terminus for proper localization to the tonoplast. Moreover, ERD6-like family members show homology to the mammalian glucose transporter (GLUT) family especially GLUT6 and GLUT8. GLUT8 was shown to be associated with late endosomes and lysosomes and contains a cytoplasmic N-terminal endosomal/lysosomal sorting-motif (DE]XXXL[LI]) (Augustin et al., 2005). Similar to ESL1, ERD6 contains 12 putative transmembrane domains and a conserved major facilitated superfamily domain (Kiyosue et al., 1998; Yamada et al., 2010).

Transport assays identified ESL1 as facilitated diffusion transporter, which is not dependent on a proton gradient (Yamada et al., 2010). It is suggested that ESL1 functions in the efflux of sugars such as hexoses from the vacuole into the cytoplasm (Yamada et al., 2010). ERDL6 was shown to function as a proton-coupled glucose exporter (Klemens et al., 2014). Similar to the closely related tonoplast localized putative sugar transporter of *Beta vulgaris*, ERD6 showed no sugar transport activity against the tested substrates D-galactose, D-fructose, D-xylose or 3-O-methylglucose in yeast (Kiyosue et al., 1998).

ERD6 is induced upon flg22 (Zipfel et al., 2004), cold and dehydration treatment (Kiyosue et al., 1994). Furthermore, *ERD6* was shown to be co-expressed with *PEN2* and *PEN3* in *Arabidopsis* (Humphry et al., 2010). Analysis of *erd6* mutants revealed enhanced disease symptoms to different pathogens in comparison to the wild-type (Humphry et al., 2010). For example, increased sporulation of *G. orontii* and chlorosis was observed on leaves of *erd6* mutants 10 dpi. Metabolomic analysis showed significantly reduced levels of I3A and RA in *erd6* mutants similar to the *pen2-2* mutant phenotype 16 hours after *E. pisi* inoculation. Additionally, in comparison to the wild type and *pen2-2*, the amount of I3G is significantly increased in *erd6*. These results suggest a putative involvement of ERD6 in the transport of the PEN2 substrate precursor I3G (Humphry et al., 2010). However, further inves-

tigation is needed to determine whether ERD6 acts as an I3G transporter involved in cell-autonomous remobilization of intracellularly stored I3G in plant-microbe interactions.

1.6 Thesis aims

The *Arabidopsis* cytochrome P450 monooxygenase CYP81F2 and the myrosinase PEN2 are important components for broad-spectrum pre-invasion defense against filamentous plant pathogens, including non-adapted powdery mildews (Lipka et al., 2005). PEN2 is targeted to both peroxisomes and mitochondria. Pathogen-induced recruitment and arrest of mitochondrial subpopulations were observed at sites of attempted fungal invasion. Moreover, mitochondrial immobilization is accompanied by the accumulation of PEN2 on the outer mitochondrial membrane (Fuchs et al., 2016). PEN2 was shown to form pathogen-triggered oligomers and dimers of higher order in the periphery of arrested mitochondria (Fuchs et al., 2016). CYP81F2 is localized to the ER. Upon, pathogen attack, the ER structurally reorganizes in proximity to the arrested mitochondria (Fuchs et al., 2016). Furthermore, CYP81F2 functions in the pathogen-induced biosynthesis of 4MI3G, which is a substrate of the PEN2 myrosinase. PEN2 catalyzes the hydrolyzation of 4MI3G, resulting in the formation of toxic hydrolysis products (Bednarek et al., 2009; Clay et al., 2009). Furthermore, the ABC transporter PEN3 is proposed to transport potentially antimicrobial PEN2 IG-metabolism products across the plasma membrane and into the apoplast to restrict pathogen entry at the cell periphery (Stein et al., 2006; Matern et al., 2019). These pathogen-induced and cell-autonomous defense mechanisms at the site of attempted fungal invasion very likely require sensing of the potential intruder by the plant. However, it is unknown how CYP81F2- and PEN2-mediated defense responses are connected to pathogen recognition. A potential scenario is that the sensing of microbe-associated molecular patterns (MAMPs) might be required for pre-invasive resistance.

Therefore, the first aim of this study was to investigate the role of MAMP-dependent signaling for CYP81F2 accumulation, ER rearrangement, mitochondrial arrest and PEN2 aggregate formation. To this end, CYP81F2-RFP or PEN2-GFP-TA_{PEN2} expressing plants were analyzed after infiltration with either chitin or flagellin. To further characterize PEN2-GFP-TA_{PEN2} aggregate formation after MAMP treatment, time-course analysis and co-expression experiments with either peroxisomal or mitochondrial marker lines were performed.

The second aim of this project was to identify and characterize novel important molecular components contributing to PEN2-mediated pathogen entry control. In order to identify molecular components involved in the mechanisms and signaling pathways in pathogen-induced reorganization of the ER, PEN2 aggregate formation, mitochondrial clustering and immobilization, a double transgenic line

expressing both PEN2-GFP-TA_{PEN2} and CYP81F2-mKate2 was generated and characterized. The selected line might be used for a CLSM-based forward genetic screen.

Molecular components involved in pre-invasive non-host resistance were previously shown to share a similar set of co-expressed genes in *Arabidopsis*. In total, 164 genes were identified to be co-regulated with PEN2 and PEN3 in *Arabidopsis* (Humphry et al., 2010). To identify additional compounds required for PEN2-mediated resistance, two of these co-expressed genes, *AT1G08930* (*Early response to dehydration* 6 (*ERD6*)) and AT1G55450 (*S-adenosyl-L-methionine-dependent methyltransferase;* named SAM-MT) were selected for further analysis in this study. To test the contribution of these two genes in penetration resistance, *erd6* and *sam-mt* mutants were analyzed after inoculation with non-adapted and adapted powdery mildews. Moreover, ERD6 was further characterized concerning subcellular localization and indole glucosinolate metabolite levels in *erd6* mutants by an LC-MS-based nontargeted metabolome approach to get insights into its biological function and involvement in indole glucosinolate-mediated defense.

Recently, the Glutathione-S-transferase class-tau member 13 (GSTU13) was identified as an important molecular component of the PEN2 defense pathway for IG metabolism (Piślewska-Bednarek et al., 2018). To investigate whether the contribution of GSTU13 for pre-invasive disease resistance requires a specific subcellular localization, pathogen-induced protein translocation or organelle compartmentalization, GSTU13 was analyzed using fluorescently-tagged proteins stably expressed in *gstu13-1* mutant and PEN2-GFP-TA_{PEN2} plants.

To gain new insights into the molecular mechanisms of PEN2-mediated pathogen entry control, IP-MS experiments were conducted using PEN2-GFP-TA_{PEN2} expressing plants in the *pen2-1* mutant background to identify putative PEN2 interaction partners.

2 Material and Methods

2.1 Material

2.1.1 Plants

2.1.1.1 *Arabidopsis thaliana*

Arabidopsis thaliana (L.) Heynh. accessions Columbia-0 (Col-0) and Col-3 *gl1* were used as wild-type lines (J. Dangl, University of North Carolina, Chapel Hill, NC USA). T-DNA mutant lines from the SALK collection (Alonso et al., 2003) were obtained from the Nottingham Arabidopsis Stock Centre (NASC) and T-DNA mutant lines from the GABI collection from GABI-KAT (Kleinboelting et al., 2012). T-DNA mutant lines used in this work are listed in Table 1. Transgenic lines and double transgenic lines generated and/or used in this study are listed in Table 2 and Table 3, respectively.

Table 1. *Arabidopsis thaliana* T-DNA insertion lines used in this study.

Allele	AGI locus	Background	T-DNA/Mutagen	Reference
sam-mt-1	AT1G55450	Col-0	SALK_025395	This work
sam-mt-2	AT1G55450	Col-0	SALK_087716C	This work
cyp81f2-2	AT5G57220	Col-0	GABI_097D04	Rosso et al., 2003
erd6-1	AT1G08930	Col-0	SALK_137614	Humphry et al., 2010
erd6-3	AT1G08930	Col-0	SALK_025395	This work
gbpl3-1	AT5G46070	Col-0	GABI_028F01	This work
gbpl3-2	AT5G46070	Col-0	SALK_08366	This work
gbpl3-3	AT5G46070	Col-0	SALK_078672	This work
gstu13-1	AT1G27130	Col-0	SALK_022297	Piślewska-Bednarek et al., 2018
pen2-1	AT2G44490	Col-3 *gl1*	EMS	Lipka et al., 2005
pen2-2	AT2G44490	Col-0	GABI_134C04	Rosso et al., 2003

Table 2: Single transgenic *Arabidopsis thaliana* lines used in this study.

Transgene	Background	Vector	Selection marker	Reference
CYP81F2-RFP	*cyp81f2-2*	*pAM-MCS-NotI-pCYP81F2:::CYP81F2-RFP*	Kan^R	Fuchs et al., 2016
ERD6-mTurquoise2	*erd6-1*	*pHG175-pERD6::ERD6-mTurquoise2*	$Sulf^R$	This work
GSTU13-RFP	*gstu13-1*	*pHG175-pGSTU13::GSTU13-RFP*	$Sulf^R$	This work
MEMB12-mCherry	Col-0	*pNIGEL17-pUBQ10::MEMB12-mCherry*		Geldner et al., 2009

PEN2-GFP-TA_{PEN2}	*pen2-1*	*pAMPAT-MCS-NotI-pPEN2::PEN2-GFP-TA_{PEN2}*	Basta®^{R}	Lipka et al*.*, 2005
PEN2-GFP-$TA_{PEN2\Delta TM}$	*pen2-1*	*pAMPAT-MCS-NotI-pPEN2::PEN2-GFP-$TA_{PEN2\Delta TM}$*	Basta®^{R}	Fuchs et al*.*, 2016
RabA1g-mCherry	Col-0	*pNIGEL17-pUBQ10::RabA1-mCherry*	Hyg^R	Geldner et al*.*, 2009
RabA5d-mCherry	Col-0	*pNIGEL17-pUBQ10::RabA5d-mCherry*	Hyg^R	Geldner et al*.*, 2009
Rha1-mCherry	Col-0	*pNIGEL17-pUBQ10::Rha1-mCherry*	Hyg^R	Geldner et al*.*, 2009
RFP-GSTU13	*gstu13-1*	*pHG175-pGSTU13-RFP-GSTU13*	Sulf^R	This work

Table 3. Double transgenic *Arabidopsis thaliana* lines used in this study.

Transgene	Back-ground	Vector	Selection marker	Reference
ERD6-mTurquoise2 MEMB12-mCherry[1]	*erd6-1*		Sulf^R Hyg^R	This work
ERD6-mTurquoise2 RabA1g-mCherry[1]	*erd6-1*		Sulf^R Hyg^R	This work
ERD6-mTurquoise2 RabA5d-mCherry[1]	*erd6-1*		Sulf^R Hyg^R	This work
ERD6-mTurquoise2 Rha1-mCherry[1]	*erd6-1*		Sulf^R Hyg^R	This work
PEN2-GFP-TA_{PEN2} CYP81F2-mKate2	Col-3 *gl1*	*pHG148-pPEN2::PEN2-GFP-TA_{PEN2}-pCYP81F2::CYP81F2-mKate2*	Basta®^{R}	This work
PEN2-GFP-TA_{PEN2} ERD6-mTurquoise2	*pen2-1*	*pHG175-pERD6::ERD6-mTurquoise2*	Basta®^{R} Sulf^R	This work
PEN2-GFP-TA_{PEN2} GSTU13-RFP	*pen2-1*	*pHG175-pGSTU13::GSTU13-RFP*	Basta®^{R} Sulf^R	This work
PEN2-GFP-TA_{PEN2} RFP-GSTU13	*pen2-1*	*pHG175-pGSTU13-RFP-GSTU13*	Basta®^{R} Sulf^R	This work
PEN2-GFP-TA_{PEN2} RFP-PTS1	*pen2-1*		Basta®^{R} Kan^R	Fuchs et al*.*, 2016
PEN2-GFP-TA_{PEN2} ScCox4-RFP	*pen2-1*		Basta®^{R} Kan^R	Fuchs et al*.*, 2016

[1] Double transgenic line was generated by crossing

2.1.1.2 *Nicotiana benthamiana*

Seeds of *N. benthamiana* were originally obtained by T. Romeis (Biochemistry of Plants, Institute of Biology, Freie Universität Berlin). 5-4-week-old *N. benthamiana* plants were used for *Agrobacterium tumefaciens*-mediated transient expression experiments.

2.1.2 Fungal pathogens

2.1.2.1 *Blumeria graminis f.sp. hordei*

The non-adapted powdery mildew *Blumeria graminis f.sp. hordei* (*Bgh*) Isolate K1 (Lipka et al., 2005) was used for *Arabidopsis* inoculation experiments.

2.1.2.2 *Erysiphe pisi*

The non-adapted pea powdery mildew *Erysiphe pisi* Birmingham Isolate (Lipka et al., 2005) was used for inoculation experiments of *Arabidopsis* plants.

2.1.2.3 *Golovinomyces orontii*

The adapted powdery mildew *Golovinomyces orontii* (Lipka et al., 2005) was used for *Arabidopsis* infection experiments. *G. orontii* was originally obtained from the Max-Planck-Institute for Plant Breeding Research, Cologne, Germany.

2.1.3 Bacterial strains

2.1.3.1 *Escherichia coli*

The chemically competent *Escherichia coli* (*E. coli*) strain TOP10 *(*F$^-$ *mcr*A *Δ(mrr-hsd*RMS-*mcr*BC*) Φ*80*lacZ*Δ M15 *Δlac*X74 *rec*A1 *ara*D139 *Δ(ara-leu)* 7697 *gal*U *gal*K *rps*L *(*Str^R*) end*A1 *nup*G*)* (Invitrogen^{TM}, Carlsbad, USA) was used for cloning and amplification of plasmids.

2.1.3.2 *Agrobacterium tumefaciens*

For transient expression experiments in *N. benthamiana* leaves and the generation of stable transgenic *Arabidopsis* plants, the electro-competent *Agrobacterium tumefaciens* (*A. tumefaciens*) strain GV3101 (Koncz and Schell, 1986) was utilized. The strain used in this work carries the helper plasmid pMP90RK conferring resistance to kanamycin.

2.1.4 Vectors

Vectors used or generated in this work are listed in Table 4.

Table 4. Vectors used or generated in this work.

Name	Description	Selectable marker for bacteria and plants	Reference
pHG148_pUBQ10-	Expression of *mKate2-N7* under the	Amp^R, Basta®^{R}	Hassan

mKate2-N7-35S-eGFP-LTI6b (V2)[1]	ubiquitin promoter (nucleus marker) and expression of *eGFP-LTI6b* under control of the 35S promoter (plant plasma membrane marker)		Ghareeb
pHG175-p35S-mTQ2-N7-p-SAS (C3)[1]	Expression of *mTurquoise2-N7-p-SAS* (synthetic SA synthase) under control of the 35S promoter	Amp^R, $Sulf^R$	Hassan Ghareeb
pHG175-pERD6::ERD6-mCitrine (pLW21)[1]	Expression of *ERD6* gDNA under control of the endogenous promoter with a C-terminal mCitrine tag	Amp^R, $Sulf^R$	This work
pHG175-pERD6::ERD6-RFP (pLW20)[1]	Expression of *ERD6* gDNA under control of the endogenous promoter with a C-terminal RFP tag	Amp^R, $Sulf^R$	This work
pHG175-pERD6::ERD6-mTurquoise2 (pLW4)[1]	Expression of *ERD6* gDNA under control of the endogenous promoter with a C-terminal mTurquoise2 tag	Amp^R, $Sulf^R$	This work
pHG175-pERD6::ERD6(L11A)-mTurquoise2 (pLW18)[1]	Expression of *ERD6* gDNA under control of the endogenous promoter with a C-terminal mTurquoise2 tag	Amp^R, $Sulf^R$	This work
pERD6::ERD6(L12A)-mTurquoise2 (pLW19)[1]	Expression of *ERD6* gDNA under control of the endogenous promoter with a C-terminal mTurquoise2 tag	Amp^R, $Sulf^R$	This work
pHG175-pERD6::ERD6(L11/12A)-mTurquoise2 (pLW17)[1]	Expression of *ERD6* gDNA under control of the endogenous promoter with a C-terminal mTurquoise2 tag	Amp^R, $Sulf^R$	This work
pHG175-pERD6::ERD6(M7L)-mTurquoise (pLW23)[1]	Expression of *ERD6* gDNA under control of the endogenous promoter with a C-terminal mTurquoise2 tag	Amp^R, $Sulf^R$	This work
pAMPAT-MCS-35S::RFP-ERD6[1]	Expression of *ERD6* cDNA under control of the 35S promoter with an N-terminal RFP tag	Amp^R, $Basta^{®R}$	Rene Fuchs
pHG175-pGSTU13::GSTU13-RFP (pLW7)[1]	Expression of *GSTU13* gDNA under control of the endogenous promoter with a C-terminal RFP tag	Amp^R, $Sulf^R$	This work
pHG175-pGSTU13::RFP-GSTU13 (pLW8)[1]	Expression of *GSTU13* gDNA under control of the endogenous promoter with an N-terminal RFP tag	Amp^R, $Sulf^R$	This work
pHG148-pPEN2::PEN2-GFP-TA$_{PEN2}$-pCYP81F2::CYP81F2-mKate (pLW1)[1]	Expression of *PEN2* cDNA under control of the endogenous promoter with a GFP tag between the globular enzymatic part of PEN2 and the C-terminal extension and expression of *CYP81F2* cDNA under control of the native promoter with a C-terminal mKate2 tag	Amp^R, $Basta^{®R}$	This work

[1] Binary vector for *A. tumefaciens* mediated transformation of plants

2.1.5 Oligonucleotides

The oligonucleotides used in this work were purchased from Thermo Fisher Scientific (Waltham, Massachusetts, USA). Lyophilized oligonucleotides were resuspended and diluted with ultrapure water to a final concentration of 100 µM. For standard usage, working solutions with a concentration of 10 µM were prepared and stored at -20°C. Table 5 lists all oligonucleotides used in this study.

Table 5. Oligonucleotides used in this study.

Name	Nucleotide Sequence (5´-3´)	Application
Primers used for genotyping		
oLW106	AAGCTTTTGAAGTCCTTTGGC	genotyping of *at1g55450-1*
oLW107	GGGATTAAAACGACATCGTTTG	genotyping of *at1g55450-1*
oHG170	ATTTTGCCGATTTCGGAAC	SALK left border T-DNA primer (LBb1.3)
oLW104	GCCAGAGCTGACTTTGAAAAC	genotyping of *at1g55450-2*
oLW105	CGTTCTTTAGCTTTCATTGCG	genotyping of *at1g55450-2*
oHG170	ATTTTGCCGATTTCGGAAC	SALK left border T-DNA primer (LBb1.3)
oLW13	TCCCAGTCAAAGCATTGAATC	genotyping of *cyp81f2-2*
oLW14	CCTCTTCTTGCAGATTTGACG	genotyping of cyp81f2-*2*
UU41	CCCATTTGGACGTGAATGTAGACAC	GABI left border T-DNA primer
oLW49	AATTGCACCTAAACATGTCCG	genotyping of *erd6-1*
oLW48	TGCCAATAGCACTTGGAAATC	genotyping of *erd6-1*
oHG170	ATTTTGCCGATTTCGGAAC	SALK left border T-DNA primer (LBb1.3)
oLW101	ACGATGTTGTTTTGCGAATTC	genotyping of *erd6-3*
oLW100	ACCACCGTTTTCTGTCATGTC	genotyping of *erd6-3*
oHG170	ATTTTGCCGATTTCGGAAC	SALK left border T-DNA primer (LBb1.3)
oLW175	TTGATCATGCATTTTCACGTAAG	genotyping of *gbpl3-1*
oLW174	CAGTTCCGTCAAGAGCTGTTC	genotyping of *gbpl3-1*
UU41	CCCATTTGGACGTGAATGTAGACAC	GABI left border T-DNA primer
oLW175	TTGATCATGCATTTTCACGTAAG	genotyping of *gbpl3-2*
oLW174	CAGTTCCGTCAAGAGCTGTTC	genotyping of *gbpl3-2*
oHG175	ATTTTGCCGATTTCGGAAC	SALK left border T-DNA primer (LBb1.3)
oLW168	AGAAACCACACATTTAGGCCC	genotyping of *gbpl3-3*
oLW169	CACGAACATGCTTGACAAAAG	genotyping of *gbpl3-3*
oHG175	ATTTTGCCGATTTCGGAAC	SALK left border T-DNA primer (LBb1.3)
oLW108	CACTCATGCATAGCGAAGAGG	genotyping of *gstu13-1*
oLW109	GATCCGATTTACGGATATGGG	genotyping of *gstu13-1*
oHG170	ATTTTGCCGATTTCGGAAC	SALK left border T-DNA primer (LBb1.3)
oLW5	TTTGGAACTGCTTCATCTTCTTATCAGG	genotyping of *pen2-1* (Lipka et al., 2005)
oLW6	CCTGTACAAGAAAT CAATCACAGATCTTCA	genotyping of *pen2-1* (Lipka et al., 2005)
oLW20	AGGCTTTCTCTTTGGAACTGC	genotyping of *pen2-2*
oLW21	TCCTTCGACATCATCTGGATC	genotyping of *pen2-2*
UU41	CCCATTTGGACGTGAATGTAGACAC	GABI left border T-DNA primer
olW184	TCCTGCCCGTCACCGAAATC	Identification of the T-DNA insertion position
oLW189	TGGCCAAGCAATGGAAAGC	
Primers used for expression analysis		

Actin-fw Actin-rev	TGCGACAATGGAACTGGAATG GGATAGCATGTGGAAGTGCATAC	Semi-quantitative RT-PCR of *Actin1*
oLW136 oLW137	TTGCTCTAGTCGGCGGAGATAAC GTAAGCACAGTAAGCCGCCACTC	Semi-quantitative RT-PCR of *AT1G55450*
oLW138 oLW139	GTTAGCGGATGCTTACCAGAACG GGCTGCCACGATCTCAAGAAACC	Semi-quantitative RT-PCR of *AT1G55450*
oLW140 oLW137	GTGGACTCCACGTTCCCGTTTAG GTAAGCACAGTAAGCCGCCACTC	Semi-quantitative RT-PCR of *AT1G55450*
oLW132 oLW133	AGTAGTCGGATTGGTGCCATGTG ACGCCGATGCAAGTGAAGATGGG	Semi-quantitative RT-PCR of *ERD6*
oLW134 oLW135	GAGCTCCGGTGTTACCTATTATGC AATACGATCGAACTGGCGGAGAC	Semi-quantitative RT-PCR of *ERD6*
oLW128 oLW129	CAGGCTGGCTTTGTGTAGCATTG GACTAGGACTGTTGCCAGCATTG	Semi-quantitative RT-PCR of *ERD6*
oLW130 oLW131	TCCAAGATGGCTGGCGAAGTTAG CTAAGGTCCCAGCTGACACTTTC	Semi-quantitative RT-PCR of *ERD6*
Primers used for cloning/site-directed mutagenesis		
oLW211 oLW212	CAACAACTCTGTGCAAGCGGCCG-CAATGGTGAGCAAGGGCGAGGA TGATTTTTGCGGACTCTAGACTAGTCTACTT-GTACAGCTCGTCCA	Cloning of *pERD6::ERD6-mCitrine* (pLW21); Amplification of mCitirine
oLW204 oLW205	CAACAACTCTGTGCAAGCGGCCG-CAATGGCCTCCTCCGAGGACGT TTTTTGCGGACTCTAGACTAG-TTTAGGCGCCGGTGGAGTGGCGGC	Cloning of *pERD6::ERD6-RFP* (pLW20); Amplification of RFP
oLW74 oLW120	TGATCCCGGCCAGGGTGGCCGGTACAC-TGTTTATTGCATTTCTGA CACCATTGCGGCCGCTTGCACAGAGTTGTTGAG-CA	Cloning of *pERD6::ERD6-mTurquoise2* (pLW4); Amplification of the promoter and the gene sequence of *ERD6*
oLW82 oLW121	GTGATTTTTGCGGACTCTAGACTAGTTACTT-GTACAGCTCGTCCA GTGCAAGCGGCCGCAATGGTGAG-CAAGGGCGAGGA	Cloning of *pERD6::ERD6-mTurquoise2* (pLW4); Amplification of *mTurquoise2*
oLW207 oLW208	ATGCTCTTTTGTCTCTCC GGAAAAAGGGgcACTCAGGAAG	Site-directed mutagenesis for generation of *pERD6::ERD6(L11A)-mTurquoise2* (pLW18)
oLW209 oLW210	AAAAGGGTTAgcCAGGAAGAGCTTAAG TCCATGCTCTTTTGTCTC	Site-directed mutagenesis for generation of *pERD6::ERD6(L12A)-mTurquoise2* (pLW19)
oLW207 oLW206	ATGCTCTTTTGTCTCTCC GGAAAAAGGGgcagcCAGGAAGAGCTTAAG	Site-directed mutagenesis for generation of *pERD6::ERD6(L11/12A)-mTurquoise2* (pLW17)
oLW218 oLW219	ACAAAAGAGCcTGGAAAAAGG CTCTCCATTCCAAAAAGTC	Site-directed mutagenesis for generation of *pERD6::ERD6(M7L)-mTurquoise2* (pLW23)
oLW90 oLW126	TGATCCCGGCCAGGGTGGCCGGTACAAC-CTTTCAAGCCTTTTACA GGCCATTGCGGCCGCCTGAACATTGAACTTTT-GCT	Cloning of *pGSTU13::GSTU13-RFP* (pLW7); Amplification of the promoter and the gene sequence of *GSTU13*

oLW93	GTGATTTTTGCGGACTCTAGACTAG-TCAGGCGCCGGTGGAGTGGC	Cloning of *pGSTU13::GSTU13-RFP* (pLW7); Amplification of *RFP*
oLW127	GTTCAGGCGGCCGCAATGGCCTCCTCCGAG-GACGT	
oLW94	TGATCCCGGCCAGGGTGGCCGGTACAAC-CTTTCAAGCCTTTTACA	Cloning of *pGSTU13::RFP-GSTU13* (pLW8); Amplification of the *GSTU13* promoter sequence
oLW95	TGATGACGTCCTCGGAG-GAGGCCATGACTTCTTCTGGTTTTTATT	
oLW96	AGATCAATAAAAACCAGAA-GAAGTCATGGCCTCCTCCGAGGACGT	Cloning of *pGSTU13::RFP-GSTU13* (pLW8); Amplification of *RFP*
oLW97	TATCGTTCTGAGCCATT-GCGGCCGCGGCGCCGGTGGAGTGGCGGC	
oLW98	CCACTCCACCGGCGCCGCGGCCG-CAATGGCTCAGAACGATACAGT	Cloning of *pGSTU13::RFP-GSTU13* (pLW8); Amplification of the gene sequence of *GSTU13*
oLW99	TGATTTTTGCGGACTCTAGACTAGTCAC-TGAACATTGAACTTTTG	
oLW31	CGCTCACCATTGCCCCTGCGCCAGCGGCCG	Cloning of *pPEN2::PEN2-GFP-TA$_{PEN2}$-pCYP81F2:: CYP81F2-mKate2* (pLW1); Amplification of the promoter and cDNA sequence of *CYP81F2*
oLW60	GCCCTTGATATCCAC-GTGCGGTCCGTCATATTTACCTATT	
oLW32	GCGCAGGGGCAATGGTGAGCGAGCTGATTAA	Cloning of *pPEN2::PEN2-GFP-TA$_{PEN2}$-pCYP81F2::CYP81F2-mKate2* (pLW1); Amplification of *mKate2*
oLW61	TGATTTTTGCGGACTCTAGACTAG-TTCATCTGTGCCCCAG	
oLW66	CCAAAATCCAGTGACCGGCCCATGCCTG-CAGGTCGACGAAAAAAAAAAAGG	Cloning of *pPEN2::PEN2-GFP-TA$_{PEN2}$-pCYP81F2::CYP81F2-mKate2* (pLW1); Amplification of the promoter and PEN2-GFP-*TA$_{PEN2}$* cDNA sequence
oLW67	TGAACGATCGGG-GAAATTCGAGCTCCTCAATTATTAGCTCCTTTG	
Primers used for sequencing		
oLW176	CCCTTATCTGGGAACTACTC	Sequencing of *pERD6::ERD6-mCitrine* (pLW21) and *pERD6::ERD6-RFP* (pLW20)
oLW177	CATACTTCTGCAACGGAGAG	Sequencinf of *pERD6::ERD6(L11A)-mTurquoise2* (pLW18), *pERD6::ERD6(L12A)-mTurquoise2* (pLW19), *pERD6::ERD6(L11/12A)-mTurquoise2* (pLW17) and *pERD6::ERD6(M7L)-mTurquoise2* (pLW23)
oLW48	TGCCAATAGCACTTGGAAATC	Sequencing of *pERD6::ERD6-mTurquoise2* (pLW4)
oLW52	GAAAGTTCCCTAACGAAGAC	
oLW121	GTGCAAGCGGCCGCAATGGTGAG-CAAGGGCGAGGA	
oLW128	CAGGCTGGCTTTGTGTAGCATTG	
oLW134	GAGCTCCGGTGTTACCTATTATGC	
oLW177	CATACTTCTGCAACGGAGAG	
oHG40	TCGTGCTGCTTCATGTGGTC	
oLW65	ACCCGCCAATATATCCTGTC	
oLW1	AGTTCCAGTACGGCTCCAAG	Sequencing of *pGSTU13::GSTU13-RFP* (pLW7)
oLW2	CCGTCCTCGAAGTTCATCAC	
oLW110	CGTTCCTTCAATCCTTCCTTC	
oHG65	ACCCGCCAATATATCCTGTC	

oLW1	AGTTCCAGTACGGCTCCAAG	Sequencing of *pGSTU13::RFP-GSTU13* (pLW8)
oLW2	CCGTCCTCGAAGTTCATCAC	
oLW51	CTGGTGATTTTTGCGGACTC	
oLW109	GATCCGATTTACGGATATGGG	
oHG65	ACCCGCCAATATATCCTGTC	
oLW3	TTCCATGGCCAACACTTGTC	Sequencing of *pPEN2::PEN2-GFP-TA$_{PEN2}$-pCYP81F2::CYP81F2-mKate2*
oLW4	CTTCAGCACGTGTCTTGTAG	
oLW8	TTCATCGACCAATCTCTCTT	
oLW11	ACCAACTCCGTTTCCTATCG	
oLW14	CCTCTTCTTGCAGATTTGACG	
oLW20	AGGCTTTCTCTTTGGAACTGC	
oLW54	TGAAGCATCGTGCGTGGTTG	
oLW55	TGTCATGGTGGACCTTTTTG	
oLW58	TCAAGAACACAGAGAAAGAT	
oLW62	GCATGGACGAGCTGTACAAG	
oLW68	TCTCCAGAATAATGTGTGAG	
oLW69	GCATTAGCCTCTTTCGTAAC	
oLW70	CATGCTTCTAGCGCACGCAG	
oLW71	CGGCGGATGTCGGCCGGGCG	
oHG40	TCGTGCTGCTTCATGTGGTC	
oHG41	ACATGGCCCTGAAGCTCGTG	
oHG65	ACCCGCCAATATATCCTGTC	
oLW107	GGGATTAAAACGACATCGTTTG	Sequencing of *at1g55450-1* PCR products
oLW105	CGTTCTTTAGCTTTCATTGCG	Sequencing of *at1g55450-2* PCR products
oLW175	TTGATCATGCATTTTCACGTAAG	Sequencing of *gbpl3-1 and gbpl3-2* PCR products
oLW169	CACGAACATGCTTGACAAAAG	Sequencing of *gbpl3-3* PCR products
oLW49	AATTGCACCTAAACATGTCCG	Sequencing of *erd6-1* PCR products
oLW101	ACGATGTTGTTTTGCGAATTC	Sequencing of *erd6-2* PCR products
olW184	TCCTGCCCGTCACCGAAATC	Sequencing of the inverse PCR product
oLW189	TGGCCAAGCAATGGAAAGC	

2.1.6 Enzymes

2.1.6.1 Restriction endonucleases

Restriction endonucleases were purchased from New England Biolabs (Frankfurt am Main, Germany) or Thermo Fisher Scientific (Waltham, USA). Enzymes were used with the provided 10x reaction buffers according to the manufacturer´s specifications.

2.1.6.2 Polymerases and nucleic acid modifying enzymes

Standard polymerase chain reaction (PCR, 2.2.3.4) and semi-quantitative reverse transcription PCR (semi-qRT PCR, 2.2.3.15) were performed using homemade *Taq* DNA polymerase. For cloning purposes, PCR products were amplified with the iProof™ High-Fidelity DNA polymerase (Bio-Rad, Munich, Germany, 2.2.3.4) and the NEBuilder® HiFi DNA Assembly Master Mix (New England Biolabs,

Ipswich, USA) was used for assembly of plasmids. cDNA was synthesized from total RNA utilizing the RevertAid™ H Minus Reverse Transcriptase (Thermo Fisher Scientific, Waltham, USA) (2.2.3.14). For ligation of DNA fragments, the T4 DNA ligase (Thermo Fisher Scientific, Waltham, USA) (2.2.3.9) was used. All enzymes were applied according to the manufacturer´s instructions.

2.1.6.3 Trypsin

For protein digestion prior to liquid chromatography-mass spectrometry (LC-MS) analysis Sequencing Grade Modified Trypsin (Promega, Madison, Wisconsin, USA) was used.

2.1.7 Chemicals

Chemicals used in this study were purchased from abcam (Cambridge, UK), AppliChem (Darmstadt, Germany), BioRad (Munich, Germany), Difco (Heidelberg, Germany), Duchefa (Haarlem, The Netherlands), Intas (Göttingen, Germany), Invitrogen (Karlsruhe, Germany), Macherey Nagel (Düren, Germany), Promega (Madison, Wisconsin, USA), Roth (Karlsruhe, Germany), Sigma-Aldrich (Munich, Germany), Thermo Fisher Scientific (Waltham, USA) or VWR (Darmstadt, Germany).

2.1.8 Antibiotics

Antibiotic stock-solutions were prepared, filter-sterilized (pore size of 0.2 µm) and stored at -20°C. Table 6 shows Antibiotics used in this study.

Table 6: Antibiotics used in this work.

Antibiotic	Stock concentration	Final concentration	Solvent
Carbenicillin (Carb)	50 mg/ml	50 µg/ml	ddH_2O
Gentamycin (Gent)	50 mg/ml	50 µg/ml	ddH2O
Kanamycin (Kan)	50 mg/ml	50 µg/ml	ddH_2O
Rifampicin (Rif)	20 mg/ml	20 µg/ml	DMSO
Sulfadiazin (Sulf)	7.5 mg/ml	7.5 µg/ml	ddH_2O

2.1.9 Antibodies

Primary and secondary antibodies applied for immunoblot analysis are summarized in Table 7. Antibodies were aliquoted and long-time stored at -80°C. Used aliquots were stored at 4°C.

Table 7. Antibodies used in this study.

Primary antibody	Source	Dilution	Supplier
α-GFP	Rat, monoclonal	1:5000	ChromoTek (Martinsried, Germany)
α-PEN2	Rabbit, polyclonal	1:10000	Eurogentec (Seraing, Belgium)
α-RFP	Rat, monoclonal	1:5000	ChromoTek, (Martinsried, Germany)
α-t-RFP	Rabbit, polyclonal	1:5000	Evrogen (Moscow, Russia)
Secondary antibody	**Source**	**Dilution**	**Supplier**
α-rat lgG AP conjugate	Rabbit, polyclonal	1:5000	Sigma-Aldrich (Munich, Germany)
α-rabbit lgG AP conjugate	Goat, polyclonal	1:5000	Sigma-Aldrich (Munich, Germany)

2.1.10 Inhibitors

Table 8 shows all inhibitors used for pharmacological experiments. Inhibitors were prepared in indicated stock solutions and stored at -20°C.

Table 8. Inhibitors used in this work.

Inhibitor	Stock concentration	Working concentration	Solvent	Source
Concanamycin A (ConcA)	100 µM	1 µM	DMSO	abcam
MG132	50 mM	50 µM	DMSO	abcam
Wortmannin (Wm)	10 mM	30 µM	DMSO	abcam

2.1.11 Media

Media were prepared using ultrapure water and sterilized by autoclaving (121°C, 100 kPa, 20 min). Heat-sensitive compounds were filter-sterilized (pore size of 0.2 µm) and added to media at 60°C or below. Table 9 lists all media used in this study.

Table 9. Media used in this work.

Medium	Composition	
Bacterial growth medium		
Luria-Bertani broth (LB)	Peptone Yeast extract NaCl for LB agar plates 1.5 % (w/v) agar (bacterial grade) was added.	10 g/l 5 g/l 5 g/l
Double yeast tryptone (DYT) medium	Tryptone Yeast extract	16.0 g/ l 10.0 g/ l

	NaCl	10.0 g/ l
	for LB agar plates 1.5 % (w/v) agar (bacterial grade) was added.	
***Arabidopsis thaliana* in-vitro growth medium**		
½ Murashige and Skoog (MS)	MS medium including Gamborg B5 vitamins Sucrose Adjust pH to 5.7 with KOH For ½ MS agar plates 0.7 % (m/v) plant agar was added.	2.2 g/l 10 g/l

2.1.12 Buffers and solutions

Buffers and solutions listed in Table 10 were generated with ultrapure water. Additional used buffers and solutions are indicated in the corresponding method section.

Table 10. Buffers and solutions used in this study.

Buffer/Solution	Composition	
Agarose gel electrophoresis and PCR		
Agarose solution	Agarose TAE-Buffer	1 -2% (w/v) 1x
DNA loading dye (6x)	Sucrose 0.5 M EDTA, pH 8.0 Bromophenol blue ddH_2O	4 g 2ml 25 mg Add 10 ml
PCR reaction buffer for *Taq* (10x)	Tris base KCl $MgCl_2$ Triton X-100 Adjust pH to 9.0 with KOH	100 mM 500 mM 15 mM 1 %
TAE buffer (50x)	Tris base Glacial acetic acid 0.5 M EDTA, pH 8	2 M 57.1 ml/l 100 ml/l
***Agrobacterium tumefaciens* infiltration**		
Infiltration medium	$MgCl_2$ MES Acetosyringone Adjust pH to 5.4 with KOH	10 mM 10 mM 150 µM
Genomic DNA extraction from *Arabidopsis thaliana*		
Extraction buffer	Tris-HCl, pH 7.5 NaCl EDTA	0.2 M 1.25 M 0.025 M

	SDS	0.5 % (w/v)
Histochemical staining for microscopy		
Aniline Blue staining solution	Aniline Blue in 150 mM KH_2PO_4 buffer, pH 9.5	0.01 % (m/v)
Plasmid isolation		
Buffer P1	Tris-HCl, pH 8 EDTA, pH 8 RNase A	50 mM 10 mM 100 µg/ml
Buffer P2	NaOH SDS	200 mM 1 % (w/v)
Buffer P3	Potassium acetate Acetic acid	3 M 2 M
Preparation of chemically competent *E. coli* cells		
RF I solution	RbCl $MnCl_2$x $4H_2O$ Potassium acetate $CaCl_2$ x 2 H_2O Glycerol Adjust pH with acetic acid to 5.8	100 mM 50 mM 30 mM 10 mM 15 % (w/v) 5.8
RF II solution	MOPS RbCl $CaCl_2$ x 2 H_2O Glycerol Adjust pH to 6.8 with NaOH	10 mM 10 mM 75 mM 15 % (w/v) 6.8
Protein extraction from *Arabidopsis thaliana*		
CERK1 extraction buffer	Sucrose HEPES-KOH pH 7.5 Glycerol Na_2MoO_4 NaF EDTA DTT Triton X-100 Protease inhibitor cocktail (PIC)	250 mM 100 mM 5 % (v/v) 1 mM 25 mM 10 mM 1 mM 0.5 % (w/v) 1:100
Protease inhibitor cocktail (PIC, 100x, 200ml)	4-(2-aminoethyl) benzenesulfonyl fluoride hydrochloride (AEBSF) Bestatin hydrochloride Pepstatin A Leupeptin hemisulfate E-64 (trans-epoxysuccinyl-L-leucylamido-(4-guanidino)butane) Phenantroline (1, 10-phenantroline monohy-	1 g 5 mg 10 mg 100 mg 10 mg 10 g

	drate) All compounds were dissolved separately in a small amount of DMSO, combined and filled up to 200 ml with DMSO. 2 ml aliquots were prepared and stored at -20°C.	
Proteomics		
Elution buffer I	Tris-HCl, pH 7.5 Urea Sequencing Grade Modified Trypsin DTT Buffer has to be freshly prepared due to instability of urea solution	50 mM 2 M 5 µg/ ml 1 mM
Elution buffer II	Tris-HCl, pH 7.5 Urea Iodoacetamide (IAM) Buffer has to be freshly prepared due to instability of urea solution	50 mM 2 M 5 mM
Wash/Dilution buffer	Tris-HCl, pH 7.5 NaCl EDTA	10 mM 150 mM 0.5 mM
SDS-PAGE and immunoblot analysis		
4x SDS loading buffer	Tris-HCl, pH 6.8 DTT SDS Glycerol Bromophenol blue Store at -20°C	200 mM 400 mM 8 % (w/v) 40 % (v/v) 0.1 % (w/v)
10 x SDS running buffer	Glycine Tris SDS	2 M 250 mM 1 % (w/v)
20 x Transfer buffer	Tris Boric acid pH	1 M 1 M 8.3
20 x Tris Buffered Saline - Tween (TBS-T)	NaCl Tris-HCl pH 8.0 Tween-20	3 M 200 mM 1%
Alkaline Phosphatase (AP) buffer	Tris-HCl, pH 9.5 NaCl $MgCl_2$	100 mM 100 mM 50 mM
Coomassie staining solution	Ethanol Acetic acid ddH_2O Coomassie Brilliant Blue R-250	300 ml 100 ml 300 ml 0.05 % (w/v)

Destaining solution for PVDF membranes	Ethanol Acetic acid ddH_2O	300 ml 100 ml 300 ml
TBS-T + milk powder	20 x TBS-T Skimmed Milk Powder ddH_2O	50 ml 40 g/l 1 l

2.2 Methods

2.2.1 Plant methods

2.2.1.1 *Arabidopsis thaliana*

2.2.1.1.1 Surface sterilization of *Arabidopsis* seeds

To eliminate potential contaminations of pests, *Arabidopsis* seeds were frozen in plastic bags for 2 days at -20°C. To remove microbial contaminations, two different sterilization techniques using either chlorine gas (2.2.1.1.1.1) or ethanol (2.2.1.1.1.2) were applied.

2.2.1.1.1.1 Seed surface sterilization with chlorine gas

For *Arabidopsis* seed surface sterilization using chlorine gas, a glass beaker was placed in a desiccator and 15 ml of sodium hypochlorite (NaClO) was added. Seed packages were placed on a platform of the desiccator and 5 ml of 37 % Hydrochloric acid (HCl) were pipetted into the NaClO. Immediately, the desiccator was closed. Seeds were sterilized for at least 4 hours or overnight. The procedure was performed under a fume hood.

2.2.1.1.1.2 Seed surface sterilization with ethanol

For *Arabidopsis* seed surface sterilization using ethanol, seeds were transferred into a 2 ml reaction tube, washed three times with 70 % EtOH and 0.05 % Tween-20 for 2 min and once with 100 % EtOH for 1 min. For *Arabidopsis* cultivation on soil, seeds were poured on filter paper and dry seeds were directly transferred to soil. For *Arabidopsis* cultivation for *in-vitro* cultures on ½ MS plates, seeds were poured on sterile filter paper under a laminar flow hood. Dry seeds were carefully distributed on ½ MS plates.

2.2.1.1.2 Maintenance and cultivation of *Arabidopsis* plants on soil

Sterilized seeds were directly sown on moist soil (Frühstorfer Erde, Type T, Archut), which was steamed twice for 30 min at 90°C, to eliminate soil-borne pathogens and pests. Pots were placed on a tray and covered with a transparent lid to increase humidity and promote seed germination. Plant

trays were transferred to an environmentally controlled growth chamber (Johnson Controls, Milwaukee, WI, USA) with short-day conditions (8 h light at 22° C, 16 h darkness at 20° C, 140 mol m^{-2} s^{-1} light intensity and 65 % relative humidity). After seed germination, transparent lids were removed and plants were pricked out after 7 days. 6-8 week-old plants were transferred to an environmentally controlled growth chamber with long-day conditions (16 h light at 22° C, 8 h darkness at 20° C, 140 mol m^{-2} s^{-1} light intensity and 65 % relative humidity) to promote flower development and seed production. For seed collection, aerial parts of the plants were covered with paper bags prior to the maturation of siliques. As required, plants were bottom watered every 2-3 days using tap water.

2.2.1.1.3 Crossing *Arabidopsis*

To generate crosses of different transgenic *Arabidopsis* lines, magnifying glasses and fine tweezers were used. In total, 4-5 inflorescences of the maternal line were selected and opened flower buds, leaves and developed siliques were cut off the stem. Next, the carpel of a closed flower bud was carefully isolated by removal of sepals, petals and stamina. Anthers of a paternal flower were used for pollinating the exposed stigma of the maternal flower. The stem containing the pollinated stigma was labeled. Following silique development, the siliques were covered with a small paper bag for the collection of mature siliques.

2.2.1.1.4 *Agrobacterium*-mediated stable transformation of *Arabidopsis*

The floral dip method according to Clough and Bent 1998 was used for the generation of stable transgenic *Arabidopsis* plants. To induce flower development 2-4-week-old *Arabidopsis* plants were transferred from short day to long-day conditions. 5 ml of LB liquid medium supplemented with the appropriate antibiotics were inoculated with a single colony of *A. tumefaciens* cells carrying the plasmid of interest, incubated for 2 days at 28°C and shaking with 200 rpm in the Certomat® BS-1 incubator (Sartorius-Stedim Biotech, Göttingen, Germany). 300 ml LB liquid medium supplemented with the appropriate antibiotics were inoculated with the pre-culture and incubated at 28 °C at 180 rpm overnight. The culture was grown to a cell density of OD_{600} of 0.6 -1.2. Cells were harvested by centrifugation for 20 min at 4000 rpm at RT (Heraeus Multifuge 3 SR+, Thermo Fisher Scientific, Waltham, USA) and resuspended in 300 ml 5 % sucrose solution + 0.05 % Silwet L-77. Inflorescences of *Arabidopsis* plants were dipped in the *A. tumefaciens*-solution for 30-60 s. Dipped plants were covered with a black plastic bag to enhance humidity and create low light conditions for 16-24 h. The cover was removed and plants were grown under long-day conditions to promote seed production.

2.2.1.1.5 Selection of stably transformed *Arabidopsis* plants

2.2.1.1.5.1 BASTA selection of transgenic *Arabidopsis* plants on soil

T1 seeds were densely sown on square pots, covered with a transparent lid and transferred to short-day conditions for seed germination. Following seed germination, seedlings were sprayed with 0.05 % Basta® herbicide solution (200 g/ l glufosinate, Bayer CropScience, Monheim am Rhein, Germany). The treatment was repeated 2-3 times in an interval of 2 days. Successfully transformed *Arabidopsis* seedlings carrying the phosphinothricin acetyltransferase (PAT) gene survived the BASTA® herbicide treatment and were transplanted into single pots.

2.2.1.1.5.2 *In vitro* selection of transgenic A*rabidopsis* plants

Seeds were surface sterilized as described in 2.2.1.1.1. and transferred on ½ MS agar plates supplemented with either sulfadiazine (final concentration of 7.5 µg/mL) or phosphinothricin (PPT; final concentration of 10 µg/mL). Plants were cultivated in an environmentally controlled growth chamber (Johnson Controls, Milwaukee, WI, USA) with short-day conditions (8 h light at 22° C, 16 h darkness at 20° C, 140 mol m^{-2} s^{-1} light intensity and 65 % relative humidity). 10-14 days after germination, resistant seedlings were transplanted to soil.

2.2.1.1.6 MAMP- and pharmacological inhibitor treatment of *Arabidopsis* leaves

To analyze MAMP induced accumulation of PEN2-GFP-TA_{PEN2} aggregate formation and CYP81F2-RFP accumulation, detached leaves of 4-7 week-old plants were placed into a beaker and were vacuum-infiltrated with either 100 µg/ml chitin or 50 nM flagellin (EZBiolab) using a desiccator. The infiltration solution was carefully removed and leave samples were covered with parafilm containing small holes. Different incubation times are indicated in respective figures and legends. For proteomics experiments, chitin infiltrated leaf material was carefully dried, frozen in liquid nitrogen and stored at -80°C.

For Confocal laser scanning microscopy analysis following pharmacological treatment, *Arabidopsis* leaf pieces of 4-5-week-old plants were vacuum-infiltrated with inhibitor solutions with or without 100 µg/ml chitin using a syringe.

2.2.1.1.7 Infection of *Arabidopsis* plants

2.2.1.1.7.1 Inoculation and maintenance of *Blumeria graminis f.sp. hordei*

Bgh used for inoculation experiments was cultivated on barley plants (*Hordeum vulgare* cv. Golden Promise) in an environmentally controlled Percival AR-66L3 chamber (CLF Plant Climatics, Wertingen, Germany) with short-day conditions (8 h light at 22° C, 16 h darkness at 20° C, 140 mol m^{-2} s^{-1} light

intensity and 65 % relative humidity). 9-day old barley plants were infected with *Bgh* conidiospores generated on older infected barley. For conidiospore production, *Bgh* was grown on barley plants 10 to 14 days prior to infection experiments. 4-5 week-old *Arabidopsis* plants were randomized on trays and infected using a settling tower (Lipka et al., 2005). Plants were analyzed 20 hpi by CLSM and fungal invasion and cell death rate (2.2.1.1.7.4) were analyzed 72 hpi.

2.2.1.1.7.2 Inoculation and maintenance of *Erysiphe pisi*

E. pisi used for inoculation experiments was cultivated on pea plants (*Pisum sativum*, kleine Rheinländerin) in an environmentally controlled Percival AR-66L3 chamber (CLF Plant Climatics, Wertingen, Germany) with short-day conditions (8 h light at 22° C, 16 h darkness at 20° C, 140 mol m^{-2} s^{-1} light intensity and 65 % relative humidity). 16-day-old pea plants were infected with *E. pisi* conidiospores generated on older infected pea plants. For spore production, *E. pisi* was grown on pea plants 14 days prior to infection experiments. 4-5 week-old *Arabidopsis* plants were randomized on trays and infected using a settling tower (Lipka et al., 2005). Plants were analyzed 20 hpi by CLSM and fungal invasion and cell death rate (2.2.1.1.7.4) were analyzed 72 hpi.

2.2.1.1.7.3 Inoculation and maintenance of *Golovinomyces orontii*

G. orontii, used for inoculation experiments, was cultivated on *Arabidopsis* Col-0 plants in an environmentally controlled Percival AR-66L3 chamber (CLF Plant Climatics, Wertingen, Germany) with short-day conditions (8 h light at 22° C, 16 h darkness at 20° C, 140 mol m^{-2} s^{-1} light intensity and 65 % relative humidity). 5-week old *Arabidopsis* plants were infected with *G. orontii* conidiospores generated on older infected *Arabidopsis* plants. For conidiospore production, *G. orontii* was grown on *Arabidopsis* plants 10 to 14 days prior to infection experiments. 4-5 week-old *Arabidopsis* plants were randomized on trays and brush inoculated. Fungal invasion and cell death rate (2.2.1.1.7.4) were analyzed 72 hpi.

2.2.1.1.7.4 Analysis of fungal penetration and cell death rate

For penetration resistance assays, *Bgh, E. pisi* and *G. orontii* were used. *Arabidopsis* leaves were inoculated with the respective powdery mildew. Infected leaves were harvested in 80 % Ethanol 72 hpi and cleared for 10-14 days. To stain callose, 80 % Ethanol was removed and samples were incubated in 150 mM KH_2PO_4 containing 0.01% Anilin blue overnight in the dark. For staining of fungal structures, samples were transferred into Coomassie Brilliant Blue solution, washed with ultrapure water and mounted on a microscope slide using 50 % Glycerol. Samples were analyzed using the Leica

DM5000 B microscope with UV excitation. The formation of papillae, callose encased haustoria, single-cell death and secondary hyphae were counted.

2.2.1.2 Methods for working with *Nicotiana benthamiana*

2.2.1.2.1 Cultivation and maintenance of *Nicotiana benthamiana*

Chlorine gas was used for *N. benthamiana* seed surface sterilization. Sterilized seeds were transferred on soil and plants were grown in an environmentally controlled growth chamber with long-day conditions (16 h light at 25° C, 8 h darkness at 22° C, 140 mol m^{-2} s^{-1} light intensity and 65 % relative humidity). Approximately 5-week-old plants were used for transient expression experiments.

2.2.1.2.2 *Agrobacterium*-mediated transient transformation of *Nicotiana benthamiana* leaves

For the transient transformation of *N. benthamiana* leaves, 5 ml of DYT liquid medium with appropriate antibiotics were inoculated with a single colony of *A. tumefaciens* GV3101 pMP90RK cells containing the construct of interest (2.2.2.6). Bacterial cells were incubated at 28°C and 200 rpm shaking in the Certomat® BS-1 incubator (Sartorius-Stedim Biotech, Göttingen, Germany) for 2 days. 5 ml DYT liquid medium with appropriate antibiotics were inoculated with 50 µl pre-culture. The main culture was grown overnight to a cell density of OD_{600} of 0.8 -1.2. at 28°C and 200 rpm. The cell culture was pelleted by centrifugation (Heraeus Multifuge 3 SR+, Thermo Fisher Scientific, Waltham, USA) at 4000 rpm for 20 min at RT. The supernatant was discarded and the pellet was resuspended in infiltration medium with 150 µM acetosyringone at an OD_{600} of 0.4. Cultures were incubated at least for 2 hours at RT. Leaves of 5-week-old *N. benthamiana* plants were infiltrated using a 1 ml needle-less syringe. Infiltrated areas were labeled and plants were directly transferred to a growth chamber with long-day conditions. Plants were analyzed 2-3 days after infiltration by CLSM.

2.2.2 Methods for working with bacteria

2.2.2.1 Cultivation of *E. coli*

LB agar plates or LB liquid medium supplemented with respective antibiotics as selective markers were used for *E. coli* cell cultivation. Table 6 lists all antibiotics utilized in this work. *E. coli* cells grown on LB agar plates were incubated at 37°C in an IPP 500 incubator (Memmert, Schwabach, Germany). LB liquid medium was inoculated with a single colony of *E. coli* cells grown on an LB agar plate. Liquid cultures were incubated at 37°C and 220 rpm shaking in an Innova 4230 incubator (New Brunswick Scientific, Edison, New Jersey, USA).

2.2.2.2 Cultivation of *A. tumefaciens*

A. tumefaciens GV3101 (pMP90RK) cells (2.1.3.2) were grown on DYT agar plates or DYT liquid medium containing appropriate antibiotics (Table 6) as selective markers. *A. tumefaciens* cells grown on DYT agar plates were incubated at 28°C in an IPP 500 incubator (Memmert, Schwabach, Germany) for 2-3 days. Liquid cultures were incubated at 28°C and 220 rpm shaking in an Innova 4230 incubator (New Brunswick Scientific, Edison, New Jersey, USA) for 2-3 days.

2.2.2.3 Preparation of chemically competent *E. coli* cells

For competent *E. coli* TOP10 cell preparation, 100 ml LB liquid medium supplemented with 10 mM MgCl2 and 10 mM MgSO4 were inoculated with 1 ml of overnight culture and cultured to a cell density OD_{600} of 0.4-0.6 at 37°C and 260 rpm shaking. The cell culture was incubated for 20 min on ice, divided into pre-cooled 50 ml falcons and harvested by centrifugation (swing-out centrifuge; Heraeus multifuge 3SR+, Thermo Fisher Scientific, Waltham, USA) at 3000 rpm for 15 min at 4°C. All following steps were performed on ice. The cell pellet was resuspended in 8.3 ml ice-cold RFI-solution. The cells were pooled and incubated for at least 40 min on ice, followed by centrifugation at 4°C for 15 min at 3000 rpm. The cells were resuspended in 3 ml pre-chilled RFII-solution and incubated for at least 15 min on ice. Subsequently, 50 µl aliquots of competent *E. coli* cell suspension in pre-cooled 1.5 ml Eppendorf tubes were frozen in liquid nitrogen and stored at -80°C.

2.2.2.4 Preparation of electro-competent *A. tumefaciens* cells

For the preparation of *A. tumefaciens* electro-competent cells, 4 ml of DYT medium containing appropriate antibiotics were inoculated with a single *A. tumefaciens* colony from a DYT agar plate. The cell culture was incubated for 2 days at 28°C and 200 rpm shaking. 500 µl of the pre-culture was added to 250 ml of DYT liquid medium supplemented with appropriate antibiotics. The main-culture was cultivated to a cell density OD_{600} of 0.6 - 1.2 at 28°C and 200 rpm, incubated on ice for 30 min, divided into pre-cooled 50 ml falcons and cells were harvested by centrifugation (swing-out centrifuge; Heraeus multifuge 3SR+, Thermo Fisher Scientific, Waltham, USA) at 4000 rpm for 10 min at 4°C. The pellet was resuspended in 50 ml of pre-cooled sterile ultrapure water. Centrifugation and resuspension steps were repeated twice with 25 ml and 10 ml pre-cooled sterile ultrapure water. The cell pellet was resuspended in 10 ml cold sterile ultrapure water containing 10 % glycerol. Cells were centrifuged at 4000 rpm for 10 min at 4°C. The last step was repeated and cells were resuspended in 2.5 ml cold 10 % glycerol. Subsequently, 50 µl aliquots of electro-competent cell suspension in pre-cooled 1.5 ml Eppendorf tubes were shock frosted in liquid nitrogen and stored at -80°C.

2.2.2.5 Transformation of chemically competent *E. coli* cells

For the transformation of chemo-competent *E. coli* TOP10 cells, 50 µl aliquots were thawed on ice. Subsequently, 3 µl of a NEBuilder® HiFi DNA Assembly reaction or 0.5-1 µL of a plasmid for a retransformation were added, gently mixed and incubated on ice for 20 min. After the incubation, the mixture was heat-shocked at 42°C for 45 s. Afterward, 600 µl LB liquid medium were added and cells were incubated for 20 min at 37°C. The transformation mixture was centrifuged in a tabletop centrifuge (Heraeus Pico21, Thermo Fisher Scientific, Waltham, USA) at 600 rpm for 1 min. Half of the supernatant was discarded. The cell pellet was resuspended in the remaining medium, plated on LB agar plates containing appropriate antibiotics and incubated overnight at 37°C.

2.2.2.6 Transformation of electro-competent *A. tumefaciens* cells

For the transformation of *A. tumefaciens* cells, 50 µl aliquots were thawed on ice, 0.5 µl plasmid DNA was added, gently mixed and the mixture was pipetted into a pre-chilled sterile electroporation cuvette with 0.1 cm electrode distance. A Micro Pulser™ (BioRad, München, Germany) apparatus (setting: 25 µF, 2.5 kV and 400 Ω) was used for *A. tumefaciens* electroporation. The transformation mixture was pulsed once and was immediately placed back on ice. 600 µl liquid DYT medium was added and the cell solution was transferred into a sterile 1.5 ml microcentrifuge tube. The sample was incubated for 2-3 h at 28°C and 200 rpm shaking. 100 µl of the transformation mixture was plated on a DYT solid agar plate containing appropriate antibiotics and the plate was incubated for 2-3 days at 28°C.

2.2.2.7 Storage of bacterial cultures

Bacterial cells grown on solid medium were short-term stored for 3-4 weeks at 4°C. For long-term storage, glycerol stocks of the respective bacteria were generated by mixing 1 ml overnight culture with 1 ml 65 % sterile glycerol. Subsequently, bacterial cells were frozen in liquid nitrogen and stored at -80°C.

2.2.3 Molecular biology methods

2.2.3.1 Isolation of genomic DNA (gDNA) from *Arabidopsis thaliana*

2.2.3.1.1 Isolation of gDNA for PCR amplification

A small *Arabidopsis* leaf was harvested and transferred in a 2 ml microcentrifuge tube containing 3 stainless metal balls. Samples were frozen in liquid nitrogen. Plant material was homogenized utilizing the TissueLyser LT (Qiagen, Hilden, Germany) two times for 1 min. 300 µl DNA extraction buffer was added and samples were incubated for 5 min on a IKA® VIBRAX VXR basic at 1000 rpm. Subse-

quently, samples were centrifuged for 5 min at RT at 14.000 rpm in a table top centrifuge (Heraeus Pico21, Thermo Fisher Scientific, Waltham, USA). The supernatant was transferred to a new tube and 300 µl of isopropanol, pre-cooled to -20°C, was added. After incubation for 5 min at RT, samples were centrifuged for 5 min at RT at 14.000 rpm. The supernatant was discarded and the pellet was centrifuged for an additional minute. The remaining isopropanol was carefully removed with a pipette and the pellet was dried for 30 min at 55°C in a Thermomixer (Eppendorf, Hamburg, Germany). The genomic DNA pellet was dissolved in 50 µl ddH_2O and incubated in a Thermomixer at 55° shaking with 800 rpm for 10 min. Isolated genomic DNA was stored at -20°C.

2.2.3.1.2 Isolation of gDNA for inverse PCR

For isolation of high-quality gDNA for inverse PCR, the DNeasy® Plant Mini Kit (Qiagen, Hilden, Germany) was used according to the manufacturer´s instructions.

2.2.3.2 Isolation of plasmid DNA from *E. coli*

Isolation of plasmid DNA from *E. coli* was performed as described in Birnboim and Doly, 1979. 2 ml of *E. coli* overnight culture were transferred to a 2 ml microcentrifuge tube and pelleted by centrifugation for 1 min at 13.000 rpm at RT in a tabletop centrifuge (Heraeus Pico21, Thermo Fisher Scientific, Waltham, USA). After discarding the supernatant, the pellet was resuspended in 200 µl P1 buffer. 200 µl P2 buffer was added, mixed gently by inverting the tube and the samples were incubated for approximately 3-5 min at RT. To stop the cell lysis reaction, 200 µl P3 buffer was added and gently mixed by inverting the tube 6-10 times. Samples were centrifuged for 10 min at 13.000 rpm at RT. The supernatant was transferred into a 1.5 ml microcentrifuge tube containing 96 % ethanol p.a and centrifuged for 5 min at 13.000 rpm at RT. The supernatant was discarded, the gDNA pellet was washed with 70 % ethanol p.a and centrifuged for 1 min at 13000 rpm. The supernatant was discarded and the pellet was centrifuged for an additional minute at 13.000 rpm. The remaining ethanol was carefully removed with a pipette and the pellet was air-dried at RT. The plasmid DNA pellet was dissolved in 50 µl ddH_2O and incubated in a Thermomixer at RT° shaking with 800 rpm for 10 min. Isolated plasmid DNA was stored at -20°C.

2.2.3.3 Isolation of plasmid DNA from *A. tumefaciens*

Isolation of plasmid DNA from *A. tumefaciens* was performed as described in 2.2.3.2 with slight changes. 200 µl of an *A. tumefaciens* culture were centrifuged at 13000 rpm for 1 min (Heraeus Pico21, Thermo Fisher Scientific, Waltham, USA). The supernatant was discarded and the pellet was used for the isolation of plasmid DNA.

2.2.3.4 Polymerase chain reaction (PCR)

Different polymerases were applied depending on the purpose. For cloning processes, the iProof™ High Fidelity PCR kit (BioRad, Munich, Germany) was used according to the manufacturer's instructions and for standard analytical tests, such as genotyping a homemade *Taq* Polymerase was used. Additionally, for identification of a T-DNA insertion position in the genome of *Arabidopsis* an inverse PCR approach was applied using Phusion High-Fidelity DNA Polymerase (Thermo Fisher Scientific, Waltham, MA, USA). The PCR reaction and the program for the iProof™ High Fidelity DNA polymerase (Table 11 and 12), the standard PCR reaction and program for the *Taq* polymerase (Table 13 and 14) and the PCR reaction and program of the Phusion High-Fidelity DNA Polymerase (Table 15 and 16) for the inverse PCR are described below. Based on the expected fragment size and the synthesis rate of the respective polymerase the elongation time was set. Calculation of annealing temperatures of the primers was done by the Clone Manager Professional Suite v 8 (Sci-Ed Software, Denver, US) *in silico.* PCR programs were run on MyCycler™ and T100™ Thermocycler (Bio-Rad, Munich, Germany) machines.

Table 11. PCR reaction using iProof™ High Fidelity DNA polymerase.

Component	Concentration
HF buffer (10 x)	2.5 µl
Forward primer (10 µM)	2.5 µl
Reverse primer (10 µM)	2.5 µl
dNTPs (10 mM)	0.4 µl
iproof Polymerase	0.5 µl
Template DNA	1.0 µl
ddH_2O	33.1 µl

Table 12. PCR program for iProof™ High Fidelity DNA polymerase.

Step	Temperature	Time	
Initial denaturation	98°C	5 min	
Denaturation	98°C	10 s	35 x
Annealing	55-62°C	30 s	
Elongation	72 °C	30 s/kb	
Final elongation	72°C	10 min	
	4°C	10 min	
		∞	

Table 13. Standard PCR reaction using homemade *Taq* Polymerase.

Component	Concentration
Reaction buffer (10 x)	2.5 µl
Forward primer (10 µM)	0.5 µl
Reverse primer (10 µM)	0.5 µl
dNTPs (10 mM)	0.5 µl
$MgCl_2$	0.2 µl
Taq Polymerase	1.0 µl
Template DNA	0.5 µl
ddH_2O	19.3 µl

Table 14. Standard PCR program for homemade *Taq* Polymerase.

Step	Temperature	Time	
Initial denaturation	94°C	min	
Denaturation	94°C	30 s	35 x
Annealing	55-62°C	30 s	
Elongation	72 °C	1 min/kb	
Final elongation	72°C	10 min	
	4°C	∞	

Table 15. Inverse PCR reaction using Phusion High-Fidelity DNA Polymerase.

Component	Concentration
Phusion HF buffer (5 x)	10 µl
Forward primer (10 µM)	2.5 µl
Reverse primer (10 µM)	2.5 µl
dNTPs (10 mM)	0.4 µl
Phusion Polymerase	0.5 µl
Ligated genomic DNA	2.0 µl
ddH_2O	32.1 µl

Table 16. Inverse PCR program for Phusion High-Fidelity DNA Polymerase.

Step	Temperature	Time	
Initial denaturation	98°C	40 s	
Denaturation	98°C	15 s	35 x
Annealing	58°C	30 s	
Elongation	72 °C	3 min	
Final elongation	72°C	10 min	
	4°C	∞	

2.2.3.5 Agarose gel electrophoresis

Agarose gel electrophoresis was performed for visualization, separation and determination of the size of nucleic acids. Agarose gel concentrations varied from 1 - 2 % depending on the analyzed fragment size. Agarose was dissolved in 1 x TAE by boiling in a microwave. 5 µl HDgreenTM (Intas, Göttingen, Germany) was added to 100 ml gel after cooling down to 60°. Subsequently, the gel was poured into a casting tray. After polymerization, the gel was placed in a Sub-Cell GT tank (BioRad, Munich, Germany) and covered with 1 x TAE buffer. Samples containing 6 x DNA loading dye and a GeneRuler™ 1 kb, 100 bp plus or 50 bp DNA ladder (Thermo Fisher Scientific, Waltham, USA) were loaded into the wells of the gel. An electrical field with a constant voltage of 90 -120 V, depending on the size of the fragment and percentage of the gel, was applied to the gel chamber. Visualization of DNA was done on a Genoplex Transilluminator (UV at 312 nm) gel documentation and analysis system (VWR, Radnor, Pennsylvania, USA).

2.2.3.6 Purification of DNA fragments

The NucleoSpin® Gel and PCR Clean-up kit (Macherey-Nagel, Düren, Germany) was applied for direct or agarose gel purification of DNA fragments and PCR products and was used according to the manufacturer's specifications.

2.2.3.7 Photometric measurement of DNA and RNA concentration

The concentration and the purity of DNA and RNA were determined photometrically using NanoDrop™ One Microvolume UV-Vis Spectrophotometer (Thermo Fisher Scientific, Waltham, USA). The purity of nucleic acids was determined by the ratio of absorbance at 260 nm and 280 nm. The optimal A260/A280 ratio for purified DNA and RNA is around 1.8 and 2.0, respectively.

2.2.3.8 Restriction endonuclease digestion of DNA

The restriction digestion of DNA was done via standard or FastDigest® enzymes from Thermo Fisher Scientific (Waltham, USA). Enzymes were applied according to the manufacturer's instructions.

Restriction reactions:

Plasmid DNA or cleaned-up PCR product	1 µg
10x reaction buffer	2 µl
Restriction enzyme	2-5 U
add 20 µl vol. with ddH_2O	

The reaction was incubated at enzyme-specific temperatures for 45 min (FastDigest®) or 4-16 h (standard enzymes). Restriction digestion was applied for the analysis of plasmids, cloning, genotyping and gDNA digestion for inverse PCR.

2.2.3.9 Ligation of gDNA fragments for inverse PCR

For self-ligation of gDNA fragments for inverse PCR, the T4 DNA ligase (Thermo Fisher Scientific, Waltham, USA) was applied. 100 ng of digested and purified gDNA was used. A ligation mixture of 20 µl contained 1 U of T4 DNA ligase and was incubated overnight at 16°C.

2.2.3.10 NEBuilder DNA assembly

Cloning of plasmids was performed using the NEBuilder (New England Biolabs, Ipswich, MA, USA) DNA assembly method. Primers containing appropriate 20 bp overhangs overlapping with the sequence in the desired plasmid were used for PCR amplification of the insert. The backbone construct was digested by restriction endonucleases. For assembly of insert and backbone, the NEBuilder HiFi DNA Assembly Master Mix (New England Biolabs, Ipswich, MA, USA) was applied according to the manufacturer's instructions. The mixture was incubated for 1 h at 50°C using a Thermocycler. The generated product was directly transformed into chemo-competent *E. coli* cells.

2.2.3.11 Q5 site-directed mutagenesis

The Q5® Site-Directed Mutagenesis Kit (New England Biolabs, Ipswich, Massachusetts, USA) was used for site-directed mutagenesis. The Kit was applied according to the manufacturer´s specification.

2.2.3.12 Sequencing of plasmids and PCR products

Sequencing reactions were performed by Microsynth Seqlab (Göttingen, Germany). Sequencing results were evaluated using Geneious™ software version 8.1.8 (Biomatters Ltd.; Kearse *et al.,* 2012) or Clone Manager Professional Suite v 8 (Sci-Ed Software, Denver, US).

2.2.3.13 Isolation of *Arabidopsis* RNA from leaves

For RNA extraction, 10 Arabidopsis rosettes were pooled and ground with mortar and pestle in liquid nitrogen. 80-90 mg of fine powder were transferred into a 2 ml safe-seal Eppendorf tube and one 5 mm and two 3 mm metal balls were added. The powder was homogenized utilizing a pre-cooled TissueLyser LT (Qiagen, Hilden, Germany) three times for 1 min. RNA isolation from homogenized plant material was performed with the innuPREP Plant RNA Kit (Analytik Jena, Jena, Germany) according to the manufacturer´s instructions. 55 µl RNase free water was used for RNA elution. RNA concentration was determined with the NanoDropTM One Microvolume UV-Vis Spectrophotometer (Thermo Fisher Scientific, Waltham, USA) and adjusted to an equal amount. To investigate the quantity and quality RNA was analyzed on a 2% agarose gel.

2.2.3.14 Synthesis of complementary DNA (cDNA)

For cDNA synthesis, 1 µg isolated total RNA (2.2.3.13) was mixed with 1 µl 100 µM oligo(dT) primers. The mixture was incubated at 65°C for 5 min and transferred to ice. The RevertAid H Minus First Strand cDNA Synthesis kit (Thermo Fisher Scientific, Waltham, USA) for reverse transcription was used according to the manufacturer's instructions. A 1:5 – 1:15 dilution of the obtained cDNA was used for semi-quantitative PCR.

2.2.3.15 Semi-quantitative reverse transcription PCR (Semi-qRT-PCR)

Generated and diluted cDNA as described in 2.2.3.14 was used for Semi-qRT-PCR with homemade *Taq* polymerase. The semi-qRT-PCR reaction and program (Table 17 and 18) are described below. Based on the expected fragment size and the synthesis rate of the respective polymerase the elongation time was set. Calculation of annealing temperatures of the primers was done by the Clone Manager Professional Suite v 8 (Sci-Ed Software, Denver, US) *in silico.* PCR programs were run on MyCycler™ and T100™ Thermocycler (Bio-Rad, Munich, Germany) machines.

Table 17. semi-qRT-PCR reaction using homemade *Taq* polymerase.

Component	Concentration
cDNA 1:15	3 µl
10x *Taq* buffer	2.5 µl
primer 1 (10 µM)	0.5 µl
primer 2 (10 µM)	0.5 µl
dNTPs (10 mM)	0.5 µl
Taq Polymerase	1 µl
ddH_2O	17 µl

Table 18. Semi-qRT-PCR program.

Step	Temperature	Time	
Initial denaturation	94°C	5 s	
Denaturation	94°C	30 s	24-28 x
Annealing	55-62°C	30 s	
Elongation	72 °C	1 min/kb	
Final elongation	72°C	10 min	
	4°C	∞	

2.2.4 Biochemical methods

2.2.4.1 Protein extraction and purification from *Arabidopsis*

2.2.4.1.1 Small-scale total protein extraction

Protein extracts were prepared from 80-90 mg frozen leaf material or frozen plant powder. Samples were transferred into 1.5 ml microcentrifuge tubes and frozen in liquid nitrogen. 200 µl CERK1 extraction buffer supplemented with Protease Inhibitor Cocktail (PIC, 1:100) and one small spoon of quartz sand was added. The leave material was ground using the IKA® RW20 digital drill (IKA-Werke, Staufen, Germany) with a glass pistil at 1000 rounds/min for 30-60 s. The pistil was washed with 200 µl of CERK1 extraction buffer containing PIC and the extraction buffer was collected in the microcentrifuge tube. 800 µl CERK1 extraction buffer containing PIC was added to obtain a volume of 1200 µl and samples were centrifuged for 6 min at 4°C and 13.000 rpm. Total protein extracts (supernatant) were transferred into new 1.5 ml microcentrifuge tubes and protein concentration was determined using the Bradford assay (2.2.4.2). The protein concentrations were equalized to 1 - 2 µg/ml. For storage of the samples at -20°C, 75 µl of the adjusted protein extract was mixed with 25 µl 4x SDS buffer.

2.2.4.1.2 Large-scale total protein extraction

For proteomics experiments, large-scale total protein extraction was performed. 10 g of either untreated or chitin vacuum-infiltrated leaf tissue were ground using a mortar and pestle. To obtain fine plant powder, 5 ml of pre-ground leaf material were ground using a mortar and pestle and half a spoon of quartz sand. The sample was set aside until it was about to thaw. Then, 10 ml of CERK1-extraction buffer supplemented with PIC was added and the sample was mixed using the pestle. The plant material was transferred into a 50 ml tube. The mortar and pestle were washed with 4 ml CERK1-extraction buffer containing PIC and the material was collected in the 50 ml tube. Washing was repeated using 1 ml of CERK1-extraction buffer containing PIC. Samples were centrifuged (Heraues multifuge 3SR+; thermos Fisher Scientific, Waltham, USA) for 5 min at 4°C and 4000 rpm. Total protein extracts (supernatant) were filtered using a CellTrics filter (50 µM, Sysmex, Kōbe, Japan), protein concentration was determined using the Bradford assay (2.2.4.2) and the protein concentration was equalized.

2.2.4.1.3 Small-scale microsomal extraction

Microsomal extractions were prepared from 80-90 mg frozen leaf material or frozen plant power. Samples were transferred in 1.5 ml microcentrifuge tubes and frozen in liquid nitrogen. Protein extracts were prepared with detergent-free CERK1 extraction buffer (without Triton X-100) containing PIC and extraction was performed as described in 2.2.4.1.1. Samples were centrifuged for 5 min at 4°C and 1000 rpm, protein concentration was determined using the Bradford reagent (2.2.4.2) and the protein concentration was equalized. Adjusted total protein extracts were transferred into ultracentrifugation tubes (Eppendorf, Hamburg, Germany) and centrifuged at 100000 xg in a Sorvall WX ultracentrifuge (Thermo Scientific™, Waltham, USA) for 30 min at 4 °C. The supernatant (soluble fraction) was transferred to a new tube. The microsomal pellet was washed with detergent-free CERK1 extraction buffer and centrifuged for 10 min at 4°C and 13000 rpm. The microsomal pellet was solubilized in CERK1 extraction buffer containing Triton X-100 and PIC using a plastic pistil. The sample was centrifuged for 10 min at 4°C and 13000 rpm. The supernatant (microsomal fraction) was transferred to a new tube and mixed with 4 x SDS loading dye.

2.2.4.2 Protein concentration measurement according to Bradford

The method for quantification of protein concentration according to Bradford (1976) was used. The Roti-Quant Bradford reagent (Carl Roth, Karlsruhe, Germany) was diluted 1:5 in ultrapure water. For the generation of a calibration curve, bovine serum albumin (BSA) was used as a standard. A series of 0, 3, 5, 7, 10 and 15 µg BSA was prepared in cuvettes. Next, 3 µl of each total protein extract was

transferred into a cuvette. Samples were prepared in duplicates. Subsequently, 1 ml of 1:5 diluted Bradford reagent was added to each of the cuvettes containing dilution BSA or the total protein extracts, incubated at RT for 10 min and then the absorbance at 595 nm was determined with a WPA Biowave II photometer (Biochrom AG, Berlin, Germany). A standard curve was generated by plotting the absorption of the BSA standard solutions against the measured protein concentration. The protein concentration was calculated and samples were equalized to 1-2 µg/µl with CERK1 extraction buffer.

2.2.4.3 GFP-pulldown from total protein extracts for proteomics experiments

For Proteomics experiments, GFP-Trap® agarose beads (ChromoTek, Martinsried, Germany) were washed with CERK1-extraction buffer supplemented with PIC and centrifuged for 2 min at 4°C and 2000 xg. Washing was repeated three times. 50 µl GFP-Trap® agarose beads were transferred to the total protein extracts containing 10-15 mg protein. Samples were incubated for 5 hours at 4°C and 20 rpm. Following incubation, samples were processed as described in 2.2.4.7.

2.2.4.4 SDS-polyacrylamide gel electrophoresis (SDS-PAGE)

Denaturing SDS-PAGE was performed for the separation of proteins according to their molecular weight. For the generation of a polyacrylamide gel system, a resolving gel was prepared (Table 19), poured between two glass plates with 1.5 mm spacing in a gel stand. The resolving gel was covered with isopropanol. After gel polymerization at RT, isopropanol was removed and the stacking gel (Table 19) was poured on top of the resolving gel. Immediately, a comb was inserted. The resolving gel concentration was depended on the purpose of the experiment and the expected protein size. For immunoblot analysis, 10 % acrylamide gels were used. The Mini-PROTEAN® 3 system (BioRad, Munich, Germany) was applied for SDS-PAGE. Gels were placed in the running apparatus and the tank was filled with 1x SDS-running buffer. Samples were boiled at 95°C for 5 min, centrifuged for 1 min at RT and 13000 rpm. 15-20 µl of the sample were loaded. For estimation of the molecular size, the PageRuler™ Prestained Plus Protein Ladder (Thermo Fisher Scientific, Waltham, USA) was used. 1.5 mm gels were run at 30 mA per gel for approximately 1,5 h using a PowerPac™ HC power supply (BioRad, Munich, Germany). The protein separation process was stopped when the bromophenol blue front reached the end of the gel. The gel apparatus was disassembled and the gel was used for immunoblot analysis.

Table 19. Composition of SDS-PAGE gel buffers and mixtures used in this work.

SDS PAGE Gel Buffers (250 ml)		
10 % resolving gel buffer	1 M Tris-HCl (pH = 8.8)	143.6 ml
	10 % SDS	3.79 ml
	ddH_2O	102.53 ml
Stacking gel buffer	1 M Tris-HCl (pH = 6.8)	38.85 ml
	10 % SDS	3.06 ml
	ddH_2O	208.24 ml
SDS-PAGE gel mixes (10 ml)		
10 % resolving gel	10 % resolving gel buffer	6.6 ml
	30 % acrylamide	3.3 ml
	APS (10 %)	0.1 ml
	TEMED	0.004 ml
Stacking gel	Stacking gel buffer	8.16 ml
	30 % acrylamide	1.66 ml
	APS (10 %)	0.05 ml
	TEMED	0.005 ml

2.2.4.5 Immunoblot analysis (Western blot)

Extracted total proteins (2.2.4.1) were separated by SDS-PAGE (2.2.4.4) prior to immunoblot analysis. A polyvinylidene difluoride (PVDF) membrane with a pore size of 0.45 µm (Carl Roth, Karlsruhe, Germany) was transferred into methanol for activation. Electroblotting in the TRANS-BLOT® CELL (Bio-Rad, Munich, Germany) apparatus was used for the transfer of proteins to the activated PVDF membrane. The wet/tank blotting system was assembled as followed:

cathode

---

black grid of clamp

sponge

Whatman paper

gel (facing the cathode)

Methanol activated PVDF membrane

Whatman paper

sponge

transparent grid of clamp

---

anode

Pre-cooled 1x transfer buffer was filled in the tank of the blotting system and blotting was performed at 100 V for 90 min at 4°C. Following disassembly of the blotting apparatus, the PVDF membrane was transferred in 10 ml 1x TBS-T containing 4 % milk powder and incubated for at least 1 h on a rotary shaker at RT. After blocking, the solution was replaced by 1x TBS-T containing 4 % milk powder and the primary antibody (Table 7). The membrane was incubated at 4°C overnight shaking. The primary antibody-solution was discarded and the PVDF membrane was washed 6 times with 1x TBST-T containing 4 % milk powder for 15 min. Next, the membrane was incubated with the secondary antibody (Table 7) for at least 2 h at RT on a rotary shaker. The secondary antibody solution was discarded and the membrane was washed 6 times with 1x TBST-T for 15 min. For equilibration, the membrane was incubated in Alkaline Phosphatase (AP) buffer for 5 min. Subsequently, 500 µl Immuno-Star™ AP substrate (BioRad, Munich, Germany) was distributed on the membrane-covered in a plastic bag. The membrane was incubated in the dark for 5-10 min to increase the signal intensity and chemiluminescence was detected using the ChemiDoc™ Touch detection device (BioRad, Munich, Germany).

2.2.4.6 Staining of PVDF membranes

For visualization of protein bands, the PVDF membranes were stained with Coomassie brilliant blue (CBB). The PVDF membranes were transferred to CBB-staining solution and incubated slightly shaking for 5 min at RT. The membrane was rinsed with water, transferred to destaining solution and incubated shaking at RT to remove the background. Last, the destained membrane was rinsed with water and was allowed to dry.

2.2.4.7 LC-MS based proteomics

2.2.4.7.1 Sample preparation

To identify putative PEN2-GFP-TA_{PEN2} interactors, proteomics experiments were performed. After total protein extraction (2.2.4.1.2) and GFP-pulldown assays (2.2.4.3) GFP-Trap® agarose beads were washed with 4 ml pre-cooled CERK1 extraction buffer containing PIC and centrifuged for 2 min at 4°C and 2500 xg. The washing step was repeated two times. Next, GFP-Trap® agarose beads were washed with 4 ml cold Wash/Dilution buffer and centrifuged for 2 min at 4°C and 2500 xg. The washing and centrifugation steps were repeated once. GFP-Trap® agarose beads were transferred to 1.5 ml protein LoBind tubes (Eppendorf, Hamburg, Germany) and washed with 1 ml of Wash/Dilution buffer and centrifuged for 2 min at 4°C and 2500 xg. The buffer was carefully removed with an insulin syringe and GFP-Trap® agarose beads were resuspended in 1x bead volume of Elution buffer I containing Sequencing Grade Modified Trypsin (Promega, Madison, Wisconsin, USA). Samples were incubated at 30°C for 2 h and 400 rpm shaking using a thermomixer. The supernatant was transferred

to a new tube, beads were resuspended in 2x bead volumes of Elution buffer II and centrifuged for 2 min at 2500 g and 4°C. The supernatant was combined with the previously collected supernatant and the resuspension step was repeated with 2x bead volumes of Elution buffer II. The supernatant was transferred to the previously collected supernatant. The pooled supernatant was incubated in a thermomixer overnight at 32°C and 400 rpm shaking. To stop the tryptic digestion, 1 µl trifluoroacetic acid (TFA) per 25 µl GFP-Trap® agarose beads, was added. For peptide purification C18 stop-and-go extractions tips (Stage Tips), containing a C_{18} matrix were used as described in Rappsilber et al*.,* 2003 and Rappsilber et al*.,* 2007. Stage tips were placed with an appropriate adapter in 2 ml microcentrifuge tubes. Then, 30 µl of 100 % methanol was loaded into the stage tip. The air between the matrix and the solution was removed by carefully flicking the stage tips. The C18 tips were centrifuged for 2 min and 6000 xg. Next, 30 µl 100 % acetonitrile was added and centrifuged for 1 min and 6000 xg. Last, 30 µl 0.1 % formic acid was loaded and the stage tips were centrifuged for 1 min and 6000 xg. Equilibrated stage tips were transferred to a new 1.5 ml protein LoBind tube. Samples were loaded to the C_{18} stage tips and centrifuged for 5 min and 1800 xg. After the complete solution of the sample passed through the stage tip, the C_{18} matrix was washed with 15 µl 0.1 % formic acid. The C18 stage tip was centrifuged for 2 min at 1800 xg followed by a second centrifugation step for 2 min at 2600 xg. The stage tips were transferred to new 1.5 ml Protein LoBind tubes. For elution of purified peptides, 50 µl of 70 % acetonitrile 0.1 % formic acid were added and the C18 tips were centrifuged for 4 min at 1800 xg followed by a second centrifugation step for 2 min at 3000 xg. C18- purified peptides were dried in a vacuum at 45°C using the Eppendorf concentrator plus (Eppendorf, Hamburg, Germany) and stored at -20°C until needed.

2.2.4.7.2 Liquid chromatography - Mass spectrometry (LC-MS) for proteomics

Purified and dried peptides were dissolved in 20 µl LC-MS sample buffer (2% acetonitrile, 0.1% formic acid). Samples were incubated for 1 h at RT and shaking at 800 rpm using a thermomixer and transferred into an ultrasonic bath for 10 min. Subsequently, samples were incubated for 10 min at RT and 800 rpm and placed in an ultrasonic bath for 10 min. The Service Unit LC-MS Protein Analytics at the Institute of Microbiology and Genetics, Georg August-University Göttingen, performed LC-MS experiments. All solvents and acids used for LC-MS analysis had optima grade for LC-MS (Thermo Fisher Scientific). For peptide separation, 2 µl of each sample were subjected to reverse-phase liquid chromatography using an RSLCnano Ultimate 3000 system (Thermo Fisher Scientific, Waltham, Massachusetts, USA). Peptides were loaded on an Acclaim® PepMap 100 C18 HPLC pre-column (100 µm x 2 cm, C18, 5 µm, 100 Å; Thermo Fisher Scientific) with 0.07 % TFA. Acclaim® PepMap RSLC columns (75 µm x 50 cm, C18, 2 µm, 100 Å; Thermo Fisher Scientific) running a water-acetonitrile gradient at a

flow rate of 300 nl/ min were utilized for analytical separation of peptides. Peptides eluting during the gradient were online transferred into the mass spectrometer (Q Exactive HF, Thermo Scientific) by nano-electrospray ionization (nESI) using the Nanospray Flex Ion Source (Thermo Scientific) at a spray voltage of 1.5 kV (liquid junction). The acquisition of full MS scans within a mass range of 300 to 1650 m/ z was recorded at a resolution of 30.000 followed by data-dependent top 10 fragmentation (HCD) at a resolution of 15.000 (dynamic exclusion enabled) (Kerstin Schmitt, personal communication). The XCalibur software (4.0, Thermo Fisher Scientific, Waltham, Massachusetts, USA) was used for LC-MS method programming and data acquisition. For protein extracts from *Arabidopsis* leaf material database searches were performed against the Araport11 protein database (Cheng et al., 2017) using Proteome Discoverer™ version 2.2. The search algorithms Mascot and SequestHT were applied to calculate Peptide Spectrum Matches (PSMs). The digestion mode was defined to trypsin and the maximum of missed cleavage sites was set to three. The mass tolerance for precursor ions was 10 ppm and the decoy mode was reverse with a false discovery rate of 0.01 (Kerstin Schmitt, personal communication).

2.2.4.8 UPLC-TOF-MS-based non-targeted metabolomics

2.2.4.8.1 Sample preparation

Leaves of 4-week-old Col-0, *pen2-2*, *erd6-1* and complemented *erd6-1* plants expressing *ERD6-mTurquoise2* either unchallenged or after inoculation with conidiospores of *Bgh*, *E. pisi* or *G. orontii* were analyzed by a non-targeted metabolomics approach using ultra-high-performance liquid chromatography coupled to a quadrupole time-of-flight mass spectrometer (UHPLC-QTOF-MS). The rosette tissue of 10 plants per genotype and treatment were harvested at 24 hpi and 48 hpi and immediately frozen in liquid nitrogen. Overall, samples of three independent experiments were used for analysis. To obtain fine plant powder, the leaf tissue was homogenized using the Mixer Ball Mill MM400 (Retsch, Germany) for 1 min at 30 l/s. Sample extraction was performed by Sabine Freitag (Service Unit for Metabolomics and Lipidomics, Goettingen Center for Molecular Biosciences, University of Goettingen). All solvents and acids used for metabolite extraction had optima grade for LC-MS. For extraction, 40 mg of homogenized plant material was transferred into a pre-cooled 2 ml Eppendorf cup. Immediately, 800 µl 80 % methanol were added followed by vortexing and incubation for 2 x 15 min in an ultrasonic bath. Next, the samples were centrifuged at 4°C and 16000 x g for 15min. 400 µl of the supernatant were transferred into a 1.5 ml Eppendorf cup and dried under a stream of nitrogen. The samples were re-suspended in 20 µl methanol and vortexed. After adding 80 µl water, the samples were vortexed and centrifuged at 4°C and 16000 x g for 15 min to get rid of the soluble

material. Finally, 80 µl of the sample was transferred into a glass micro vial, covered with argon and used for analysis.

2.2.4.8.2 UHPLC-QTOF-MS

The non-targeted metabolome analysis was performed by Dr. Kirstin Feussner (Service Unit for Metabolomics and Lipidomics, Goettingen Center for Molecular Biosciences, University of Goettingen). All solvents and acids used for UHPLC-MS analysis had optima grade for LC-MS. For metabolic fingerprinting, an UHPLC (1290 Infinity, Agilent Technologies, Germany) coupled to a QTOF-MS (6540 UHD Accurate-Mass Q-TOF, Agilent Technologies; Germany) with Dual Jet Stream Technology as electrospray ionization (ESI) source (Agilent Technologies, Germany) was used. Sample separation was performed using an ACQUITY UPLC HSS T3 column (2.1 x 100 mm, 1.8 µm particle size, Waters Corporation, USA) and the following solvent system: solvent A (water, 0.1% (*v/v*) formic acid) and B (acetonitrile, 0.1% (*v/v*) formic acid). The gradient was set as following: 0 - 3 min: 1% - 20% B; 3 - 8 min: 20% - 100% B; 8 - 12 min: 100% B with a flow rate of 500 µl/min. The QTOF-MS device was used with a frequency of 2 GHz in the mass range from *m/z* 50 – *m/z* 1700. The parameter of the Dual Jet Stream source was set as following: capillary voltage to 3000 V, nozzle and fragmentor voltage to 200 V and 100 V, respectively as well as drying and sheath gas to 250 °C and 300 °C, respectively, with 8 l/min gas flow each. Mass Hunter Workstation Acquisition software B.05.01 (Agilent Technologies, USA) was used to monitor data acquisition in positive as well as negative ESI mode. Mass Hunter Qualitative Analysis software B.05.01 (Agilent Technologies, USA) was applied for Q-TOF-MS data analysis.

For peak picking and alignment, the software Profinder B.08.02 (Agilent Technologies, Germany) was used. The data sets, which were generated from the plant material 48 hpi, contained 717 feature (negative ESI mode) and 1284 feature (positive ESI mode), respectively. All metabolite features were ranked, filtered, merged, clustered, visualized and assigned to metabolites using the MarVis-Suite (Kaever et al., 2015, http://marvis.gobics.de). After filtering, 91 features (negative ESI mode), respectively 176 features (positive ESI mode) were selected with a false discovery rate (FDR) < 0.01. Clustering by one-dimensional self-organizing maps (1D-SOMs) organized all 267 metabolite features by pattern similarity and represented them by 10 prototypes. Finally, the accurate mass information of the features was used for an automated database search against KEGG (https://www.genome.jp/kegg/), BioCyc (https://biocyc.org) and in-house-databases, which provide tentative identification. To confirm metabolite identity, fragmentation analyses of the selected marker metabolites was performed using again the 1290 Infinity UHPLC system coupled with the 6540 UHD Accurate-Mass Q-TOF LC-MS system in the targeted MS/MS mode. The structure of the

following metabolites was confirmed by accurate fragment information: proline ($[M+H]^+$ 116.0707, *m/z* 70.0651, in accordance with MassBank PT102863), nicotinamide-beta-riboside ($[M+H]^+$ 255.098, *m/z* 124.0386, *m/z* 106.0289, *m/z* 80.049, *m/z* 80.049, *m/z* 78.034, in accordance with MassBank ML005101 for nicotinamide), 4-coumaroylagmatine ($[M+H]^+$ 277.1662 *m/z* 260.1389, *m/z* 147.0438, *m/z* 119.0489, *m/z* 91.0542, in accordance with MassBank PR311080/ PR311079), feruloylagmatine ($[M+H]^+$ 307.1662, *m/z* 290.0879, *m/z* 177.0484, *m/z* 145.0278, *m/z* 117.0332, in accordance with MassBank PR311014/ PR311015), indol-3ylmethyl-glucosinolate ($[M-H]^-$ 447.0546, *m/z* 96.9605, *m/z* 74.9915, in accordance with MassBank CE000583), 4-hydroxy-3-indolylmethyl-glucosinolate ($[M-H]^-$ 463.0486, *m/z* 96.9604, *m/z* 74.9914), 4-methoxy-3-indolylmethyl-glucosinolate ($[M-H]^-$ 477.0648, *m/z* 96.9602, *m/z* 74.9915, in accordance with MassBank CE000526), camalexin ($[M+H]^+$ 201.0476, *m/z* 160.0218, *m/z* 142.0524, *m/z* 116.0492, *m/z* 89.0385, in accordance with MassBank PB000525), O-malonyl hydroxycamalexin hexoside ($[M+H]^+$ 465.0955, *m/z* 217.043, *m/z* 189.0477, *m/z* 156.0673, *m/z* 58.9952), hydroxycamalexin hexoside ($[M+H]^+$ 379.0947, *m/z* 217.0433, *m/z* 189.0481, *m/z* 156.0682, *m/z* 58.9951), dihydroascorbigen hexoside ($[M+H]^+$ 468.1502, *m/z* 204.0682, *m/z* 188.0713, in accordance with Böttcher et al., 2014), salicylic acid glucoside ($[M-H]^-$ 299.0768, *m/z* 137.0247, *m/z* 93.0347, in accordance with MassBank EQ369654 for salicylic acid).

2.2.5 Microscopy and Image Analysis

2.2.5.1 Confocal laser scanning microscopy

CLSM was performed using the Leica TCS SP5 and Leica TCS SP8 system (Leica, Wetzlar, Germany) equipped with the LAS AF Leica Application Suite Version 2.7.2 and LAS X 3.5.1.18803, respectively. Small leaves or leaf pieces were water-mounted on an object slide. Appropriate lasers and emission filters were used for microscopic analysis. Emitted fluorescence was detected using Leica HyD detectors. Table 20 shows the excitation and emission wavelengths of the fluorophores used in this work.

Table 20. Excitation and emission wavelengths used for confocal microscopy

Fluorophore	Excitation	Emission
mCitrine	514 nm (Argon laser)	525-560 nm
mCherry/RFP	561 nm (DPSS laser)	580-620 nm
GFP	488 nm (Argon laser)	500-540 nm
mKate2	561 nm (HeNe laser)	620-640 nm
mTurquoise2	458 nm (Argon laser)	462-485 nm
Chlorophyll autofluorescence		740-770 nm

Sequential scanning was used to scan fluorophores with overlapping emission wavelengths. Furthermore, a bidirectional scan and a line average of 3 were used. Z-stacks were recorded 1 µm apart. Images used for ERD6-mTurquoise2 endosome quantification were scanned at 400 Hz with a resolution of 512 x 512 pixels. Images for MAMP induced PEN2-GFP-TA_{PEN2} aggregate quantification were scanned at 200 Hz with a resolution of 1024 x 1024 pixels. The Leica LAS X 3.5.1.18803 software, Fiji-ImageJ software (ImageJ 1.49m; Schindelin *et al.,* 2012) and Adobe Photoshop CS5 software packages were used for image processing. Adobe Illustrator CS5 was used to prepare the final figures. For comparability, images within one figure were adjusted using the same settings.

2.2.5.2 PEN2-GFP-TA_{PEN2} aggregate quantification

CLSM Images for PEN2-GFP-TA_{PEN2} aggregate quantification were generated using the Mark and Find feature of the Leica LAS AF Leica Application Suite Version 2.7.2. For each image area, 11 focal plane images with a distance of 1 µm were recorded. Image processing and PEN2-GFP-TA_{PEN2} aggregate quantification were performed using Fiji-ImageJ. For export of z-stack maximum projections from proprietary Leica .lif files. The plugin "LIF Projector" was used (https://biii.eu/lif-projector). Aggregate counting was performed with the scripts "PEN2 Particle Counter" and "PEN2 Particle Number" developed by Dr. Hassan Ghareeb (Table S1).

The script "PEN2 Particle Counter" was applied to enhance the visibility of PEN2-GFP-TA_{PEN2} aggregates in images. The Unsharp Mask algorithm was applied to increase the contrast at the edges of PEN2-GFP-TA_{PEN2} aggregates. To smooth the edges of the image, the Gaussian blur algorithm was utilized and the signal at the edges of PEN2-GFP-TA_{PEN2} aggregates was enhanced by increasing the radius. Next, the background was subtracted and the contrast was adjusted to increase the sensitivity of PEN2-GFP-TA_{PEN2} aggregate detection. The MaxEntropy algorithm was applied for segmentation of the image by auto thresholding and followed by labeling of PEN2-GFP-TA_{PEN2} aggregates in magenta. The script "PEN2 Particle number" was used to determine the number of PEN2-GFP-TA_{PEN2} aggregates using the Analyze Particles command. The results were exported in CSV format. A visual representation of PEN2-GFP-TA_{PEN2} aggregate quantification is shown in Figure S1.

2.2.5.3 ERD6-mTurquoise2 vesicle quantification

CLSM Images for ERD6-mTurquoise2 endosome quantification were generated using the Mark and Find feature of the Leica LAS X 3.5.1.18803 software. For each image area, 13 focal plane images with a distance of 1 µm were recorded. Image processing and ERD6-mTurquoise2 endosome quantification were performed using Fiji-ImageJ. First, images were exported from lif files and converted into maximum z-projections using LIF Projector (https://biii.eu/lif-projector). Then the contrast was en-

hanced to increase the sensitivity of vesicle quantification. This was performed with the same settings for all images with an experiment using the batch processing tool with the following macro:

```
run("Brightness/Contrast...");
setMinAndMax(6, 135);
run("Apply LUT");
```

For appropriate endosome detection, the machine learning tool Trainable WEKA segmentation was used to design a classifier. The two classes “vesicles” and “background” were defined. The classifier was applied to images and probability maps were generated indicating the probability of each pixel belonging to the defined class. On the probability maps generated by the WEKA tool, image segmentation was performed by auto thresholding applying the MaxEntropy algorithm for vesicle labeling. The number of vesicular structures was determined using the Analyze Particles command and the results were exported in CSV format.
These operations were carried out in batch for all images within an experiment using the batch processing tool and the following macro:

```
//Deletion of uneeded stack slices
run("Duplicate...", "duplicate");
setSlice(2);
run("Delete Slice");
// Thresholding
setAutoThreshold("MaxEntropy dark");
run("NaN Background");
setOption("BlackBackground", false);
run("Make Binary");
//Particle counting
run("Analyze Particles...", "display summarize");
```

An illustration of ERD6-mTurquoise2 vesicle quantification is shown in Figure S2.

2.2.6 Statistical analysis

Boxplots were generated using OriginPro 2020. Statistical differences were determined using Prism-GraphPad 8. To analyze normal distribution the Shapiro-Wilk´s test was performed. For data that is normally distributed, a one-way or two-way analysis of variance (ANOVA) followed by Tukey´s post-hoc test was performed. For data that is not normally distributed, the Kruskal-Wallis ANOVA followed by Dunn´s post-hoc test was used.

3 Results

The *Arabidopsis thaliana* atypical myrosinase PEN2 is required for broad-spectrum invasion resistance to filamentous plant pathogens, including non-adapted powdery mildews (Lipka et al., 2005). PEN2 is a tail-anchored protein with dual-membrane targeting to peroxisomes and mitochondria. Moreover, pathogen-induced recruitment and immobilization of mitochondrial subpopulations were observed at sites of attempted fungal invasion. Additionally, mitochondrial arrest is accompanied by peripheral accumulation of PEN2-GFP-TA$_{PEN2}$ (Fuchs et al., 2016). PEN2-GFP-TA$_{PEN2}$ was shown to form pathogen-triggered oligomers and dimers of higher order in the periphery of arrested mitochondria. Simultaneously, PEN2 substrate production by the cytochrome P450 monooxygenase CYP81F2 is coordinated on the surface of the endoplasmic reticulum (ER), which becomes structurally reorganized in immediate proximity to the immobilized mitochondria (Fuchs et al., 2016). Exclusive targeting of PEN2 to the outer membrane of mitochondria complements the *pen2* mutant phenotype supporting the functional importance of the mitochondrial PEN2 protein subpool for controlled local production of PEN2 hydrolysis products at subcellular plant-microbe interaction domains (Fuchs et al., 2016). However, the underlying mechanisms and signaling pathways that function in pathogen-induced concerted reorganization of the ER and mitochondrial clustering and immobilization are still unknown. The aim of this project was to identify and characterize novel important molecular components contributing to PEN2-mediated pathogen entry control. Additionally, the role of MAMP-dependent signaling for CYP81F2 accumulation, ER rearrangement, mitochondrial arrest and PEN2 aggregate formation was evaluated.

3.1 Investigation of MAMP induced CYP81F2-RFP accumulation, mitochondrial immobilization and PEN2-GFP-TA$_{PEN2}$ aggregate formation

3.1.1 Confocal laser scanning microscopy analysis of MAMP dependent CYP81F2 accumulation

PEN2-GFP-TA$_{PEN2}$ forms pathogen-induced aggregates associated with the periphery of immobilized mitochondria at sites of attempted fungal penetration. Additionally, pathogen attack induced cell-autonomous expression of the ER-anchored CYP81F2 and revealed focal accumulation and a close association to immobilized mitochondria at pathogen-invasion sites (Fuchs et al., 2016).

To analyze MAMP induced CYP81F2-RFP accumulation, *pCYP81F2::CYP81F2-RFP* expressing Col-0 plants in the *cyp81f2-2* mutant background (Fuchs et al., 2016) were treated with either water, chitin or flagellin (Figure 9). Confocal laser scanning microscopy (CLSM) analysis revealed that in epidermal

cells, the fluorescence signal of CYP81F2-RFP was not detectable in samples vacuum infiltrated with water. However, a strong RFP-fluorescence signal of ER-associated CYP81F2 could be observed post chitin and flagellin infiltration. CYP81F2-RFP fluorescence showed a reticulate distribution and localization around the nucleus, indicating an association of CYP81F2-RFP with the ER. The observed induction of CYP81F2-RFP following MAMP treatment was similar to the cell-autonomous accumulation of CYP81F2-RFP after pathogen attack. In contrast, no ER rearrangement was observed after MAMP treatment.

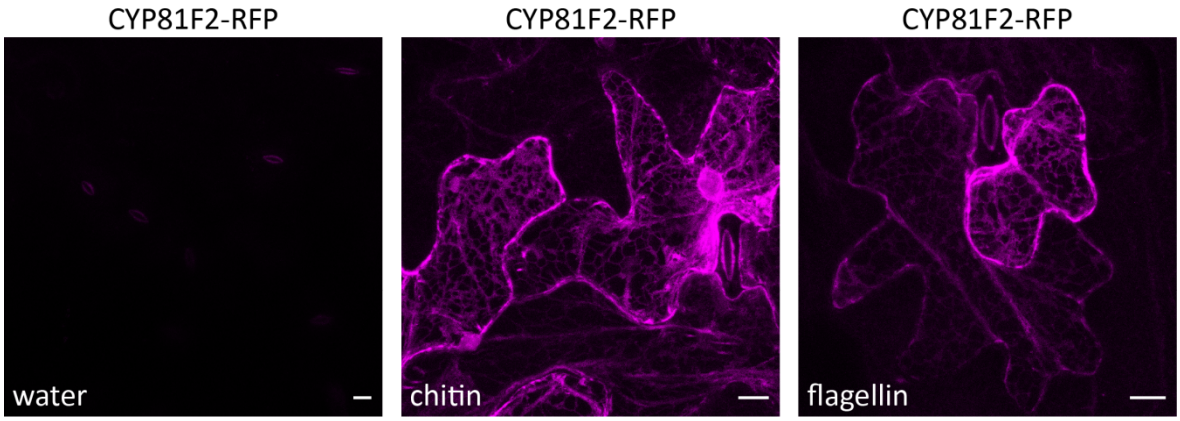

Figure 9. MAMPs induce accumulation of CYP81F2-RFP. CLSM images of transgenic *Arabidopsis* epidermal leaf cells expressing *CYP81F2-RFP* under control of the native promoter 20 hours after vacuum infiltration with water, chitin (100 µg/ml) or flagellin (50 nM). Images show representative maximum z-projections. Z-stack size 7-12 focal planes recorded 1 µm apart. Scale bar = 10 µm.

3.1.2 Confocal laser scanning microscopy analysis of MAMP induced mitochondrial arrest and PEN2-GFP-TA$_{PEN2}$ aggregate formation

Upon pathogen attack, subpopulations of mitochondria are recruited and arrested at sites of attempted fungal invasion. Additionally, mitochondrial immobilization is associated with peripheral PEN2-GFP-TA$_{PEN2}$ aggregate formation (Fuchs et al., 2016). To investigate whether MAMP treatment induces mitochondrial arrest and PEN2-GFP-TA$_{PEN2}$ aggregate formation, *pPEN2::PEN2-GFP-TA$_{PEN2}$* expressing Col-3 *gl1* plants in the *pen2-1* mutant background (Lipka et al., 2005) were analyzed by CLSM untreated or 20 hours after chitin or flagellin vacuum infiltration (Figure 10A). This analysis showed a constitutive expression of *PEN2-GFP-TA$_{PEN2}$* and no mitochondrial immobilization and PEN2-GFP-TA$_{PEN2}$ aggregate formation in untreated epidermal cells. However, chitin and flagellin vacuum infiltration elicited mitochondrial accumulation and arrest associated with PEN2-GFP-TA$_{PEN2}$ aggregate formation. To support these findings and to analyze mitochondrial immobilization and PEN2-GFP-TA$_{PEN2}$ aggregate formation after MAMP treatment in more detail a quantitative time-course analysis was performed (Figure 10B). In collaboration with Dr. Hassan Ghareeb, an ImageJ-based script for PEN2-GFP-TA$_{PEN2}$ aggregate quantification was developed. The method used maxi-

mum z-projection images of leaf epidermal cells and comprises automated subtraction of background noise, contrast adjustment to increase the sensitivity of PEN2-GFP-TA_{PEN2} aggregate detection followed by identification and counting of fluorescent signals associated with PEN2-GFP-TA_{PEN2} aggregates (Figure S1). PEN2-GFP-TA_{PEN2} aggregate formation was analyzed at 1, 3, 6, and 20 hours after water, chitin and flagellin vacuum infiltration (Figure 10B). PEN2-GFP-TA_{PEN2} aggregate formation was observed 1 and 3 hours post infiltration (hpi) in all investigated samples. However, flagellin infiltration triggered a higher number of PEN2-GFP-TA_{PEN2} aggregates in comparison to chitin and water infiltration 1 and 3 hpi. Additionally, the number of PEN2-GFP-TA_{PEN2} aggregates increased continuously during the time course experiment after chitin infiltration. In contrast to chitin infiltrated samples, PEN2-GFP-TA_{PEN2} aggregate formation is reduced 6 hours after flagellin infiltration and increased again at 20 hpi (Figure 10B). These results indicate that mitochondrial arrest and PEN2-aggregate formation is induced upon the perception of MAMPs.

PEN2 is a tail-anchored protein with dual-targeting to both peroxisomes and mitochondria. However, only mitochondria are arrested at pathogen invasion sites. Peroxisomes retained their mobility and showed unaltered PEN2-GFP-TA_{PEN2} localization pattern after pathogen attack (Fuchs et al., 2016). For evaluation of the association of PEN2-GFP-TA_{PEN2} with peroxisomes and mitochondria after MAMP treatment, leaves of transgenic *Arabidopsis pen2-1* lines co-expressing *pPEN2::PEN2-GFP-TA_{PEN2}* and the peroxisomal matrix marker *RFP-Peroxisome Targeting Signal1* (RFP-PTS1) (Fuchs et al., 2016) were vacuum infiltrated with either chitin or flagellin. CLSM demonstrated, no accumulation and immobilization of RFP-tagged peroxisomes. In addition, no PEN2-GFP-TA_{PEN2} aggregate formation was observed in the periphery of RFP-PTS1-tagged peroxisomes 20 hours after MAMP treatment (Figure 11). These results indicate that PEN2-GFP-TA_{PEN2} aggregate formation occurred on other membrane compartments accumulating after MAMP treatment.

To analyze the immobilization of mitochondrial subpopulation and PEN2-GFP-TA_{PEN2} aggregate formation after MAMP treatment, experiments with double transgenic *Arabidopsis pen2-1* lines expressing *pPEN2::PEN2-GFP-TA_{PEN2}* with the mitochondrial matrix marker *ScCOX4-RFP* (Saccharomyces cerevisiae Cytochrome C Oxidase IV fused to RFP) (Fuchs et al., 2016) were performed. CLSM analysis showed that organelle immobilization and PEN2-GFP-TA_{PEN2} aggregate formation are restricted to mitochondrial subpopulations after chitin and flagellin treatment (Figure 12A). Similar to plant-microbe interaction sites, subpopulations of clustered and arrested RFP-tagged mitochondria develop foci of intense PEN2-GFP-TA_{PEN2} fluorescence after chitin treatment (t_0-t_{15}), which is followed by the disappearance of the GFP-hyperfluorescence and returning mobility of mitochondria over time (t_{25}-t_{35}) (Figure 12B).

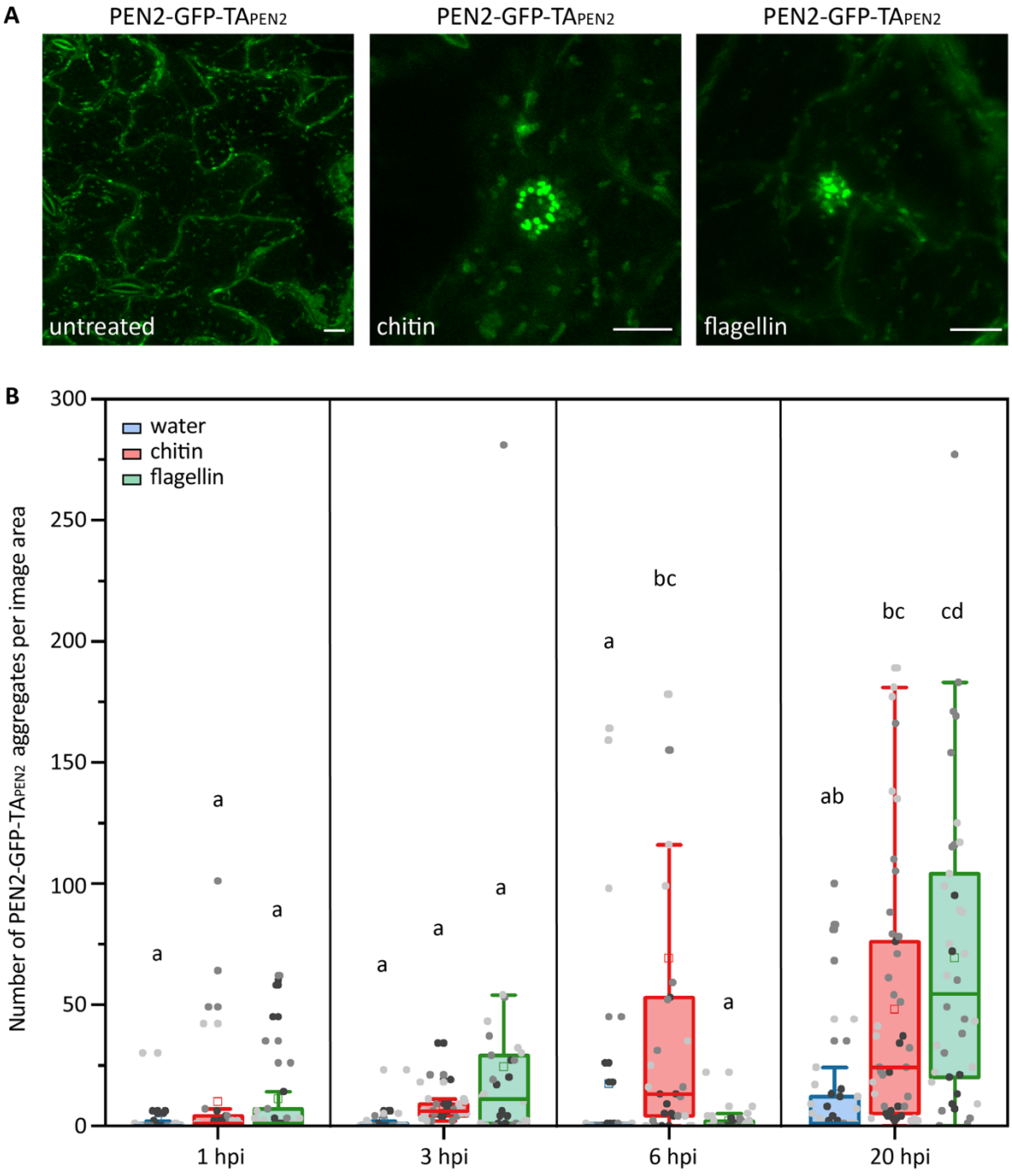

Figure 10. Mitochondrial accumulation and PEN2 aggregate formation can be induced by MAMP treatment. **(A)** CLSM images of transgenic *Arabidopsis* leaf epidermal cells expressing *PEN2-GFP-TA$_{PEN2}$* under control of the endogenous promoter untreated and 20 hours after chitin or flagellin infiltration. Images are maximum projections of 6-10 focal planes recorded 1 µm apart. Scale bar = 10 µm. **(B)** Quantification of MAMP-triggered PEN2-GFP-TA$_{PEN2}$ aggregate formation per image area after water, chitin or flagellin vacuum infiltration in epidermal cells over time. Data of three independent biological experiments are represented in an individual box plot. For each replicate, 3-4 images (Z-stack size= 11 focal planes recorded 1 µm apart) of 3 individual plants per genotype were analyzed (9-12 images per replicate, 27-36 images in total). Individual boxplots include whiskers (values within the 1.5-fold interquartile range), first and third quartile (lower and upper box limits) and median (middle horizontal line). The mean value is depicted by a square and data points of different experiments are indicated as gray scale. Letters show significant differences between genotypes (two-way ANOVA ($P < 0.01$); Tukey post-hoc test). hpi = hours post infiltration.

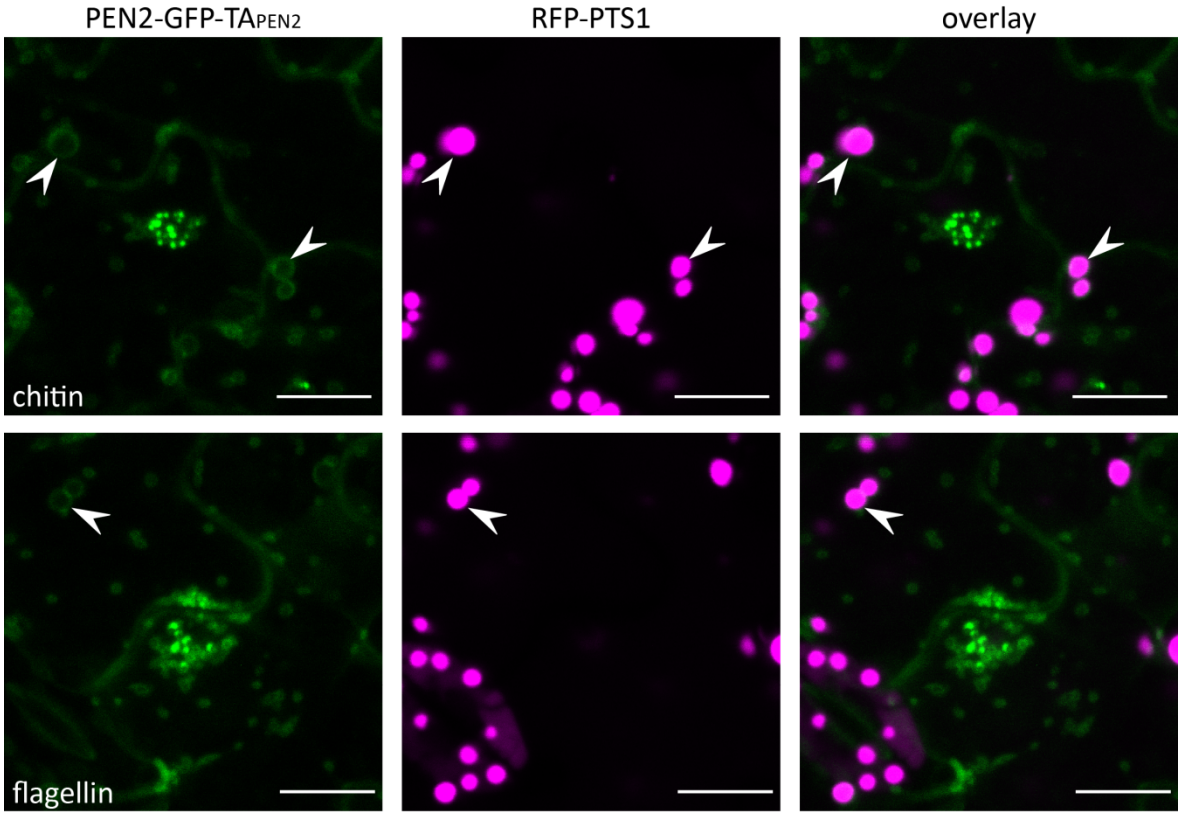

Figure 11. Peroxisomes do not accumulate and immobilize after MAMP treatment and show unaltered peripheral PEN2 localization patterns. CLSM images of *PEN2-GFP-TA$_{PEN2}$* co-expressed with the peroxisomal matrix marker *RFP-PTS1* 20 hours after chitin and flagellin vacuum infiltration. PEN2-GFP-TA$_{PEN2}$ is shown in green and the peroxisomal marker RFP-PTS1 in magenta. Arrowheads indicate PEN2-GFP-TA$_{PEN2}$ in the periphery of RFP-tagged peroxisomes. Images are maximum projections of 6-7 focal planes recorded 1 µm apart. Scale bar = 10 µm.

Additionally, MAMP treatment induced a partially different phenotype as observed after pathogen penetration. Besides accumulating subpopulations of mitochondria with peripheral PEN2-GFP-TA$_{PEN2}$ aggregate formation, foci of elevated PEN2-GFP-TA$_{PEN2}$ fluorescence intensity in the periphery of immobilized single mitochondria were observed (Figure 13A). To analyze PEN2-GFP-TA$_{PEN2}$ aggregate formation in the periphery of single mitochondria in more detail, time-lapse CLSM analysis after chitin infiltration was performed (Figure 13B). These analyzes showed that some single mitochondria with foci of elevated PEN2-GFP-TA$_{PEN2}$ fluorescence intensity are mobile and others remained arrested. Taken together, these results indicate that MAMPs induce the accumulation and immobilization of subpopulations of mitochondria that are associated with peripheral PEN2-GFP-TA$_{PEN2}$ aggregate formation. In addition, MAMPs trigger single mitochondria with foci of elevated PEN2-GFP-TA$_{PEN2}$ fluorescence intensity that are either mobile or arrested.

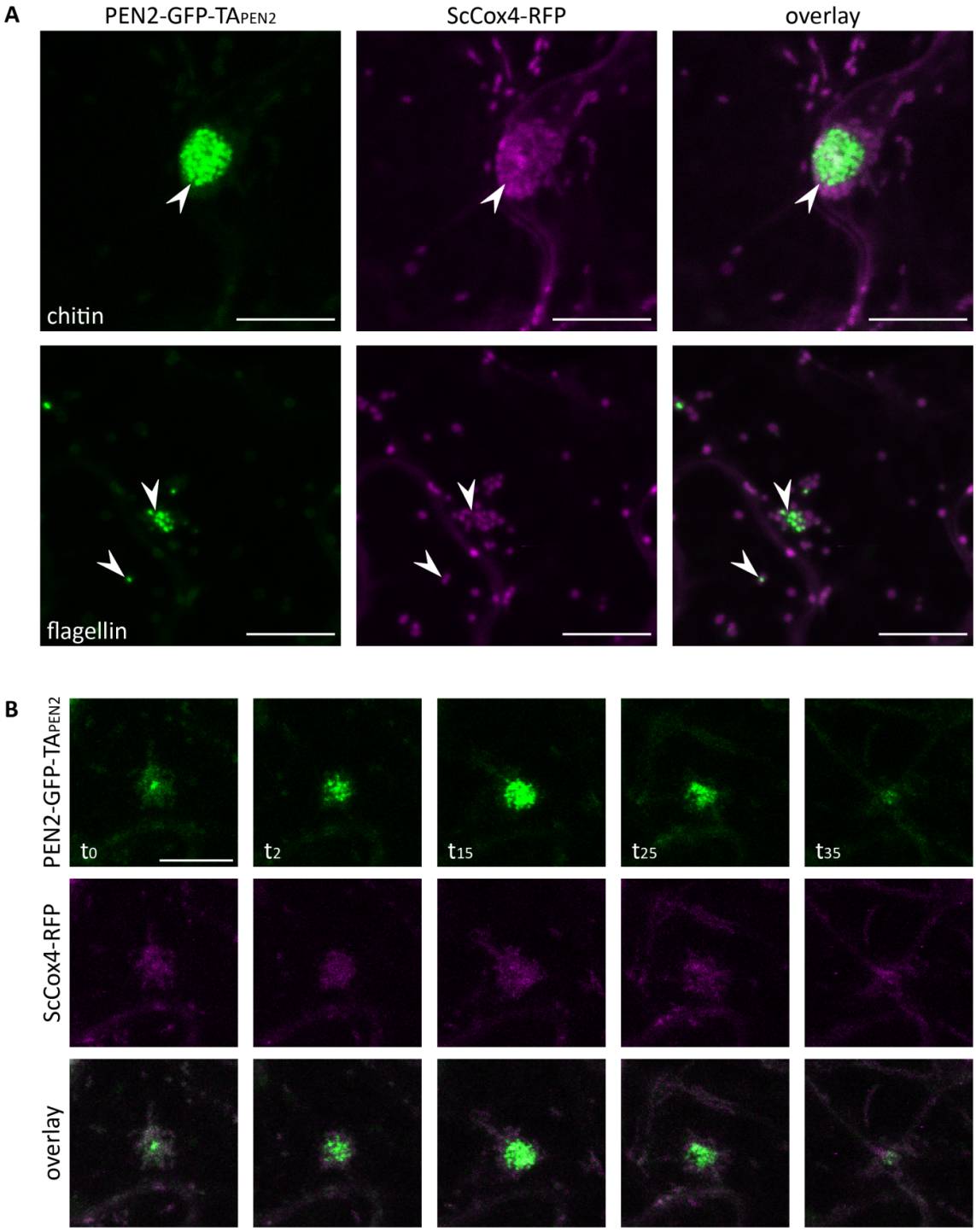

Figure 12. Organelle immobilization and PEN2 aggregate formation are restricted to mitochondrial subpopulations after MAMP treatment. Double transgenic leaf epidermal cells of *Arabidopsis* plants expressing both *PEN2-GFP-TA$_{PEN2}$* and the mitochondrial matrix marker *ScCOX4-RFP* 20 hours after vacuum infiltration with chitin or flagellin. PEN2-GFP-TA$_{PEN2}$ is shown in green and the mitochondrial marker ScCox4-RFP in magenta. CLSM images are representative maximum z-projections of 8-10 focal planes recorded 1 µm apart. Scale bar = 10 µm. **(A)** Arrowheads indicate PEN2-GFP-TA$_{PEN2}$ aggregate formation in the periphery of RFP-tagged immobilized mitochondria. **(B)** CLSM time-lapse imaging 8 hours after chitin vacuum infiltration illustrates PEN2-GFP-TA$_{PEN2}$ aggregate formation in the periphery of accumulated and arrested subpopulations of mitochondria (t_0-t_{15}), followed by the disappearance of the intense PEN2-GFP-TA$_{PEN2}$ fluorescence (t_{25}-t_{35}) over time. t= time (min) with t_0= 8 hours after chitin infiltration.

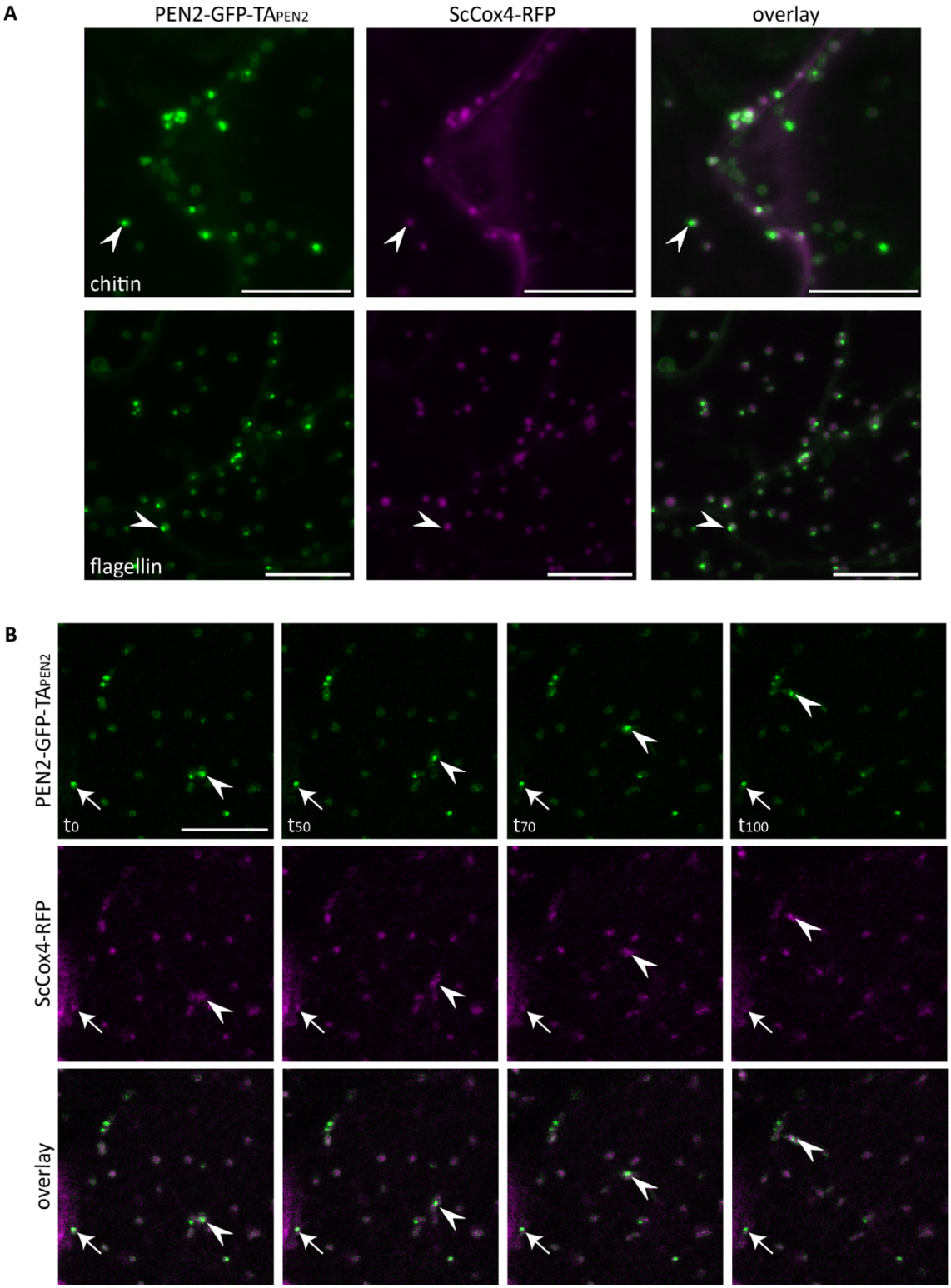

Figure 13. Chitin and flagellin treatment induce foci of elevated PEN2-GFP-TA$_{PEN2}$ fluorescence intensity in the periphery of single mitochondria. CLSM images of double transgenic *Arabidopsis* plants expressing *PEN2-GFP-TA$_{PEN2}$* with the mitochondrial marker *ScCOX4-RFP* after chitin and flagellin infiltration. PEN2-GFP-TA$_{PEN2}$ is shown in green and the co-expressed mitochondrial marker ScCox4-RFP in magenta. Images are maximum projections of 6-8 focal planes recorded 1 µm apart. Scale bar = 10 µm. **(A)** Arrowheads point to the accumulation of PEN2-GFP-TA$_{PEN2}$ in the periphery of single RFP-tagged mitochondria 20 hours post chitin and flagellin vacuum infiltration. **(B)** CLSM time-lapse analysis of leaf epidermal cells co-expressing *PEN2-GFP-TA$_{PEN2}$* and mitochondrial marker *ScCOX4-RFP* directly after chitin infiltration. Arrowheads indicate a single and mobile

RFP-tagged mitochondrion and arrows point to a single and immobilized RFP-tagged mitochondrion associated with intense PEN2-GFP-TA_{PEN2} fluorescence over time. t= time (s).

3.2 Generation and characterization of a double transgenic line co-expressing *PEN2-GFP-TA_{PEN2}* and *CYP81F2-mKate2*

The atypical myrosinase PEN2 and the cytochrome P450 monooxygenase CYP81F2 are important molecular components of glucosinolate-dependent defense against powdery mildews (Lipka et al., 2005; Bednarek et al., 2009; Clay et al., 2009; Fuchs et al., 2016). Subpopulations of mitochondria are recruited and arrested at sites of attempted fungal invasion, which coincides with aggregate formation of PEN2. Simultaneously, biosynthesis of the PEN2 substrate by CYP81F2 is coordinated at the surface of the ER which becomes structurally rearranged in proximity to the immobilized mitochondria underneath the fungal invasion site (Fuchs et al., 2016). However, pathways regulating the recruitment and activity of PEN2 and CYP81F2 involved in pathogen defense are unknown. To investigate the underlying mechanisms that coordinate pathogen-triggered reorganization of the ER and mitochondrial accumulation and arrest, a forward CLSM-based screen will be performed to isolate mutants with altered localization of PEN2-GFP-TA_{PEN2} and CYP81F2-RFP after inoculation with non-adapted powdery mildews.

A new double transgenic line expressing both *pPEN2::PEN2-GFP-TA_{PEN2}* and *pCYP81F2::CYP81F2-mKate2* was generated. To reduce the amount of T-DNA segregating in the background, a construct was produced containing one T-DNA with both *pPEN2::PEN2-GFP-TA_{PEN2}* and *pCYP81F2::mKate2* (Figure 14A) using the Colorful system (Ghareeb et al., 2016). The construct was transformed into *Arabidopsis* Col-3 *gl1*. In total, 5 independent single insertion lines were identified in the T2 generation. These lines were propagated to identify homozygous lines.

Selected homozygous lines of the T3 generation were screened for *PEN2-GFP-TA_{PEN2}* and *CYP81F2-mKate2* expression in unchallenged leaf epidermal cells (Figure 14B) and 20 hours post infection (hpi) with *Bgh* (Figure 14E) by CLSM. Stable transgenic *Arabidopsis* plants expressing *pPEN2::PEN2-GFP-TA_{PEN2}* (Lipka et al., 2005) and *pCYP81F2::CYP81F2-RFP* (Fuchs et al., 2016) served as controls and were analyzed unchallenged (Figure 14C and D) and 20 hours after *Bgh* infection (Figure 14F and G). CLSM of the double transgenic line showed a constitutive expression of *PEN2-GFP-TA_{PEN2}* and a similar localization pattern of GFP-tagged PEN2 (Figure 7B) in unchallenged leaf epidermal cells similar to the single transgenic line expressing *PEN2-GFP-TA_{PEN2}* (Figure 14C). However, the double transgenic line contained slightly higher PEN2-GFP-TA_{PEN2} fluorescence intensities.

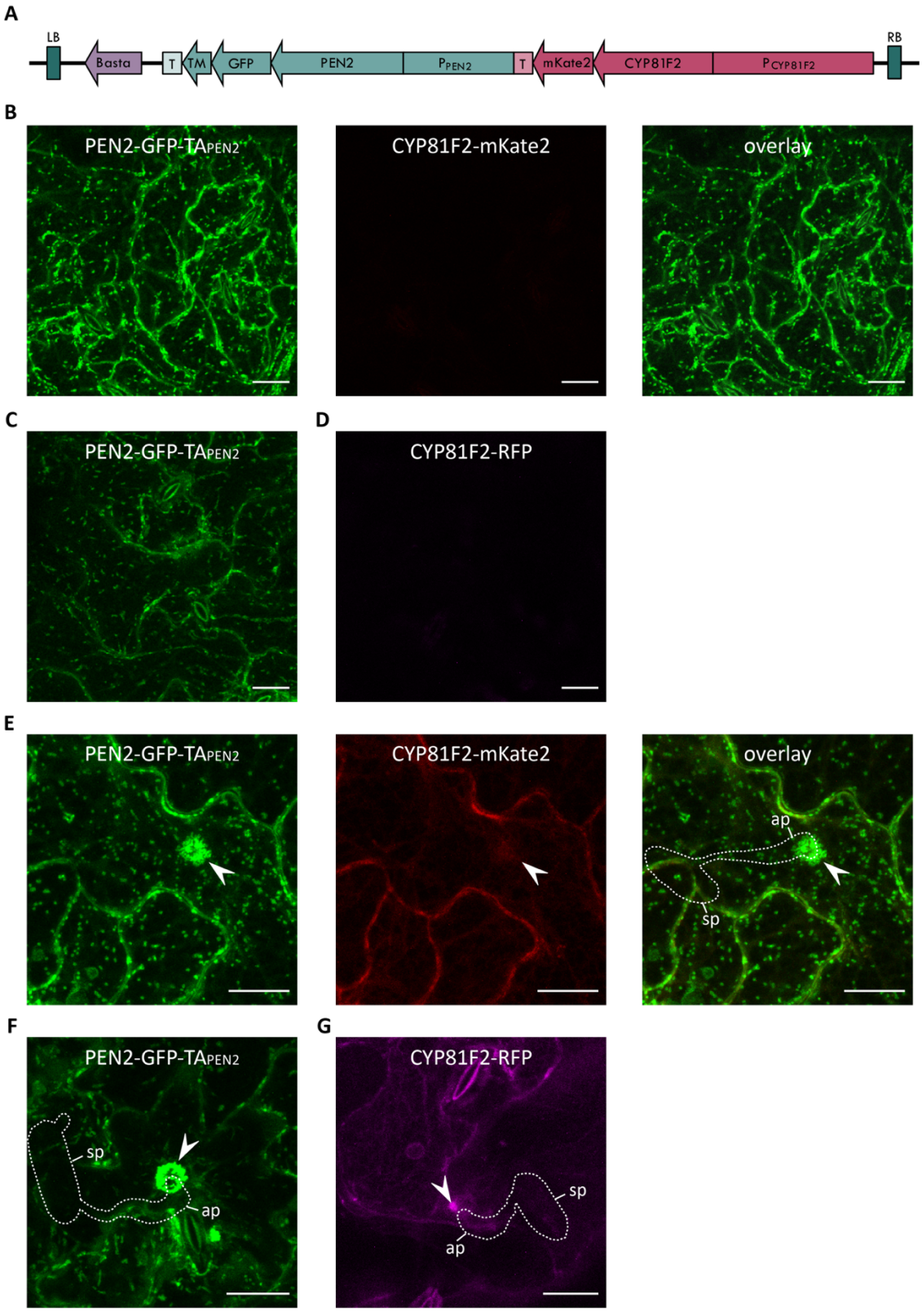

Figure 14. Subcellular localization of co-expressed PEN2-GFP-TA$_{PEN2}$ and CYP81F2-mKate2. (A) Scheme illustrates the T-DNA of the double transgenic line. The T-DNA contains both *PEN2-GFP-TA$_{PEN2}$* (green) and *CYP81F2-mKate2* (red) under the control of their endogenous promoters. LB= Left border, RB= Right border, T= Terminator (pA35S). **(B and E)** CLSM images of one selected double transgenic line co-expressing *P$_{PEN2}$::PEN2-GFP-TA$_{PEN2}$* and *P$_{CYP81F2}$::CYP81F2-mKate2* in unchallenged *Arabidopsis* leaf epidermal cells (B) or 20 hpi with

Bgh (E). **(C, D, F and G)** CLSM images of the control lines expressing *PEN2-GFP-TA$_{PEN2}$* (C and F) or *CYP81F2-RFP* (D and G) in unchallenged (C and D) and 20 hpi with *Bgh* (F and G). Unchallenged epidermal cells exhibit no detectable CYP81F2-mKate2 or CYP81F2-RFP fluorescence (B and D). Arrowheads point towards the site of attempted fungal invasion. The fungal spore (sp) and the appressorium (ap) are outlined by dashed lines. PEN2-GFP-TA$_{PEN2}$ is shown in green, CYP81F2-mKate2 in red and CYP81F2-RFP in magenta. Images show maximum projections of 11 focal planes recorded 1 µm apart. Scale bar = 20 µm.

The double transgenic line expressing *CYP81F2-mKate2* and the single transgenic line expressing *CYP81F2-RFP* exhibited no detectable CYP81F2-mKate2 (Figure 14B) or CYP81F2-RFP (Figure 14D) fluorescence signal in unchallenged epidermal cells. CLSM analysis of the double transgenic line 20 hours after *Bgh* infection showed recruitment and immobilization of mitochondrial subpopulations associated with PEN2-GFP-TA$_{PEN2}$ aggregate formation at the sites of attempted fungal penetration (Figure 14E). Furthermore, *CYP81F2-mKate2* expression in a network-like structure and a focal-accumulation pattern at pathogen-interaction sites (Figure 14E), comparable to the control lines (Figure 14G), were observed in the double transgenic line at 20 hpi with *Bgh.* These results indicate that the double transgenic line exhibits similar localization and accumulation of PEN2 and CYP81F2 in comparison to the single transgenic lines.

To evaluate protein levels of PEN2-GFP-TA$_{PEN2}$ and CYP81F2-mKate2 in the double transgenic line, SDS-PAGE (2.2.4.4) and western blot analysis (2.2.4.5) were performed using either the α-PEN2 or α-t-RFP antibody (Figure 15). Col-3 *gl1*, *pen2-1*, *cyp81f2-2* and the single transgenic line PEN2-GFP-TA$_{PEN2}$ served as controls. The Predicted molecular weight for PEN2 is 63.9 kDa, 26.9 kDa for GFP, 55.7 kDa for CYP81F2 and 26.1 kDa for mKate2. Therefore, PEN2-GFP-TA$_{PEN2}$ fusion proteins were expected to show a molecular mass of approximately 90,8 kDa and CYP81F2-mKate2 of approximately 81,8 kDa. Immunoblotting confirmed the expression of full-length PEN2-GFP-TA$_{PEN2}$ and CYP81F2-mKate2 fusion proteins in three tested homozygous transgenic lines containing a single T-DNA insertion. Overall, PEN2-GFP-TA$_{PEN2}$ protein levels were slightly increased in comparison to the single transgenic line expressing PEN2-GFP-TA$_{PEN2}$ confirming the results obtained by CLSM. PEN2-GFP-TA$_{PEN2}$ protein levels showed no differences in uninfected and *Bgh* infected leaves at 20 hpi. It is important to note that the double transgenic line in the Col-3 *gl1* background exhibited wild-type PEN2 protein levels in addition to the PEN2-GFP-TA$_{PEN2}$ fusion protein. The PEN2-GFP-TA$_{PEN2}$ protein abundance is slightly higher in comparison to endogenous PEN2 protein levels. Furthermore, the double transgenic line showed *Bgh*-induced expression of CYP81F2-mKate2. Unfortunately, the α-t-RFP antibody detected an unspecific band similar to the size of CYP81F2-mKate2. Taken together, these results indicate that the double transgenic lines slightly overexpress PEN2-GFP-TA$_{PEN2}$.

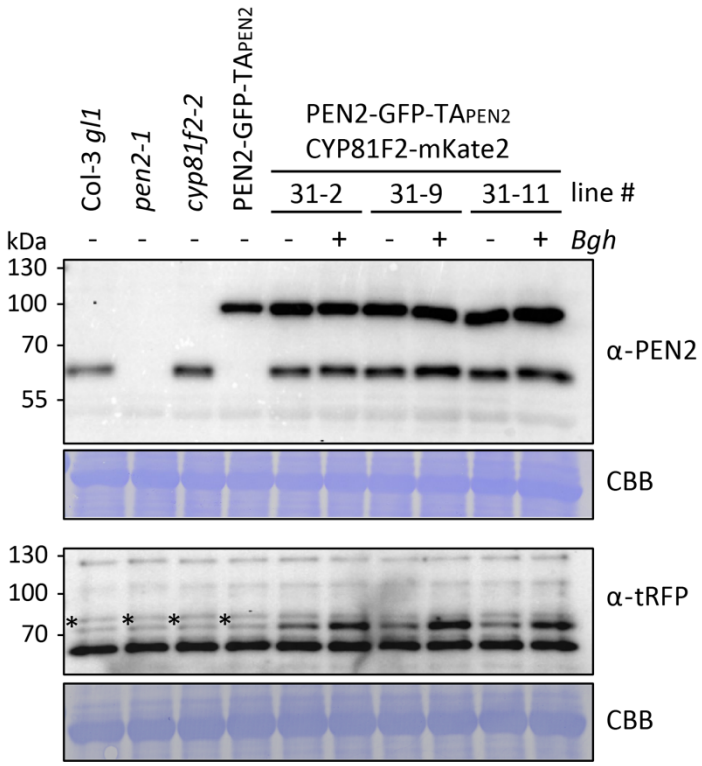

Figure 15. Immunoblot analysis of the double transgenic line co-expressing P_{PEN2}-PEN2-GFP-TA_{PEN2} and $P_{CYP81F2}$-CYP81F2-mKate2. Protein levels of three independent Col-0 *gl1* plants co-expressing *P_{PEN2}::PEN2-GFP-TA_{PEN2}* and *$P_{CYP81F2}$::CYP81F2-mKate2* unchallenged and at 20 hpi with *Bgh*. Col-0 *gl1*, *pen2-1*, *cyp81f2-2* and PEN2-GFP-TA_{PEN2} were used as controls. Immunoblotting was performed with either the α-PEN2 (upper panel) or α-t-RFP (lower panel) antibody. Numbers represent homozygous transgenic lines containing a single T-DNA insertion. The black asterisks mark an unspecific band similar to the size of CYP81F2-mKate2. Coomassie Brilliant Blue (CBB) staining of the membrane served as loading control.

For identification of the T-DNA insertion site in the genome of the double transgenic line expressing *PEN2-GFP-TA_{PEN2}* and *CYP81F2-mKate2,* an inverse PCR approach was performed (Figure 16). Genomic DNA was digested using the *HindIII* restriction enzyme. *HindIII* recognition sites in the T-DNA are indicated in Figure 16A. For self-circulation of the *HindIII*-digested genomic DNA a ligation was performed and followed by amplification of the T-DNA flanking genomic region using oligonucleotides depicted in Figure 16A. After performing an agarose gel electrophoresis (Figure 16B), the PCR products were sequenced. Basic Local Alignment Search Tool (BLAST) analysis of the upper band identified only PEN2 cDNA sequence of the T-DNA. BLAST analysis of the lower band identified the genomic region of *BASIC LEUCINE-ZIPPER 48* (bZIP48; AT2G04038) on chromosome 2. Sequence alignment to the genomic region of bZIP48 confirmed the T-DNA insertion position in the promoter region of bZIP48. The T-DNA insertion was 554 bp upstream of the bZIP48 gene. Taken together, a homozygous double transgenic line expressing full-length *PEN2-GFP-TA_{PEN2}* and *CYP81F2-mKate2* was identified. An inverse PCR-approach revealed the T-DNA insertion in the promoter region of bZIP48 on chromosome 2. CLSM of GFP-tagged PEN2 and mKate2-tagged CYP81F2 showed expected localization and accumulation pattern unchallenged and 20 hpi with *Bgh*. The selected line might be used

for a CLSM-based forward genetic screen to identify novel molecular components required for PEN2-mediated disease resistance.

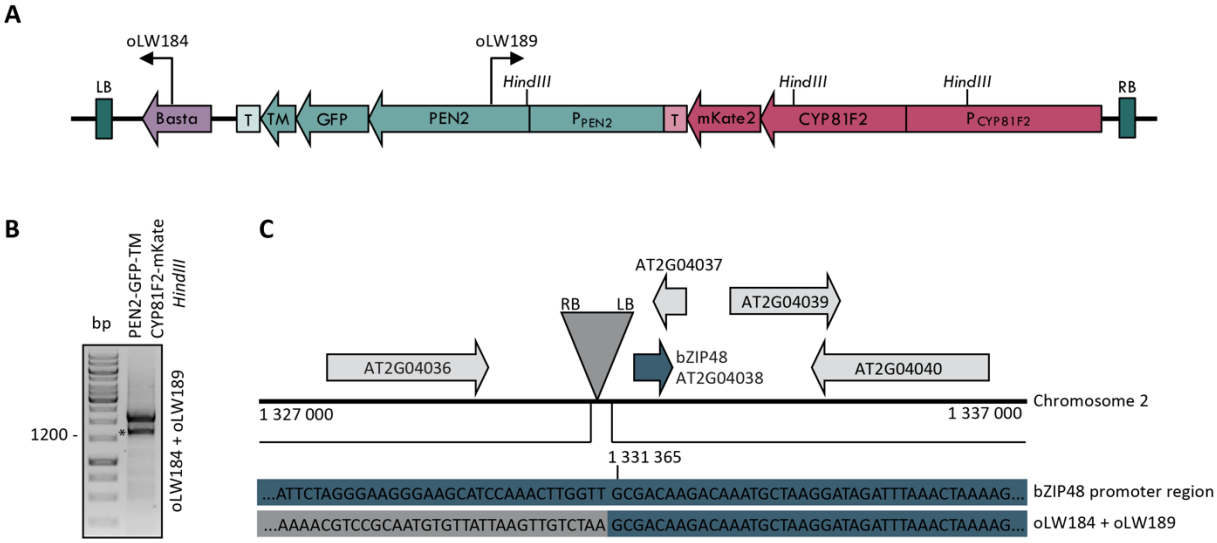

Figure 16. Identification of the T-DNA insertion site in the genome of a double transgenic line co-expressing P_{PEN2}::PEN2-GFP-TA_{PEN2} and $P_{CYP81F2}$::CYP81F2-mKate2. (A) Scheme illustrates the T-DNA of the double transgenic line. The T-DNA contains both *PEN2-GFP-TA_{PEN2}* (green) and *CYP81F2-mKate2* (red) under control of their endogenous promoters. The restriction enzyme *HindIII* used for gDNA digestion is indicated. Black arrows depict oligonucleotides oLW184 and oLW189 used for inverse PCR. LB= Left border, RB= Right border, T= Terminator (pA35S). **(B)** Agarose gel electrophoresis of PCR products generated by inverse PCR. Purified gDNA was digested with *HindIII*, followed by self-ligation and inverse PCR using the oligonucleotides indicated in (A). The PCR products were sequenced using the oligonucleotides oLW184 and oLW189. **(C)** Schematic overview of the T-DNA insertion in the promoter region of bZIP48 on chromosome 2. The PCR product indicated with an asterisk (B) was sequenced, followed by BLAST analysis and sequence alignment to the identified genomic region of bZIP48. Section of the sequence alignment shows the LB sequence of the T-DNA (grey) and the promoter region of bZIP48 (blue). The position of the T-DNA integration site is indicated as a grey triangle.

3.3 GSTU13

3.3.1 Analysis of GSTU13 subcellular localization

Recent work by Piślewska-Bednarek *et al.,* 2018 revealed that the Glutathione-S-transferase class-tau member 13 (GSTU13) is an important molecular component of the PEN2 defense pathway for IG metabolism. It is suggested that GSTU13 mediates the conjugation of the unstable I3G-ITCs with GSH indicating the involvement in the formation of I3A and RA upon PEN2 IG hydrolysis (Figure 7). Additionally, it was shown that GSTU13 is required for 4OGlcI3F biosynthesis upon pathogen attack (Piślewska-Bednarek et al., 2018). To analyze whether the contribution of GSTU13 for pre-invasive disease resistance requires a specific subcellular localization, pathogen-induced protein translocation or organelle compartmentalization, transgenic *Arabidopsis* plants were generated expressing *pGSTU13::GSTU13-RFP* or *pGSTU13::RFP-GSTU13* in the *gstu13-1* mutant background. CLSM analysis of transgenic T1 plants showed a constitutive expression of both N- and C-terminally RFP-tagged GSTU13 in unchallenged epidermal cells. GSTU13-RFP fluorescence signals were detected in the cytosol, the nucleus and punctate structures (Figure 17A and B).

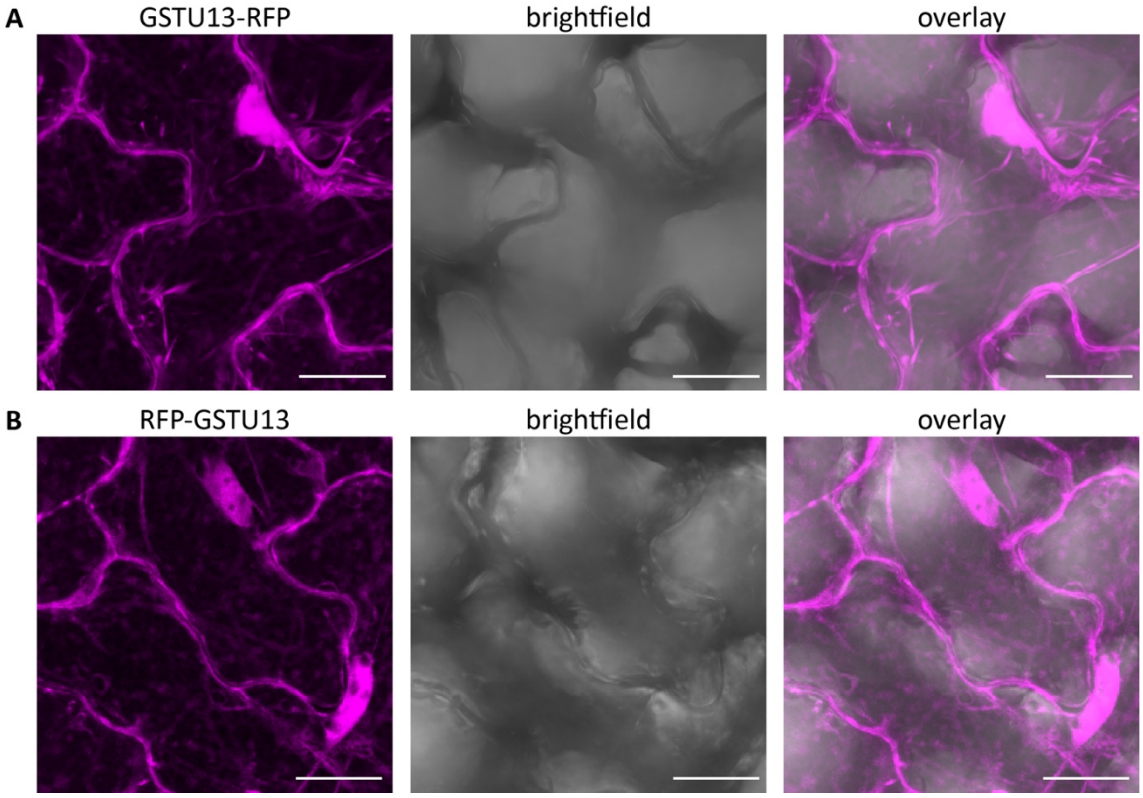

Figure 17. Subcellular localization of N- and C-terminally RFP-tagged GSTU13. CLSM images of transgenic *Arabidopsis* leaf epidermal cells expressing *GSTU13-RFP* **(A)** and *RFP-GSTU13* **(B)** under control of the endogenous promoter in the *gstu13-1* mutant background. N- and C-terminally tagged GSTU13 is shown in magenta. Images are maximum projections of 15 focal planes recorded 1 µm apart. Scale bar = 20 µm.

To evaluate the subcellular localization of GSTU13 in more detail, transgenic *Arabidopsis* plants were generated co-expressing PEN2-GFP-TA_{PEN2} and N- or C-terminally tagged GSTU13 under control of the endogenous promoter in the *pen2-1* mutant background. Unchallenged leaf epidermal cells showed no clear co-localization of GSTU13-RFP (Figure 18A) or RFP-GSTU13 (Figure 18B)-labeled punctate structures with PEN2-GFP-TA_{PEN2} positive membrane compartments. Furthermore, CLSM analysis 20 hours after *Bgh* infection revealed that GSTU13-RFP fluorescence accumulates around some, but not all of the plant-fungal interaction sites, as well as in close proximity to immobilized mitochondria that are decorated with PEN2-GFP-TA_{PEN2} aggregates (Figure 18C). Different intensity levels of GSTU13-RFP fluorescence might reflect distinct stages of attempted *Bgh* invasion, due to unsynchronized germination of *Bgh* conidiospores and cell wall penetration after inoculation. Future experiments should investigate the subcellular localization of GSTU13 in more detail. GSTU13-RFP and RFP-GSTU13 seemed to complement the reduced amounts of I3A in the *gstu13-1* mutant upon flg22-treatment, indicating that both fusion proteins are functional (Pawel Bednarek, personal communication, data not shown).

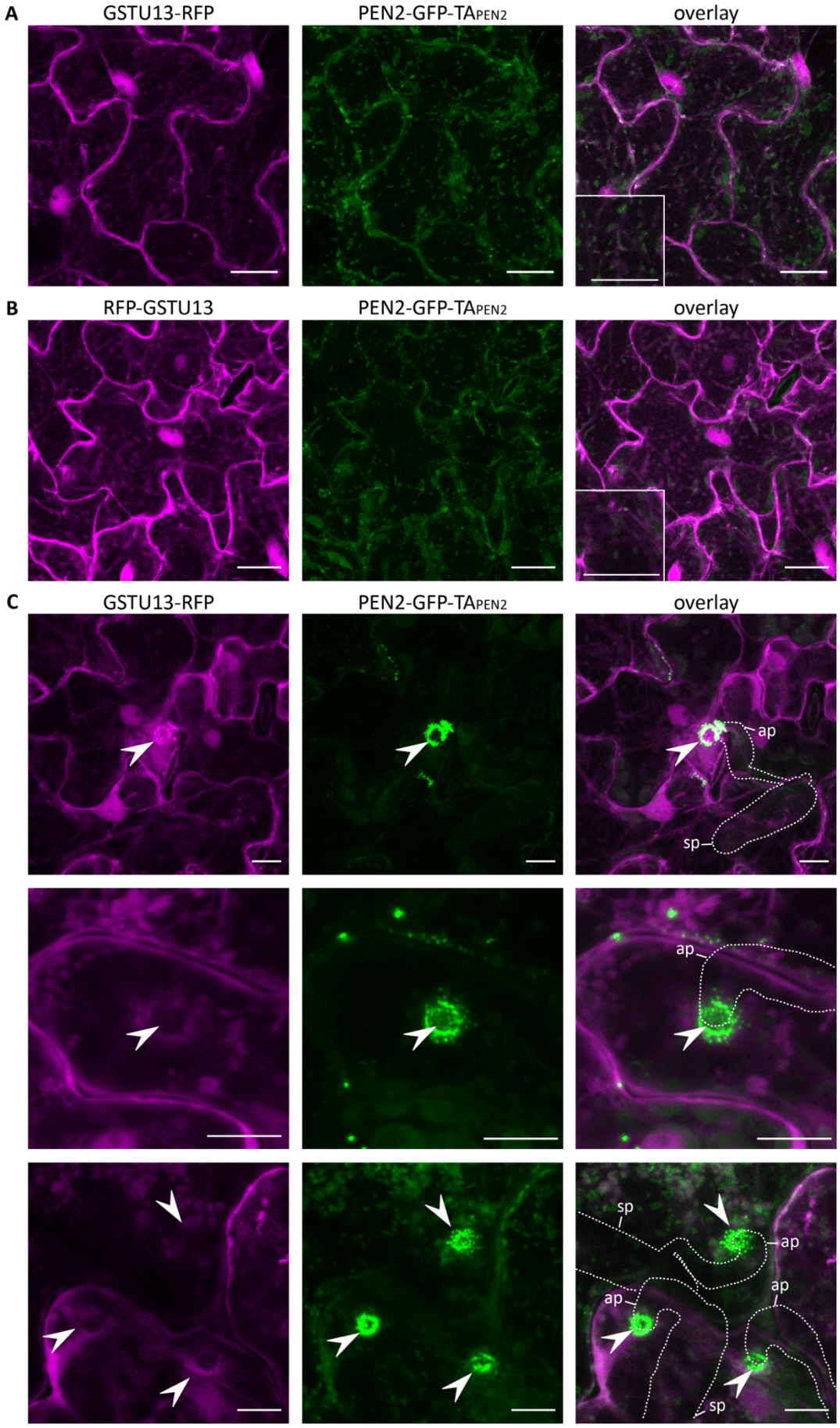
A
GSTU13-RFP
PEN2-GFP-TAPEN2
overlay
B
RFP-GSTU13
PEN2-GFP-TAPEN2
overlay
C
GSTU13-RFP
PEN2-GFP-TAPEN2
overlay
ap
sp
ap
sp
ap
ap
ap
sp

Figure 18. GSTU13-RFP and RFP-GSTU13 do not co-localize with PEN2-GFP-TA$_{PEN2}$. (A and B) Unchallenged *Arabidopsis* leaf epidermal cells stably co-expressing *PEN2-GFP-TA$_{PEN2}$* and *GSTU13-mRFP* **(A)** or *PEN2-GFP-TA$_{PEN2}$* and *RFP-GSTU13* **(B)** under control of the native promoter in the *pen2-1* background were analyzed by CLSM. Both N- and C-terminally RFP-tagged GSTU13 do not overlap with PEN2-GFP-TA$_{PEN2}$ membrane compartments. Inset: Zoomed section of the image. Scale bar = 20 µm. **(C)** CLSM images of *Arabidopsis* leaf epidermal cells expressing both PEN2-GFP-TA$_{PEN2}$ and GSTU13-RFP in the *pen2-1* mutant background 20 hpi with *Bgh*. Arrowheads point towards the site of attempted fungal penetration. The fungal spore (sp) and the appressorium (ap) are outlined by dashed lines. PEN2-GFP-TA$_{PEN2}$ is shown in green and co-expressed GSTU13-RFP/RFP-GSTU13 in magenta. Images are maximum projections of 10-13 focal planes recorded 1 µm apart. Scale bar = 10 µm.

3.4 Analysis of the PEN2 co-expressed genes *Early Response to Dehydration 6* (*ERD6*) and the *S-adenosyl-L-methionine-dependent methyltransferase* (*AT1G55450*)

One aim of this work was the identification and characterization of further important molecular components required for PEN2-mediated entry control against non-adapted powdery mildew. Humphrey *et al*., 2010 showed that defense components involved in powdery mildew penetration resistance are co-regulated in both the dicot *Arabidopsis* and the monocot barley (*Hordeum vulgare*). In *Arabidopsis*, *PEN2* is co-expressed with the ABC-transporter *PEN3* and *MLO2*, one of the seven-transmembrane domain containing proteins involved in plant immunity against powdery mildew disease. However*, PEN1*, *VAMP722* and *SNAP33* were not as highly co-expressed with *PEN2* (Humphry et al., 2010) confirming the results that PEN1 and PEN2 act in two genetically independent pathogen penetration control mechanism (Lipka et al., 2005; Stein et al., 2006). Additionally, these molecular defense components share a similar set of co-expressed genes in dicots and monocots. In total, 164 genes were identified to be co-expressed with PEN2 and PEN3 in *Arabidopsis* (Humphry et al., 2010). Two of these genes, *AT1G08930* (*Early response to dehydration* 6 (*ERD6*)) and AT1G55450 (*S-adenosyl-L-methionine-dependent methyltransferase*) were selected for further analysis.

3.4.1 ERD6

3.4.1.1 Isolation and characterization of *erd6* T-DNA insertion lines

ERD6 is co-expressed with *PEN2* and *PEN3* in *Arabidopsis* (Humphry et al., 2010). Analysis of *erd6* mutants revealed enhanced susceptibility to different pathogens in comparison to the wild-type. Moreover, increased sporulation and of *G. orontii* was observed on leaves of *erd6* mutants 10 days post infection (dpi) (Humphry et al., 2010). Metabolomics analysis revealed reduced levels of I3A and RA in *erd6* T-DNA insertion mutants similar to the *pen2-2* mutant phenotype 16 hours after inoculation with *E. pisi*. Additionally, in comparison to *pen2-2* and the wild type, the amount of the PEN2 substrate I3G was significantly increased whereas 4MI3G levels were not significantly different after pathogen attack, suggesting a putative involvement of ERD6 in the transport of the PEN2 substrate I3G (Humphry et al., 2010). Previous studies indicated that GLS are transported from the vasculature, the site of biosynthesis, to the epidermis (Li et al., 2011; Madsen et al., 2014; Nintemann et al., 2018). In leaves, cell to cell distribution of GLS is suggested to occur via the intracellular symplastic pathway by diffusion through PD (Andersen et al., 2013; Madsen et al., 2014, 2014; Xu et al., 2017; Hunziker et al., 2019). For the storage of GLS in epidermal leaf cells, GLS are assumed to be transported from the cytosol into the vacuole by an unknown vacuolar importer (Madsen et al., 2014). Based on these previous findings, one hypothesis is that the preformed and vacuolar stored PEN2 substrate I3G is transported into the cytoplasm by a vacuolar GLS exporter, to facilitate the accessi-

bility of the substrate to PEN2. To analyze the involvement of ERD6 as a putative vacuolar GSL exporter in cell-autonomous remobilization of intracellularly stored I3G in plant-microbe interactions, at first, two independent T-DNA insertion lines, *erd6-1* (*SALK137614;* Humphry *et al.,* 2010) and *erd6-3* (*SALK025395*, this study) were obtained from NASC. PCR-based genotyping revealed a T-DNA insertion in the 9th exon in *erd6-1* as well as in the 6th intron in *erd6-3* (Figure 19A). The T-DNA insertion in *erd6-1* disrupts *ERD6* in the region encoding the predicted major facilitator sugar transporter-like domain and the T-DNA insertion in *erd6-3* disrupts the gen in the region encoding the 5th transmembrane domain (Figure 19B). Homozygous *erd6-1* and *erd6-3* lines were isolated and analyzed for disruption of the functional transcript using a semi-quantitative RT-PCR approach (Figure 19C). No transcript of *ERD6* was detected in *erd6-1* and *erd6-3* utilizing the T-DNA spanning oligonucleotides oLW132/oLW133 and oLW128/oLW129, respectively. However, oligonucleotides binding downstream of the T-DNA insertion (oLW134/oLW135 and oLW131/oLW132) detected a reduced amount of *ERD6* transcript levels in both T-DNA mutant lines. Transcript detection with downstream T-DNA oligonucleotides often results from a promoter in the construct next to the left border of the inserted T-DNA (Ülker et al., 2008).

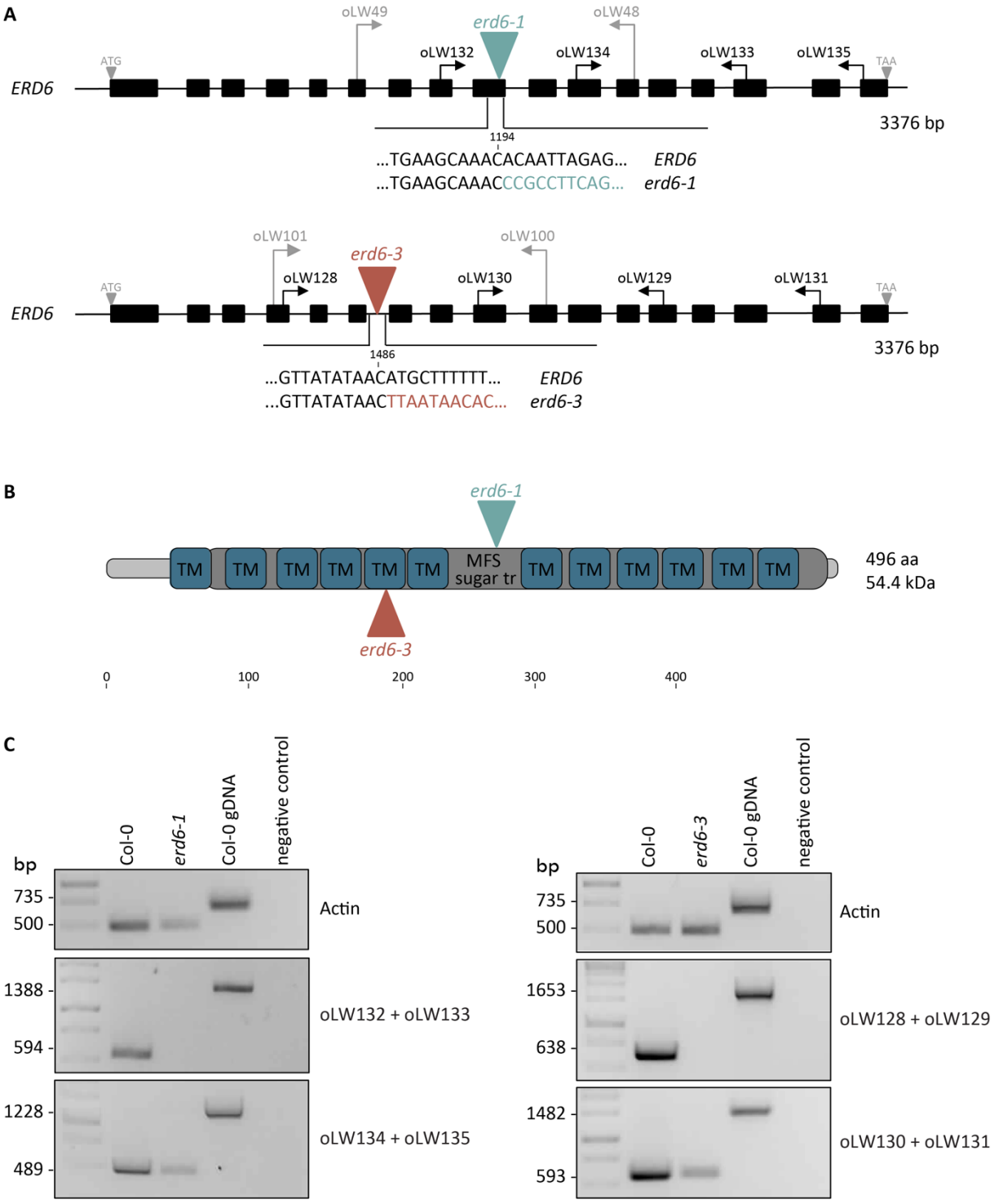

Figure 19. Characterization of *erd6* T-DNA insertion mutants. (A) Schematic gene structure of *ERD6.* Black boxes illustrate exons and solid lines represent introns, start (ATG) and stop codons (TAA) are depicted by light grey triangles. The T-DNA insertion position in mutant lines is indicated as light green triangle (*erd6-1*; *SALK137614*) and red triangle (*erd6-3; SALK025395*) in (A) and (B). The site of T-DNA insertion was confirmed by sequencing. Grey arrows represent the position and orientation of oligonucleotides used for PCR-based genotyping and black arrows depict oligonucleotides used for semi-quantitative reverse transcription PCR (C). LB= left border T-DNA primer; bp= base pairs. **(B)** Schematic illustration of the predicted protein domain organization of ERD6. Protein features and -domains were predicted using the TMHMM Server 2.0 (http://www.cbs.dtu.dk/services/TMHMM/, Krogh et al., 2001) and the TAIR integrated INTERPROSCAN and MyHits (http://myhits.isb-sib.ch, Pagni et al., 2004), respectively. The predicted Major facilitator sugar transporter-like domain (IPR005828) is illustrated in dark grey and contains 12 predicted transmembrane domains

(TM) that are indicated by blue squares. **(C)** Semi-quantitative reverse transcription PCR of wild type Col-0, *erd6-1* and *erd6-3*. RNA was extracted from pools of ten plants per line of 4-week-old plants. PCR product sizes are indicated on the left and oligonucleotides used for PCR analysis are depicted on the right. bp= base pairs.

Next, *erd6-1* and *erd6-3* mutant plants were challenged with conidiospores of the non-adapted powdery mildew *Bgh* and *E. pisi* and the adapted powdery mildew *G. orontii*. Wild-type Col-0 and *pen2-2* plants were included as controls. The formation of papillae, haustoria, cell death in epidermal cells and hyphae was counted 72 hpi. Both mutant lines showed wild-type-like penetration phenotypes after *Bgh* and *G. orontii* infection (Figure 20A and C). However, *erd6-1* and *erd6-3* transporter mutants showed elevated invasive growth rates of the non-adapted powdery mildew *E. pisi,* similar to the *pen2-2* mutant (Figure 20B). In comparison to the wild type Col-0, a significantly reduced number of papillae and a significantly higher number of hyphae formation were observed for *erd6* plants similar to *pen2-2*. These results confirm a contribution of ERD6 to the penetration resistance against *E. pisi* at 72 hpi. However, ERD6 is not required for defense against *Bgh* and *G. orontii* at 72 hpi.

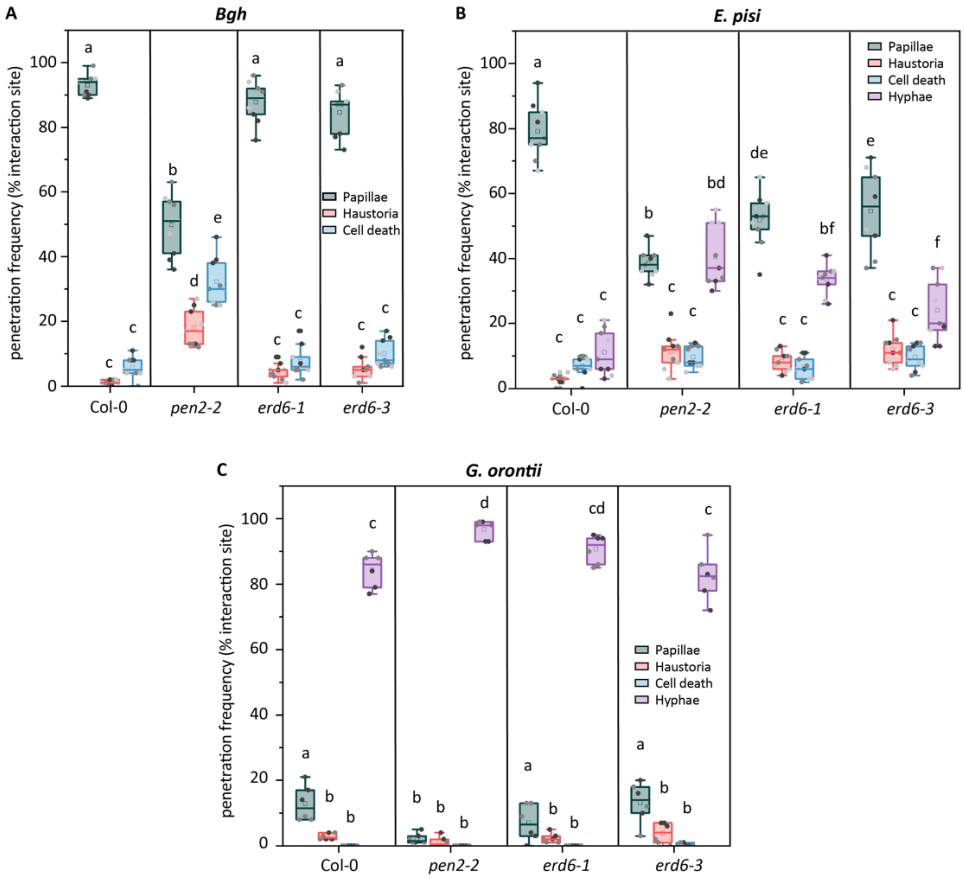

Figure 20. ERD6 is required for nonhost penetration resistance against *E. pisi*. Boxplots represent frequencies of papillae formation, haustorium formation, single-cell death and growth of hyphae at *Bgh* **(A)** *E. pisi* **(B)** and *G. orontii* **(C)** interaction sites on 4-week-old *Arabidopsis* Col-0, *pen2-2*, *erd6-1* and *erd6-3* at 72 hpi. Boxplots contain data from three (A) and (B) or two (C) independent biological replicates. For each replicate, 100 interaction sites of three individual plants per genotype were analyzed. Individual boxplots include whiskers (values within the 1.5-fold interquartile range), first and third quartile (lower and upper box limits) and median (middle

horizontal line). The mean value is depicted by a square and data points of different experiments are indicated as gray scale. Letters show significant differences between genotypes (two-way ANOVA (P<0.0001 (A) and (C); P<0.001 (B)); Tukey post-hoc test).

3.4.1.2 Analysis of the subcellular behavior of ERD6

3.4.1.2.1 ERD6 is localized to MVBs and the lumen of the vacuole

To identify the subcellular localization of ERD6, transgenic *Arabidopsis* plants expressing *pERD6::ERD6-mTurquoise2* in the *erd6-1* mutant background were generated. CLSM revealed *ERD6-mTurquoise2* expression in punctate structures and potentially in the lumen of the vacuole in unchallenged epidermal cells (Figure 21).

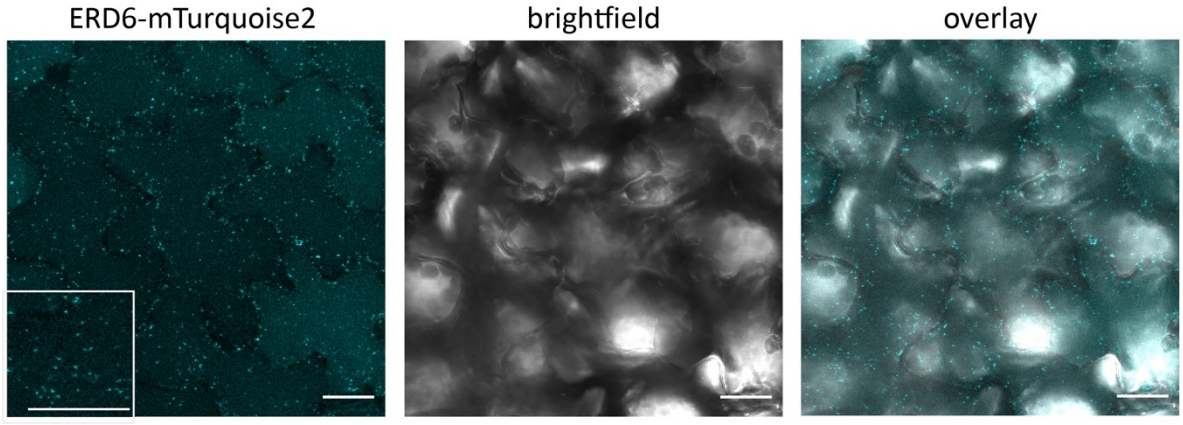

Figure 21. Subcellular localization of ERD6-mTurquoise2. *Arabidopsis* leaf epidermal cells stably expressing *ERD6-mTurquoise2* under control of the native promoter in the *erd6-1* background were analyzed by CLSM. Images are representative maximum projections with a size of 14 µm recorded 1 µm apart. ERD6-mTurquoise2 is shown in cyan. Inset: Zoomed section of the image. Scale bar = 20 µm.

To test whether the ERD6-mTurquoise2 fusion protein is functional, two independent transgenic lines expressing *ERD6-mTurquoise2* under the endogenous promoter were analyzed for penetration resistance against *E. pisi* (Figure 22A). Both independent transgenic lines showed full restoration of resistance to *E. pisi* at 72 hpi. Epidermal cells of both the transgenic lines and wild-type Col-0 plants comprised no significant differences in the formation of papillae, haustoria, cell death and hyphae. *erd6-1* and *pen2-2* mutant plants exhibited a reduced number of papillae and a significantly higher number of hyphae formation, in comparison to ERD6-mTurquoise2 transgenic lines and Col-0. These results indicate that ERD6-mTurquoise2 fully complements the deficient pathogen entry defense phenotype of the *erd6-1* mutant. Additionally, the macroscopic phenotype of *ERD6-mTurquoise2* expressing plants and the controls Col-0, *pen2-2* and *erd6-1* was evaluated with the adapted powdery mildew *G. orontii* at 20 dpi. Increased fungal growth was observed on *pen2-2* and *erd6-1* mutant plants, whereas growth of *G. orontii* on *erd6-1* was not as strong as observed on *pen2-2*. The results suggest a potential role of ERD6 in resistance during later time points of *G. orontii* infection. Fur-

thermore, *ERD6-mTurquoise2* expressing plants showed a sporulation phenotype comparable to wild-type Col-0, indicating complementation of the enhanced *G. orontii* sporulation phenotype of *erd6-1*.

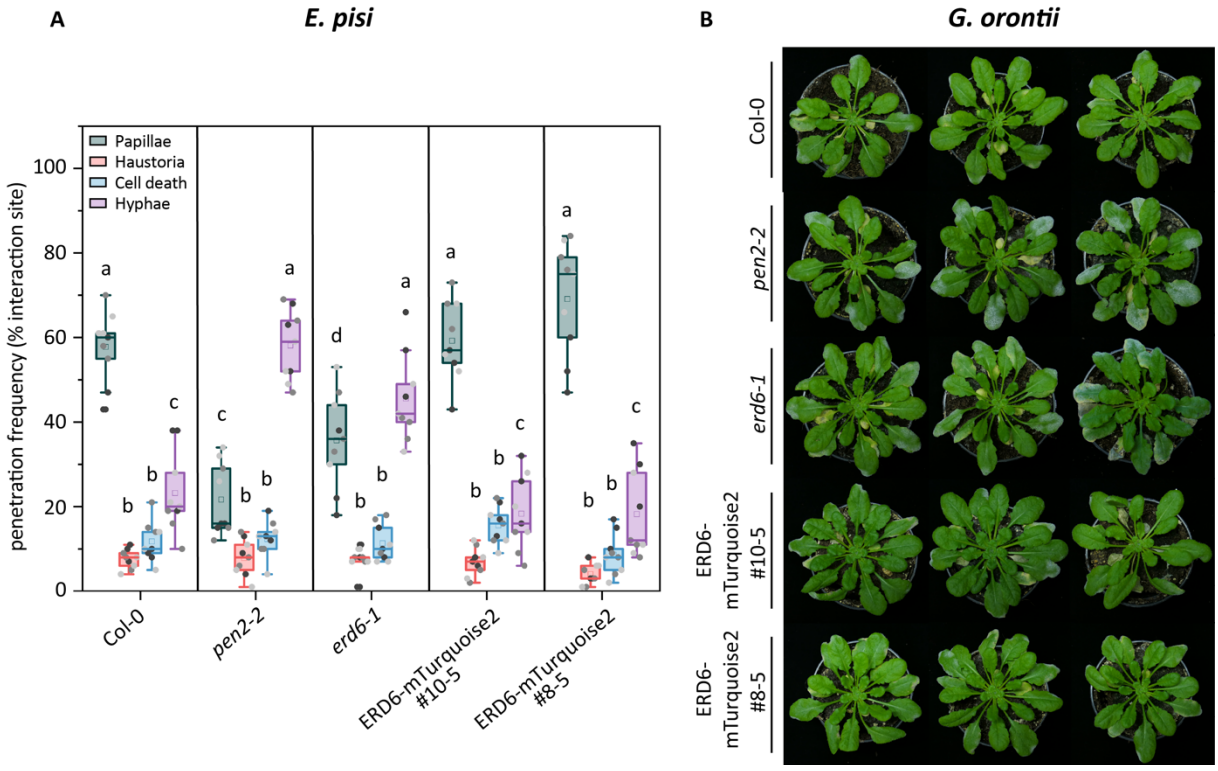

Figure 22. ERD6-mTurquoise2 complements the deficient pathogen entry control phenotype of *erd6*. (A) Boxplots represent frequencies of papillae formation, haustorium formation, single-cell death and growth of hyphae at *E. pisi* interactions sites on 4-week-old *Arabidopsis* Col-0, *pen2-2*, *erd6-1* and two independent lines expressing *ERD6-mTurquoise2* in the *erd6-1* background at 72 hpi. Boxplots contain data of three independent biological replicates. For each replicate, 100 interaction sites of three individual plants per genotype were analyzed. Individual boxplots include whiskers (values within the 1.5-fold interquartile range), first and third quartile (lower and upper box limits) and median (middle horizontal line). The mean value is depicted by a square and data points of different experiments are indicated as gray scale. Letters show significant differences between genotypes (two-way ANOVA (P<0.01); Tukey post-hoc test). **(B)** Phenotypes of *G. orontii* infected 7-week-old *Arabidopsis* Col-0, *pen2-2*, *erd6-1*, ERD6-mTurquoise2 #10-5 and ERD6-mTurquoise2 #8-5 plants 20 days after inoculation. Three representative images of one experiment per genotype are shown.

Stable expression of ERD6-mTurquoise2 restored penetration resistance to *E. pisi* at 72 hpi and enhanced sporulation of *G. orontii* during late infection. Therefore, *ERD6-mTurquoise2* expressing *erd6-1* plants were further characterized by immunoblot analysis (Figure 23). First, 4 independent *ERD6-mTurquoise2* expressing plants in the T1 generation and the controls Col-0 and *erd6-1* were evaluated unchallenged or 20 hpi with *Bgh* or *E. pisi*. Total proteins were extracted using a buffer containing Triton X-100. SDS-PAGE followed by immunoblotting using the α-GFP antibody, recognizing GFP-derivates such as mTurquoise2, revealed ERD6-mTurquoise2 runs differently on SDS-PAGE than its expected molecular weight (Figure 24A). ERD6-mTurquoise2 fusion proteins were expected to display

a molecular mass of approximately 81 kDa. However, a weak ERD6-mTurquoise2 specific band of approximately 60 kDa was identified. The reduced apparent mass might result from alternative splicing of the ERD6 mRNA or cleavage of the ERD6 protein. Furthermore, a high amount of mTurquoise2 cleavage products with a molecular size of 26,9 kDa were identified, suggesting ERD6-mTurquoise2 degradation and proteolysis. No differences in ERD6-mTurquoise2 protein amount or apparent mass were observed after pathogen inoculation (Figure 23A). Next, microsomal protein extraction of ERD6-mTurquoise2 expressing plants in the T2 generation was performed (Figure 23B). The microsomal and soluble protein fraction was used for immunoblot analysis. ERD6-mTurquoise2 was highly enriched in the microsomal fraction in comparison to the soluble protein fraction. A clear signal of the approximately 60 kDa ERD6-mTurquoise2 band was observed. Additionally, western blot analysis of the microsomal fraction revealed bands of a high molecular weight, suggesting ERD6-mTurquoise2 large complex or aggregate formation.

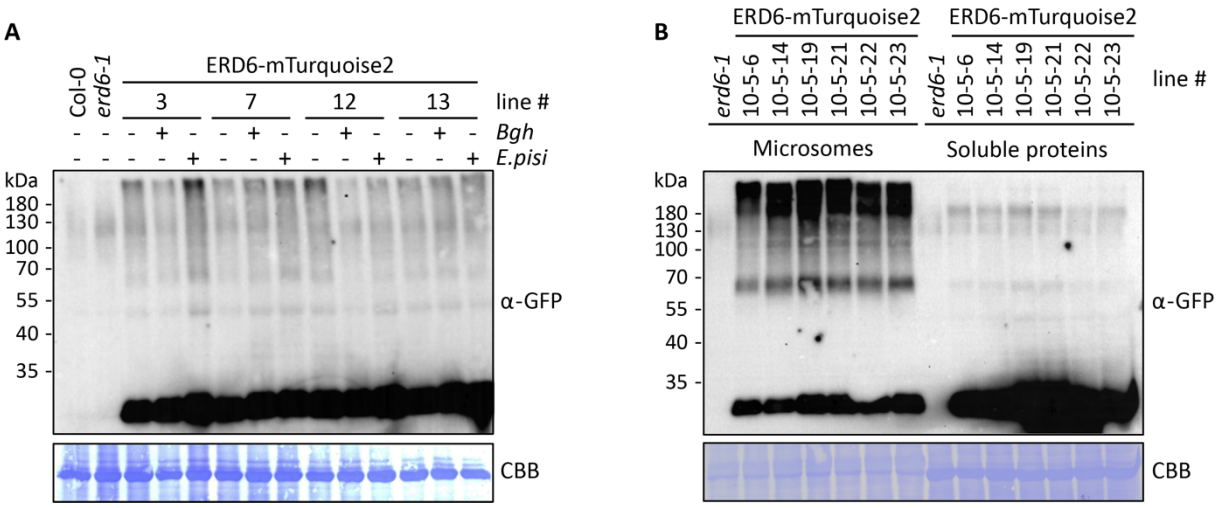

Figure 23. ERD6-mTurquoise2 runs differently on SDS-PAGE than its expected molecular weight. (A) Western blot of total protein extracts derived from unchallenged, *Bgh* or *E. pisi* inoculated 6-week-old *erd6-1* plants stably expressing *ERD6-mTurquoise2* under control of the native promoter. A detached leaf assay of the T1 generation was performed and leaves were harvested 20 hpi. Numbers are representing four independent lines. Col-0 and *erd6-1* were included as controls. Western blot was probed using α-GFP antibody. Coomassie Brilliant Blue (CBB) staining of the PVDF membrane (lower panel) served as loading control. **(B)** Microsomes and soluble proteins were extracted from unchallenged *erd6-1* plants stably expressing *ERD6-mTurquoise2* under the endogenous promoter, analyzed by 10% SDS-PAGE and Western blotting using α-GFP antibody. *erd6-1* was included as negative control. Numbers indicate transgenic lines of the T2 generation containing a single T-DNA insertion. Coomassie Brilliant Blue (CBB) staining of the membrane served as loading control.

To analyze the potential role of ERD6 glucosinolate transport in defense against non-adapted powdery mildews in more detail, double transgenic *Arabidopsis* plants co-expressing *pERD6::ERD6-mTurquoise2* and *pPEN2::PEN2-GFP-TA$_{PEN2}$* in the *pen2-1* mutant background were generated and analyzed by CLSM. No co-localization of ERD6-mTurquoise2 associated punctate structures with PEN2-GFP-TA$_{PEN2}$ positive organelles were observed in leaf epidermal cells unchallenged (Figure 24A)

and 20 hpi with *E. pisi* (Figure 24B). However, examination of plant-microbe interaction sites at 20 hpi with *E. pisi* revealed that some, but not all fungal penetration sites are surrounded by ERD6-mTurquoise2 associated punctate structures in proximity to subpopulations of clustered and arrested mitochondria with peripheral PEN2-GFP-TA_{PEN2} aggregates (Figure24B). Similar results were obtained after inoculation with *Bgh* (data not shown). Differences in ERD6 accumulation might reflect distinct stages of attempted *Bgh*/*E. pisi* invasion, due to unsynchronized germination of *Bgh* conidiospores and cell wall penetration after inoculation. To analyze the subcellular behavior of ERD6-mTurquoise2 associated vesicular structures in more detail, time-lapse CLSM analysis 20 hpi with *E. pisi* was performed (Figure 24C). This analysis revealed that accumulation of ERD6-mTurquoise2 positive vesicles in proximity to the attempted fungal invasion site was only transient.

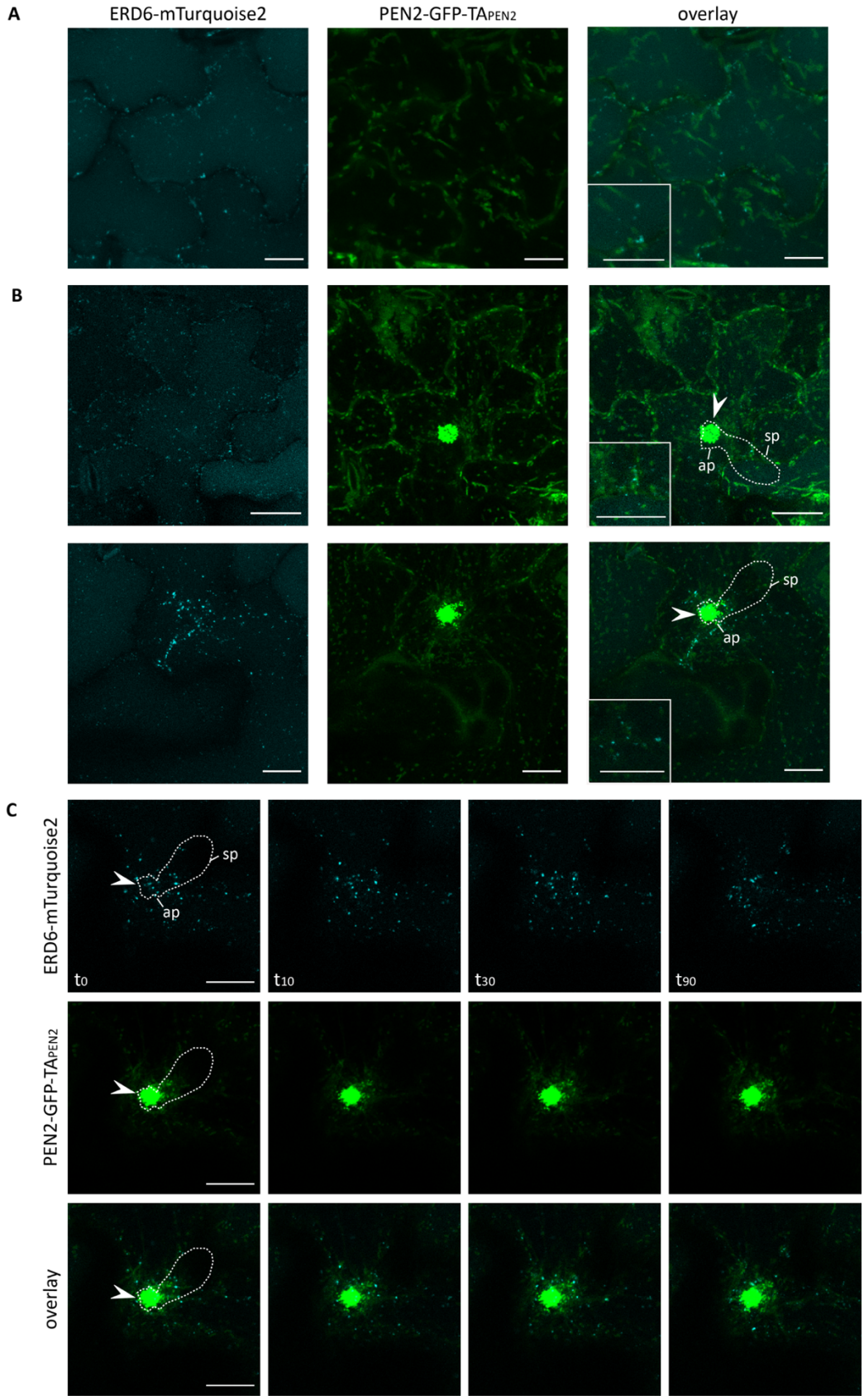

Figure 24. ERD6-mTurquoise2 associated vesicles do not colocalize with PEN2-GFP-TA$_{PEN2}$ positive membrane compartments. CLSM images of transgenic leaf epidermal cells co-expressing *PEN2-GFP-TA$_{PEN2}$* and *ERD6-mTurquoise2* in the *pen2-1* mutant background unchallenged **(A)** and 20 hpi with *E. pisi* **(B)**. Images are representative maximum projections of 9-13 focal planes recorded 1 µm apart. Inset: Zoomed section of the image.

(C) Single plane CLSM time-lapse imaging of epidermal cells expressing both PEN2-GFP-TA_{PEN2} and ERD6-mTurquoise2 at 20 hpi with *E. pisi*. A zoomed section of the plant-pathogen interaction site of the lower image from (B) is shown. Arrowheads point towards the site of attempted fungal penetration. t= time (s) with t_0= 20 hpi. PEN2-GFP-TA_{PEN2} is shown in green and ERD6-mTurquoise2 in cyan. The fungal spore (sp) and the appressorium (ap) are outlined by dashed lines. Scale bar = 20 µm.

To identify the subcellular structures ERD6-mTurquoise2 is associated with, CLSM analysis was performed on, *pERD6::ERD6-mTurquoise2* expressing plants crossed with lines expressing either markers for the Golgi (*pUBQ10::MEMB12-mCherry;* Geldner *et al*., 2009), early endosomes (*pUBQ10::RabA1g-mCherry or pUBQ10::RabA5d-mCherry;* Geldner *et al*., 2009) or multivesicular bodies/ late endosomes (*pUBQ10::Rha1-mCherry;* Geldner *et al*., 2009). Marker lines of the endosomal trafficking pathway were obtained from NASC. CLSM analysis demonstrated no association of ERD6-mTurquoise2 with the Golgi (Figure 125A) and recycling endosomes (Figure 25C and D). However, ERD6-mTurqouse2 showed an overlapping signal with the Rha1-mCherry marker (Figure 25B) indicating ERD6-mTurquoise2 localization to LE/MVB.

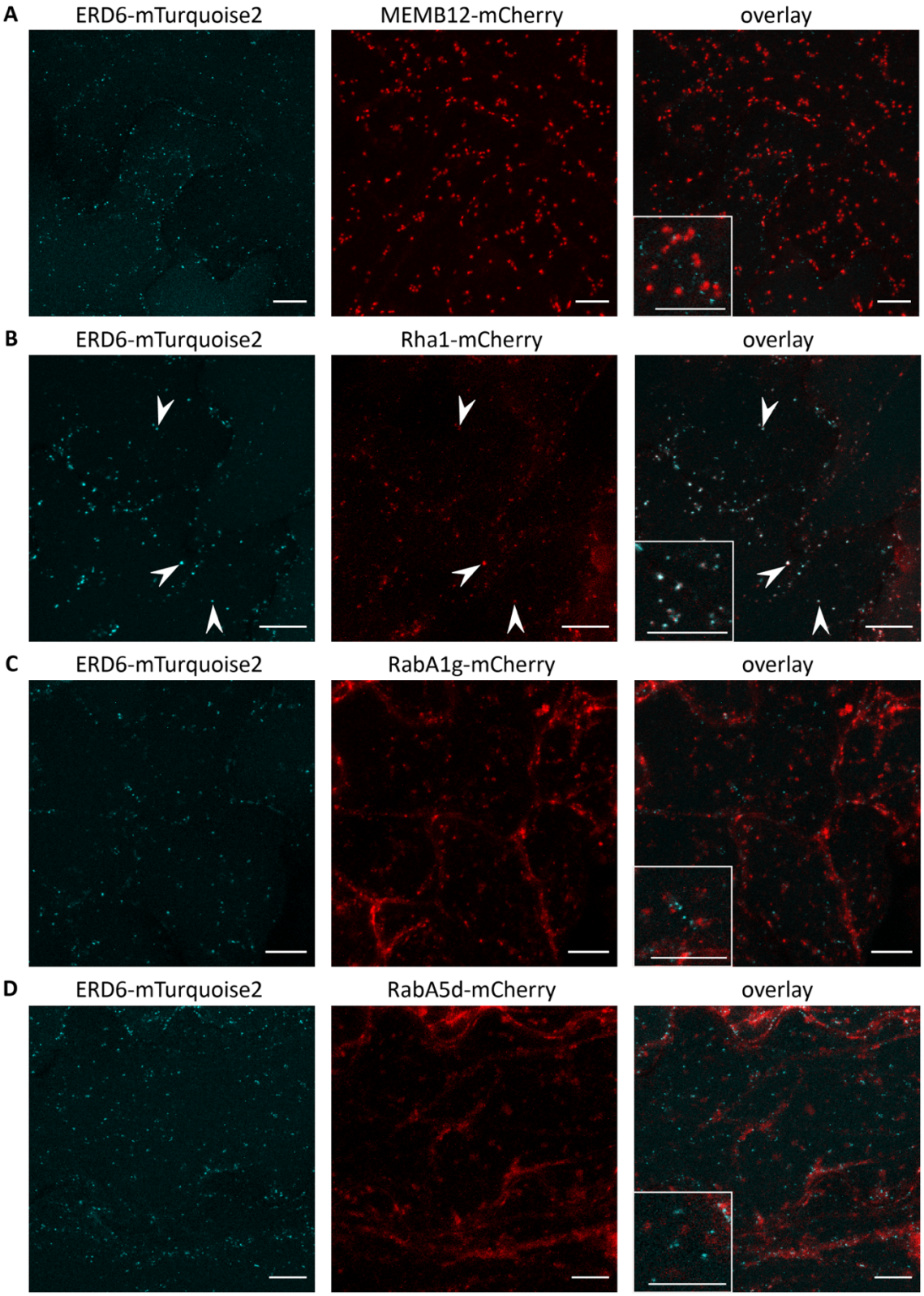

Figure 25. ERD6-mTurquoise2 co-localizes with the LE/MVB marker Rha1-mCherry. CLSM images of *Arabidopsis* leaf epidermal cells co-expressing ERD6-mTurquoise2 with the Golgi marker MEMB12-mCherry **(A)**, the LE/MVB marker Rha1-mCherry **(B)**, and the recycling endosomal markers RabA1g-mCherry **(C)** and RabA5d-mCherry **(D)**. Arrowheads point towards overlapping ERD6-mTurquoise2- and Rha1-mCherry-labelled endosomes (B). ERD6-mTurquoise2 is shown in cyan and co-expressed mCherry fusion proteins in red. Inset: Zoomed section of the image. Images are maximum projections of 13 focal planes recorded 1 µm apart. Scale bar = 10 µm.

To analyze ERD6-mTurquoise2 positive vesicles in more detail, endomembrane trafficking inhibitors (2.1.10) were applied for the investigation of vesicle trafficking pathways and mechanisms. Detached leaves of 4-week-old *pERD6::ERD6-mTurquoise2* expressing plants in the *erd6-1* mutant background were infiltrated either with or without chitin in the respective inhibitor solution. The samples were examined in regard to endosome formation 1 hour after infiltration by CLSM. Furthermore, CLSM images for the quantification of ERD6-mTurquoise2 vesicle abundance were generated. First, the control samples untreated and samples with or without chitin/DMSO were evaluated. Surprisingly, the number of ERD6-mTurquoise2 associated vesicles was highly reduced after infiltration with water, water with DMSO, chitin and chitin with DMSO in comparison to the untreated control (Figure 26AI, II, III and BI, II, III; Figure 27). In the following step, the inhibitors of endosomal trafficking ConcanamycinA (ConcA) and Wortmannin (Wm) and the proteasome inhibitor Carbobenzoxy-Leu-Leu-leucinal (MG132), blocking proteasomal protein degradation, were applied. ConcA is an inhibitor of vacuolar V-ATPases (H^+-ATPases) which disables trafficking at the TGN, transport of proteins to LEs/MVBs and to the vacuole resulting in accumulation of endosomes in the cell (Huss et al., 2002; Dettmer et al., 2006; Robinson et al., 2008; Irani and Russinova, 2009). In comparison to water (Figure26AI, AII and 27) and chitin-treated controls (Figure 26BI,BII and 27), infiltration of ConcA significantly increased ERD6-mTurquoise2-tagged vesicle abundance (Figure 26AIV,BIV and 27).

Wm inhibits phosphatidylinositol 3-kinases affecting vacuolar trafficking, MVBs and endocytosis. The pharmaceutical compound specifically interferes with the formation of internal vesicles in MVBs leading MVBs to cluster and enlarge via homo- and heterotypic fusions with post-Golgi TGN vesicles (Wang et al., 2009; Takáč et al., 2012). CLSM of leaves, co-treated with either water or chitin and Wm, revealed ERD6-mTurquoise2 associated vesicles of larger size potentially representing enlarged and clustered MVBs (Figure 26AV and BV). However, ERD6-mTurquoise2-tagged vesicle abundance in Wm infiltrated samples was not significantly different from water and chitin-treated control samples (Figure 27).

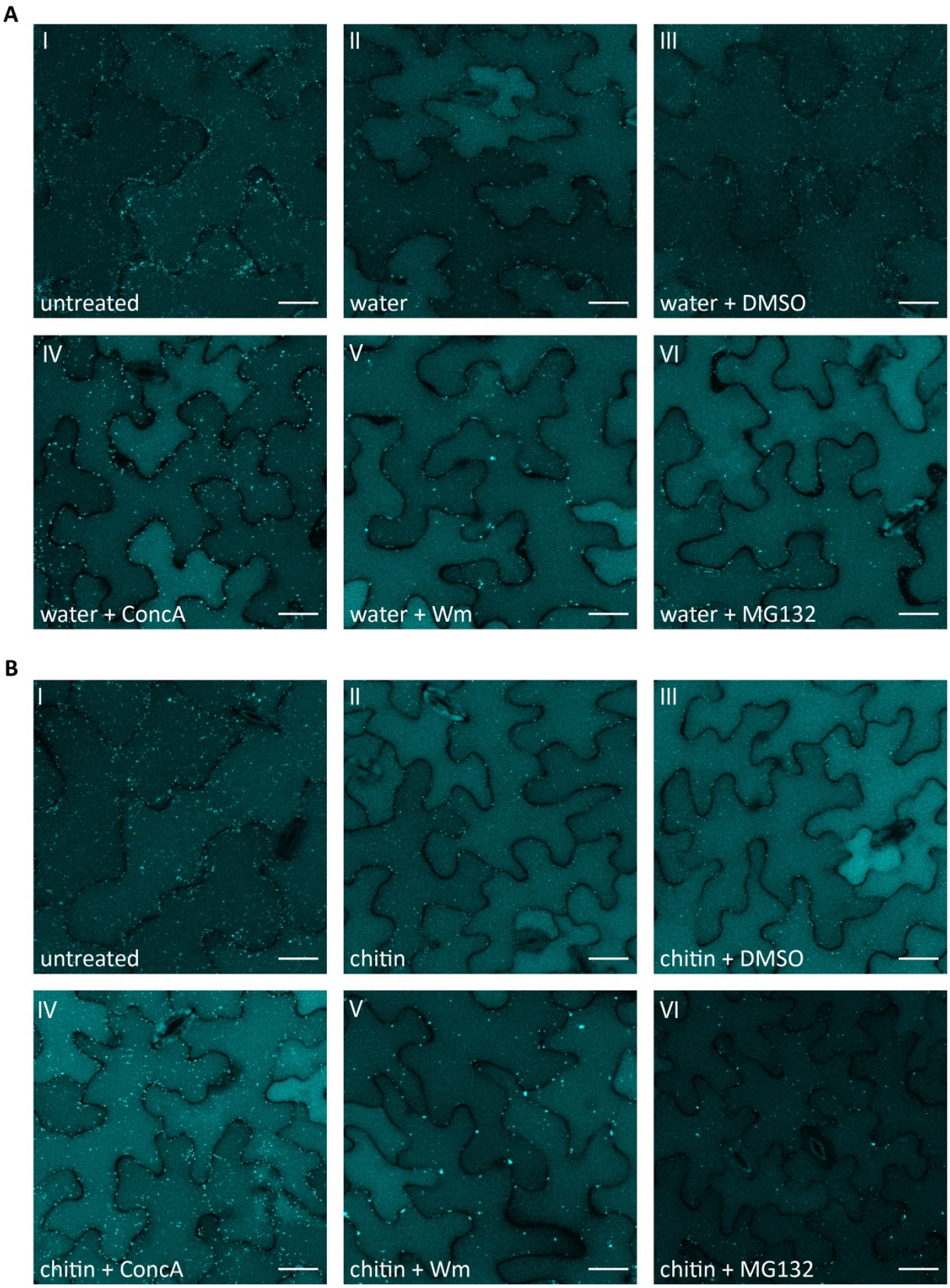

Figure 26. Effects of endomembrane trafficking pathway- and proteasome inhibitors on ERD6-mTurquoise2. 4-week-old *Arabidopsis* plants expressing *ERD6-mTurquoise*2 were infiltrated with either water and the indicated inhibitor (ConcA (1 µM), Wm (30 µM) and MG132 (50 µM)) **(A)** or chitin and the indicated inhibitor **(B)**. The inhibitor solvent DMSO was used as control. Leaf epidermal cells were analyzed 1 hour post infiltration by

CLSM. Images are maximum projections of 13 focal planes taken 1 µm apart. ERD6-mTurquoise2 fluorescence is depicted in cyan. Scale bar = 20 µm.

Additionally, the influence of MG132 on ERD6-mTurquoise2 vesicle trafficking was analyzed by CLSM. ERD6-mTurquoise2 positive vesicles were quantified. The proteosome inhibitor MG132 had no effect on ERD6-mTurquoise2-tagged vesicles (Figure 26AVI and BVI; Figure 27). Furthermore, CLSM analysis revealed differences in the signal intensities of ERD6-mTurquoise2 in the lumen of the vacuole (Figure 26). Leaf samples (Figure 26AIV, -V, -VI and BII, -III, -IV, -V) displayed enhanced fluorescence intensities of mTurquoise2-tagged ERD6 in comparison to leaves untreated (Figure 26AI, BI), with or without DMSO (Figure 26 AII, II) and co-treated with chitin and MG132 (Figure 26VI).

Taken together, these results suggest that ERD6-mTurquoise2 is constitutively transported via LEs/MVBs to the vacuole and potentially deposited for degradation in the vacuole.

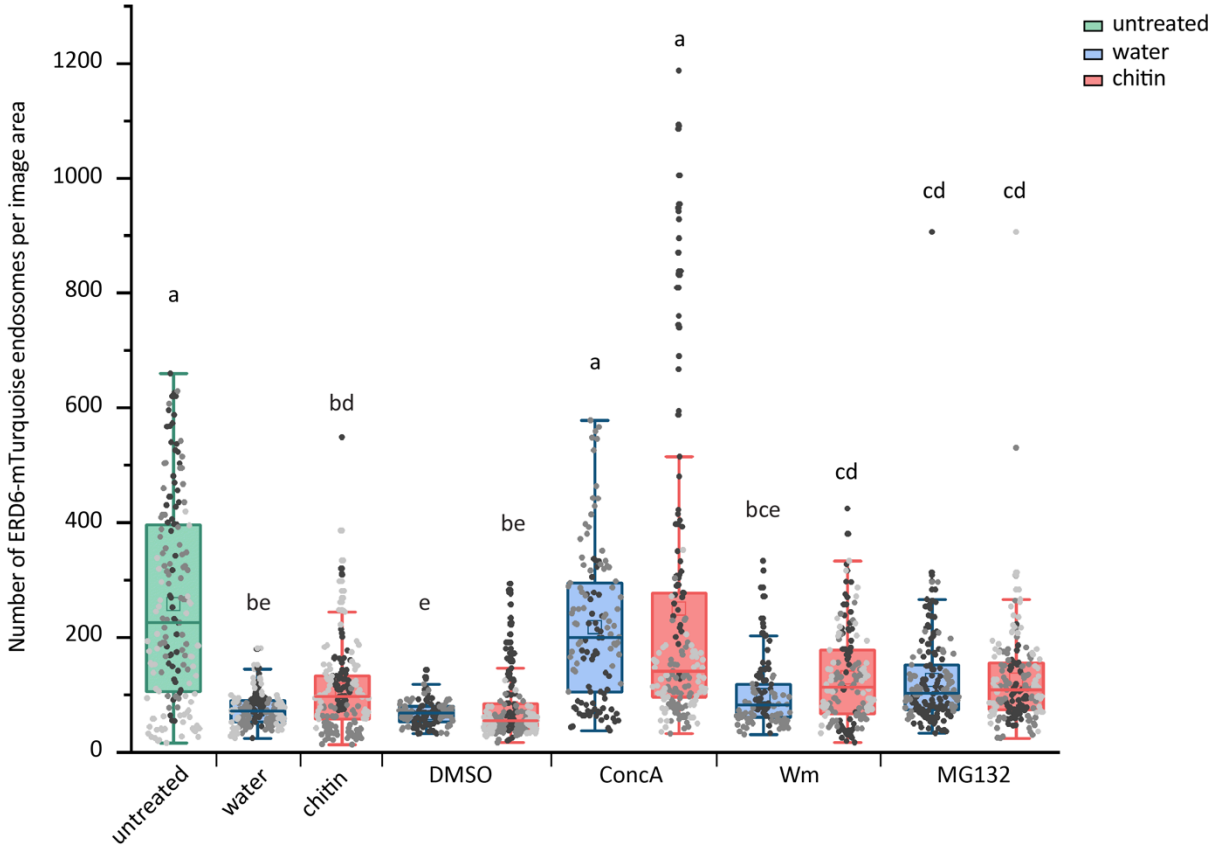

Figure 27. Endomembrane trafficking inhibitors affect ERD6-mTurquoise2 positive endosomes. Quantification of ERD6-mTurquoise2 positive endosomes untreated and 1 hour after water or chitin infiltration with the respective inhibitor (ConcA (1 µM), Wm (30 µM) and MG132 (50 µM)). The inhibitor solvent DMSO was used as control. Data of three independent biological experiments are represented in an individual box plot for untreated and chitin infiltrated samples. Data of two independent biological experiments are represented in an individual boxplot for water infiltrated samples. For each replicate, 9-13 images of 5 individual plants were analyzed. Boxplots include whiskers (values within the 1.5-fold interquartile range), first and third quartile (lower and upper box limits) and median (middle horizontal line). The mean value is depicted by a square and

data points of different experiments are indicated as gray scale. Letters show significant differences between genotypes (Kruskal-Wallis ANOVA ($P < 0.0001$); Dunn´s post-hoc test).

3.4.1.2.2 ERD6-mTurquoise2 localization to LEs/MVBs requires an N-terminal sorting Motif

Di-leucine-based [DE]XXXL[LI] motifs in the cytosolic domain of transmembrane proteins from mammals and yeast were shown to mediate subcellular sorting to the tonoplast or endosomes/lysosomes (Bonifacino and Traub, 2003; Pedrazzini et al., 2013). The GLUCOSE TRANSPORTER 8 (GLUT8), a mammalian homolog to the ERD6-like genes, is localized to LE or lysosomes and harbors a highly conserved cytoplasmic N-terminal [DE]XXXL[LI] late endosomal/lysosomal sorting signal. Mutating the glutamate to arginine interferes with GLUT8 endocytosis and incorrectly sortes the transporter to the plasma membrane (Augustin et al., 2005). Sequence analysis of GLUT8 with members of the ERD6-like family revealed that the N-termini of most ERD6-like family transporters harbor a similar di- or tri-leucine-based motif (Yamada et al., 2010), but not a strictly defined [DE]XXXL[LI] motif. ESL1, the closest homolog of ERD6 was shown to require an N-terminal LXXXLL motif for proper tonoplast localization. Mutagenesis of leucine to alanine revealed that ESL1(L10A)-GFP is mainly localized to the ER, whereas ESL1(L14A)-GFP and ESL1(L15A)-GFP were sorted to the plasma membrane (Yamada et al., 2010), suggesting that the LXXXLL motif is a novel di-leucine motif that mediates sorting of proteins to the tonoplast. To test whether the proposed N-terminal di-leucine-based motif of ERD6 is responsible for its localization to MVBs or the lumen of the vacuole, single ERD6(L11A)-mTurquoise2 and ERD6(L12A)-mTurquoise2 and a double leucine to alanine ERD6(L11/12A)-mTurquoise2 mutant constructs were generated by site-directed mutagenesis (Figure 28).

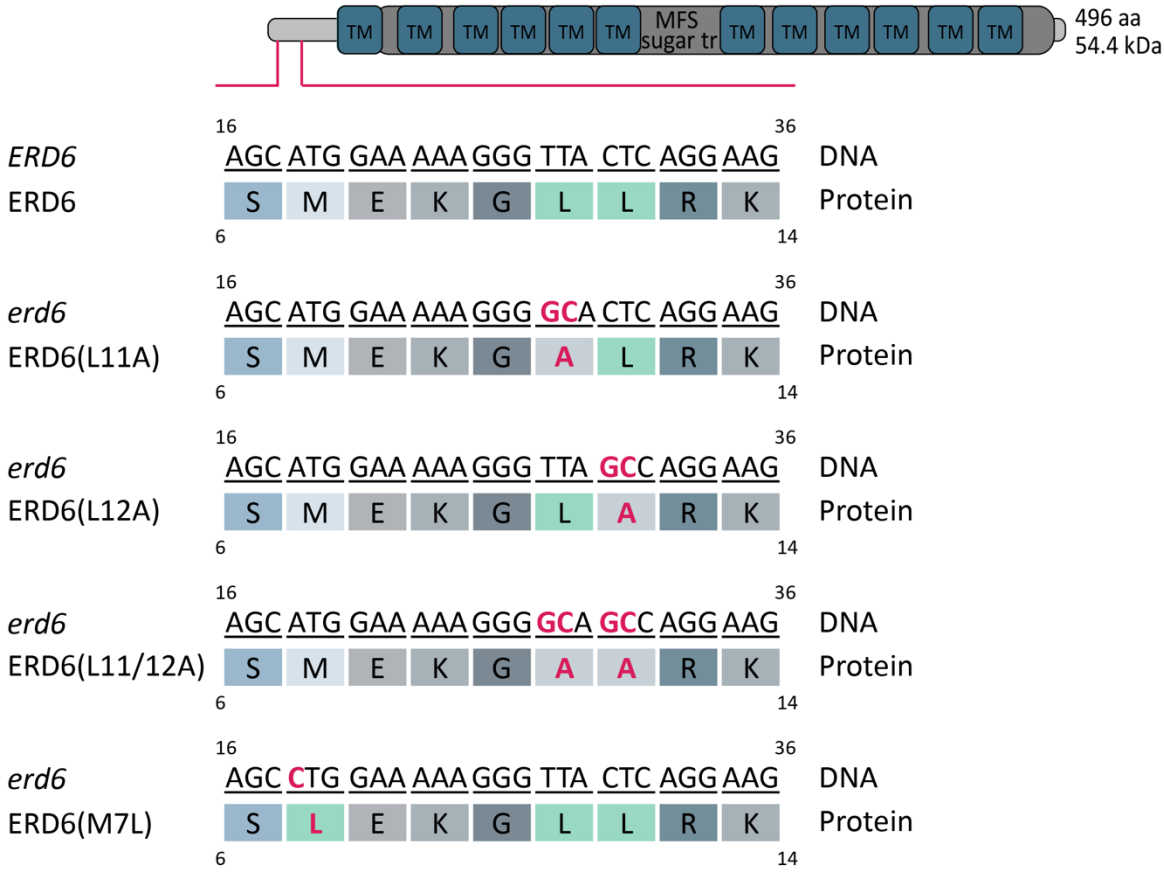

Figure 28. Wild type and mutant versions of the ERD6 N-terminal sequence. Schematic representation of predicted ERD6 protein domain organization. The predicted Major facilitator sugar transporter-like domain is illustrated in dark grey and contains 12 predicted transmembrane domains (TM) that are indicated by blue squares. The red line marks the position of amino acid changes. A Section of ERD6 DNA and Protein sequence is shown. Nucleotide exchange generated by site-directed mutagenesis is depicted in red. Amino acids (6-14) of the N-terminus of wild type ERD6 and ERD6(L11A), ERD6(L12A), ERD6(L11/12A) and ERD6(M7L) are indicated in single letter code. Leucine to alanine (L11A, L12A and L12/12A) and methionine to leucine (M7L) amino acid exchanges are indicated in red.

Localization studies were performed in *N. benthamiana* transiently expressing either wild type ERD6-mTurquoise2 or mutant versions of C-terminally mTurquoise2-tagged ERD6 under the control of the endogenous promoter. Wild-type ERD6-mTurquoise2 localized to vesicular structures and the lumen of the vacuole (Figure 29A). Furthermore, ERD6-mTurquoise2 fluorescence was observed in structures similar to cytoplasmic strands or the ER. All analyzed mutant variants (Figure 29B, C, D, E) showed relatively low ERD6-mTurquoise2 fluorescence in comparison to the wild-type mTurquoise2-tagged ERD6. ERD6(L11A)-mTurquoise2 (Figure 29B), ERD6(L12A)-mTurquoise2 (Figure 29C) or ERD6(L11/12A)-mTurquoise2 (Figure 29D) showed wild type-like subcellular localization two days after infiltration, indicating that both leucines are not required for ERD6 endosomal or vacuolar sorting. The first leucine of the LXXXLL motif in the N-terminus of ESL1 was reported to be important for the localization of ESL1 to the tonoplast (Yamada et al., 2010). To investigate whether the generation of an LXXXLL motif in the N-terminus of ERD6-mTurquoise2 can localize ERD6-mTurquoise2 to the

tonoplast, the methionine residue N-terminal of the ERD6 di-leucine signal was mutated to leucine (Figure 29B). Subcellular localization studies were performed in *N. benthamiana* transiently expressing *pERD6::ERD6(M7L)-mTurquoise2*. CLSM was performed two days after infiltration. In comparison to wild-type ERD6-mTurquoise2 (Figure 29A), the ERD6(M7L)-mTurquoise2 mutant might show reduced vesicular structures relative to vacuolar signals, indicating that the methionine is potentially important for ERD6-mTurquoise2 targeting to LE/MVBs. These results suggest that ERD6-mTurquoise2 potentially requires an N-terminal sorting signal for ERD6 localization to MVBs. However, the putative N-terminal sorting signal of ERD6 needs further investigation and quantitative analysis.

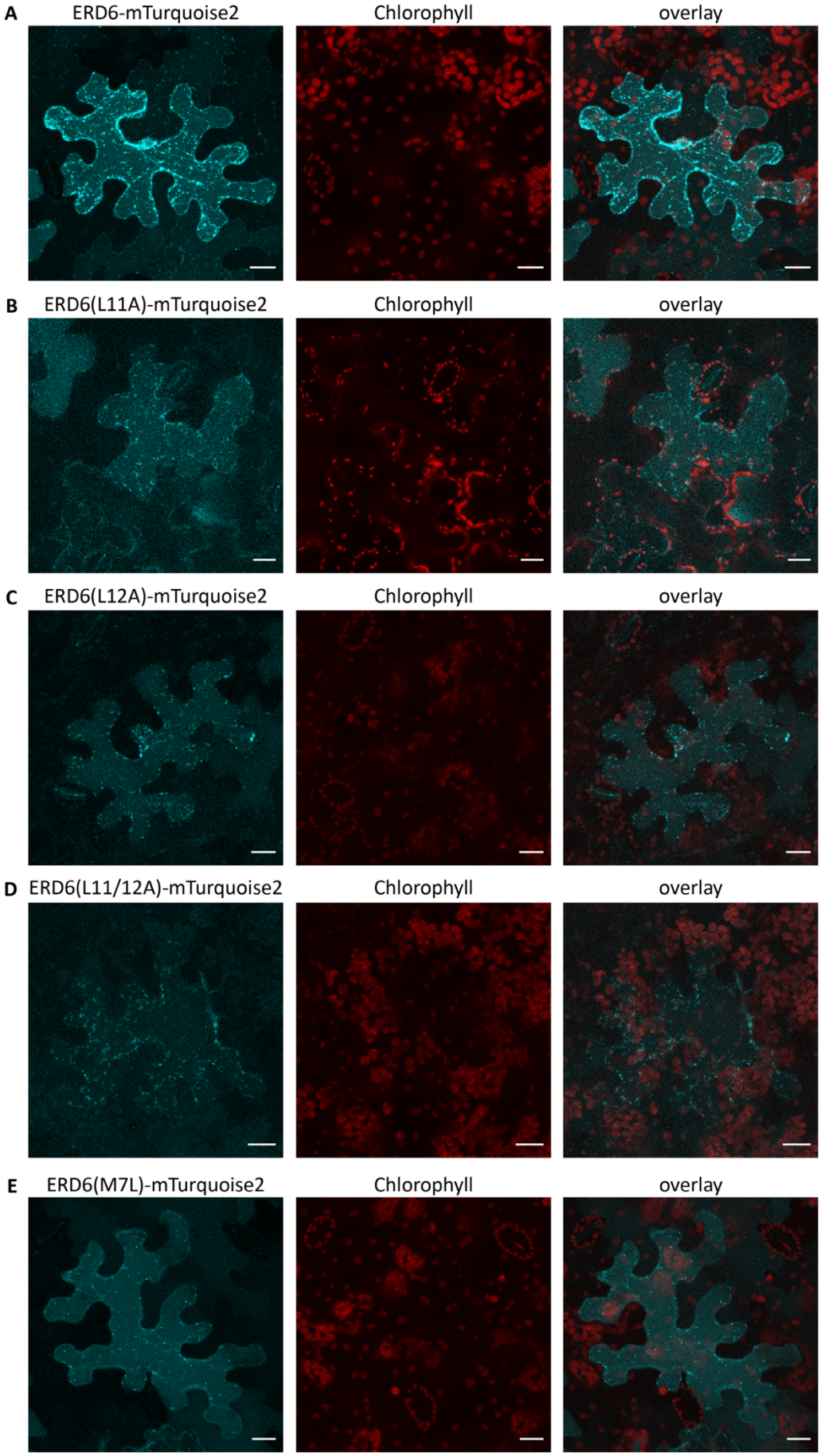
A
ERD6-mTurquoise2
Chlorophyll
overlay
B
ERD6(L11A)-mTurquoise2
Chlorophyll
overlay
C
ERD6(L12A)-mTurquoise2
Chlorophyll
overlay
D
ERD6(L11/12A)-mTurquoise2
Chlorophyll
overlay
E
ERD6(M7L)-mTurquoise2
Chlorophyll
overlay

Figure 29. Subcellular localization of wild type ERD6-mTurquoise2 and variants with mutated di-leucine motif in *N. benthamiana*. CLSM images of *N. benthamiana* leaf epidermal cells transiently expressing *ERD6-mTurquoise2* **(A)**, *ERD6(L11A)-mTurquoise2* **(B)**, *ERD6(L12A)-mTurquoise2* **(C)**, *ERD6(L11/12A)-mTurquoise2* **(D)** and *ERD6(M7L)-mTurquoise2* **(E)** under control of the endogenous promoter two days after *Agrobacterium* infiltration. ERD6-mTurquoise2 fluorescence is depicted in cyan and autofluorescence of chloroplasts in red. Images are maximum projections of 15-21 focal planes recorded 1 µm apart. Scale bar = 20 µm.

3.4.1.2.3 ERD6 subcellular localization is influenced by either an N-terminal fluorescence tag or overexpression

ERD6 is highly expressed in the vegetative rosette similar to PEN2 (Winter et al., 2007). However, CLSM analysis of *Arabidopsis* leaf epidermal cells revealed a relatively weak fluorescence of mTurquoise2-tagged ERD6. Therefore, constructs were generated where ERD6 was tagged with different fluorophores. *Agrobacterium*-mediated transient expression of *pERD6::ERD6-mCitrine*, *pERD6::ERD6-RFP* and *35S::RFP-ERD6* in *N. benthamiana* leaves was utilized to perform subcellular localization studies two days after infiltration. CLSM revealed that ERD6-mTurquoise2 (Figure 30A) and ERD6-mCitrine (Figure 30B) was mainly localized to vesicular structures as well as to the lumen of the vacuole. Transient expression of *pERD6::ERD6-RFP* in *N. benthamiana* showed high fluorescence in the lumen of the vacuole and few vesicular structures (Figure 30C). Interestingly, N-terminal RFP-tagged ERD6 was exclusively localized to the lumen of the vacuole (Figure 30D). These results suggest that either the N-terminal fluorescence tag or overexpression impact the subcellular localization of ERD6.

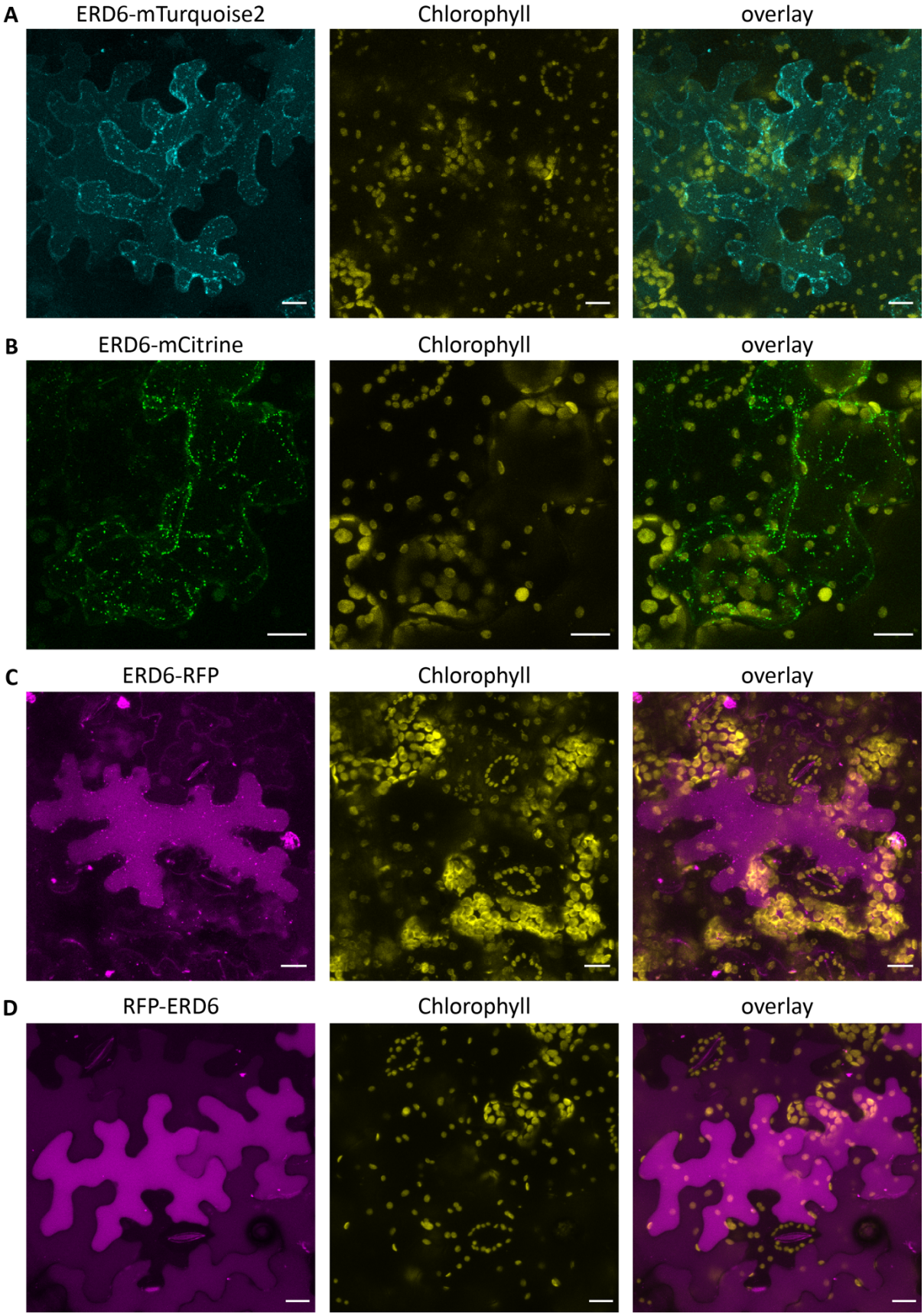

Figure 30. Subcellular localization of ERD6-mTurquoise2, ERD6-mCitrine, ERD6-RFP and RFP-ERD6 in *N. benthamiana*. CLSM analysis of *N. benthamiana* cells transiently expressing ERD6-mTurquoise2 **(A)**, ERD6-mCitrine **(B)**, ERD6-RFP **(C)** under the control of the native promoter and RFP-ERD6 **(D)** under control of the 35S promot-

er two days after *Agrobacterium* infiltration. ERD6-mTurquoise2 fluorescence is shown in cyan, ERD6-mCitrine in green and ERD6-RFP and RFP-ERD6 in magenta. Chlorophyll autofluorescence is depicted in yellow. Images are representative maximum projections of 16-21 focal planes recorded 1 µm apart. Scale bar = 20 µm.

3.4.1.3 Identification of metabolite profiles

To identify marker metabolites important for pre-invasive resistance against powdery mildews, the metabolome of leaf tissue of Col-0, *pen2-2*, *erd6-1* and plants expressing *ERD6-mTurquoise2* in the *erd6-1* mutant background were analyzed either unchallenged or after pathogen attack. 4-week-old plants were either challenged with conidiospores of the non-adapted powdery mildew *Bgh*, *E. pisi*, the adapted powdery mildew *G. orontii* or remained untreated. Methanol extraction (2.2.4.8.1) was performed from homogenized rosette leaves of 10 plants per genotype harvested at 24 and 48 hpi. Overall, samples of three independent experiments were used for the non-targeted metabolome approach (2.2.4.8). Data sets containing several thousand metabolite features were obtained for the analyses of the plants harvested 24 hpi and 48 hpi, respectively. Data obtained from the samples at 24 hpi are not shown in detail here. A metabolite feature is characterized by a retention time, an accurate mass and an intensity profile over all the analyzed samples. To identify and select metabolite features of interest, the data sets were ranked and filtered, by ANOVA combined with multiple testing to obtain false-discovery rates (FDR) using the software MarVis (Kaever et al., 2015). After filtering, 91 features (negative ESI mode) and 176 features (positive ESI mode) were selected with a FDR below 0.01 from the plant material 48 hpi. For data analysis and visualization, the intensity profiles of the 267 metabolite features were used for clustering by means of one-dimensional self-organizing maps (1D-SOMs) using MarVis and visualized in a heatmap (Figure 31A) (Kaever et al. 2015). The metabolite features were clustered by pattern similarity and represented in 10 clusters. The clusters contained metabolite profiles that were highly affected by the genotype and/or the pathogen infection at 48 hpi (Figure 31B). Metabolites of interest, such as tryptophan-derived indole glucosinolates and metabolism products, as well as metabolites with a function related to immunity, were selected from this metabolomic data.

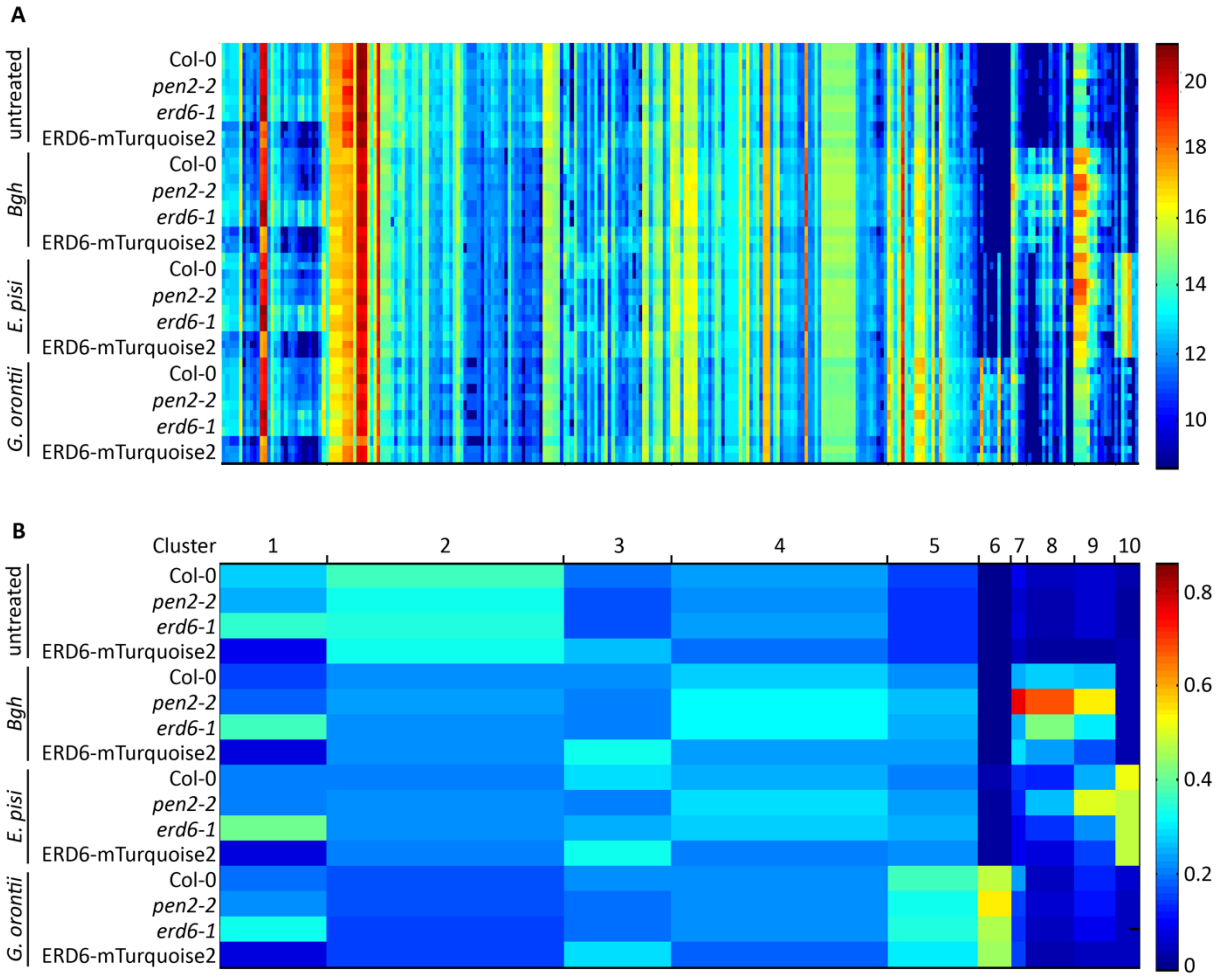

Figure 31. Metabolite fingerprinting of leaf tissue of Col-0, *pen2-2*, *erd6-1* and *erd6-1* plants expressing ERD6-mTurquoise2 untreated and 48 hours after pathogen inoculation. Data of three independent biological experiments are represented in the heatmap. The software tool MarVis was used for data visualization and analysis. Significant metabolite features were determined by ANOVA combined with multiple testing (FDR <0.01). The colors of the heatmap represent the intensity values of metabolite profiles. The intensity legend with the respective intensity values is shown on the right. Treatment and genotypes are indicated on the left. **(A)** Heatmap representation of 267 metabolite profiles, obtained by metabolome analysis of rosette leaf tissue of wild-type Col-0, *pen2-2* and *erd6-1* mutants and *erd6-1* plants expressing *ERD6-mTurquoise2* untreated and 48 hours after *Bgh*, *E. pisi* and *G. orontii* inoculation. **(B)** Heat map of 10 metabolite clusters, which sum up 267 metabolite profiles of Col-0, *pen2-2*, *erd6-1* and plants expressing *ERD6-mTurquoise2* in the *erd6-1* background untreated and 48 hours after *Bgh*, *E. pisi* and *G. orontii* inoculation. The metabolite features were clustered by pattern similarity. Clusters are indicated on the top. The width of a cluster determines the number of metabolite profiles assigned to the cluster.

Cluster 1 represents metabolites, which are highly accumulated in the *erd6-1* mutant compared to Col-0, *pen2-2* and *erd6-1* plants expressing *ERD6-mTurquoise2* unchallenged and after pathogen attack. The PEN2 substrate I3G (Figure 32A, Table 21) (Bednarek et al., 2009), the CYP81F2 oxidation product 4OHI3G (Figure 32B, Table 21) (Bednarek et al., 2009; Clay et al., 2009) and dihydroascorbigen containing a hexose moiety (DiHydroAsc Hex; Figure 32C, Table 21) were identified as metabolite markers in cluster 1. DiHydroAsc Hex was shown to be generated following the I3G enzymatic breakdown by myrosinases. PEN2-mediated I3G hydrolysis results in the generation of a highly un-

stable aglycone, which can react to form an indol-3-ylmethyl isothiocyanate (I3G-ITC) (Bednarek et al., 2009). To produce different biologically active indole compounds, the I3G-ITC can directly react with glutathione, water, amino acids, various plant metabolites and ascorbate (Agerbirk et al., 2008). The reaction of I3G-ITC with ascorbate results in the loss of the ITC and the formation of ascorbigen (Agerbirk et al., 2008). The ascorbigen is further processed by oxidation and glycosylation, resulting in the formation of DiHydroAsc Hex. In complemented *erd6-1* plants, slightly reduced intensity profiles of I3G, 4OHI3G and DiHydroAsc Hex were observed in comparison to Col-0. The selected metabolite profiles in cluster 1 showed the same pattern at 24 hpi (data not shown) and 48 hpi.

Besides the PEN2/CYP81F2 substrate I3G and the IGMT1/IGMT2 substrate 4OHI3G, the intensity profile of the PEN2 substrate 4MI3G, which is required for pathogen entry control against non-adapted powdery mildews, was identified in cluster 4 (Figure 32D; Table 21). The intensity values of 4MI3G accumulated in *pen2-2* and *erd6-1* after inoculation with both *Bgh* and *E. pisi*, whereas *Bgh* induced a stronger effect in comparison to *E. pisi*.

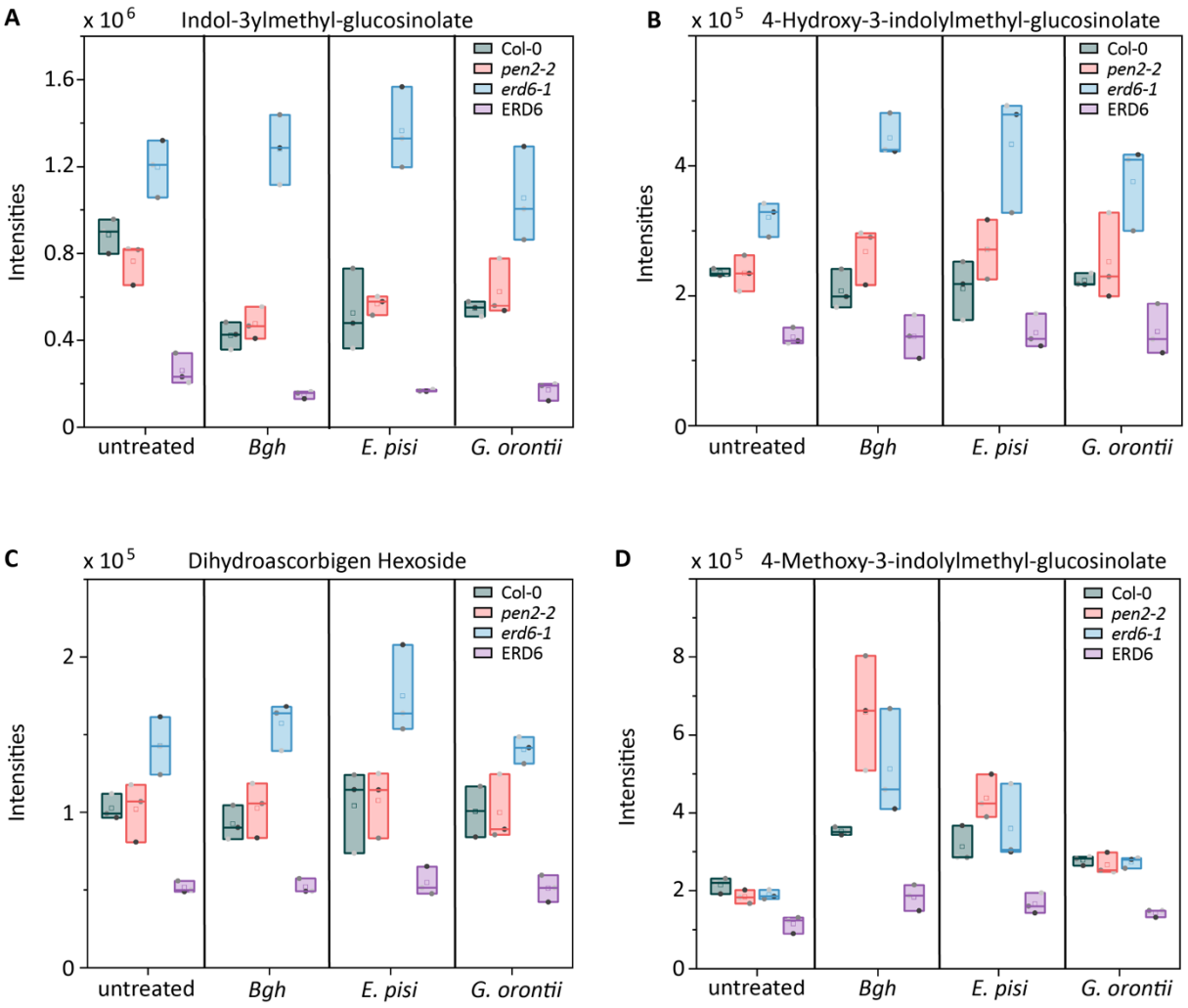

Figure 32. Indole glucosinolate metabolite markers identified in *Arabidopsis* rosettes unchallenged and 48 hours after powdery mildew inoculation. Boxplots represent relative intensity values of selected metabolite markers of 4-week-old *Arabidopsis* Col-0, *pen2-2*, *erd6-1* and *ERD6-mTurquoise2* (indicated as ERD6) expressing plants untreated and 48 hours after *Bgh*, *E. pisi* or *G. orontii* infection. Boxplots visualize data from three independent biological experiments. Individual boxplots include first and third quartile (lower and upper box limits) and median (middle horizontal line). The mean value is depicted by a square and values from individual experiments by solid gray dots (experiment 1- light gray; experiment 2- medium gray and experiment 3- dark gray). **(A)** The metabolite profiles of indol-3ylmethyl-glucosinolate, 4-hydroxy-3-indolylmethyl-glucosinolate and dihydroascorbigen hexoside were identified in cluster 1. **(B)** Cluster 4 contained the intensity profile of 4-methoxy-3-indolylmethyl-glucosinolate.

Bgh inoculation resulted in highly increased signal intensities in the *pen2-2* mutant. These intensity profiles of metabolite features were identified in clusters 7 and 8. In cluster 7, the metabolite profile of 4-coumaroylagmatine (Figure 33A, Table 21) and feruloylagmatine (Figure 33B, Table 21), belonging to the group of the hydroxycinnamic acid amides (HCAAs), were identified. HCAAs are secondary metabolites, which function as antimicrobial compounds and strengthening the cell wall of the plant against microbial degradation (Muroi et al., 2009; Campos et al., 2014). The metabolite profiles of salicylic acid glucoside (SAG) (Figure 33C, Table 21), hydroxycamalexin hexoside (Figure 33D, Table 21) and O-malonyl hydroxycamalexin hexoside (Figure 33E, Table 21) were represented in cluster 8. The intensity values of 4-coumaroylagmatine and feruloylagmatine (Figure 32A and B), as well as hydroxycamalexin hexoside and O-malonyl hydroxycamalexin hexoside (Figure 32 D and E) were highly enriched in the *pen2-2* upon *Bgh* inoculation at 24 hpi (data not shown) and 48 hpi, whereas the intensity values of the SAG metabolite profile (Figure 33C) were only enhanced in the *pen2-2* mutant at 48 hpi with *Bgh* and *E. pisi*. Cluster 9 contains metabolite features that showed highly enriched intensity values after *Bgh* and *E. pisi* attack. Camalexin (Figure 33F, Table 21) and pipecolate (Pip; Figure 33G, Table 21), which is a non-proteinous amino acid derived from lysine catabolism (Návarová et al., 2012), were represented in this cluster (Figure 32F). Pip is highly induced after pathogen attack and associated with systemic acquired resistance (SAR) (Návarová et al., 2012). The intensity profile of Pip accumulated at 24 hpi (data not shown) and 48 hpi, whereas the Camalexin profile was only enriched at 48 hpi after inoculation with both non-adapted fungi.

Cluster 3 contained metabolite profiles with rather different intensity patterns. An unknown metabolite profile (Table 21) was identified with a retention time (RT) of 2.2 min and a mass of 129.05.72 Da in cluster 3 (data not shown). The intensity value of the unknown feature was reduced in the *pen2-2* mutant after *Bgh* and *E. pisi* inoculation in comparison to Col-0, *erd6-1* and the ERD6-mTurquoise2 #10-5 complementation line at 24 hpi (data not shown) and 48 hpi.

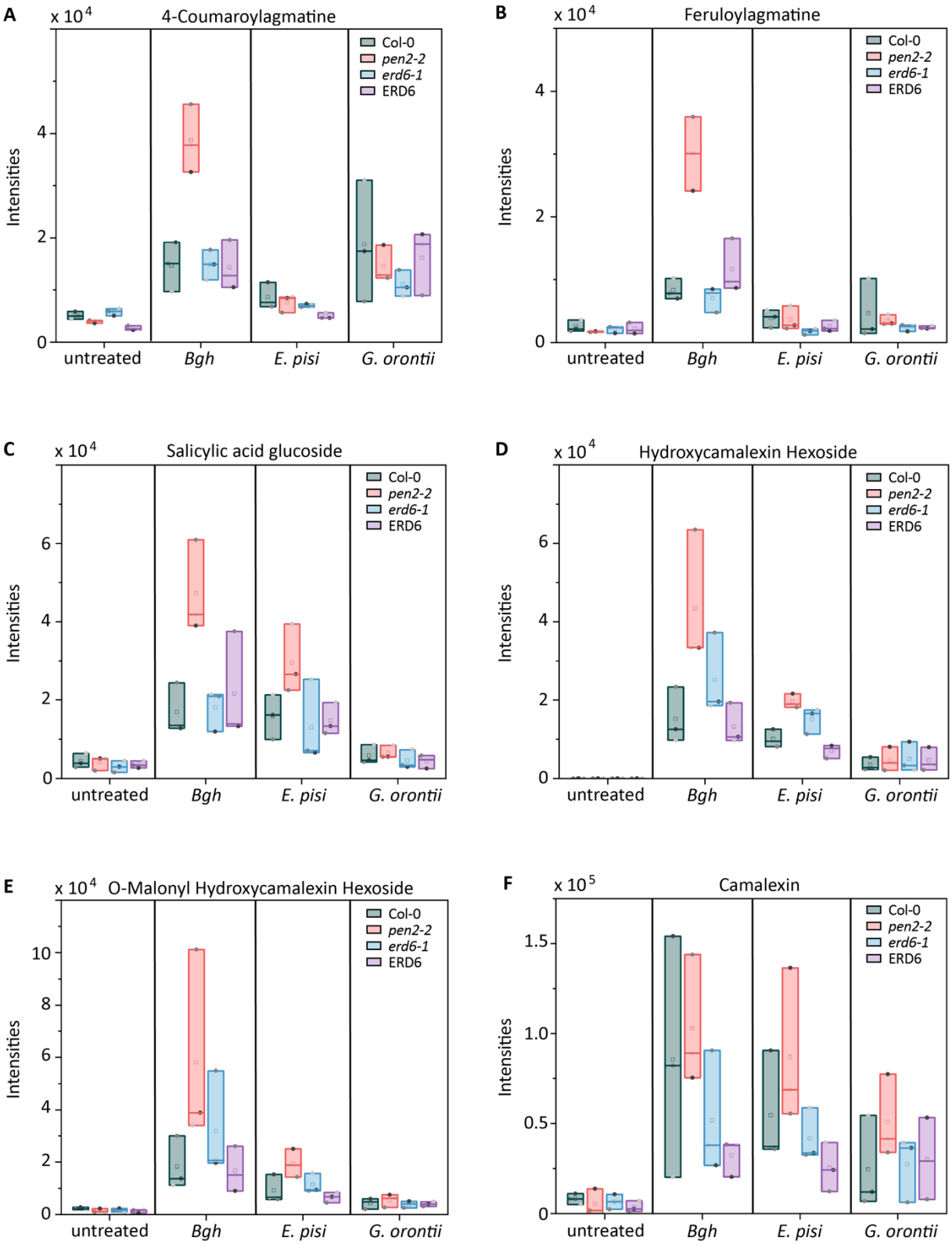
A
x 10^4
4-Coumaroylagmatine
B
x 10^4
Feruloylagmatine
C
x 10^4
Salicylic acid glucoside
D
x 10^4
Hydroxycamalexin Hexoside
E
x 10^4
O-Malonyl Hydroxycamalexin Hexoside
F
x 10^5
Camalexin
Intensities
Col-0
pen2-2
erd6-1
ERD6
untreated
Bgh
E. pisi
G. orontii

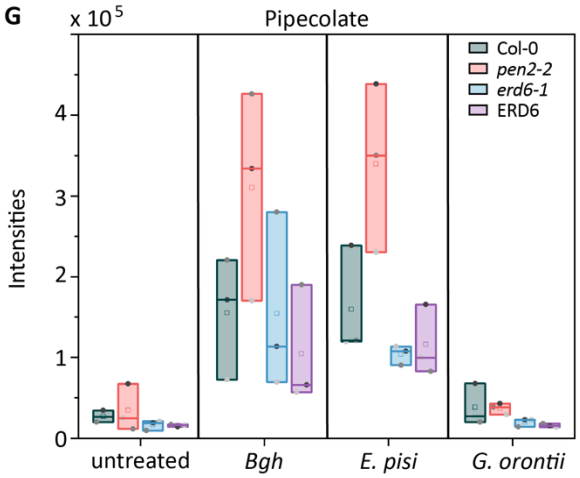

Figure 33. Genotype-specific metabolite markers identified in *Arabidopsis* rosettes 48 hours after pathogen challenge. Boxplots represent relative intensity values of selected metabolite markers of 4-week-old *Arabidopsis* Col-0, *pen2-2*, *erd6-1* and *ERD6-mTurquoise2* (indicated as ERD6) expressing plants untreated and 48 hours after *Bgh*, *E. pisi* or *G. orontii* infection. Boxplots visualize data from three independent biological experiments. Individual boxplots include first and third quartile (lower and upper box limits) and median (middle horizontal line). The mean value is depicted by a square and values from individual experiments by solid gray dots (experiment 1- light gray; experiment 2- medium gray and experiment 3- dark gray). The metabolite profiles of 4-coumaroylagmatine **(A)** and feruloylagmatine **(B)** were identified in cluster 7. In cluster 8, the metabolite profile of salicylic acid glucoside **(C)**, hydroxylcamalexin hexoside **(D)** and O-malonyl hydroxycamalexin hexoside **(E)** were identified. The metabolite profile of camalexin **(F)** and pipecolate **(G)** was identified in cluster 9.

Various metabolite profiles were strongly affected by pathogen attack. The metabolite profile of the amino acid proline was identified in cluster 2 (Figure 34A, Table 21). This cluster contained metabolite features that were genotype independent and showed reduced intensity values at 48 hpi with *Bgh*, *E. pisi* and *G. orontii* in comparison to the unchallenged samples. No changes of the intensity profile of proline were observed upon pathogen inoculation at 24 hpi (data not shown). The metabolic profile of nicotinamide adenine dinucleotide (NAD; Figure 34B, Table 21), was identified in cluster 10. NAD is a vitamin B3-derived cofactor that functions in metabolic reactions and signaling events (Berger et al., 2004; Noctor et al., 2006; Makarov et al., 2019). Cluster 10 included highly enriched intensity profiles of metabolite features of all genotypes after *E. pisi* infection at 24 hpi (data not shown) and 48 hpi (Figure 34B, Table 21). Cluster 6 represents metabolite profiles with intensity values that are enriched after *G. orontii* infection in all tested genotypes. Two unknown metabolite profiles (Table 21) were identified with a RT of 0.98 min and 3.07 min and a mass of 302.1474 Da and 199.1208 Da, respectively (data not shown).

Taken together, these results indicate that powdery mildew attack, as well as the activity of PEN2 and ERD6 highly affect the composition of *Arabidopsis* leaf metabolite profiles, required for resistance against powdery mildews.

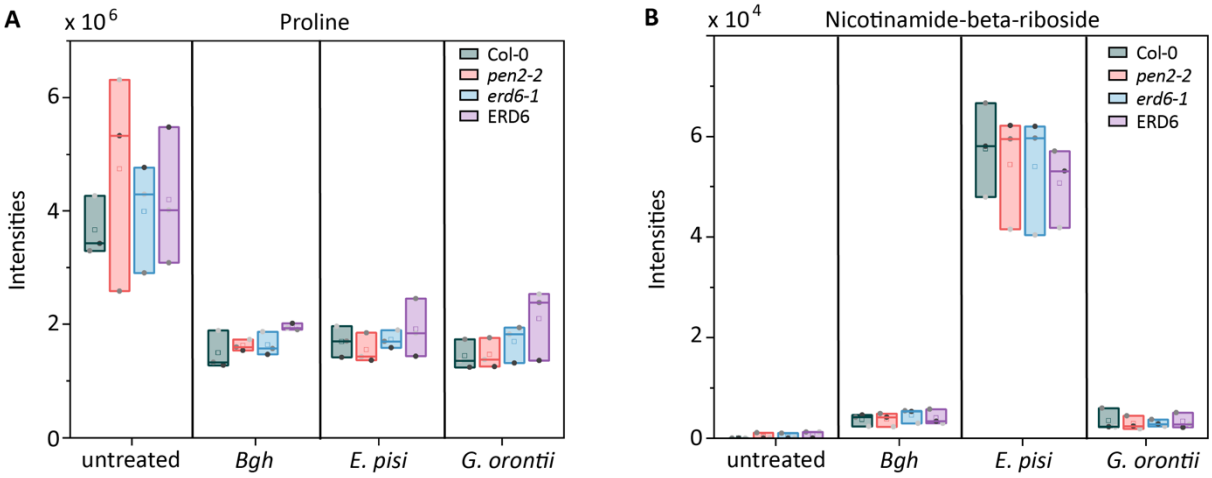

Figure 34. Infection-specific metabolite markers identified in *Arabidopsis* rosettes 48 hours after pathogen challenge. Boxplots represent relative intensity values of selected metabolite markers of 4-week-old *Arabidopsis* Col-0, *pen2-2*, *erd6-1* and *erd6-1* plants expressing *ERD6-mTurquoise2* (indicated as ERD6) untreated and 48 hours after *Bgh*, *E. pisi* or *G. orontii* infection. Boxplots visualize data from three independent biological experiments. Individual boxplots include first and third quartile (lower and upper box limits) and median (middle horizontal line). The mean value is depicted by a square and values from individual experiments by solid gray dots (experiment 1- light gray; experiment 2- medium gray and experiment 3- dark gray). **(A)** The metabolite profile of proline was represented in cluster 2. **(B)** Cluster 10 contained the metabolite profile of nicotinamide-beta-riboside.

Table 21. Retention time and mass of selected metabolite profiles.

Metabolite marker	Cluster	Retention time (min)	Mass (Da)
Indol-3ylmethyl-glucosinolate (I3G)	1	2.85	448.0614
4-Hydroxy-3-indolylmethyl-glucosinolate (4OHI3G)	1	2.03	464.0559
Dihydroascorbigen hexoside (DiHydroAsc Hex)	1	3.3	469.1575
Proline	2	0.64	115.0633
Unknwon	3	2.2	129.0572
4-Methoxy-3-indolylmethyl-glucosinolate (4MI3G)	4	3.44	478.0721
Unknown	6	0.98	302.1474
Unknown	6	3.07	199.1208
4-Coumaroylagmatine	7	3.03	276.1583
Feruloylagmatine	7	2.87	306.1686
Salicylic acid glucoside (SAG)	8	2.84	300.0841
Hydroxycamalexin Hexoside	8	4.33	378.0874
O-Malonyl hydroxycamalexin hexoside	8	4.6	464.0882
Pipecolate	9	0.85	129.0791
Camalexin	9	5.54	200.0403
Nicotinamide-beta-riboside	10	0.68	254.0907

3.4.2 S-adenosyl-L-methionine-dependent methyltransferase (AT1G55450)

3.4.2.1 Isolation and characterization of *S-adenosyl-L-methionine-dependent methyltransferase* T-DNA insertion lines

Biochemical and genetic analyzes revealed that the P450 monooxygenase CYP81F2 is required for the hydroxylation of the PEN2-substrate precursor I3G leading to the formation of the 4MI3G glucosinolate intermediate after pathogen attack (Bednarek et al., 2009; Clay et al., 2009). Pfalz *et al.,* 2011 demonstrated by using metabolic engineering in *N. benthamiana* that the resulting 4OHI3G intermediate was methylated by both INDOLE GLUCOSINOLATE O-METHYLTRANSFERASE (IGMT1) and IGMT2 to produce the PEN2 substrate 4MI3G. So far contribution of IGMT1 and IGMT2 in PEN2-mediated nonhost resistance has not been confirmed in *Arabidopsis*.

Humphrey *et al*., 2010 showed that defense components involved in powdery mildew penetration resistance are co-regulated in *Arabidopsis*. PEN1 was highly co-expressed with SNAP33 and VAMP722, whereas PEN2 was co-regulated with PEN3. Moreover, PEN2 and PEN3 shared a similar set of co-expressed genes (Humphry et al., 2010). The methyltransferase *S-adenosyl-L-methionine-dependent methyltransferase* (*AT1G55450*) was found to be co-expressed with *PEN2* and *PEN3*, suggesting that it may have a function in powdery mildew entry control. S-adenosyl-L-methionine-dependent methyltransferase (*AT1G55450*) in the following is referred to as SAM-MT. To analyze the role of SAM-MT in defense against powdery mildews in *Arabidopsis*, two independent T-DNA insertion lines *SALK025395* and *SALK087716C* were obtained from NASC. PCR-based genotyping identified a T-DNA insertion in the promoter region of SAM-MT in *SALK025395* as well as in the second exon in the *SALK087716C* line (Figure 35A). *SALK025395* was named *sam-mt-1* and *SALK087716C* was termed *sam-mt-2.* The T-DNA insertion in the second exon of *sam-mt-2* disrupts *SAM-MT* in the region encoding the methyltransferase domain (Figure 35B). Homozygous lines of *sam-mt-1* and *sam-mt-2* were isolated and analyzed for disruption of the transcript using a semi-quantitative RT-PCR approach (Figure 35C). Transcripts of *SAM-MT* in *sam-mt-1* were detected applying the oligonucleotides binding downstream of the T-DNA insertion (oLW136/oLW137), which might result from a promoter in the vector close to the left border of the inserted T-DNA (Ülker et al., 2008). No transcripts of *SAM-MT* were observed in *sam-mt-2* using The T-DNA spanning oligonucleotides (oLW138/oLW139) and the oligonucleotides binding downstream of the T-DNA insertion (oLW140/oLW137), respectively. However, the oligonucleotides binding downstream of the T-DNA insertion (oLW140/oLW137) revealed a fragment, similar in size to the gDNA Col-0 control, suggesting potential gDNA contamination.

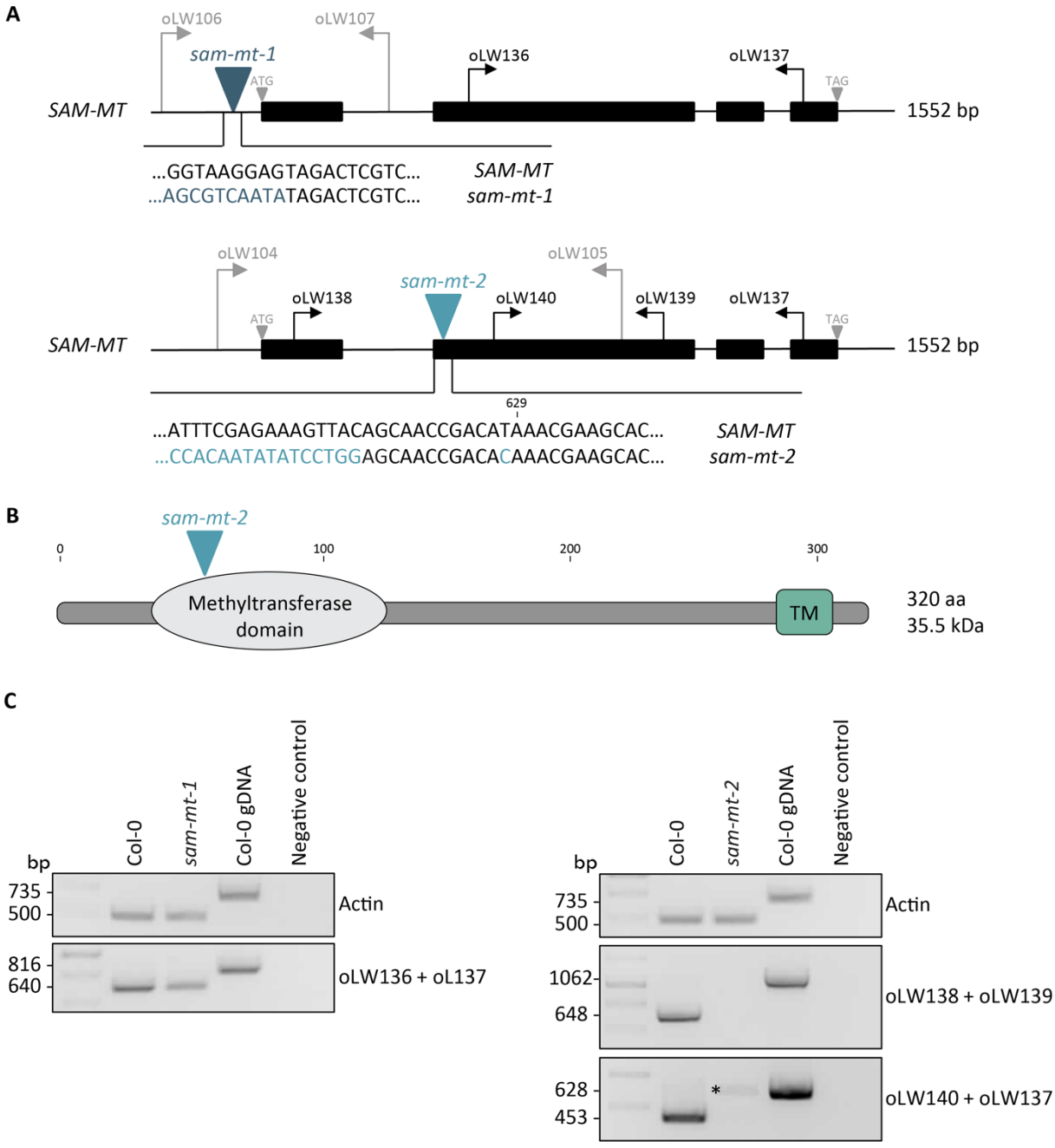

Figure 35. Characterization of *sam-mt* T-DNA insertion mutants. (A) Schematic gene structure of *SAM-MT.* Black boxes illustrate exons and solid lines represent introns, start (ATG) and stop codons (TAG) are depicted by light grey triangles. The T-DNA insertion position in mutant lines is indicated as dark blue triangle (*sam-mt-1; SALK025395*) and light blue triangle (*sam-mt-2; SALK087716C*) in (A) and (B). The site of T-DNA insertion was confirmed by sequencing. Grey arrows represent the position and orientation of oligonucleotides used for PCR-based genotyping and black arrows depict oligonucleotides used for semi-quantitative reverse transcription PCR (C). LB= left border T-DNA primer, bp= base pairs. **(B)** Schematic illustration of the predicted protein domain organization of SAM-MT. Protein domains were predicted using SMART (http://smart.embl-heidelberg.de/, Letunic and Bork, 2018) and TAIR integrated INTERPROSCAN. The predicted transmembrane domain (TM) is indicated by a green square and the predicted methyltransferase domain is illustrated in light grey. **(C)** Semi-quantitative reverse transcription PCR of wild type Col-0, *sam-mt-1* (*SALK06496*) and *sam-mt-2* (*SALK087716C*). RNA was extracted from pools of 10 plants per line of 4-week-old plants. PCR product sizes are indicated on the left and oligonucleotides used for PCR analysis are indicated on the right. The asterisk indicates a PCR product resulting from a potential gDNA contamination. bp= base pairs.

To investigate a potential role of SAM-MT in pre-invasive resistance against powdery mildews, *sam-mt-1*, *sam-mt-2* mutants, the wild-type Col-0 and *pen2-2* were inoculated with conidiospores of the non-adapted powdery mildews *Bgh* and *E. pisi* and the adapted powdery mildew *G. orontii*. To analyze penetration resistance, the formation of papillae, haustoria, cell death in epidermal cells and hyphae was evaluated at 72 hpi. Both mutant lines showed wild-type-like penetration phenotypes after infection with *Bgh, E. pisi* or *G. orontii* (Figure 36).

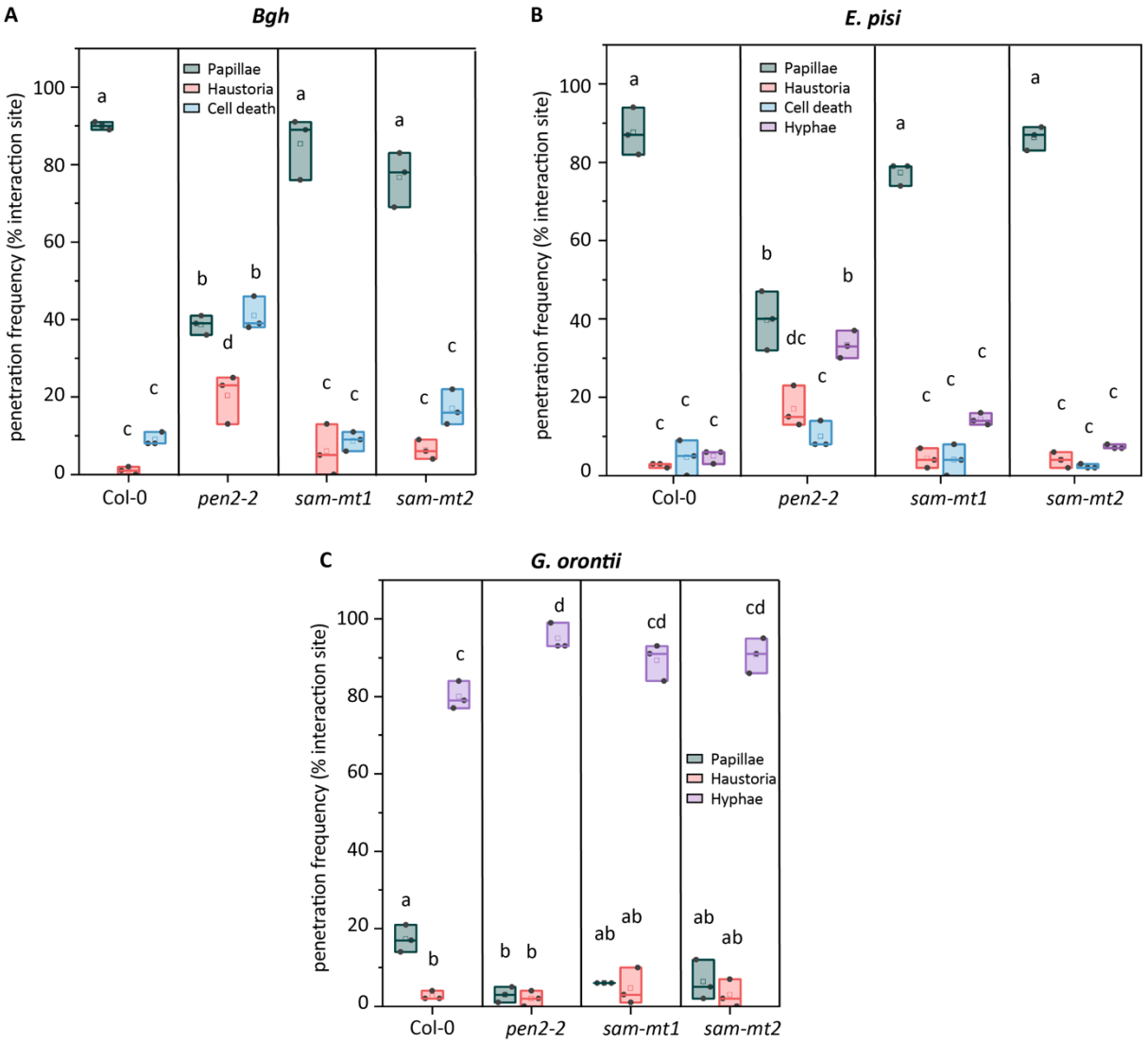

Figure 36. SAM-MT is not required for nonhost penetration resistance against *Bgh*, *E. pisi* and *G. orontii*. Penetration resistance at *Bgh* **(A)** *E. pisi* **(B)** and *G. orontii* **(C)** interactions sites on 4-week-old *Arabidopsis* Col-0, *pen2-2*, *sam-mt1* and *sam-mt2* at 72 hpi. The formation of papillae, haustoria, single-cell death and hyphae was counted. Boxplots represent data of one experiment. 100 interaction sites of three individual plants per genotype were analyzed. Individual boxplots include first and third quartile (lower and upper box limits) and median (middle horizontal line). The mean value is depicted by a square and data points of the experiment are indicated in gray. Letters show significant differences between genotypes (two-way ANOVA ($P<0.0001$ (A) and (C); $P<0.001$ (B)); Tukey post-hoc test).

In comparison to the wild-type and *sam-mt* mutants, a significantly reduced number of papillae and a significantly higher number of haustoria and epidermal cells undergoing cell death were observed in *pen2-2* plants 72 hpi with *Bgh*. Additionally, *pen2-2* mutants showed significantly reduced numbers of papillae and a significantly higher number of hyphae formation 72 hpi with *E. pisi*. The results suggest that SAM-MT is not involved in entry control against powdery mildews.

3.5 Identification of PEN2 interactors by immunoprecipitation and mass spectrometry

The regulatory pathways that coordinate the accumulation and immobilization of mitochondrial subpopulations and PEN2-aggregate formation are unknown. To gain new insights into the molecular mechanisms of PEN2-mediated pathogen entry control, IP-MS experiments were conducted to identify putative PEN2 interaction partners. Proteomics experiments were performed with stable transgenic *Arabidopsis pen2-1* plants expressing either *pPEN2::PEN2-GFP-TA$_{PEN2}$* (Lipka et al., 2005) or *pPEN2::PEN2-GFP-TA$_{PEN2\Delta TM}$* (Fuchs et al., 2016). PEN2-GFP-TA$_{PEN2\Delta TM}$ was used to differentiate between potential interactors of mitochondria-associated PEN2 and other PEN2 interactors. The *pen2-1* mutant served as a negative control. PEN2-GFP-TA$_{PEN2\Delta TM}$ lacks the entire predicted C-terminal transmembrane domain of PEN2 and is localized to the cytoplasm in *Arabidopsis.* The mislocalized protein was not able to fully complement the enhanced disease phenotype of the *pen2-1* mutant (Fuchs et al., 2016). To identify putative PEN2 interactors, detached leaves of 6-7-week-old *Arabidopsis* plants were either vacuum-infiltrated with chitin or remained untreated. Mitochondria accumulation and PEN2-GFP-TA$_{PEN2}$ aggregate formation were evaluated by CLSM and samples were harvested 3 hours after chitin infiltration.

Total protein extracts were prepared and utilized for affinity purification using GFP-trap agarose beads (2.2.4.3). Samples were analyzed by SDS-PAGE and Immunoblot analysis prior to mass spectrometry (MS) analysis, to check for successful protein purification and pulldown of PEN2-GFP-TA$_{PEN2}$ and PEN2-GFP-TA$_{PEN2\Delta TM}$. Total protein extracts, the flow through (Figure 37A) and the total protein extracts and GFP pulldowns (Figure 37B) were probed using the α-PEN2 antibody. As expected, the PEN2-GFP-TA$_{PEN2}$ fusion protein showed a molecular mass of approximately 90,8 kDa and PEN2-GFP-TA$_{PEN2\Delta TM}$ exhibited an expected molecular weight of approximately 88,9 kDa. The protein amount of both fusion proteins was reduced in the flow through after the GFP-pulldown. Importantly, Western blot analysis confirmed enrichment of the fusion proteins in untreated and chitin infiltrated samples in the GFP pulldown (Figure 37B).

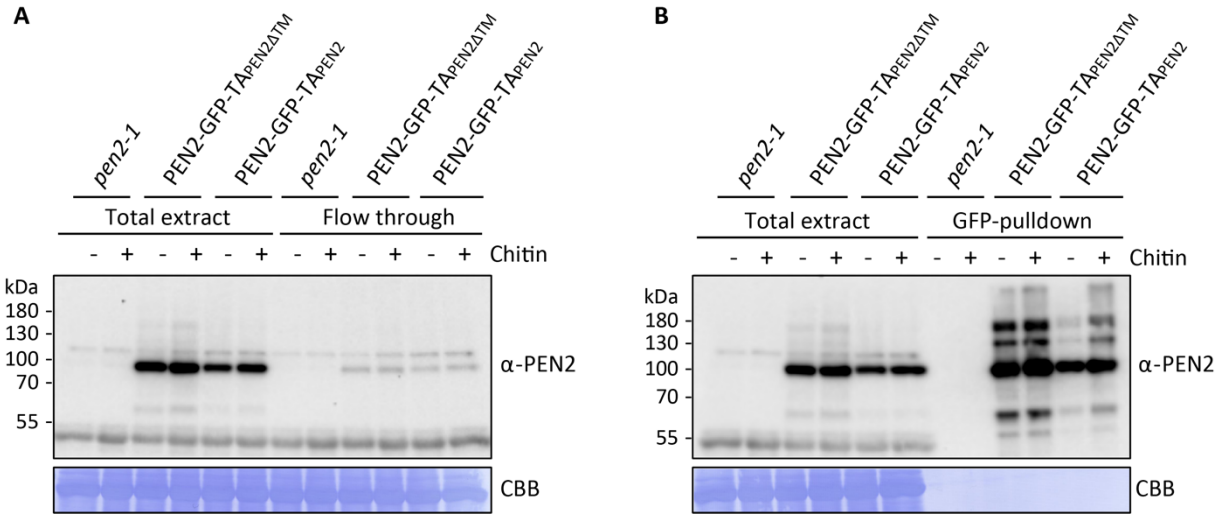

Figure 37. Enrichment of PEN2-GFP-TA$_{PEN2}$ and PEN2-GFP-TA$_{PEN2\Delta TM}$ by immunoprecipitation. Immunoblot analysis of total protein extracts, flow throughs **(A)** and GFP-pulldowns **(B)** derived from either untreated plants or 3 hours after chitin infiltration. Plant material: 7-week-old *pen2-1*, PEN2-GFP-TA$_{PEN2\Delta TM}$ and PEN2-GFP-TA$_{PEN2}$ lines. Total protein extracts were used for GFP-pulldown for 5 hours. Protein extracts, flow throughs and GFP-pulldowns (upper panel) were analyzed by Western Blotting using an α-PEN2 antibody. Coomassie Brilliant Blue (CBB) staining of the membrane (lower panel) served as loading control.

LC-MS analysis was performed (2.2.4.7.2) after completing affinity purification, on-bead tryptic digestion and C18 peptide purification (2.2.4.7.1). Database searches were conducted against the Araport11 protein database (Cheng et al., 2017) using Proteome Discoverer^{TM} version 2.2. The search algorithms Mascot and SequestHT were applied to calculate Peptide Spectrum Matches (PSMs). In total, 31 proteins were co-purified with PEN2-GFP-TA$_{PEN2}$ which were absent in the *pen2-1* control samples in 3 independent biological replicates (Table S2). Only proteins with at least one assigned protein unique peptide were considered for further analysis. The identified 17 proteins, resulting from this selection process, are shown in Table 22. The sum of all PSMs obtained for all samples within three independent biological replicates was used to rank potential PEN2 interactors by abundance. As expected, peptides corresponding to PEN2-GFP-TA$_{PEN2}$ and PEN2-GFP-TA$_{PEN2\Delta TM}$ were identified in untreated and chitin-infiltrated samples in high abundance. Unfortunately, *pen2-1* mutant samples showed weak contamination in the first experiment, potentially due to processing the control samples directly after PEN2-GFP-TA$_{PEN2}$ and PEN2-GFP-TA$_{PEN2\Delta TM}$ samples by LC-MS. The LC-MS running order was adjusted for replicate 2 and 3, starting with *pen2-1* mutant samples and followed with the samples PEN2-GFP-TA$_{PEN2}$ and PEN2-GFP-TA$_{PEN2\Delta TM}$. Peptides corresponding to different putative PEN2-GFP-TA$_{PEN2}$ interactors were identified in a relatively low abundance in the various samples.

Table 22. Proteins identified by LC-MS as putative interaction parters of PEN2-GFP-TA$_{PEN2\Delta TM}$ and PEN2-GFP-TA$_{PEN2}$. The peptide-spectrum matching scores (PSMs) obtained for PEN2-GFP-TA$_{PEN2}$ and the possible interaction partners of PEN2-GFP-TA$_{PEN2}$ are shown. Listed proteins were found in 3 independent biological experiments. The Guanylate-binding family protein was selected for further analysis and is highlighted in bold.

Accession	Name	Peptide-Spectrum matching score (PSM)												sum of PSMs
		Experiment 1				Experiment 2				Experiment 3				
		pen2-1		PEN2-GFP-TAPEN2ΔTM		PEN2-GFP-TA$_{PEN2}$		*pen2-1*		PEN2-GFP-TA$_{PEN2\Delta TM}$		PEN2-GFP-TA$_{PEN2}$		
		untreated	chitin	untreated	chitin	untreated	chitin	untreated	chitin	untreated	chitin	untreated	chitin	
AT2G44490	**Glycosyl hydrolase superfamily protein**	**10**	**2**	**340**	**302**	**221**	**258**	**0**	**0**	**275**	**282**	**201**	**213**	3256
AT3G21370	beta glucosidase 19	0	0	3	7	0	4	0	0	5	10	0	4	35
AT5G46070	**Guanylate-binding family protein**	**0**	**0**	**0**	**2**	**0**	**8**	**0**	**0**	**0**	**4**	**0**	**12**	**30**
AT4G24780	Pectin lyase-like superfamily protein	0	0	0	1	0	5	0	0	0	0	0	6	20
AT1G58290	Glutamyl-tRNA reductase family protein	0	0	0	4	0	4	0	0	0	2	2	0	16
AT3G26400	eukaryotic translation initiation factor 4B1	0	0	0	0	0	6	0	0	0	0	0	6	14
AT3G05910	Pectinacetylesterase family protein	0	0	0	0	0	2	0	0	2	0	0	4	14
AT1G67680	SRP72 RNA-binding domain-containing protein	0	0	0	2	0	0	0	0	0	2	0	2	14
AT5G27120	NOP56-like pre RNA processing ribonucleoprotein	0	0	0	0	0	2	0	0	0	0	0	2	13
AT3G12670	CTP synthase family protein	0	0	4	0	0	0	0	0	4	0	0	2	13
AT1G76810	eukaryotic translation initiation factor 2 (eIF-2) family protein	0	0	0	1	0	6	0	0	0	2	0	0	11
AT3G54660	glutathione reductase	0	0	0	0	0	2	0	0	3	0	0	4	11
AT3G13570	SC35-like splicing factor 30A	0	0	0	0	0	2	0	0	0	0	0	2	10
AT2G30000	PHF5-like protein	0	0	2	2	0	2	0	0	0	0	0	2	10
AT4G38740	rotamase CYP 1	0	0	0	0	0	2	0	0	0	0	0	1	8
AT1G18450	actin-related protein 4	0	0	0	0	0	2	0	0	0	2	0	2	8
AT1G72930	toll/interleukin-1 receptor-like protein	0	0	0	0	4	0	0	0	0	0	1	0	7
AT1G25350	glutamine-tRNA ligase 2C	0	0	0	1	0	0	0	0	0	2	0	0	5

The most promising candidate Guanylate-binding family protein-like 3 (GBPL3) was selected for further analysis. The selection of GBPL3 was based on different criteria. First, peptides corresponding to GBPL3 were absent in *pen2-1* mutant samples and enriched in the PEN2-GFP-TA$_{PEN2}$ chitin infiltrated sample in all biological replicates. Moreover, GBPL3 could be distinguished from closely related other GBPLs by protein unique peptides in all three replicates (Figure S3). Additionally, transcription in the vegetative rosette, predicted subcellular localization to mitochondria and/or cytoplasm (http://aramemnon.uni-koeln.de/; https://suba.live/) and evidence for a potential involvement in immune responses were important selection criteria. Guanylate binding proteins (GBP) have been described as important molecular components in cell-autonomous immunity against a broad spectrum of intracellular pathogens in mammals (Kim et al., 2012; Tretina et al., 2019). After pathogen invasion, GBPs were shown to be recruited to both the membrane of the invading pathogen and to the host membrane, where they function in the recruitment of additional defense-related proteins (Modiano et al., 2005; Kim et al., 2011; Foltz et al., 2017).

3.5.1.1 Isolation and characterization of *gbp3* T-DNA insertion lines

GBPL3 was identified as a putative PEN2 interaction partner. So far, the involvement of GBPs in plant immunity is unknown. To address the contribution of GBPL3 to PEN2-mediated pathogen entry control, T-DNA insertion lines of the putative PEN2-interaction candidate were obtained from NASC. *GK_028F01* was named *gbpl3-1*, *SALK_08366 gbpl3-2* and *SALK_078672 gbpl3-3.* The position of the T-DNA of *gbpl3-1*, *gbpl3-2* and *gbpl3-3* was determined by PCR-based genotyping followed by sequencing (Figure 38B). For the T-DNA mutant lines *gbpl3-1* and *gbpl3-2* carrying a T-DNA insertion in the promoter region of GBPL3, homozygous lines were isolated. However, only heterozygous *gbpl3-3* plants harboring the T-DNA in the first intron were identified via PCR-based genotyping (Figure 38C). To attempt the isolation of homozygous seedlings that potentially did not survive soil propagation, segregating seeds from a heterozygous *gbpl3-3* parent plant were sown on ½ MS solid medium. Nevertheless, no homozygous seedlings could be identified (data not shown).

So far, only heterozygous *gbpl3-3* mutant plants and the control plants Col-0 and *pen2-2* were inoculated with conidiospores of the non-adapted powdery mildew *Bgh* and analyzed for penetration resistance. Interaction sites were evaluated 72 hpi (Figure 38D). No significant differences were observed for the formation of papillae, haustoria and cell death in epidermal cells of heterozygous *gbpl3-3* and wild-type Col-0 plants. In comparison to *gbpl3-3* mutants and Col-0, a significantly reduced number of papillae and a significantly higher number of epidermal cells undergoing cell death were observed for *pen2-2* plants. The result suggests that the heterozygous T-DNA insertion of *gbpl3-3* does not affect penetration resistance towards *Bgh*.

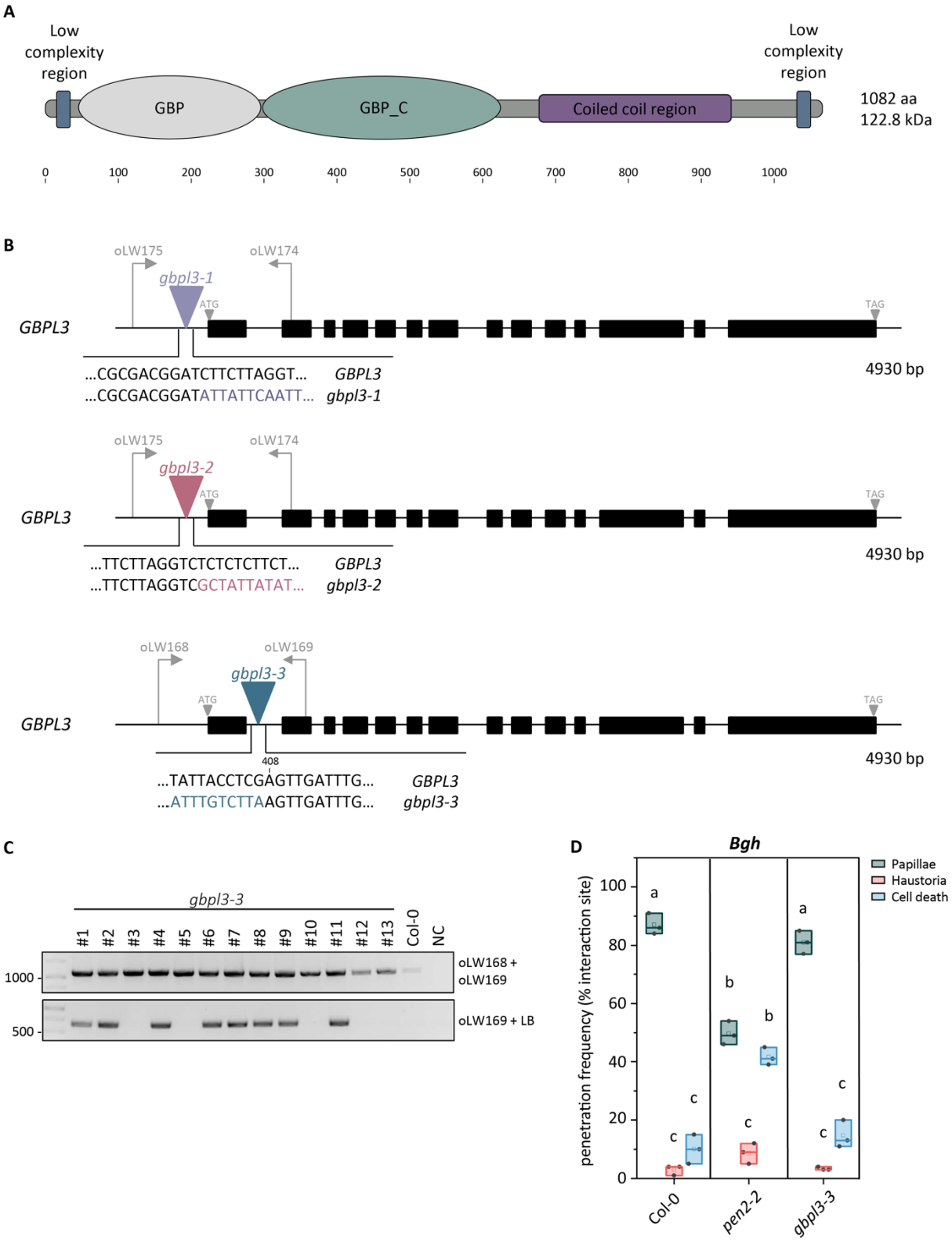

Figure 38. Characterization of *gbpl3* T-DNA insertion mutants. (A) Schematic illustration of the predicted protein domain organization of GBPL3. The predicted guanylate-binding protein N-terminal domain (GBP) is indicated in light grey, the predicted guanylate-binding protein C-terminal domain (GBP_C) is illustrated in green, the coiled-coil region in purple and the regions of low complexity in blue **(B)** Schematic gene structure of *GBPL3.* Black boxes illustrate exons and solid lines represent introns, start (ATG) and stop codons (TAG) are depicted by light grey triangles. The T-DNA insertion position in mutant lines is indicated as purple triangle

(*gbpl3-1*; *GK028F1*), red triangle (*gbpl3-2*; *SALK08366*) and turquoise triangle (*gbpl3-3*; *SALK078672*). The site of T-DNA insertion was confirmed by sequencing. Grey arrows represent the position and orientation of oligonucleotides used for PCR-based genotyping. LB= left border T-DNA primer, bp= base pairs. **(C)** PCR-based genotyping of *gbpl3-3*. T-DNA flanking primers used for genotyping are indicated in (A). No homozygous *gbpl3-3* plants were identified in PCR-based genotyping analysis. **(D)** Penetration resistance at *Bgh* interactions sites on 4-week-old *Arabidopsis* Col-0, *pen2-2* and *gbpl3-3* at 72 hpi. The formation of papillae, haustoria, single-cell death and hyphae was counted. Boxplots contain data from one experiment. 100 interaction sites of three individual plants per genotype were analyzed. Individual boxplots include first and third quartile (lower and upper box limits) and median (middle horizontal line). The mean value is depicted by a square and data points of the experiment are indicated in gray. Letters show significant differences between genotypes (two-way ANOVA (P<0.0001); Tukey post-hoc test).

4 Discussion

The atypical myrosinase PEN2 and the P450 monooxygenase CYP81F2 were identified as important molecular components required for indole glucosinolate (IG)-mediated defense against powdery mildews (Bednarek et al., 2009; Lipka et al., 2005; Fuchs et al., 2016; Clay et al., 2009). CYP81F2 is involved in the pathogen-induced biosynthesis of 4-methoxyindol-3-ylmethyl glucosinolate (4MI3G), providing the PEN2 substrate required for pathogen entry control (Bednarek et al., 2009; Clay et al., 2009). PEN2 hydrolyses 4MI3G, leading to the formation of toxic hydrolysis products. PEN2 is a tail-anchored protein, which is localized to both peroxisomes and mitochondria (Lipka et al., 2005; Fuchs et al., 2016). Fuchs *et al*., 2016 demonstrated that subpopulations of mitochondria cluster and immobilize at sites of attempted fungal penetration. The mitochondrial arrest is accompanied by peripheral accumulation of PEN2-GFP-TA_{PEN2} (Fuchs et al., 2016). PEN2-GFP-TA_{PEN2} was shown to form pathogen-triggered oligomers and dimers of higher order on the outer mitochondrial membrane of immobilized mitochondria. CLSM analysis revealed cell-autonomous accumulation of the ER-localized CYP81F2 upon pathogen attack. Furthermore, the ER was shown to rearrange in proximity to immobilized mitochondrial clusters at the attempted fungal invasion site (Fuchs et al., 2016). These pathogen-triggered and cell-autonomous defense responses at the site of attempted fungal invasion very likely require sensing of the potential intruder by the plant. However, it is unknown how CYP81F2- and PEN2-mediated defense mechanisms are connected to pathogen recognition. A potential scenario is that the perception of microbe-associated molecular patterns (MAMPs) might be required for pre-invasive defense responses. Therefore, the first part of this study focused on the role of MAMP-dependent signaling in pathogen-induced ER rearrangement, accumulation of CYP81F2 as well as accumulation and immobilization of mitochondrial subpopulations associated with PEN2 aggregates.
Several molecular components required for indole glucosinolate (IG)-mediated pre-invasive resistance are still unknown. Therefore, the second part of this work focuses on the identification and characterization of molecular components required for CYP81F2/PEN2-mediated defense against non-adapted powdery mildews.

4.1 MAMP treatment triggers CYP81F2 accumulation, mitochondrial clustering and immobilization and PEN2 aggregate formation

4.1.1 Chitin and flagellin induce the accumulation of CYP81F2

To investigate, whether MAMPs are sufficient to trigger CYP81F2-RFP accumulation and ER reorganization, *pCYP81F2::CYP81F2-RFP* expressing plants in the *cyp81f2-2* background (Fuchs et al., 2016) were treated with either water, chitin or flagellin and analyzed by CLSM (see section 3.1.1). This analysis demonstrated that MAMP treatment strongly induces the accumulation of CYP81F2-RFP in a reticulate distribution and around the nucleus, whereas no RFP-fluorescence signal of ER-associated CYP81F2 could be observed in water treated samples in leaf epidermal cells (Figure 9). These findings indicate that chitin and flagellin trigger CYP81F2-RFP accumulation. Furthermore, the induction of CYP81F2-RFP after MAMP treatment was comparable to the pathogen-triggered cell-autonomous accumulation of CYP81F2-RFP in epidermal cells (Fuchs et al., 2016).

One could imagine that perception of MAMPs activates downstream signaling required for IG-mediated pre-invasive resistance. Perception of flg22 and chitin by the receptors FLS2 and CERK1, respectively, was shown to trigger intracellular activation of MAPK cascades, including the two redundant MITOGEN-ACTIVATED PROTEIN KINASE3 (MPK3) and MPK6 (Miya et al., 2007; Thulasi Devendrakumar et al., 2018). MPK3 and MPK6 are involved in the activation of various plant defense responses including IG, camalexin and ethylene biosynthetic pathways (Sun et al., 2018; Thulasi Devendrakumar et al., 2018). *In vivo* activation of MPK3 and MPK6 induces the synthesis of the PEN2 substrate 4-methoxyindol-3-ylmethyl glucosinolate (4MI3G) and the endproduct raphanusamic acid (RA), whereas the concentration of the precursor indol-3-ylmethyl glucosinolate (I3G) decreased (Lassowskat et al., 2014).

Another example of the involvement of MAMP signaling in IG-mediated preinvasive resistance is that upon infection with *B. cinerea*, MPK3/MPK6 together with their substrate ETHYLENE RESPONSE FACTOR6 (ERF6) are involved in the biosynthesis of I3G and the conversion of I3G to 4MI3G (Xu et al., 2016). Moreover, upon pathogen attack, MPK3 and MPK6 signaling through ERF6 is required to regulate the expression of the two transcription factors MYB51 and MYB122, which function in the transcriptional control of IG core structure biosynthesis, as well as *CYP81F2*, *INDOLE GLUCOSINOLATE O-METHYLTRANSFERASE 1* (*IGMT1*) and *IGMT2* (Xu et al., 2016). MYB51 was shown to activate the transcription of *CYP79B2*, *CYP79B3* and *CYP83B1* and *SUPERROOT1* (*SUR1*) which are involved in the biosynthesis of I3G (Gigolashvili et al., 2007; Frerigmann and Gigolashvili, 2014). *myb51* mutants showed reduced concentrations of I3G and 4MI3G and enhanced susceptibility against non-adapted powdery mildew (Humphry et al., 2010). Xu *et al*., 2016 proposed that decreased levels of I3G upon

pathogen attack, result from a rapid turnover of I3G to 4MI3G and is not due to a reduction of I3G biosynthesis. Taken together, these findings suggest that the accumulation of CYP81F2 and the conversion of I3G to 4MI3G is induced by MAMP treatment. This is likely due to the perception of MAMPs by the corresponding PRRs followed by MPK3/MPK6/ERF6 signaling and activation of MYB51/MYB122 (Figure 39).

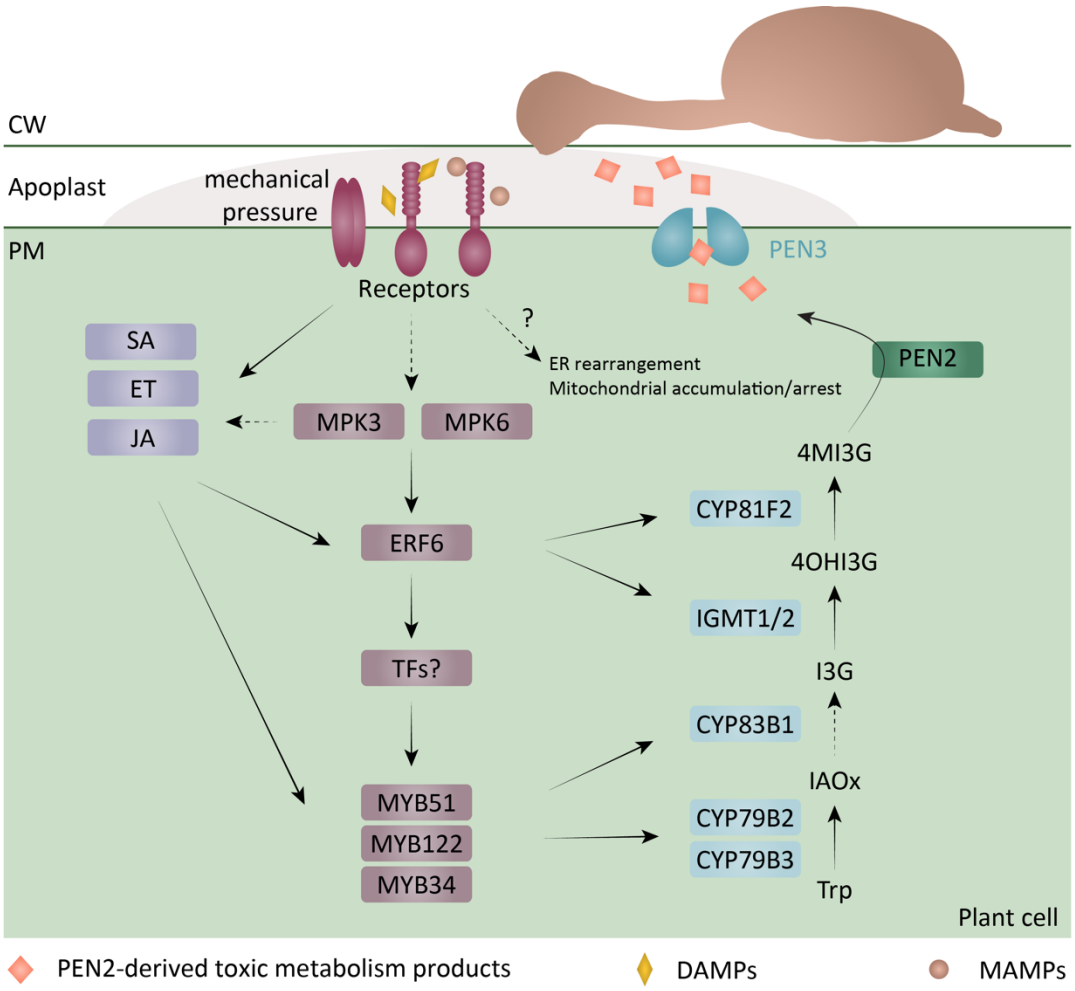

Figure 39. Proposed model of the induction of indole glucosinolate biosynthesis and their metabolism products. Powdery mildew attack generates diverse local signals such as MAMPs, DAMPs and/or mechanical signals at the site of attempted fungal penetration. Perception of these signals by different receptors leads to the activation of the MPK3 and MPK6 cascade as well as hormone biosynthesis, which contributes to the induction of signaling pathways required for finetuning of IG biosynthesis as well as ER rearrangement and accumulation and immobilization of mitochondrial subpopulations. The MPK3 and MKP6 substrate ERF6 activates transcription of *CYP81F2* and *IGMT1/IGMT2*, which are required for the biosynthesis of the PEN2 substrate 4MI3G. ERF6 is also involved in the activation of the transcription factors MYB51 and MYB122 through a yet unidentified transcription factor. This results in the induction of enzymes required for IG core structure biosynthesis, including CYP79B2/B3 and CYP83B1, which are required for the biosynthesis of I3G from the precursor tryptophan. In parallel with the MPK3/6-mediated pathway, MYB34, MYB51, MYB122 and ERF6 were also shown to be positively regulated by hormones. PEN2 mediates the hydrolysis of 4MI3G, leading to the formation of toxic metabolism products, which are transported by the ABC-transporter PEN3 into the apoplast to terminate attempted fungal invasion. Trp, Tryptophan; IAOx, indole-3-acetaldoxime; I3G, indole-3-ylmethyl glucosinolate, 4OHI3G, 4-hydroxy-indol-3-yl-methyl glucosinolate; 4MI3G, 4-methoxyindol-3-ylmethyl glucosinolate. ET, ethylene; JA, jasmonic acid; SA, salicylic acid. This model is based on this study and Kim et al., 2003; Lipka et al.,

2005; Stein et al., 2006; Denoux et al., 2008; Bednarek et al., 2009; Clay et al., 2009; Sønderby et al., 2010; Pfalz et al., 2011; Frerigmann and Gigolashvili, 2014; Xu et al., 2016.

Besides the accumulation of CYP81F2, other defense compounds involved in IG-mediated pathogen entry control accumulated after chitin (Ramonell et al., 2005) and flagellin (Zipfel et al., 2004) treatment. These findings further support the hypothesis that pre-invasive resistance requires MAMP perception at the cell surface by the corresponding PRRs. Fuchs, 2012 and Fuchs et al., 2016 showed that attempted fungal invasion induced CYP81F2 transcript abundance and protein levels, respectively. These findings are consistent with a previous study that revealed flg22-induced expression of *CYP81F2*. Besides *CYP81F2*, genes encoding the indole glucosinolate methyltransferases IGMT1, the syntaxin PEN1, PEN2, the ABC transporter PEN3 and the phytochelatin synthase PEN4 were shown to be transcriptionally induced after flagellin treatment (Zipfel et al., 2004). Moreover, Clay *et al*., 2009 revealed that flg22 treatment triggers the synthesis of 4MI3G in a CY81F2-dependent manner. The expression of *CYP81F2* and both methyltransferases *IGMT1* and *IGMT2*, which are involved in 4-methoxylation of the CYP81F2 oxidation product 4-hydroxy-indol-3-yl-methyl glucosinolate (4OHI3G), are highly upregulated after chitin treatment (Hunziker et al., 2019).

MAMP treatment induced the accumulation of CYP81F2-RFP. However, no reorganization of the ER was observed after MAMP treatment. It might be possible that fungal attack leads to a local and selective MAMP-stimulus at the site of attempted penetration. In contrast, MAMP treatment results in the distribution of chitin or flagellin within the entire apoplast, which might lead to a broad spread of the MAMP-stimulus. Therefore, one could imagine that a local stimulus is required for the direction and coordination of ER rearrangement, which is absent in MAMP treated leaves. Another explanation would be that perception of a mixture of MAMPs and/or additional elicitors such as DAMPs or a mechanical stimulus by the plant might induce ER reorganization upon attempted fungal invasion. Hardham *et al*., 2008 demonstrated that touching an epidermal cell using a glass microneedle triggered rearrangement of the ER at the site of contact. To explain the lack of ER rearrangement after MAMP treatment, one could hypothesize that during attempted fungal penetration reorganization of the ER in proximity to the invasion site depends on the perception of high pressure generated by the penetration of appressoria to facilitate mechanical entry (Figure 39). In *Arabidopsis,* perception of mechanical force such as touch, gravity, osmotic pressure and pathogen invasion is suggested to require the activation of mechanosensitive (MS) ion channels. These proteins were shown to convert mechanical pressure into ion flux (Basu and Haswell, 2017). Recently, the *Arabidopsis* MECHANOSENSITIVE CHANNEL OF SMALL CONDUCTANCE-LIKE 4 (MSL4) was identified to function in PTI (Zhang et al., 2017b). MSL4 was shown to interact with the ACCELERATED CELL DEATH6 (ACD6) *acd6-1* mutant, which showed an autoimmune phenotype including accumulation of the phytohormone salicyl-

ic acid (SA), partially PRR-dependent callose biosynthesis, as well as increased pathogen resistance (Rate et al., 1999; Vanacker et al., 2001; Lu et al., 2003, 6, 2005, 6; Zhang et al., 2014). Zhang *et al*., 2017 revealed that *msl4* mutants exhibit increased bacterial growth of *Pseudomonas syringae pv. maculicola* ES4326 hrcC^{-} and reduced callose deposition after chitin and flagellin treatment. This suggests that perception of mechanical pressure by an MS ion channel could lead to downstream signaling involved in ER rearrangement upon pathogen attack.

Another explanation would be that a local mechanical pressure, induces the release of plant-derived molecules, so-called danger-associated molecular patterns (DAMPs) by cells that are undergoing pathogen invasion. DAMP perception would result in activation of downstream signaling pathways required for ER reorganization in proximity to the plant-pathogen contact sites. It also seems possible that ER rearrangement requires the perception of a mixture of signals such as MAMPs, DAMPS and/or mechanical stimuli (Figure 39).

4.1.2 PEN2 aggregate formation is triggered by MAMP treatment

Previous studies showed that *PEN1-PEN4* genes are transcriptionally activated upon flg22 (Zipfel et al., 2004) and chitin (Ramonell et al., 2005) treatment. The chitin-triggered induction of all *PEN* genes is reduced in *cerk1* mutant plants, suggesting that IG-mediated defense mechanisms are stimulated by MAMP perception at the cell surface by PRRs (Lipka et al., 2010). Furthermore, Assat *et al*., 2004 and Underwood and Sommerville 2013 demonstrated that MAMPs trigger the focal accumulation of PEN1 and PEN3. Accumulation of PEN3 in ring-like structures was induced by the perception of chitin and flagellin by the corresponding PRRs CERK1 and FLS2, respectively (Underwood and Somerville, 2013). In this study, the role of MAMP-dependent signaling for mitochondrial accumulation and immobilization as well as PEN2 aggregate formation was evaluated. *pPEN2::PEN2-GFP-TA$_{PEN2}$* expressing plants in the *pen2-1* background (Lipka et al., 2005) were analyzed by CLSM untreated or 20 hours after chitin or flagellin vacuum infiltration (see section 3.1.2). This analysis revealed constitutive expression of PEN2 and no mitochondrial accumulation and PEN2 aggregate formation in untreated epidermal cells (Figure 10A). However, chitin and flagellin vacuum infiltration elicited mitochondrial accumulation and immobilization and PEN2-GFP-TA$_{PEN2}$ aggregate formation (Figure 10A). Based on the findings that TAMRA-labelled flg22 showed an uneven distribution within the extracellular space after infiltration, Underwood and Somerville proposed that focal accumulation of PEN3-GFP after infiltration with MAMP solution appears at sites with high concentrations of PAMPs. This suggests that after MAMP infiltration, mitochondrial accumulation and PEN2-aggregate formation occurs at regions with higher concentrations of flg22 or chitin within the apoplast.

A quantitative time-course analysis at 1, 3, 6 and 20 hours after MAMP infiltration revealed that chitin infiltration triggered a continuously increasing number of PEN2-GFP-TA_{PEN2} aggregates during the time-course experiment. However, in contrast to chitin infiltrated samples, PEN2-GFP-TA_{PEN2} aggregate formation was observed to decrease 6 hours after flagellin infiltration and increased again after 20 hpi. One possible explanation for the decrease of PEN2-aggregate formation at 6 hours after flg22 infiltration would be that the degradation of flg22 in the apoplast might be faster than hydrolyzation of chitin by chitinases that are secreted into the extracellular space by the plant. Moreover, it might be possible that flg22-signaling might activate additional pathways, which are responsible for PEN2-GFP-TA_{PEN2} aggregate formation during later time points. In *Arabidopsis,* a family of plant peptides, named Peps (plant elicitor peptides) was identified that triggered activation of defense responses (Huffaker et al., 2006). Peps are suggested to be derived from PROPEPs, comprising small proteins of about 100 amino acids (Huffaker et al., 2006; Bartels and Boller, 2015). Previous studies revealed that perception of flg22 induces the transcriptional activation of *PROPEPS* and the corresponding receptors, *PEPRs* (Zipfel et al., 2004; Huffaker et al., 2006). These findings suggest that flg22-induced DAMPs, such as Peps might induce PEN2-aggregate formation at 20 hours after infiltration.

Moreover, MAMPs were demonstrated to induce jasmonic acid (JA) and ethylene (ET) biosynthesis (Denoux et al., 2008). Methyl-JA was also shown to enhance the transcription of *PROPEPs* and Pep-mediated immune responses (Holmes et al., 2018). Therefore, it might be possible that MAMPs activate hormone signaling and the expression of defense genes, which might be required for PEN2-aggregate formation. These examples emphasize that PEN2-aggregate formation might be triggered by an flg22-induced pathway during later time-points after infiltration.

The time-course analysis revealed that mitochondrial accumulation and PEN2 aggregate formation occurred also in water infiltrated samples, indicating that an additional signal induces mitochondrial arrest and the formation of PEN2 aggregates, besides MAMP-signaling. It might be possible that the infiltration pressure alone is sufficient to trigger mitochondrial clusters. These findings are in agreement with previous studies revealing that actin filaments, which mediate myosin-dependent movement of mitochondria (Yang et al., 2014), rearrange in proximity to the site of attempted pathogen invasion potentially due to a mechanical stimulus (Hardham et al., 2008). Moreover, one could imagine that perception of a mechanical stimulus also induced aggregates of PEN2. For example, the helix-loop-helix transcription factors MYC2, MYC3 and MYC4, were shown to function in the control of IG biosynthesis by direct interacting with MYB transcription factors (Schweizer et al., 2013). The expression of *MYC2* is highly upregulated upon touch (Xu et al., 2019). Therefore, one could imagine that genes required for PEN2-aggregate formation might also be induced by a touch stimulus. Significant induction of TOUCH3 (TCH3), encoding a calmodulin-like protein, was observed after touching

Arabidopsis leaves with a paintbrush (Xu et al., 2019). Humphry *et al*., 2010 revealed that *TCH3* is co-regulated with PEN2 and PEN3 in *Arabidopsis*. Furthermore, *tch3* mutants showed enhanced concentrations of I3A and RA and slightly reduced levels of 4MI3G upon infection with non-adapted powdery mildew. This further suggests a potential involvement in the perception of a mechanical stimulus in IG-mediated pre-invasive defense.

Another explanation would be that the infiltration stress alone induces phytohormone responses, which could be involved in mitochondrial arrest and PEN2 aggregate formation. Signaling pathways of the hormones ET, JA and salicylic acid (SA), are important for plant immune responses against potential invaders (Li et al., 2019). Phytohormones function in a complex interplay of antagonistic, synergistic and additive interactions. This crosstalk is important for balancing and finetuning the plant immune system (Aerts et al., 2021). MYC2, MYB34, MYB51, MYB122 and ERF6 were shown to be regulated by ethylene and jasmonate pathways (Dombrecht et al., 2007; Bednarek et al., 2009; Xu et al., 2016). In *Arabidopsis* seedlings, the transcription factor MYB51 was shown to regulate I3G as well as 4MI3G biosynthesis upon ET and salicylic acid (SA) biosynthesis. MYB34 was the regulator after JA- and abscisic acid-triggered IG biosynthesis, whereas MYB122 played only a minor role in ET/JA signaling (Frerigmann and Gigolashvili, 2014). Various studies revealed that MPK3 and MPK6 are involved in the regulation of ET biosynthesis (Kim et al., 2003; Liu and Zhang, 2004; Han et al., 2010; Li et al., 2012; Guan et al., 2015). Therefore, it might be possible that hormone biosynthesis is induced by the infiltration stress, leading to the activation of MKP3/6 and/or activation of MYB transcription factors required for PEN2 aggregate formation (Figure 39).

Another explanation for the occurrence of PEN2 aggregates after water infiltration would be that water leads to a dilution of ion concentrations within the extracellular space, which might slightly increase the pH of the apoplast. Previous studies revealed a transiently increasing apoplastic pH from 5 to 6-7 during infection of *Hordeum vulgare* by *Blumeria graminis f. sp. hordei*, suggesting that pH changes might function as a signal for the presence of a potential intruder (Felle, 2001; Felle et al., 2004).

To investigate the association of PEN2-GFP-TA_{PEN2} with peroxisomes and mitochondria after MAMP treatment, leaves of transgenic *Arabidopsis* plants co-expressing *pPEN2::PEN2-GFP-*TA_{PEN2} and either the peroxisomal matrix marker *RFP-Peroxisome Targeting Signal1* (RFP-PTS1) (Fuchs et al., 2016) or the mitochondrial marker Saccharomyces cerevisiae CYTOCHROME C OXIDASE IV-RFP (ScCOX4-RFP) (Fuchs *et al*., 2016) were analyzed by CLSM (see section 3.1.2). These analyzes revealed that peroxisomes retained their mobility and showed unaltered PEN2 localization patterns in their periphery (Figure 11). In contrast subpopulations of mitochondria were arrested and showed PEN2-aggregate formation (Figure 12A) after chitin and flagellin infiltration. These findings are in agreement with

Fuchs *et al*., 2016 revealing that only mitochondria accumulate and immobilize at pathogen invasion sites. Moreover, only mitochondria arrested at plant pathogen penetration sites showed peripheral accumulation of PEN2 (Fuchs et al., 2016). Similar to the results obtained after MAMP treatment in this study. Upon pathogen challenge, peroxisomes remained mobile and showed no PEN2-GFP-TA_{PEN2} aggregate formation (Fuchs et al., 2016), which was also observed in MAMP-treated leaves. The function of peroxisomal subpools in PEN2-mediated IG resistance is unknown and needs further investigation. Peroxisomes are involved in various oxidizing processes such as photorespiration (Liepman and Olsen, 2001, 2003), phytohormone biosynthesis, including auxin (indole acetic acid, IAA) and JA biosynthesis (Bartel et al., 2001; Zolman et al., 2001; Feussner and Wasternack, 2002; Schneider et al., 2005), signal transduction and detoxification of ROS (del Río et al., 2002; Foyer and Noctor, 2005). Therefore, it might be possible that peroxisomes might be important for the detoxification of ROS (Anjum et al., 2016) at the site of attempted fungal invasion. Moreover, another explanation would be that peroxisomal ROS might function as a signaling molecule (Su et al., 2019) to enhance the outcome of defense. Oxidative stress was also shown to induce extensions of the peroxisomal membrane known as peroxules (Sinclair et al., 2009). These structures are suggested to be involved in the interaction of peroxisomes with mitochondria and the ER to facilitate protein and metabolite exchange (Sinclair et al., 2009; Jaipargas et al., 2016; Pan et al., 2020). However, it is unknown if peroxisomes are required for the biosynthesis of the PEN2 substrate 4MI3G.

In IG-mediated resistance, mitochondria are important organelles involved in the transport of PEN2 to the pathogen penetration site and PEN2 aggregate formation. However, additional functions of mitochondria in pre-invasive resistance likely exist, since species that do not produce IGs still show accumulation of mitochondria at sites of pathogen attack. One example is barley, where mitochondria were shown to accumulate at attempted invasion sites of the barley powdery mildew *Erysiphe f.sp. graminis hordei* (Kunoh, 1972). This suggests that the recruitment of mitochondria is an evolutionarily ancient phenomenon. In contrast, the pathogen-triggered biosynthesis of IGs is restricted to the order *Brassicales* (Bednarek et al., 2011; Hofberger et al., 2013) and considered evolutionarily recent. One ancient and conserved function of mitochondria at pathogen invasion sites may simply be provision of ATP required for energy-consuming defense mechanisms (Fuchs et al., 2016). Moreover, mitochondrial function is influenced by cytosolic ROS, calcium and SA, which are derived from different defense pathways (Mur et al., 2008; Colombatti et al., 2014). Cytosolic ROS, calcium and SA can influence the mitochondrial membrane potential resulting in alterations of mitochondrial respiration. Changes in mitochondrial respiration lead to the formation of mitochondrial ROS and to alterations of the redox status of the cell, which results in transcriptional reprogramming in the nucleus

via retrograde signaling. In order to stop pathogen colonization, mitochondrial ROS induces programmed cell death responses (Colombatti et al., 2014).

This study showed that subpopulations of accumulated and immobilized RFP-tagged mitochondria develop foci of intense PEN2-GFP-TA_{PEN2} fluorescence after chitin treatment (t_0-t_{15}). All these processes are reversible over time (t_{25}-t_{35}) (Figure 12B). These findings agree with the previous study of Fuchs *et al*., 2016. However, Fuchs *et al*., 2016 suggested that the disappearance of intense GFP fluorescence at later time points may show successful defense responses and restriction of pathogen invasion. Since this process also occurred after chitin infiltration it is unlikely that it reflects successful termination of attempted fungal penetration. It might be possible that a negative feedback mechanism is activated to prevent toxication or damage of the cell due to a high concentration of toxic IG-metabolism products.

Interestingly, MAMP treatment triggered a partially different phenotype than the one observed after pathogen invasion. Besides clusters of subpopulations of mitochondria with peripheral PEN2-GFP-TA_{PEN2} aggregate formation, foci of intense PEN2-GFP-TA_{PEN2} fluorescence in the periphery of single mitochondria were observed 20 hours after chitin and flagellin infiltration (Figure 13A). Time-lapse CLSM analysis revealed that some single mitochondria with foci of intense PEN2-GFP-TA_{PEN2} fluorescence are mobile and others remained arrested. One possible explanation might be that upon powdery mildew attack perception of fungal MAMPs results in a local stimulus at the attempted fungal penetration site. This local stimulus might be required for the coordination and direction of the accumulation and immobilization of mitochondrial subpopulations. However, MAMP infiltration might result in an uneven distribution of MAMPs within the entire extracellular space, resulting in multiple sites of MAMP perception and a widespread MAMP-signal within the epidermal cell. Therefore, one could imagine that chitin and flagellin treatment induces the additional phenotype of mobile and immobilized mitochondria associated with PEN2 aggregates, due to a broad MAMP-stimulus which lacks the specific and local signal for the direction of mitochondrial accumulation and immobilization.

To consider these findings in a natural environment, attempted pathogen invasion generates diverse local signals such as self-, non-self, and/or mechanical signals. Perception of these signals contributes to the activation of signaling pathways required for finetuning of time-dependent processed in pre-invasive defense responses. Therefore, IG-mediated resistance might be a consequence of the perception of multiple signals, resulting in a coordinated and simultaneous output of defense.

4.1.3 Outlook

The findings presented here indicate that chitin and flagellin treatment triggers the accumulation of CYP81F2-RFP as well as immobilized clusters of mitochondria, which are associated with PEN2-GFP-

TA_{PEN2} aggregates in their periphery. Moreover, mobile and immobilized single mitochondria with peripheral foci of elevated PEN2-GFP-TA_{PEN2} fluorescence were induced by MAMP treatment. These results indicate that distinct signaling pathways, which potentially act in parallel might be involved in PEN2-mediated pathogen entry control.

To confirm that MAMP-induced CYP81F2-RFP accumulation and PEN2-GFP-TA_{PEN2} aggregate formation is dependent on the corresponding pattern recognition receptor (PRR), different crosses of the flagellin PRR mutant *flagellin sensing 2c* (*fls2c*) and the chitin PRR mutants *chitin elicitor receptor kinase1-2* (*cerk1-2*), *LysM-receptor-like kinase4-1* (*lyk4-1*), *lyk5-1*, *lyk4-1 lyk5-1*, *LysM-containing receptor-like protein2-1* (*lym2-1*), as well as *lym2-4* with either CYP81F2-RFP or PEN2-GFP-TA_{PEN2} were generated (data not shown). These lines will provide a useful tool to analyze the potential involvement of MAMP perception in IG-mediated defense responses. CLSM analysis, as well as quantitative evaluation of PEN2-GFP-TA_{PEN2} subcellular behavior in the different PRR mutant backgrounds, could be conducted. Moreover, these experiments could be combined with pathogen infection analysis to evaluate MAMP specific defense responses.

To analyze the role of MPK3/MPK6/ERF6 signaling and activation of MYB51/MYB122 for CYP81F2-RFP accumulation and PEN2-GFP-TA_{PEN2} aggregate formation, future experiments should analyze the subcellular behavior of CYP81F2 and PEN2 in *mpk3*, *mpk6*, *erf6* as well as *myb51* and *myb122* mutants by CLSM after MAMP treatment and powdery mildew inoculation.

To investigate a potential role of hormone signaling in CYP81F2/PEN2-mediated resistance, PEN2-GFP-TA_{PEN2} and CYP81F2-RFP expressing lines could be crossed with different JA, ET and SA mutants and analyzed by CLSM. So far, crosses of PEN2-GFP-TA_{PEN2} x *sid2-2* (*salicylic acid induction deficient 2*), CYP81F2-RFP x *npr1-1* (*nonexpressor of pr genes 1*) and CYP81F2-RFP x *ein2*, were successfully generated (data not shown) and seeds of the F1 generation were selected.

In *Arabidopsis*, the touch-induced calmodulin-like protein TCH3 (Xu et al., 2019) is suggested to function in pre-invasive resistance (Humphry *et al*., 2010). Moreover, perception of mechanical force is suggested to require the activation of mechanosensitive ion channels such as MSL4 and MSL6. These were shown to be important for PTI (Kohorn et al., 2016; Zhang et al., 2017b). This suggests a potential involvement in the perception of a mechanical stimulus in IG-mediated pre-invasive defense. To further enhance our understanding of IG-mediated pre-invasive resistance, PEN2-GFP-TA_{PEN2} and CYP81F2-RFP expressing lines should be analyzed by CLSM after touching or wounding regarding CYP81F2-RFP accumulation and PEN2-GFP-TA_{PEN2} aggregate formation. Moreover, PEN2-GFP-TA_{PEN2} and CYP81F2-RFP expressing plants could be crossed with mutants impaired in touch responses including *tch3*, *msl4* and *mls6* and analyzed either after MAMP treatment or powdery mildew inoculation by CLSM.

Investigating the mechanisms involved in mitochondrial accumulation or arrest might further help to understand how mitochondrial clusters and immobilization and PEN2 aggregate formation could be functionally connected. The distribution of mitochondria within the cell was shown to be regulated by FRIENDLY, which belongs to the CLUSTERED MITOCHONDRIA superfamily. Besides single mitochondria, *friendly* mutants showed large clusters of mitochondria (El Zawily et al., 2014). Preliminary data of lines expressing mito-GFP in the *friendly* mutant background revealed accumulation of mitochondria in proximity to the attempted *Bgh* penetration site 20 hpi (data not shown). To address the importance of mitochondrial accumulation for PEN2-aggregate formation, PEN2-GFP-TA_{PEN2} expressing plants should be analyzed in the *friendly* mutant background. CLSM time course analysis should be performed to analyze these lines in regard to mitochondrial immobilization and PEN2 aggregate formation at pathogen invasion sites. Moreover, friendly mutants could be analyzed for their disruption of pre-invasive resistance.

Fuchs *et al*., 2016 used plants expressing the mitochondrial matrix-targeted redox-sensitive GFP2 sensor (mt-roGFP2) (Schwarzländer et al., 2008; Albrecht et al., 2014) to analyze the redox status of mitochondria upon *Bgh* inoculation. mt-roGFP2 allows the measurement of the glutathione redox potential in *Arabidopsis* plants. This analysis revealed that subpopulations of immobilized mitochondria show a pathogen-induced redox imbalance, which might be due to the release of ROS (Fuchs et al., 2016). To analyze the importance of mitochondrial ROS for the mobility or immobilization of single mitochondria associated with PEN2 aggregates, CLSM analysis could be performed with *Arabidopsis* plants co-expressing PEN2-RFP-TA_{PEN2} and mt-roGFP after MAMP treatment.

To investigate the role of the cytoskeleton for PEN2-mediated pre-invasive resistance, future experiments should be performed to test if PEN2 forms aggregates on immobilized mitochondria upon treatment of PEN2-GFP-TA_{PEN2} expressing leaves with cytoskeleton inhibitors.

Overall, the proposed future analysis would provide novel insights into pathways required for mitochondrial accumulation and immobilization and PEN2-aggregate formation.

4.2 The double transgenic line co-expressing *PEN2-GFP-TA_{PEN2}* and *CYP81F2-mKate2* can be used for a forward genetic screen

The atypical myrosinase and the cytochrome P450 monooxygenase function in pathogen-triggered and cell-autonomous defense against powdery mildews (Lipka et al., 2005; Fuchs et al., 2016; Bednarek et al., 2009; Clay et al., 2009). Upon powdery mildew attack, subpopulations of mitochondria are recruited and accumulate at plant-fungal interaction sites, which is associated with aggregate formation of PEN2. Simultaneously, biosynthesis of the PEN2 substrate by CYP81F2 is coordinated at the surface of the ER which becomes rearranged close to the arrested mitochondria underneath the fun-

gal invasion site. The mechanisms involved in regulating the recruitment and activity of PEN2 and CYP81F2 involved in powdery mildew entry control remain elusive. Therefore, the second part of this study focuses on the identification and functionally characterization of molecular components contributing to CYP81F2/PEN2-mediated resistance.

To investigate the underlying mechanisms and signaling pathways contributing to pathogen-triggered CYP81F2 accumulation, reorganization of the ER and mitochondrial accumulation and arrest, a forward CLSM-based screen could be performed to isolate mutants with altered localization of PEN2-GFP-TA_{PEN2} and CYP81F2-mKate2 after infection with non-adapted powdery mildew. In this work, a double transgenic line expressing both *pPEN2::PEN2-GFP-TA_{PEN2}* and *pCYP81F2::CYP81F2-mKate2* from a single cassette was generated in the Col-3 *gl1* background (see section 3.2). The selected double transgenic line exhibited similar localization and accumulation patterns of CYP81F2-mKate2 and PEN2-GFP-TA_{PEN2} in comparison to the single transgenic lines (Figure 14). Western blot analysis confirmed the expression of full-length PEN2-GFP-TA_{PEN2} and CYP81F2-mKate2 fusion proteins in the tested homozygous transgenic line containing a single T-DNA insertion (Figure 15). Moreover, the results indicated that the double transgenic line slightly overexpresses PEN2-GFP-TA_{PEN2}. An inverse PCR approach located the T-DNA insertion site in the promoter region of *BASIC LEUCINE-ZIPPER 48* (bZIP48) on chromosome 2 (Figure 16). To further characterize the double transgenic line, transcript levels of *bZIP48* could be analyzed to investigate the influence of T-DNA insertion in the promoter region. Moreover, the selected double transgenic line could be analyzed concerning *Bgh* penetration frequencies. The fully characterized double transgenic line might be used for ethyl methanesulfonate (EMS)-mutagenesis to start a forward genetic screen. CLSM analysis should be used to analyze pathogen-induced reorganization of the ER, CYP81F2-mKate2 accumulation, the formation of mitochondrial clusters, mitochondrial arrest as well as PEN2-aggregate formation to identify mutants with altered cellular response patterns.

4.3 GSTU13

4.3.1 GSTU13 is localized in the cytosol, the nucleus and punctate structures

Previous studies showed that the Glutathione-S-transferase class-tau member 13 (GSTU13) functions in the PEN2 defense pathway for IG metabolism (see section 3.3) (Piślewska-Bednarek et al., 2018). In this work, the localization of C- and N-terminally tagged GSTU13 was investigated. Both RFP-tagged GSTU13 versions localized to the cytosol, the nucleus and punctate structures (Figure 17A and B). The RFP-tagged GSTU13 proteins have a calculated molecular mass of approximately 51 kDa and might be small enough to enter the nucleus passively (Wang and Brattain, 2007). GSTU13-RFP and RFP-GSTU13 both seemed to complement the reduced amounts of I3A in the *gstu13-1* mutant upon

flg22-treatment (Pawel Bednarek, personal communication, data not shown). This suggests that both fusion proteins are functional and that localization of GSTU13 in the cytosol, punctate structures and the nucleus reflects localization of the native protein. The finding that the Glutathione-S-transferase GSTF6, which is required for the biosynthesis of camalexin was shown to localize to the cytosol (Dixon et al., 2009), further supports the potential localization of GSTU13 to the cytosol. Analysis transgenic marker lines revealed no co-localization of PEN2-GFP-TA_{PEN2}-labelled membrane compartments with GSTU13-RFP (Figure 18A) or RFP-GSTU13 (Figure 18B)-positive punctate structures. Moreover, GSTU13-RFP fluorescence accumulated in the cytosol around some, but not all of the attempted fungal invasion sites and in close proximity to arrested mitochondria associated with PEN2-GFP-TA_{PEN2} aggregates (Figure 18C). Different fluorescence intensity levels of GSTU13-RFP at the pathogen invasion site might reflect distinct stages of attempted *Bgh* invasion, due to unsynchronized germination of *Bgh* conidiospores and cell wall penetration after inoculation.

The finding that GSTU13 accumulates in the cytoplasm beneath the plant-fungal contact site might further support the hypothesis that pre-invasive resistance requires pathogen-triggered macromolecular protein crowding. This phenomenon refers to increased concentrations of various macromolecules including proteins or higher-order complexes (Guigas and Weiss, 2016). Besides the accumulation of GSTU13 in the cytoplasm, focal accumulation of ER-localized CYP81F2, co-localization of PEN2 and PEN4 aggregates on the outer membrane of immobilized mitochondria, as well as accumulation of PEN3 in ring-like structures in the PM were identified (Ellis, 2001; Stein et al., 2006; Fuchs et al., 2016; Guigas and Weiss, 2016; Hématy et al., 2020). Protein crowding might affect protein folding, stability and enzymatic activity (Musiani and Giorgetti, 2017) of molecular components required for pre-invasive resistance. Moreover, metabolite channeling might be one consequence of molecular protein accumulation in time and a specific microcompartment (Sweetlove and Fernie, 2013). During this process intermediates of a metabolic pathway are transferred from enzyme to enzyme, which is important to control and regulate the specificity of metabolite processing, as well as the direction of substrate flux routes through the enzymatic network (Sweetlove and Fernie, 2013). Therefore, the accumulation of GSTU13 in the cytoplasm below the attempted pathogen invasion site might indicate the importance of GSTU13 localization in the cytosol for pre-invasive resistance.

Various studies revealed that the cytoplasm moves and accumulates at sites of attempted invasion of compatible and incompatible pathogens (Takemoto et al., 2003; Koh et al., 2005). This is also represented by increased cytosolic fluorescence of RFP-tagged GSTU13 of the area surrounding the attempted fungal invasion site in comparison to the rest of the cell (Figure 18C). This suggests that GSTU13 moves with the cytoplasm towards the plant-fungus interaction site. Additionally, cytosolic GSTU13 was shown to be redirected beneath the plant-fungal contact site, which was indicated by

highly elevated RFP-fluorescence at the site of attempted *Bgh* penetration. These findings suggest the involvement of additional mechanisms required for the recruitment of GSTU13 to the host-fungal interface.

4.3.2 Outlook

Besides metabolomic complementation analysis, future experiments should be performed to test if RFP-tagged GSTU13 can complement the enhanced fungal penetration phenotype of the *gstu13* mutant. Moreover, Western Blot experiments should be performed to analyze the expression of full-length RFP-GSTU13 and GSTU13-RFP and to evaluate RFP-tagged GSTU13 protein levels in unchallenged plants and upon pathogen attack.

Furthermore, transgenic lines should be generated co-expressing RFP-tagged GSTU13 and a cytoplasmic marker to confirm GSTU13 localization to the cytoplasm. These lines should be used to analyze the subcellular dynamics of the cytoplasm and recruitment and accumulation of GSTU13 by CLSM time-course analysis after pathogen inoculation.

4.4 ERD6 and SAM-MT

4.4.1 ERD6

4.4.1.1 ERD6 is involved in penetration resistance against *E. pisi*

Molecular components involved in pre-invasive defense against non-adapted powdery mildews were shown to share a similar set of co-regulated genes in *Arabidopsis* (Humphry et al., 2010). Humphry et al., 2010 identified 164 genes that were co-expressed with PEN2 and PEN3. To identify and characterize further components required for PEN2-mediated pre-invasive resistance the candidate gene *AT1G08930* (*Early response to dehydration* 6 (*ERD6*)) (see section 3.4.1) was selected for further analysis.

The putative sugar transporter ERD6 belongs to the ERD6-like family. Members of this family were shown to facilitate the transport of sugars across membranes including the plasma membrane or organellar membranes (Schäfer et al., 1977; Rausch, 1991; Rost et al., 1996; Martinoia et al., 2000). Humphry et al., 2010 revelated that *erd6* mutants showed increased susceptibility to different pathogens in comparison to Col-0. For example, enhanced penetration of *E. pisi* and growth of *G. orontii* was observed on leaves of *erd6* mutants 72 hpi and 10 dpi, respectively (Humphry et al., 2010). Metabolomics analysis showed decreased levels of I3A and RA and increased concentrations of the PEN2-substrate I3G in *erd6* 16 hours after pathogen infection. This suggests a potential function of ERD6 in the transport of the PEN2 substrate I3G (Humphry et al., 2010). It is proposed that glucosin-

olates (GLS) are transported from the site of biosynthesis (the vasculature) to the site of storage (epidermal cells) (Li et al., 2011; Madsen et al., 2014; Nintemann et al., 2018). In epidermal cells, GSLs are assumed to be transported from the cytosol into the vacuole for storage by a yet unidentified vacuolar importer (Madsen et al., 2014). To provide I3G to CYP81F2/PEN2, one hypothesis is that the preformed and vacuolar stored I3G is transported into the cytoplasm by a tonoplast-localized GLS exporter. To evaluate a potential function of ERD6 as a vacuolar GSL exporter in cell-autonomous remobilization of intracellularly stored I3G in plant-pathogen interactions, *erd6* mutants were investigated in this study (3.4.1.1). The tested T-DNA insertion lines *erd6-1* (Humphry *et al*., 2010) and *erd6-3* are compromised in the transcription of the *ERD6* gene (Figure 19C). Moreover, both mutant lines exhibited wild-type-like penetration phenotypes 72 hours after *Bgh* and *G. orontii* inoculation (Figure 20A and C). However, *erd6-1* and *erd6-3* showed enhanced invasive growth rates of the non-adapted powdery mildew *E. pisi,* similar to *pen2-2* (Figure 20B). These results suggest that ERD6 is required for penetration resistance against the non-adapted powdery mildew *E. pisi*, but does not contribute to defense against the non-adapted *Bgh* and the adapted powdery mildew *G. orontii.* One explanation could be that IG-mediated resistance relies on two independent mechanisms for providing the CYP81F2 substrate I3G. These pathways might be targeted by powdery mildew effectors. Recently, it was shown that *de novo* I3G biosynthesis is required for defense against powdery mildews (Hunziker et al., 2020). Hunziker et al., 2020 revealed by using quantitative CLSM imaging that CYP83B1-YFP and SUPERROOT1 (SUR1)-YFP, which are required for I3G biosynthesis, are induced in leaf epidermal cells after fungal inoculation. Therefore, it might be possible that pathogen-induced *de novo* I3G biosynthesis, as well as ERD6-mediated transport of I3G contribute to pre-invasive resistance. To support the hypothesis that powdery mildews target *de novo* IG biosynthesis as well as molecular components required for ERD6-mediated I3G transport it is important to consider that CYP81F2-RFP, which is required for the biosynthesis of the PEN2 substrate 4MI3G was shown to accumulate in response to *Bgh* (Fuchs et al., 2016; Hunziker et al., 2020) and *G. orontii* (Hunziker et al., 2020). However, 4MI3G concentrations were induced after *Bgh* inoculation, but not in response to *G. orontii,* suggesting decreased IG core structure biosynthesis in epidermal cells upon *G. orontii* infection (Hunziker et al., 2020). Due to delayed accumulation of SUR1 upon *G. orontii* inoculation, Hunziker *et al*., 2020 proposed that SUR1 might be a potential effector target of *G. orontii*. Since phylogenetical analysis revealed that *E*. *pisi* is more closely related to the *Arabidopsis*-adapted powdery mildew *Erysiphe cruciferarum* than to *Bgh* (Saenz and Taylor, 2011), one could imagine that an *E. pisi* effector might also target and interfere with a molecular component required for *de novo* and cell-autonomous IG biosynthesis. Therefore, it might be possible that the transport of I3G by ERD6 could be specifically required for resistance against *E. pisi*. This theory is further supported by the finding

that *pen2* and *erd6* mutants showed accumulation of the metabolite profile of 4MI3G 48 hpi after *Bgh* infection, whereas *E. pisi* only induced a slight accumulation of 4MI3G in both mutants in comparison to the untreated controls (Figure 32B). One could imagine that the slight accumulation of 4MI3G after *E. pisi* inoculation results only from ERD6-mediated I3G transport and not from *de novo* I3G biosynthesis, due to the inhibition of *de novo* I3G biosynthesis by an *E. pisi* effector. The finding that *G. orontii* does not induce the intensity profile of 4MI3G in all tested genotypes 24 hpi (data not shown) and 48 hpi might indicate that *G. orontii* effectors might target and interfere with molecular components required for pathogen-induced *de novo* IG biosynthesis (Hunziker et al., 2020) and CYP81F2/PEN2 defense pathways. The accumulation of the metabolite profile 4OHI3G in the *erd6* mutant and induction of CYP81F2-RFP after *G. orontii* infection (Hunziker et al., 2020) might indicate CYP81F2-dependent biosynthesis of 4OHI3G. However, the absence of the accumulation of the IGMT1/IGMT2 substrate 4OHI3G in Col-0 and the *erd6* complementation line indicates that both methyltransferases convert 4OHI3G to 4MI3G. One could imagine that an *G. orontii* effector might directly modify 4MI3G, resulting in absence of 4MI3G accumulation upon *G. orontii* infection.

4.4.1.2 ERD6 is localized to MVBs/LEs and the lumen of the vacuole

To investigate the subcellular localization of ERD6, stable transgenic plants expressing *ERD6-mTurquoise2* in the *erd6-1* mutant background were analyzed. CLSM analysis revealed that *pERD6::ERD6-mTurquoise2* is constitutively expressed in leaf epidermal cells in *Arabidopsis.* This finding agrees with publicly available expression data (Winter et al., 2007). ERD6-mTurquoise2 is localized to vesicular structures and the lumen of the vacuole in *Arabidopsis* (Figure 22). Stable expression of *ERD6-mTurquoise2* in the *erd6-1* mutant background fully complements the enhanced *E. pisi* penetration phenotype of the *erd6-1* mutant at 72 hpi (Figure 22A) and the increased fungal growth of *G. orontii* during late infection (Figure 22B). These findings confirm that ERD6-mTurquoise2 is a functional protein and its observed subcellular localization represents the localization of endogenous ERD6. Moreover, non-targeted metabolomic analysis of rosette leaves revealed that ERD6-mTurquoise2 fully complements the *erd6* mutant phenotype (Figure 32). Furthermore, this study confirmes the enhanced fungal growth of *G. orontii* on *erd6* (Humphry *et al*., 2010) and *pen2* (Hunziker *et al*., 2020) mutant plants during late infection. These findings indicate that both ERD6 and PEN2 are important to reduce post-invasive growth of the adapted powdery mildew.

Co-expression analysis of ERD6-mTurquoise2 with the MVB/LE marker Rha1-mCherry revealed that ERD6-mTurquoise2 is associated with MVBs/LEs in leaf epidermal cells. CLSM analysis with the pharmacological inhibitor ConcA, which disables trafficking at the TGN resulting in accumulation of endosomes in the cell (Huss et al., 2002; Dettmer et al., 2006; Irani and Russinova, 2009) revealed signifi-

cantly enhanced ERD6-mTurquoise2 vesicle abundance in leaf epidermal cells (Figure 26AIV, BIV and 27). Moreover, leaves co-treated with either water or chitin and the inhibitor Wm, showed ERD6-mTurquoise2 association with vesicles of larger size, which are potentially representing enlarged and clustered MVBs (Figure 26AV and BV) (Wang et al., 2009; Takáč et al., 2012). These experiments confirmed the association of ERD6-mTurquoise2 with MVBs/LEs. Similar to ERD6, Yamada et al., 2010 showed that ESL1, the closest homolog of ERD6, is localized to vesicular structures. Additionally, ESL1 is localized to the tonoplast. Experiments using the inhibitor Wm showed the formation of Wm compartments in *Arabidopsis* seedlings expressing *p35S::ESL1-GFP,* suggesting an association of ESL1 with MVBs (Yamada *et al*., 2010). In contrast to tonoplast localization of ESL1 (Yamada et al., 2010) and AtERDL6 (Poschet et al., 2011), ERD6 is localized to the lumen of the vacuole. These findings suggest, that ERD6 follows the secretory pathway from the ER to the Golgi and trans-Golgi network/early endosomes (TGN/EEs), and then into MVBs/LEs (Chen et al., 2011). ERD6 might be constitutively transported via MVBs into the vacuole for potential degradation. However, it cannot be excluded that ERD6 is also localized to the limiting membrane of MVBs/LEs.

Quantification of ERD6-mTurquoise2 vesicle abundance also revealed that the number of ERD6-mTurquoise2 associated vesicles was strongly reduced after infiltration with water, water with DMSO, chitin and chitin with DMSO in comparison to the untreated control (Figure 26AI, II, III and BI, II, III; Figure 27). Infiltration with water, chitin and/or inhibitors appeared to increase vacuolar signals of ERD6-mTurquoise2. Reduced numbers of ERD6-mTurquoise2 vesicles and enhanced ERD6-mTurquoise2 fluorescence intensities in the vacuolar lumen might be a response to infiltration stress, resulting in increased transport of ERD6-mTurquoise2 to the vacuole via MVBs.

To understand the potential role of ERD6 glucosinolate transport in defense against non-adapted powdery mildews in more detail, the subcellular behavior of ERD6-mTurquoise2 in plants expressing *pPEN2::PEN2-GFP-TA$_{PEN2}$* in the *pen2-1* mutant background were analyzed by CLSM 20 hpi with *E. pisi* (Figure 24). ERD6-mTurquoise2 associated punctate structures showed no co-localization with PEN2-GFP-TA$_{PEN2}$ positive organelles in unchallenged leaves (Figure 24A) or 20 hours after *E. pisi* inoculation (Figure 24B). However, analysis *of E. pisi* invasion sites 20 hpi revealed that some, but not all fungal penetration sites were surrounded by mobile and transiently accumulating ERD6-mTurquoise2-associated vesicular structures close to subpopulations of clustered and arrested mitochondria with peripheral PEN2-GFP-TA$_{PEN2}$ aggregates (Figure24B and C). The variability in the accumulation of ERD6-mTurquoise2-tagged vesicles might reflect distinct stages of attempted *E. pisi* penetration, due to unsynchronized germination of *Bgh* conidiospores and cell wall penetration after inoculation. Accumulation of ERD6-mTurquoise2 positive vesicles in proximity to the attempted fungal invasion site is in accordance with previous studies, which demonstrate accumulation of MVBs close to the plant-

pathogen interaction site (Chamberland et al., 1989; Collins et al., 2003; An et al., 2006b, 2006a; Böhlenius et al., 2010).

Proteomic analysis of isolated extracellular vesicles from the *Arabidopsis* leaf extracellular space revealed that components involved in pre-invasive resistance, including PEN1 and PEN3 are cargos of exosomes (Rutter and Innes, 2017). ERD6 could not be identified in the published proteomics data of extracellular vesicles (Rutter and Innes, 2017), indicating that ERD6 is not a cargo of ILV secreted into the extracellular space.

In mammals, the DXXLL and the [DE]XXXL[LI] sorting signals have been identified, which mediate the sorting of proteins to endosomes and lysosomes (Bonifacino and Traub, 2003). Augustin et al., 2005 revealed that GLUT8, the mammalian homolog of the ERD6-like family, was shown to harbor a cytoplasmic N-terminal endosomal/lysosomal sorting-motif ([DE]XXXL[LI]), required for its association with LEs and lysosomes. Moreover, ESL1 was demonstrated to require a novel LXXXLL motif in the N-terminus for proper localization to the tonoplast. Using site-directed mutagenesis, the proposed N-terminal di-leucine sorting motif of ERD6 ([M]XXXLL) was investigated (Figure 29 and 30). To analyze whether the di-leucine-based motif is required for the localization of ERD6 to MVBs and/or the lumen of the vacuole, single ERD6(L11A)-mTurquoise2 and ERD6(L12A)-mTurquoise2 and a double leucine to alanine ERD6(L11/12A)-mTurquoise2 mutant constructs were generated (Figure 29) and investigated by CLSM in *N. benthamiana* (Figure 30). These localization studies revealed wild type-like subcellular localization patterns of ERD6 mutant variants (Figure 30B, C, D). These results suggest that both leucines are not required for ERD6 endosomal or vacuolar sorting. The observed fluorescence signal of ERD6-mTurquoise2 mutant variants in transiently transformed *N. benthamiana* leaves (Figure 22B, C, D, E) was in general relatively low in comparison to the wild-type mTurquoise2-tagged ERD6, suggesting that the mutations in the N-terminus might influence proper folding of the ERD6-mTurquoise2 protein. The first leucine of the LXXXLL motif in the N-terminus of ESL1 was reported to be important for the localization of ESL1 to the tonoplast (Yamada et al., 2010). The methionine residue N-terminal of the ERD6 di-leucine signal was mutated to leucine. However, the generation of an LXXXLL motif in the N-terminus of ERD6-mTurquoise2 (Figure 29), similar to ESL1, did not result in tonoplast localization of ERD6(M7L)-mTurquoise2 (Figure 30 E). However, potentially reduced numbers of ERD6(M7L)-mTurquoise2-associated vesicular structures in comparison to the wild-type ERD6 protein in *N. benthamiana* were observed. This suggests that the methionine in the N-terminus of ERD6 might be required for targeting ERD6-mTurquoise2 to LE/MVBs. However, future experiments need to investigate the N-terminal motif of ERD6 in more detail as well as in combination with quantitative analysis.

ERD6 was shown to be highly expressed in rosette leaf tissue in *Arabidopsis*, similar to *PEN2* (Winter et al., 2007). However, relatively weak fluorescence of mTurquoise2-tagged ERD6 was observed in *Arabidopsis* leaf epidermal cells by CLSM. Therefore, constructs were generated, which contained pERD6::ERD6-mCitrine (This work), pERD6::ERD6-RFP (This work) and 35S::RFP-ERD6 (Rene Fuchs) (3.4.1.2.5). CLSM analysis of transiently transformed *N. benthamiana* leave cells revealed that ERD6-mTurquoise2 (Figure 30A), ERD6-mCitrine (Figure 30B) and ERD6-RFP (Figure 30C) were localized to vesicular structures. Moreover, ERD6-RFP showed increased fluorescence and ERD6-mCitrine exhibited reduced fluorescence in the lumen of the vacuole. This phenomenon might be explained by the different fluorophore properties. Light emission of fluorescence proteins generally decreases with lower pH (Shen et al., 2013; Stoddard and Rolland, 2019). The pH sensitivity of fluorophores is described by th pKa, which indicated the pH at which 50% of the protein pool shows fluorescence. mTurquoise2, which is a cyan variant of the GFP protein, has a p*Ka* of 3.1 (Goedhart et al., 2012), whereas the p*Ka* mRFP is 4.5 (fpbase.org). Yellow proteins are known for their high pKa values and sensitivity to low pH (Stoddard and Rolland, 2019). The pKa value of mCitrine is 5.7 (fpbase.org). The pKa values indicate that both fluorescence proteins mTurquoise2 and RFP might exhibit more stable fluorescence intensities in the lumen of the vacuole in comparison to mCitrine. Additionally, differences between the fluorescence proteins in degradation speed in the vacuole might play a role. In contrast to C-terminally tagged ERD6 versions, the N-terminally tagged *35S::RFP-ERD6* was almost exclusively localized to the lumen of the vacuole (Figure 30D). These results suggest that either overexpression or the N-terminal RFP-tag influences the subcellular localization of ERD6. It might be possible that enhanced protein concentrations of ERD6 might lead to increased transport of the protein to the vacuole via MVBs.

4.4.1.3 ERD6-mTurquoise2 runs differently on SDS-PAGE than its expected molecular weight

Immunoblot analysis revealed that mTurquoise2-tagged ERD6 runs differently on SDS-PAGE than its expected molecular mass (3.4.1.2.2). Two gene models for ERD6 are predicted in TAIR10, both of which lead to a protein of approximately 54 kDa. Consequently, the ERD6-mTurquoise2 fusion protein has an expected molecular weight of approximately 81 kDa. However, high molecular weight bands (>180 kDa) and a band of approximately 60 kDa were identified to be specific for ERD6-mTurquoise2 in Western Blots total protein extracts or microsomal preparations (Figure 23). The 60 kDa signal might result from cleavage of the ERD6 protein either *in planta* or during extraction. A recent study revealed that at least two C-terminal TM helices of the mammalian glucose transporter GLUT8, which is a homolog of the ERD6-like family, are cleaved from the protein. Approximately 50% of the overall GLUT8 protein pool was shown to be cleaved (Alexander et al., 2020). GLUT8 was

shown to be associated with late endosomes and lysosomes (Augustin et al., 2005). However, the cleaved C-terminal part of GLUT8 was localized to a different vesicular population (Alexander et al., 2020).

The high molecular weight band of ERD6-mTurquoise2 suggests that ERD6 forms aggregates or large complexes (Figure 23B). Usually, boiling samples in SDS loading dye results in denatured proteins and the release of protein interactions. Moreover, the reducing agent DTT, present in the SDS loading dye, should lead to dissociation of disulfide bridges. The reason for the formation of stable ERD6-mTurquoise2 aggregates remains elusive. However, one could imagine that the transport activity of ERD6 might be regulated by the formation of aggregates. In mammals, the glucose transporter GLUT1 was shown to form multimeric complexes of higher order at the PM (Pessino et al., 1991; De Zutter et al., 2013). GLUT1 monomers were shown to form homodimeric and homotetrameric complexes. In comparison to the GLUT1 monomer, GLUT1 complexes showed enhanced sugar transport activities (Hebert and Carruthers, 1991). Moreover, redox-dependent oligomerization of the *Solanaceous tuberosum* sucrose transporter StSUT1 was observed in membrane microdomains (Liesche et al., 2010).

Since ERD6-mTurquoise2 is found in the vacuole lumen, degradation products are not unexpected. In total protein extracts using Triton X-100 (Figure 23B) and microsomal fractions (Figure 23B) of mTurquoise2-tagged ERD6 expressing plants, a high amount of mTurquoise2 cleavage products with a molecular mass of 26,9 kDa were identified, suggesting ERD6-mTurquoise2 degradation and proteolysis in the vacuole.

Even though previous reports show that *ERD6* is induced upon chitin (Ramonell et al., 2005) and flagellin (Zipfel et al., 2004) treatment, no differences in ERD6-mTurquoise2 protein amount or apparent mass were observed after pathogen inoculation in Western Blot analysis. This result is in accordance with CLSM data of ERD6-mTurquoise2 expressing plants, which revealed no elevated ERD6-mTurquoise2 signal intensities after *E. pisi* inoculation (Figure 24B). Similar to ERD6, PEN2 protein levels showed no differences at 24 hpi with *Bgh*, whereas gene expression of *PEN2* is induced upon *Bgh* (Fuchs, 2012). These findings suggest that ERD6 and PEN2 regulation might result from potential post-translational modifications during attempted pathogen invasion.

4.4.1.4 *pen2* and *erd6* affect the composition of *Arabidopsis* leaf metabolite profiles

This study showed that ERD6 is associated with MVBs/LEs (3.4.1.2.1, Figure 25B) which accumulate at powdery mildew contact sites and in proximity to clustered and immobilized mitochondria decorated with PEN2-aggregates (Figure 25B). Humphrey *et al*., 2010 revealed enhanced indol-3-ylmethyl glucosinolate (I3G) as well as reduced levels of raphanusamic acid (RA) and indol-3-ylmethyl amine (I3A)

levels in *erd6* mutants unchallenged and 16 hours after *E. pisi* infection. These findings suggest a potential function of ERD6 in the transport of I3G to the attempted pathogen invasion site.

To analyze the metabolite composition in rosette tissue of the *erd6* mutant in more detail a non-targeted metabolomics approach was performed (3.4.1.3). The metabolome of leaves of Col-0, *pen2-2*, *erd6-1* and plants expressing *ERD6-mTurquoise2* in the *erd6-1* mutant background were analyzed either unchallenged or after inoculation with the non-adapted powdery mildews *Bgh, E. pisi* or the adapted powdery mildew *G. orontii* at 24 and 48 hpi. After ranking and filtering of the obtained metabolite profiles, by ANOVA combined with multiple testing to obtain false-discovery rates (FDR) a subset of 267 metabolite features (48 hpi), with a FDR below 0.01 were clustered and visualized in a heatmap (Figure 31B). Metabolite features were clustered according to their pattern similarity and represented in 10 clusters. The clusters contained metabolite features that were highly affected by the genotype and/or powdery mildew infection. Metabolite profiles of interest, such as tryptophan-derived indole glucosinolates and metabolism products, as well as metabolites with a function related to immunity, were selected from this metabolomic data.

Four tryptophan-derived indole glucosinolates (IG) were identified to accumulate in the *erd6-1* mutant, suggesting that ERD6 might function in the transport of IGs. Cluster 1 represents metabolite profiles that are highly induced in *erd6-1* mutant plants unchallenged and after pathogen inoculation in comparison to Col-0, *pen2-2* and complemented *erd6-1* (Figure 32A, B, C). These metabolite profiles showed the same pattern at 24 hpi and 48 hpi. In this cluster, the metabolite profiles of the PEN2 substrate I3G, the INDOLE GLUCOSINOLATE O-METHYLTRANSFERASE 1 (IGMT1) and IGMT2 substrate 4-hydroxy-indol-3-yl-methyl glucosinolate (4OHI3G) and dihydroascorbigen containing a hexose moiety (DeHydroAsc Hex), were identified. The accumulation of the I3G metabolite profile in *erd6* mutants is in agreement with the study of Humphry et al., 2010. Besides, I3G, 4OHI3G and DiHydroAsc Hex, the PEN2 substrate 4-methoxyindol-3-ylmethyl glucosinolate (4MI3G), required for powdery mildew entry control, was found to be elevated in the *pen2-2* and *erd6* mutant after inoculation with non-adapted powdery mildews in cluster 4 (Figure 32D). These findings might indicate the transport of these substances in an ERD6-dependent manner.

The finding that I3G and 4OHI3G accumulate in *erd6* under unchallenged conditions indicates that ERD6 might be required to retain I3G as well as 4OHI3G levels in the cytoplasm. In *Arabidopsis,* it was shown that glucosinolates are constitutively generated in the vasculature (Nintemann et al., 2018). It is proposed that glucosinolates are transported from the site of biosynthesis to epidermal cells for storage in the vacuole (Li et al., 2011; Madsen et al., 2014; Nintemann et al., 2018). Besides the function of glucosinolates in defense against microbial pathogens and herbivores (Halkier and Gershenzon, 2006; Hopkins et al., 2009; Pedras et al., 2011), these secondary metabolites were linked to,

hormone signaling, the circadian clock, root growth, onset of flowering as well as biomass (Jeschke et al., 2019). Therefore, one could imagine that ERD6 might function in maintaining I3G as well as 4OHI3G levels in the cytoplasm in the absence of pathogen attack. However, upon pathogen attack, ERD6 might provide the CYP81F2 substrate I3G, which is required for powdery mildew entry control.

The accumulation of 4OHI3G in the *erd6-1* under unchallenged conditions might indicate the activity of CYP81F2 and CYP81F1 as well as CYP81F3. Besides CYP81F2, CYP81F1 and CYP81F3 were shown to convert I3G to 4MI3G. (Pfalz et al., 2011). However, CYP81F2 was shown to be the major CYP81F required for pathogen-triggered 4-hydroxylation of the PEN2 substrate I3G (Bednarek et al., 2009; Clay et al., 2009). The metabolite profile of 4OHI3G further increased upon powdery mildew inoculation in comparison to Col-0, *pen2-2* and *ERD6-mTurquoise2* expressing plants. After 4-hydroxylation of I3G by CYP81F2, the resulting product 4OHI3G is suggested to be directly processed by both IGMT1 and IGMT2 into the PEN2 substrate 4MI3G (Pfalz et al., 2011). Enzymatic activation of 4MI3G by PEN2 results in the generation of toxic metabolism products, required for defense against powdery mildews (Bednarek et al., 2009). However, due to the toxicity of PEN2-derived metabolism products, the plant requires an effective mechanism for regulation, compartmentalization and detoxification of these secondary metabolites and/or precursor substrates. One could imagine that ERD6 is a bi-directional IGs transporter, facilitating temporary storage of 4OHI3G and 4MI3G in MVBs upon high 4OHI3G/4MI3G concentrations in the cytoplasm. In plants, several bi-directional sugar transporters were identified. For example, the *Pisium sativum* SUCROSE FACITITATOT1 (SUT1) and SUF4, the *Phaseolus vulgaris* SUF1 (Zhou et al., 2007) and several *Arabidopsis* SUGARS WILL EVENTUALLY BE EXPORTED TRANSPORTERs (SWEETs), including as SWEET1 (Chen et al., 2010) and SWEET17 (Guo et al., 2014). In mammals, the LE-localized StAR-related lipid transfer domain-3 (STAND3) was shown the mediate the transport of cholesterol into LE (Wilhelm et al., 2017). Therefore, one could imagine that a mechanism for the transport and temporary storage of indole glucosinolates in MVBs might exist in *Arabidopsis*.

Besides I3G, the abundance of the PEN2 substrate 4MI3G increased in *pen2-2* and *erd6-1* after inoculation with both *Bgh* and *E. pisi*, with *Bgh* inducing a stronger effect than *E. pisi* at 24 hpi (data not shown) and 48 hpi. Humphry *et al*., 2010 revealed no differences in 4MI3G levels in *erd6-1* mutants unchallenged and 16 hpi with *E. pisi*, indicating that 4MI3G accumulates during later stages of *E. pisi* infection.

Glycosylated dihydroascorbigen (DiHydroAsc Hex) highly accumulates in the *erd6-1* mutant, suggesting transport of this IG-metabolism product in an ERD6-dependent manner. DiHydroAsc Hex was shown to be generated following the I3G enzymatic breakdown by myrosinases. I3G hydrolysis by PEN2 or other myrosinases results in the formation of a highly unstable aglycone, which rapidly re-

acts to form an indol-3-ylmethyl isothiocyanate (I3G-ITC) (Agerbirk et al., 1998, 2008; Bednarek et al., 2009). The I3G-ITC reacts spontaneously with other plant metabolites, resulting in the formation of adducts with cysteine (I3G-Cys), glutathione (I3G-ITC-GSH) and ascorbate. The reaction of I3G-ITC with ascorbate or I3G-ITC with indole-3-carbinol and ascorbate results in the loss of the thiocyanate ion and the formation of ascorbigen (Agerbirk et al., 1998, 2008). The ascorbigen is further processed by oxidation and glycosylation, resulting in the formation of DiHydroAsc Hex. The study of Böttcher et al., 2014 identified the accumulation of glycosylated DiHydroAsc upon chemical complementation of *cyp79b2 cyp79b3* with indole-3-carbaldehyde, the tryptophan-derived IG. High levels of indole-3-carbaldehyde, were suggested to be reduced to indole-3-carbinol, which further reacts with ascorbigen to DiHydroAsc Hex (Böttcher et al., 2014). Taken together these findings might indicate that upon elevated I3G-ITC levels in the cytoplasm, the formation of DiHydroAsc Hex provides an effective mechanism for detoxification of I3C-ITC upon powdery mildew attack. DiHydroAsc Hex might be temporarily stored in MVBs in an ERD6-mediated manner to regulate IG-mediated pre-invasive resistance.

The metabolite profiles of proline (Figure 34A) and nicotinamide-beta-riboside (Figure 34B) were identified to be affected by fungal infection. In cluster 2, the metabolite profile of the amino acid proline was identified, which showed decreased intensity values in all genotypes upon attack fungal attack only at 48 hpi, suggesting increased proline consumption by the plant upon attempted powdery mildew invasion. In plants, proline was shown to accumulate in responses to different conditions, including salinity, drought, as well as in response to oxidative and biotic stresses (Hare and Cress, 1997; Fabro et al., 2004; Lehmann et al., 2010; Szabados and Savouré, 2010; Cecchini et al., 2011). Proline functions in various processes such as signal transduction, including salicylic acid (SA) signaling, translation, redox balance and osmoprotection (Szabados and Savouré, 2010). Therefore, one could imagine that the requirement of proline for translation, as well as the protective function in scavenging ROS might results in depleted proline levels after powdery mildew attack.

Nicotinamide-beta-riboside was highly enriched in all genotypes only after *E. pisi* inoculation at both timepoints. Nicotinamide-beta-riboside is a precursor of nicotinamide adenine dinucleotide (NAD), which is a vitamin B3-derived cofactor that functions in metabolic reactions and signaling events (Berger et al., 2004; Noctor et al., 2006; Makarov et al., 2019). A recent study revealed that the quinolinate phosphoribosyltransferase 1 (QPT1) of *Magnaporthe oryzae* QPT1 is required for axenic growth on media lacking the NAD precursor nicotinamide adenine (NA). In addition, the rice blast fungus was shown to acquire and assimilate vitamin B3 from the host plant (Wilson et al., 2019). Therefore, it might be possible that the metabolite profile of nicotinamide-beta-riboside results from accumulation in the powdery mildew *E. pisi* or the host plant *Arabidopsis*.

The *pen2-2* mutant accumulated high levels of 4-coumaroylagmatine (Figure 33A) and feruloylagmatine (Figure 33B) after *Bgh* infection (Cluster 7). Both substances belong to the group of hydroxycinnamic acid amides (HCAAs). These secondary metabolites were shown to be required for defense against pathogens (Carere et al., 2018), by acting as antimicrobial substances and strengthening the cell wall of the plant against microbial degradation (Muroi et al., 2009; Campos et al., 2014). Since the myrosinase PEN2 hydrolyzes S-glycosidic bonds, it is unlikely that PEN2 is involved in processing 4-coumaroylagmatine and feruloylagmatine, suggesting a secondary effect and/or induction of HCAAs due to the activation of additional defense mechanisms.

The phytoalexin camalexin (Figure 33F) was found to accumulate in all tested genotypes 48h after powdery mildew inoculation, especially with incompatible powdery mildew species. Interestingly, the camalexin derivates hydroxycamalexin hexoside (Figure 33H) and O-malonyl hydrocamalexin hexoside (Figure 33F) were particularly enriched in the *pen2-2* mutant at 24 and 48 hpi after *Bgh* inoculation. Camalexin is a tryptophan-derived phytoalexin (Böttcher et al., 2009; Sønderby et al., 2010). Tryptophan is converted to indole-3acetaldoxime (IAOx), which is the metabolic branching point for the biosynthesis of camalexin, indole glucosinolates as well as the phytohormone auxin (see 1.6.1) (Malka and Cheng, 2017; Glawischnig, 2007). IAOx is further processed to camalexin by CYP71A13 and CYP71B15, which is also known as PHYTOALEXIN DEFICIENT 3 (PAD3) (Schuhegger et al., 2006; Glawischnig, 2007). Böttcher *et al*., 2009 revealed that both camalexin metabolites, hydroxyl- and the O-malonyl conjugate of hydroxycamalexin, were generated downstream of CYP71B15 (PHYTOALEXIN DEFICIENT 3; PAD3) (Böttcher et al., 2009). These metabolites are suggested to result from camalexin detoxification reactions (Pedras and Ahiahonu, 2002; Böttcher et al., 2009). The accumulation of camalexin metabolism products might be explained by the activation of mechanisms that regulate defense responses. Since the metabolite profile of hydroxycamalexin hexoside and O-malonyl hydrocamalexin hexoside are comparable to the metabolite profile of 4MI3G upon powdery mildew infection, it might be possible that elevated 4MI3G concentrations in the *pen2* mutant might induce a negative feedback mechanism, which regulates detoxification processes, including the metabolism of camalexin.

Metabolite analysis also showed that inoculation with compatible powdery mildews lead to accumulation of the glycosylated form of the phytohormone salicylic acid (SAG; Figure 33C) as well as pipecolate (Pip; Figure 33G), which is a non-proteinous amino acid derived from lysine catabolism (Návarová et al., 2012). The effect can be observed in all investigated plant lines but is most pronounced in *pen2-2*. Both SA and Pip function as signaling molecules in systemic acquired resistance (SAR) (Nawrath and Métraux, 1999; Wildermuth et al., 2001; Návarová et al., 2012). SAR is an induced defense response in distal uninfected parts of the plant that mediates resistance against a broad spectrum of

pathogens (Ross, 1961; Durrant and Dong, 2004). For transport and storage of inactive forms of SA in the vacuole, the SA hydroxyl group is glucosylated, resulting in the formation of a salicylic acid glucoside (SAG) (Dempsey and Klessig, 2017; George Thompson et al., 2017). The metabolite profile of SAG was only enhanced in the *pen2-2* mutant at 48 hpi with *Bgh* and *E. pisi,* suggesting that SA is inactivated during later time points of *Bgh* and *E. pisi* infection. Moreover, due to the lack of accumulation of SAG and Pip in leaves after *G. orontii* infection, it might be possible that the adapted powdery mildew suppresses SA, as well as Pip biosynthesis, suggesting inhibited SAR. A recent study revealed that the PEN2-mediated IG hydrolysis product, I3A, is induced systemically upon local inoculation of leaves with *P. syringae.* Moreover, Pip and SA induction was shown to be important for systemic but not a local accumulation of I3A (Stahl et al., 2016). Therefore, one could imagine that pathogen-induced IG hydrolysis products might provide a general negative feedback mechanism to regulate defense molecules involved in SAR, such as the inactivation of SA and inhibition of Pip biosynthesis.

4.4.1.5 Potential role of ERD6 in IG-mediated pre-invasive resistance

Based on the findings of this work, the potential role of ERD6 in pre-invasive resistance will be presented in this chapter.

Several components required for IG-mediated pre-invasive resistance have been identified and characterized. So far CYP81F2, IGMT1/IGMT2, PEN2, GSTU13, PCS1 (PEN4) and PEN3 were discovered to function in the activation and transport of IGs to the site of attempted pathogen invasion (Lipka et al., 2005; Stein et al., 2006; Bednarek et al., 2009; Clay et al., 2009; Pfalz et al., 2011; Fuchs et al., 2016; Piślewska-Bednarek et al., 2018; Hématy et al., 2020). In this work, the putative sugar transporter ERD6 was identified as an additional molecular component required for pre-invasive resistance against powdery mildew in *Arabidopsis.* An untargeted metabolomics approach revealed that the tryptophan-derived indole glucosinolates I3G, 4OHI3G, 4MI3G and DiHydoAsc Hex accumulate in the *erd6* mutant, suggesting ERD6-mediated transport of these substances.

ERD6 was shown to localize to MVBs/EEs and the lumen of the vacuole (Figure 40B, 1). This suggests that ERD6 is associated with ILVs inside MVBs/LEs and is constitutively transported via this organelle to the lumen of the vacuole for degradation. However, it cannot be excluded that ERD6 is localized to the limiting membrane of MVBs. It is proposed that GLS are transported from the site of biosynthesis (the vasculature) to the site of storage (epidermal cells) (Li et al., 2011; Madsen et al., 2014; Nintemann et al., 2018). In epidermal cells, these secondary metabolites are assumed to be transported from the cytosol into the vacuole for storage by a yet unidentified vacuolar importer (Figure 39B, 3) (Madsen et al., 2014). The dual localization of the potential IG transporter to MVBs and the lumen of the vacuole suggests that MVBs function as a temporary storage compartment involved in the

transport I3G to the attempted pathogen invasion site and the vacuole for storage. However, the data presented in this work cannot exclude IG transport from the cytosol into the vacuole by a vacuolar importer.

Upon powdery mildew attack, ERD6-positive vesicles are redirected and transiently accumulate in close proximity to subpopulations of clustered and immobilized mitochondria associated with PEN2 aggregates at the plant-fungal interaction site. An untargeted metabolomics approach revealed accumulation of the PEN2/CYP81F2 substrate I3G, the IGMT1/IGMT2 substrate 4OHI3G, the PEN2 substrate 4MI3G, and the glycosylated form of dihydroascorbigen (DeHydroAsc Hex) in the *erd6-1* mutant (Figure 39A). These findings might indicate the transport of these substances in an ERD6-dependent manner.

Upon powdery mildew attack, ERD6 might relocalize the preformed and MVB-stored I3G (Figure 40A and B, 3). Enzymatic activation of I3G by the myrosinase PEN2 results in the formation of a highly reactive I3G-ITC, which is further processed to the endproducts RA and I3A (Figure 40A). However, these two compounds are not required for pre-invasive defense (Bednarek et al., 2009; Piślewska-Bednarek et al., 2018). Upon high concentrations of I3G-ITC in the cytoplasm, the IG-derived metabolism product might react spontaneously with ascorbate. The reaction of I3G-ITC with ascorbate results in the loss of the thiocyanate ion and the formation of ascorbigen (Agerbirk et al., 1998, 2008). The ascorbigen is further processed by oxidation and glycosylation, resulting in the formation of DiHydroAsc Hex (Figure 40). One hypothesis is that DiHydroAsc Hex might be transported in an ERD6-dependent manner into MVBs for temporary storage and provides a source of ascorbic acid upon degradation (Figure 40B, 2).

The cytochrome P450 monooxygenase CYP81F2 functions in the biosynthesis of 4MI3G providing the PEN2 substrate required for pathogen entry control (Figure 40) (Bednarek et al., 2009; Clay et al., 2009). CYP81F2-RFP was shown to localize to the ER, which becomes structurally reorganized in immediate proximity to subpopulations of clustered and immobilized PEN2-labelled mitochondria (Figure 39B) (Fuchs et al., 2016). Temporarily stored I3G inside the MVBs/LEs might be remobilized by ERD6 to provide the CYP81F2 substrate (Figure 40 B, 3). Following 4-hydroxylation of I3G by CYP81F2, the fourth position of the indole ring is directly methoxylated by IGMT1 or IGMT2 resulting in the generation of the PEN2 substrate 4MI3G (Figure 40A) (Pfalz et al., 2011). The subcellular localization of IGMT1 and IGMT2 is still unknown. The outer mitochondrial membrane-localized myrosinase PEN2 forms aggregates on clustered and immobilized mitochondrial subpopulations at the attempted fungal invasion site (Figure 40B, 4). PEN2 was shown to mediate 4MI3G hydrolyzation, leading to the formation of 4MI3G-ITC (Figure 40) (Bednarek et al., 2009; Clay et al., 2009; Piślewska-Bednarek et al., 2018).

It might be possible that ERD6 functions as a bi-directional indole glucosinolate transporter, facilitating temporary storage of 4OHI3G as well as 4MI3G inside MVBs (Figure 39A and B, 5). This process might be required for the regulation of defense responses at the plant-fungal interaction site. IG-metabolism leads to the generation of toxic metabolism products, required for defense against powdery mildews (Bednarek et al., 2009). Therefore, the plant requires an effective mechanism for regulation, compartmentalization and detoxification of these secondary metabolites and/or precursor substrates.

Recently it was shown that the Glutathione-S-transferase class-tau member 13 (GSTU13) functions redundantly with yet unidentified GSTs in the glutathione (GSH) transfer to the PEN2 hydrolysis product I3G-ITC. This results in the formation of indol-3-ylmethyl-isothiocyanate-glutathione (I3G-ITC-GSH) (Figure 39A). Moreover, GSTU13 mediates the conjugation of the unstable 4MI3G-ITCs with GSH (Figure 39A and B, 6) (Piślewska-Bednarek et al., 2018). This study provides evidence that N- and C-terminally RFP-tagged GSTU13, is localized to the cytosol, the nucleus and punctate structures. Upon attempted fungal penetration the cytosol accumulated at the attempted pathogen penetration site. Moreover, elevated RFP-tagged GSTU13 fluorescence intensities were observed in the accumulated cytosol beneath the plant-fungal contact site (Figure 40B, 6).

The PHYTOCHELATIN SYNTHASE1/PENETRATION4 (PCS1/PEN4) is translocated from the cytoplasm to clustered and immobilized mitochondrial subpopulations and co-localizes with PEN2 in aggregate structures (Figure 40, 7) (Hématy et al. 2020). However, no physical protein-protein interaction between PEN2 and PCS1 was observed, suggesting that additional PEN2 and PEN4 aggregate interactors exist (Hématy et al., 2020). Furthermore, PCS1 might function in the biosynthesis of RA and I3A, as well as 4MI3G to 4OGlcI3F, 4MO3IM and 4MOI3Cys (Figure 40A) (Matern et al., 2019; Hématy et al., 2020). However, the exact function of PEN4/PCS1 in IG metabolism remains elusive.

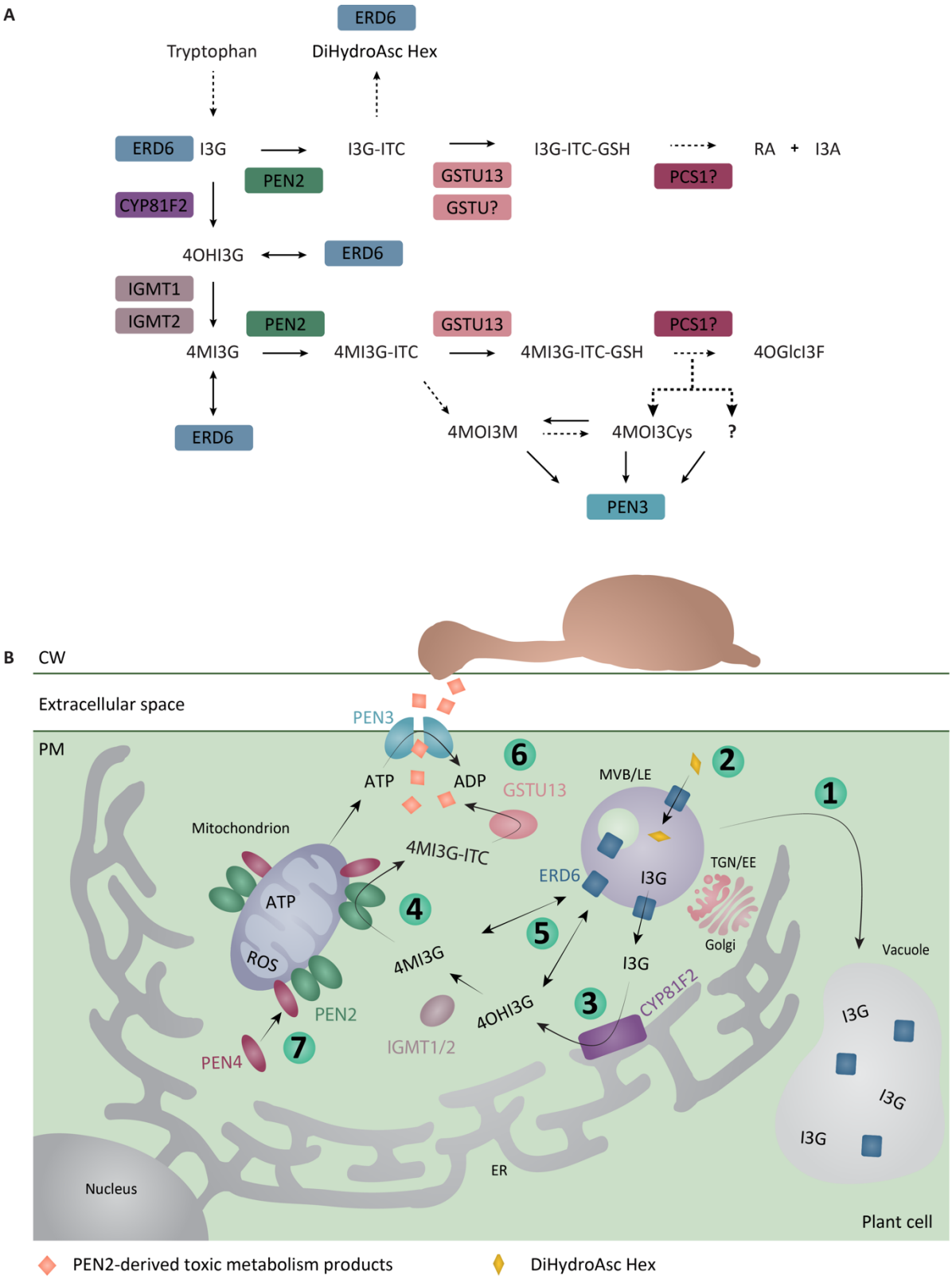

Figure 40. Model of the potential function of ERD6 in pre-invasive defense against powdery mildew. (A) A scheme depicting the role of ERD6 in powdery mildew-triggered IG metabolism in *Arabidopsis*. ERD6 might be involved in providing the PEN2 and CYP81F2 substrate I3G. Moreover, ERD6 is suggested to function in the temporary storage of 4OHI3G, 4MI3G and DiHydroAsc Hex inside MVBs. Black arrows indicate single reactions; Dashed arrows depict multiple reactions. Enzymes involved in IG-metabolism are indicated in different colors. I3G, indol-3-ylmethyl glucosinolate; I3G-ITC, indol-3-ylmethyl-isothiocyanate; I3G-ITC-GSH, indol-3-ylmethyl-

isothiocyanate-glutathione; RA, raphanusamic acid; I3A, indol-3-ylmethyl amine; 4OHI3G- 4-hydroxy-indol-3-yl-methyl glucosinolate; 4MI3G, 4-methoxyindol-3-ylmethyl glucosinolate; 4MI3G-ITC, 4-methoxyindol-3-ylmethyl-isothiocyanate; 4MI3G-ITC-GSH, 4-methoxyindol-3-ylmethyl-isothiocyanate-glutathione; 4OGlcI3F, 4-O-β-d-glucosyl-indol-3-yl formamide; 4MOI3M, 4-methoxyindol-3-methanol; 4MOI3Cys, S-(4-Methoxyindol-3-ylmethyl)cysteine; DiHydroAsc Hex, dihydroascorbigen hexoside; ERD6, EARLY RESPONSE TO DEHYDRATION 6; PEN2, PENETRATION1; CYP81F2, CYTOCHROME P450 MONOOXYGENASE; IGMT1, INDOLE GLUCOSINOLATE O-METHYLTRANSFERASE 1; IGMT2, INDOLE GLUCOSINOLATE O-METHYLTRANSFERASE 2; GSTU13, GLUTATHIONE-S-TRANSFERASE CLASS-TAU MEMBER 13; PCS1, PHYTOCHELATIN SYNTHASE 1; PEN3, PENETRATION 3. **(B) 1** ERD6 is localized to MVBs/LEs and the lumen of the vacuole, suggesting that ERD6 is constitutively transported via MVBs to the lumen of the vacuole for degradation. Upon powdery mildew attack, ERD6-positive vesicles are redirected and transiently accumulate at the plant-fungal interaction site. **2** The IG-derived metabolism product dihydroascorbigen hexoside is suggested to be transported into MVBs in an ERD6-dependent manner. **3** ERD6 might provide the preformed and MVB/LE-stored CYP81F2 substrate I3G. 4-hydroxlation of I3G by ER-localized CYP81F2 results in the formation of the 4OHI3G. The two redundant IGMT1 and IGMT2 mediate the 4-methoxylation of 4OHI3G, generating the PEN2 substrate 4MI3G. The subcellular localization of IGMT1/IGMT2 is unknown. **4** Upon the hydrolyzation of 4MI3G by the mitochondrial localized PEN2 a 4MI3G-ITC is formed. **5** 4OHI3G and 4MI3G are potential substrates of ERD6. It might be possible that ERD6 functions as a bi-directional indole glucosinolate transporter, facilitating temporary storage of IG-metabolism products inside MVBs/LEs, which might be required for the regulation of pre-invasive defense response. **5** GSTU13 accumulates in the cytoplasm beneath the attempted pathogen penetration site. GSTU13 mediates the glutathione transfer to the unstable 4MI3G-ITC-GSH. Further processing of the produced adduct results in the formation of biologically active molecules, which are secreted by the PM localized PEN3 into the apoplast to terminate attempted fungal penetration. **5** PEN4/PCS1 relocalizes from the cytoplasm to clustered and immobilized mitochondria. PCS1 might function upstream, downstream or in parallel with GSTU13 and/or PEN2. The model is based on work of this study and Lipka et al., 2005; Stein et al., 2006; Bednarek et al., 2009; Clay et al., 2009; Pfalz et al., 2011; Madsen et al., 2014; Fuchs et al., 2016; Piślewska-Bednarek et al., 2018; Matern et al., 2019; Hématy et al., 2020.

The plasma membrane-localized ABC transporter PEN3 strongly accumulates in diffuse halos and bubble-like structures beneath the invading fungal appressoria (Stein et al., 2006). PEN3 is proposed to transport potentially antimicrobial PEN2 metabolism products across the plasma membrane and into the apoplast to restrict pathogen entry at the cell periphery (Figure 40, 5) (Stein et al., 2006; Matern et al., 2019). Recently, Matern et al., 2019 identified the *Phytophthora infestans*-induced leaf surface IG-derivates 4-methoxyindol-3-methanol (4MOI3M) and S-(4-Methoxyindol-3-ylmethyl)cysteine (4MOI3Cys) as potential PEN3 substrates in *Arabidopsis*. These compounds are suggested to be derived from 4MI3G-ITC and synthesized in a PEN2- and PCS1-dependent manner.
Taken together, several molecular components required for pre-invasive resistance are still unknown and many questions are open. Future studies will provide novel insides in these molecular mechanisms and the processing of IGs, required for cell-autonomous and inducible pre-invasive defense responses in *Arabidopsis*.

4.4.1.6 Outlook

The findings presented here suggest that the MVB-associated transporter ERD6 is required for penetration resistance against the non-adapted powdery mildew *E. pisi*.

The macroscopic phenotypes showed increased *G. orontii* growth on *pen2-2* and *erd6-1* mutant plants at 20 dpi in comparison to control lines. To further confirm these findings, the number of produced spores by *G. orontii* on the *pen2-2* and *erd6-1* mutants together with the controls (Col-0 and erd6-1 expressing *ERD6-mTurquoise2*) should be quantified.

pen2 and *erd6* mutants showed accumulation of the metabolite profile of 4MI3G 48 hpi after *Bgh* infection, whereas *E. pisi* only induced a slight accumulation of 4MI3G in both mutants in comparison to the untreated controls (Figure 32D). Moreover, the accumulation of 4MI3G was absent in all tested genotypes after *G. orontii* infection. These findings might indicate that IG-mediated defense is targeted by powdery mildew effectors. Therefore, future studies should identify and characterize powdery mildew effectors required to interfere with mechanisms important for IG-mediated pre-invasive resistance. To start a comprehensive transcriptome analysis, RNA sequencing should be performed from non-adapted and adapted powdery mildews during the early stages of attempted infection. Fungal effector candidates of differentially expressed genes coding for putative secreted proteins that are specifically upregulated during early powdery mildew infection should be identified and selected from transcriptome data. Potential plant interaction partners of the putative effectors, which are involved in pre-invasive resistance should be identified by performing yeast-two-hybrid screens.

Potential effector candidates could be fluorescently tagged and analyzed concerning their subcellular localization in *Arabidopsis.* These lines could be analyzed concerning *Bgh* penetration frequencies. Elevated penetration of the non-adapted powdery mildew might indicate a potential contribution to virulence of the candidate effector.

ERD6-mTurquoise2 is localized to MVBs/LEs and the lumen of the vacuole in leaf epidermal cells. Moreover, ERD6-mTurquoise2 positive vesicles accumulate at attempted *E. pisi* invasion sites at 20 hpi. To confirm that ERD6-associated vesicles in proximity to the plant-fungal interaction site represent MVBs, plants co-expressing ERD6-mTurquoise2 with the MVB/LE marker Rha1-mCherry should be analyzed after *E. pisi* inoculation.

Mammalian and plant glucose transporters were shown to harbor specific N-terminal motifs required for proper subcellular localization (Augustin et al., 2005; Yamada et al., 2010). This study showed that mutations in the proposed di-leucine motif in the N-terminus of ERD6 (Yamada et al., 2010) did not affect ERD6 subcellular localization in *N. benthamiana*. However, the generation of a tri-leucine motif LXXXLL, similar to ESL1 (Yamada et al., 2010), resulted in potentially reduced ERD6-mTurquoise2-positive vesicles. To confirm the importance of the methionine in the putative di-leucine motif ([M]XXXLL) in the N-terminus of ERD6 for localization to MVBs, CLSM-based ERD6-positive vesicle quantification should be conducted in future experiments.

In this study, it was shown that ERD6-mTurquoise2 forms bands of a high molecular mass, suggesting stable ERD6 complex or aggregate formation. Moreover, a weak ERD6-mTurquoise2 specific band with a molecular weight of approximately 110-115 kDa was observed in the microsomal fraction, suggesting the formation of ERD6 dimer. Future experiments should be performed to analyze if ERD6 aggregate formation results from incomplete denaturation. Therefore, ERD6 protein extraction conditions for Western Blot analysis could be adjusted by using beta-mercaptoethanol instead of DTT. To reduce ERD6-mTurquoise2 aggregate formation, the boiling temperature of ERD6-mTurquoise2 samples in SDS-loading dye could be reduced. In addition, Urea could be added to the sample and/or the SDS-gel. To analyze potential dimer and homodimerization of ERD6, Co-IP experiments or FLIM-FRET analysis could be conducted using transiently co-expressing ERD6-mTurquoise2 and ERD6-mCitine in *N. benthamiana* leaves.

Immunoblot blot experiments of ERD6-mTurquoise2 expressing plants revealed a weak band with a size of approximately 60 kDa, suggesting that ERD6-mTurquoise2 exhibits a reduced apparent mass. In mammals, approximately 50% of the overall glucose transporter GLUT8 protein pool was shown to be cleaved. At least two C-terminal transmembrane helices were removed from the transporter (Alexander et al., 2020). To this end, GFP- or RFP-tagged ERD6 stable expressing lines should be generated. GFP/RFP-trap protein pulldowns from ERD6-GFP/RFP plants could be conducted to purify ERD6. Western blot experiments could be performed and the band with a reduced apparent mass could be cut out of the SDS gel and analyzed by LC-MS.

An untargeted metabolomics approach revealed that PEN2 and ERD6 affect the composition of leaf metabolite profiles in *Arabidopsis*. Besides pipecolate, all identified metabolites were confirmed by MS/MS. Therefore, future experiments should focus on the confirmation of this metabolite by MS/MS. Since untargeted metabolomics analysis only provides relative intensity values of metabolite profiles and does not allow absolute quantification of metabolite concentrations, a targeted metabolomics approach should be performed. To conduct quantitative metabolite analysis, samples should be extracted using methanol containing p-hydroxybenzyl glucosinolate as an internal standard (Andersen et al., 2013) and followed by LC-MS analysis.

The ERD6-dependent accumulation of I3G, 4OHI3G, 4MI3G and DiHydroAsc Hex might indicate potential substrates of the transporter required for pre-invasive resistance. To confirm the transport of these metabolites by ERD6, IG transport assays should be conducted in future experiments. Since 4OHI3G and 4MI3G cannot be purchased, custom-synthesized IG metabolites would have to be generated. Jørgensen *et al*., 2017 successfully applied heterologous expression of the glucosinolate transporter 1 (GTR1), GTR2 and GTR3 in *Xenopus laevis* oocytes to characterize the transport of I3G and 4-methylthiobutyl glucosinolate by the glucosinolate transporters. Analogous experiments could

be used to perform ERD6 transport assays of I3G. Besides oocytes, yeast microsomes could be used for ERD6 transport assays. External application of I3G, 4OHI3G, 4MI3G and DeHydroAsc Hex to yeast microsomes, generated from heterologously expressing ERD6 yeast cells, could be performed to investigate the import activity of ERD6.

In summary, these experiments will help to understand the function of ERD6 in pre-invasive resistance.

4.4.2 SAM-MT

The methyltransferase *S-adenosyl-L-methionine-dependent methyltransferase* (*AT1G55450*, named SAM-MT) was found to be co-expressed with *PEN2* and *PEN3*, suggesting that the protein may function in powdery mildew entry control. To investigate a potential contribution of SAM-MT in powdery mildew defense, *sam-mt* mutants were analyzed in this work (3.4.2). The T-DNA insertion line *sam-mt-2* was shown to be compromised in the transcription of the *SAM-MT* gene (Figure 34C), whereas the *sam-mt-1* mutant, which harbors a T-DNA insertion in the promoter region, exhibited *SAM-MT* transcripts. However, both mutant lines exhibited wild-type-like penetration phenotypes 72 hours after *Bgh*, *E.pisi* and *G. orontii* inoculation. These results suggest that SAM-MT is not required for penetration resistance against powdery mildew in *Arabidopsis*. However, it might be possible that SAM-MT is functionally redundant to other genes encoding enzymes with methyltransferase activity involved in the methoxylation of IGs. Metabolic engineering in *N. benthamiana* revealed that both IGMT1 and IGMT2 methylate the 4OHI3G intermediate and produce the PEN2 substrate 4MI3G (Pfalz et al., 2011). However, the contribution of IGMT1 and IGMT2 in PEN2-mediated resistance against powdery mildew has not been confirmed in *Arabidopsis*. SAM-MT together with IGMT1, IGMT2 and MPK3 were identified in the proteome of stress granules in heat-treated *Arabidopsis* seedlings (Kosmacz et al., 2019). Stress granules consist of large aggregates of mRNA and proteins and were shown to function in the regulation of the stress proteome and translatome by protein and RNA storage (Protter and Parker, 2016). These findings might indicate a potential link and functional redundancy between SAM-MT and IGMT1 and IGMT2. Future experiments should address functional redundancy and consider simultaneous disruption of *SAM-MT*, *IGMT1* as well as *IGMT2* using CRISPR-Cas9, due to genetic linkage of IGMT1 and IGMT2. Generated mutant lines should be analyzed concerning powdery mildew penetration frequencies and IGs concentrations.

An additional link of potential involvement of SAM-MT in defense against pathogen attack provides the study of Mine *et al*., 2018. The PHYTOALEXIN DEFICIENT 4 (PAD4) and SALICYLIC ACID INDUCTION DEFICIENT 2 (SID2) were shown to be required for transcriptional reprogramming in response to avirulent Pto AvrRpt2. *SAM-MT* together with *MPK3*, *MPK6*, *MYB51*, *PEN1*, *PEN3*, *ERD6* and *TCH3*

were revealed to be transcriptionally upregulated redundantly by PHYTOALEXIN DEFICIENT 4 PAD4 and SID2 4 hours post infiltration with the avirulent Pto AvrRpt2 (Mine et al., 2018). PAD4 and SID2 were shown to function redundantly during ETI, but act in a synergistic manner in the suppression of bacterial growth during PTI (Tsuda et al., 2009). Besides the involvement of PAD4 in basal immunity and ETI (Hammond-Kosack and Parker, 2003; Lipka et al., 2005; Wiermer et al., 2005; Stein et al., 2006), PAD4 was shown to function in post-invasive nonhost resistance (NHR) (Lipka et al., 2005; Stein et al., 2006). To address a potential function of SAM-MT in post-invasive NHR, *sam-mt* mutant plants should be analyzed qualitatively and quantitatively in regard to fungal growth and spore formation of *G. orontii* during later stages of infection.

4.5 The putative PEN2 interaction candidate GBPL3

To understand the molecular mechanism that coordinates the accumulation and arrest of mitochondrial subpopulations and PEN2-aggregate formation, IP-MS experiments were performed to identify putative interaction partners of PEN2 (3.5). For this purpose, leaves of stable transgenic *Arabidopsis pen2-1* plants expressing either *pPEN2::PEN2-GFP-TA$_{PEN2}$* (Lipka et al., 2005) or *pPEN2::PEN2-GFP-TA$_{PEN2\Delta TM}$* (Fuchs et al., 2016) were infiltrated either with chitin or remained untreated. Samples were incubated for 3 hours after infiltration, the PEN proteins were isolated via their GFP-tag and used for LC-MS analysis (Service Unit LCMS Protein Analytics, University of Göttingen). Only proteins with at least one assigned protein unique peptide were considered to be potential PEN2-interactors for further analysis. Peptides corresponding to PEN2-GFP-TA$_{PEN2}$ and PEN2-GFP-TA$_{PEN2\Delta TM}$ were identified in untreated and chitin-infiltrated samples in high abundance. However, peptides corresponding to different putative PEN2-GFP-TA$_{PEN2}$ interactors were identified in a relatively low abundance in the various samples. One possible explanation might be that putative chitin-triggered interaction partners of PEN2 could be highly diluted, due to whole leaf-based proteomic analysis. The most promising candidate Guanylate-binding family protein-like 3 (GBPL3) was selected for further analysis. GBPL3 was not pulled down in *pen2-1* or untreated samples and was enriched in the PEN2-GFP-TA$_{PEN2}$ chitin infiltrated sample in three biological experiments (Table 22). An additional and important selection criteria was transcription of *GBPL3* in the vegetative rosette and the predicted subcellular localization to mitochondria and/or cytoplasm (http://aramemnon.uni-koeln.de/; https://suba.live/).

In mammals, guanylate binding proteins (GBPs) have been described to function as interferon-triggered guanosine triphosphatases (GTPases) in cell-autonomous immunity against a broad spectrum of intracellular pathogens, such as bacteria, viruses and protozoa (Kim et al., 2012; Tretina et al., 2019). It might be possible that functional and mechanistic parallels of GBP-mediated immunity

could exist in plants. Upon pathogen invasion, mammalian GBPs were shown to be recruited to both the pathogen-containing vacuolar compartment and the host membrane (Modiano et al., 2005; Kim et al., 2011; Foltz et al., 2017). The pathogen-containing vacuole refers to a host-membrane-derived compartment, which is formed upon internalization of the pathogen by the host cell (Méresse et al., 1999). Due to the endosymbiogenetic origin of mitochondria (Zimorski et al., 2014), one could imagine that GBPL3 might be recruited to the outer membrane of clustered and immobilized mitochondria beneath fungal contact sites, where it might function in PEN2-aggregate formation. In mammals, it was shown that upon GBP accumulation at membranes of the pathogen containing vacuole or the host membrane, they recruit additional defense-related proteins required for oxidative defense (Kim et al., 2011; Tretina et al., 2019). GBP7 was shown to be involved in the assembly of a complex of NADPH oxidases, required for the production of superoxide to defeat listeria and mycobacteria on phagosomal membranes by transporting cytosolic complex components to the membrane (Kim et al., 2011). Moreover, GBPs were shown to be required for inflammasome complex assembly, which functions as signaling complexes and initiation of a cell death response putatively through ion efflux (Bergsbaken et al., 2009; Shenoy et al., 2012; Santos et al., 2018; Tretina et al., 2019). Therefore, one could imagine that GBPL3 might also function in the recruitment of additional molecular components required for PEN2-mediated pre-invasive resistance.

To address the contribution of GBPL3 to PEN2-mediated pathogen entry control, T-DNA insertion lines of the putative PEN2-interaction candidate were analyzed in this study (3.5.1.1). Homozygous lines were identified for both mutant lines *gbpl3-1* and *gbpl3-2*, which contain a T-DNA insertion in the promoter region of *GBPL3* (Figure 37A). However, only heterozygous *gbpl3-3* plants harboring the T-DNA in the first intron of *GBPL3* were identified via PCR-based genotyping (Figure 37B). These findings suggest that homozygous *gbpl3-3* mutants are lethal. *In vivo* germination assay (data not shown) suggested that the lack of homozygous *gbpl3* mutants is not due to failure of germination or seed lethality but possibly a defect in seed development. Since GBPL3 is also expressed in flowers, seeds and siliques (Winter *et al*., 2007), a function of GBPL3 in seed development might be possible.

Heterozygous *gbpl3-3* mutant plants showed wild-type-like penetration phenotypes 72 hours after *Bgh* inoculation. The result suggests that the heterozygous T-DNA insertion of *gbpl3-3* does not affect penetration resistance towards *Bgh*. Therefore, the potential role of GBPL3 in defense against powdery mildew could not be confirmed in this study and needs further investigation.

4.5.1 Outlook

In this work, GBPL3 was isolated as a putative PEN2 interaction partner. To address a potential function of GBPL3 in PEN2-mediated powdery mildew penetration resistance, the T-DNA insertion mu-

tants should be analyzed in more detail. Future experiments should be conducted to test if GBPL3 expression is altered in *gbpl3-1*, *gbpl3-2* and *gbpl3-3* mutants by semi-quantitative RT-PCR. If these experiments reveal reduced or absent *GBPL3* transcripts, *gbpl3-1* and *gbpl3-2* could be analyzed concerning powdery mildew penetration frequencies to identify a potential involvement of GBPL3 in pre-invasive resistance. Another possibility to identify a potential contribution of GBPL3 in pre-invasive resistance would be to analyze plants overexpressing GBPL3 and/or dominant-negative mutants of GBPL3 concerning fungal penetrations frequencies.

In this study, only heterozygous *gbpl3-3* mutants harboring the T-DNA in the first intron of *GBPL3* could be isolated via PCR-based genotyping (Figure 37B), suggesting embryo-lethality and a potential defect in seed development in homozygous *gbpl3-3* plants. To address whether *gbpl3-3* mutants exhibit a defect in seed development, siliques of heterozygous *gbpl3-3* plants could be analyzed in regard to seed development and numbers.

To further confirm the potential interaction between PEN2 and GBPL3, constructs of N- and C-terminally RFP-tagged GBPL3 could be generated. These constructs could be used for Fluorescence Lifetime Imaging Microscopy-Förster Resonance Energy Transfer (FLIM-FRET), as well as Co-IP experiments via *Agrobacterium*-mediated transient co-expression of RFP-tagged GBPL3 and GFP-tagged PEN2 in *N. benthamiana*. Moreover, further experiments could be performed to analyze stable transgenic *Arabidopsis* plants co-expressing PEN2-GFP-TA_{PEN2} and N- or C-terminally RFP-tagged GBPL3 to investigate the subcellular localization in unchallenged leaf epidermal cells, as well as potential relocalization of GBPL3 to mitochondria upon fungal attack. Moreover, these lines could be used to investigate a potential co-localization of GBPL3 in PEN2 aggregates on clustered and immobilized mitochondria underneath powdery mildew contact sites.

5 References

Abell, B.M. and Mullen, R.T. (2011). Tail-anchored membrane proteins: exploring the complex diversity of tail-anchored-protein targeting in plant cells. Plant Cell Rep **30**: 137–151.

Adachi, H., Derevnina, L., and Kamoun, S. (2019). NLR singletons, pairs, and networks: evolution, assembly, and regulation of the intracellular immunoreceptor circuitry of plants. Curr Opin Plant Biol **50**: 121–131.

Aerts, N., Mendes, M.P., and Wees, S.C.M.V. (2021). Multiple levels of crosstalk in hormone networks regulating plant defense. The Plant Journal **105**: 489–504.

Agerbirk, N., De Vos, M., Kim, J.H., and Jander, G. (2008). Indole glucosinolate breakdown and its biological effects. Phytochem Rev **8**: 101.

Agerbirk, N., Olsen, C.E., and Sørensen, H. (1998). Initial and Final Products, Nitriles, and Ascorbigens Produced in Myrosinase-Catalyzed Hydrolysis of Indole Glucosinolates. J. Agric. Food Chem. **46**: 1563–1571.

Albert, I. et al. (2015). An RLP23–SOBIR1–BAK1 complex mediates NLP-triggered immunity. Nature Plants **1**: 1–9.

Albrecht, S.C., Sobotta, M.C., Bausewein, D., Aller, I., Hell, R., Dick, T.P., and Meyer, A.J. (2014). Redesign of genetically encoded biosensors for monitoring mitochondrial redox status in a broad range of model eukaryotes. J Biomol Screen **19**: 379–386.

Alexander, C.M., Martin, J.A., Oxman, E., Kasza, I., Senn, K.A., and Dvinge, H. (2020). Alternative Splicing and Cleavage of GLUT8. Molecular and Cellular Biology **41**.

Alonso, J.M. et al. (2003). Genome-Wide Insertional Mutagenesis of Arabidopsis thaliana. Science **301**: 653–657.

An, Q., Ehlers, K., Kogel, K.-H., van Bel, A.J.E., and Hückelhoven, R. (2006a). Multivesicular compartments proliferate in susceptible and resistant MLA12-barley leaves in response to infection by the biotrophic powdery mildew fungus. New Phytol **172**: 563–576.

An, Q., Hückelhoven, R., Kogel, K.-H., and Bel, A.J.E.V. (2006b). Multivesicular bodies participate in a cell wall-associated defence response in barley leaves attacked by the pathogenic powdery mildew fungus. Cellular Microbiology **8**: 1009–1019.

Andersen, T.G. and Halkier, B.A. (2014). Upon bolting the GTR1 and GTR2 transporters mediate transport of glucosinolates to the inflorescence rather than roots. Plant Signal Behav **9**: e27740.

Andersen, T.G., Nour-Eldin, H.H., Fuller, V.L., Olsen, C.E., Burow, M., and Halkier, B.A. (2013). Integration of Biosynthesis and Long-Distance Transport Establish Organ-Specific Glucosinolate Profiles in Vegetative Arabidopsis. The Plant Cell **25**: 3133–3145.

Anjum, N.A. et al. (2016). Catalase and ascorbate peroxidase—representative H2O2-detoxifying heme enzymes in plants. Environ Sci Pollut Res **23**: 19002–19029.

Apel, K. and Hirt, H. (2004). Reactive oxygen species: metabolism, oxidative stress, and signal transduction. Annu Rev Plant Biol **55**: 373–399.

Assaad, F.F., Qiu, J.-L., Youngs, H., Ehrhardt, D., Zimmerli, L., Kalde, M., Wanner, G., Peck, S.C., Edwards, H., Ramonell, K., Somerville, C.R., and Thordal-Christensen, H. (2004). The PEN1 syntaxin defines a novel cellular compartment upon fungal attack and is required for the timely assembly of papillae. Mol Biol Cell **15**: 5118–5129.

Augustin, R., Riley, J., and Moley, K.H. (2005). GLUT8 Contains a [DE]XXXL[LI] Sorting Motif and Localizes to a Late Endosomal/Lysosomal Compartment. Traffic **6**: 1196–1212.

Baietti, M.F., Zhang, Z., Mortier, E., Melchior, A., Degeest, G., Geeraerts, A., Ivarsson, Y., Depoortere, F., Coomans, C., Vermeiren, E., Zimmermann, P., and David, G. (2012). Syndecan–syntenin–ALIX regulates the biogenesis of exosomes. Nature Cell Biology **14**: 677–685.

Bartel, B., LeClere, S., Magidin, M., and Zolman, B.K. (2001). Inputs to the Active Indole-3-Acetic Acid Pool: De Novo Synthesis, Conjugate Hydrolysis, and Indole-3-Butyric Acid b-Oxidation. J Plant Growth Regul **20**: 198–216.

Bartels, S. and Boller, T. (2015). Quo vadis, Pep? Plant elicitor peptides at the crossroads of immunity, stress, and development. J Exp Bot **66**: 5183–5193.

Barth, C. and Jander, G. (2006). Arabidopsis myrosinases TGG1 and TGG2 have redundant function in glucosinolate breakdown and insect defense. The Plant Journal **46**: 549–562.

Basu, D. and Haswell, E.S. (2017). Plant Mechanosensitive Ion Channels: An Ocean of Possibilities. Curr Opin Plant Biol **40**: 43–48.

Beck, A., Lendzian, K., Oven, M., Christmann, A., and Grill, E. (2003). Phytochelatin synthase catalyzes key step in turnover of glutathione conjugates. Phytochemistry **62**: 423–431.

Beck, M., Zhou, J., Faulkner, C., MacLean, D., and Robatzek, S. (2012). Spatio-Temporal Cellular Dynamics of the Arabidopsis Flagellin Receptor Reveal Activation Status-Dependent Endosomal Sorting. The Plant Cell **24**: 4205–4219.

Bednarek, P. (2012). Chemical warfare or modulators of defence responses - the function of secondary metabolites in plant immunity. Curr Opin Plant Biol **15**: 407–414.

Bednarek, P., Piślewska-Bednarek, M., Svatoš, A., Schneider, B., Doubský, J., Mansurova, M., Humphry, M., Consonni, C., Panstruga, R., Sanchez-Vallet, A., Molina, A., and Schulze-Lefert, P. (2009). A Glucosinolate Metabolism Pathway in Living Plant Cells Mediates Broad-Spectrum Antifungal Defense. Science **323**: 101–106.

Bednarek, P., Piślewska-Bednarek, M., Ver Loren van Themaat, E., Maddula, R.K., Svatoš, A., and Schulze-Lefert, P. (2011). Conservation and clade-specific diversification of pathogen-inducible tryptophan and indole glucosinolate metabolism in Arabidopsis thaliana relatives. New Phytol **192**: 713–726.

Bentham, A.R., Burdett, H., Anderson, P., Williams, S., and Kobe, B. (2017). Animal NLRs provide structural insights into plant NLR function. Annals of botany.

Bentham, A.R., De la Conception, J.C., Mukhi, N., Zdrzalek, R., Dreager, M., Gorenkin, D., Hughes, R.K., Banfield, M.J. (2020). A molecular roadmap to the plant immune system. JBC Reviews. **295**:14916-14934.

Berger, F., Ramírez-Hernández, M.H., and Ziegler, M. (2004). The new life of a centenarian: signalling functions of NAD(P). Trends Biochem Sci **29**: 111–118.

Bergsbaken, T., Fink, S.L., and Cookson, B.T. (2009). Pyroptosis: host cell death and inflammation. Nature Reviews Microbiology **7**: 99–109.

Bhat, R.A., Miklis, M., Schmelzer, E., Schulze-Lefert, P., and Panstruga, R. (2005). Recruitment and interaction dynamics of plant penetration resistance components in a plasma membrane microdomain. Proc Natl Acad Sci U S A **102**: 3135–3140.

Bi, G., Liebrand, T.W.H., Cordewener, J.H.G., America, A.H.P., Xu, X., and Joosten, M.H.A.J. (2014). Arabidopsis thaliana receptor-like protein AtRLP23 associates with the receptor-like kinase AtSOBIR1. Plant Signal Behav **9**: e27937.

Birch, P.R.J., Rehmany, A.P., Pritchard, L., Kamoun, S., and Beynon, J.L. (2006). Trafficking arms: oomycete effectors enter host plant cells. Trends in Microbiology **14**: 8–11.

Block, A., Li, G., Fu, Z.Q., and Alfano, J.R. (2008). Phytopathogen type III effector weaponry and their plant targets. Curr Opin Plant Biol **11**: 396–403.

Blum, R., Beck, A., Korte, A., Stengel, A., Letzel, T., Lendzian, K., and Grill, E. (2007). Function of phytochelatin synthase in catabolism of glutathione-conjugates. The Plant Journal **49**: 740–749.

Blum, R., Meyer, K.C., Wünschmann, J., Lendzian, K.J., and Grill, E. (2010). Cytosolic Action of Phytochelatin Synthase1[W][OA]. Plant Physiol **153**: 159–169.

Böhlenius, H., Mørch, S.M., Godfrey, D., Nielsen, M.E., and Thordal-Christensen, H. (2010). The Multivesicular Body-Localized GTPase ARFA1b/1c Is Important for Callose Deposition and ROR2 Syntaxin-Dependent Preinvasive Basal Defense in Barley. The Plant Cell **22**: 3831–3844.

Boller, T. and Felix, G. (2009). A Renaissance of Elicitors: Perception of Microbe-Associated Molecular Patterns and Danger Signals by Pattern-Recognition Receptors. Annual Review of Plant Biology **60**: 379–406.

Bonifacino, J.S. and Traub, L.M. (2003). Signals for sorting of transmembrane proteins to endosomes and lysosomes. Annu Rev Biochem **72**: 395–447.

Both, M., Csukai, M., Stumpf, M.P.H., and Spanu, P.D. (2005). Gene Expression Profiles of Blumeria graminis Indicate Dynamic Changes to Primary Metabolism during Development of an Obligate Biotrophic Pathogen. Plant Cell **17**: 2107–2122.

Böttcher, C., Chapman, A., Fellermeier, F., Choudhary, M., Scheel, D., and Glawischnig, E. (2014). The Biosynthetic Pathway of Indole-3-Carbaldehyde and Indole-3-Carboxylic Acid Derivatives in Arabidopsis. Plant Physiology **165**: 841–853.

Böttcher, C., Westphal, L., Schmotz, C., Prade, E., Scheel, D., and Glawischnig, E. (2009). The Multifunctional Enzyme CYP71B15 (PHYTOALEXIN DEFICIENT3) Converts Cysteine-Indole-3-Acetonitrile to

Camalexin in the Indole-3-Acetonitrile Metabolic Network of Arabidopsis thaliana. The Plant Cell **21**: 1830–1845.

Branco, R., Pearsall, E.-J., Rundle, C.A., White, R.G., Bradby, J.E., and Hardham, A.R. (2017). Quantifying the plant actin cytoskeleton response to applied pressure using nanoindentation. Protoplasma **254**: 1127–1137.

Braun, U. (2011). The current systematics and taxonomy of the powdery mildews (Erysiphales): an overview. Mycoscience **52**: 210–212.

Burdett, H., Bentham, A.R., Williams, S.J., Dodds, P.N., Anderson, P.A., Banfield, M.J., and Kobe, B. (2019). The Plant "Resistosome": Structural Insights into Immune Signaling. Cell Host & Microbe **26**: 193–201.

Cabrera, J.C., Boland, A., Messiaen, J., Cambier, P., and Van Cutsem, P. (2008). Egg box conformation of oligogalacturonides: the time-dependent stabilization of the elicitor-active conformation increases its biological activity. Glycobiology **18**: 473–482.

Campos, L., Lisón, P., López-Gresa, M.P., Rodrigo, I., Zacarés, L., Conejero, V., and Bellés, J.M. (2014). Transgenic tomato plants overexpressing tyramine N-hydroxycinnamoyltransferase exhibit elevated hydroxycinnamic acid amide levels and enhanced resistance to Pseudomonas syringae. Mol Plant Microbe Interact **27**: 1159–1169.

Cao, Y., Liang, Y., Tanaka, K., Nguyen, C.T., Jedrzejczak, R.P., Joachimiak, A., and Stacey, G. (2014). The kinase LYK5 is a major chitin receptor in Arabidopsis and forms a chitin-induced complex with related kinase CERK1. Elife **3**.

Carere, J., Powell, J., Fitzgerald, T., Kazan, K., and Gardiner, D.M. (2018). BdACT2a encodes an agmatine coumaroyl transferase required for pathogen defence in Brachypodium distachyon. Physiological and Molecular Plant Pathology **104**: 69–76.

Carney, D.S., Davies, B.A., and Horazdovsky, B.F. (2006). Vps9 domain-containing proteins: activators of Rab5 GTPases from yeast to neurons. Trends Cell Biol **16**: 27–35.

Castel, B., Ngou, P.-M., Cevik, V., Redkar, A., Kim, D.-S., Yang, Y., Ding, P., and Jones, J.D.G. (2019). Diverse NLR immune receptors activate defence via the RPW8-NLR NRG1. New Phytol **222**: 966–980.

Cecchini, N.M., Monteoliva, M.I., and Alvarez, M.E. (2011). Proline Dehydrogenase Contributes to Pathogen Defense in Arabidopsis. Plant Physiology **155**: 1947–1959.

Cesari, S., Bernoux, M., Moncuquet, P., Kroj, T., and Dodds, P.N. (2014). A novel conserved mechanism for plant NLR protein pairs: the 'integrated decoy' hypothesis. Front. Plant Sci. **5**.

Cesari, S. (2018). Multiple strategies for pathogen perception by plant immune receptors. New Phytologist **219**:17-29.

Chamberland, H., Benhamou, N., Ouellette, G.B., and Pauzé, F.J. (1989). Cytochemical detection of saccharide residues in paramural bodies formed in tomato root cells infected by Fusarium oxysporum f. sp. radicis-lycopersici. Physiological and Molecular Plant Pathology **34**: 131–146.

Chan, K.X., Phua, S.Y., Crisp, P., McQuinn, R., and Pogson, B.J. (2016). Learning the Languages of the

Chloroplast: Retrograde Signaling and Beyond. Annu Rev Plant Biol **67**: 25–53.

Chen, L.-Q. et al. (2010). Sugar transporters for intercellular exchange and nutrition of pathogens. Nature **468**: 527–532.

Chen, X., Irani, N.G., and Friml, J. (2011). Clathrin-mediated endocytosis: the gateway into plant cells. Curr Opin Plant Biol **14**: 674–682.

Cheng, C.-Y., Krishnakumar, V., Chan, A.P., Thibaud-Nissen, F., Schobel, S., and Town, C.D. (2017). Araport11: a complete reannotation of the Arabidopsis thaliana reference genome. Plant J **89**: 789–804.

Cheval, C., Samwald, S., Johnston, M.G., Keijzer, J. de, Breakspear, A., Liu, X., Bellandi, A., Kadota, Y., Zipfel, C., and Faulkner, C. (2020). Chitin perception in plasmodesmata characterizes submembrane immune-signaling specificity in plants. PNAS **117**: 9621–9629.

Chinchilla, D., Zipfel, C., Robatzek, S., Kemmerling, B., Nürnberger, T., Jones, J.D.G., Felix, G., and Boller, T. (2007). A flagellin-induced complex of the receptor FLS2 and BAK1 initiates plant defence. Nature **448**: 497–500.

Chisholm, S.T., Coaker, G., Day, B., and Staskawicz, B.J. (2006). Host-microbe interactions: shaping the evolution of the plant immune response. Cell **124**: 803–814.

Choi, H.W. and Klessig, D.F. (2016). DAMPs, MAMPs, and NAMPs in plant innate immunity. BMC Plant Biology **16**: 232.

Claus, L.A.N., Savatin, D.V., and Russinova, E. (2018). The crossroads of receptor-mediated signaling and endocytosis in plants. Journal of Integrative Plant Biology **60**: 827–840.

Clay, N.K., Adio, A.M., Denoux, C., Jander, G., and Ausubel, F.M. (2009). Glucosinolate Metabolites Required for an Arabidopsis Innate Immune Response. Science **323**: 95–101.

Collins, N.C., Thordal-Christensen, H., Lipka, V., Bau, S., Kombrink, E., Qiu, J.-L., Hückelhoven, R., Stein, M., Freialdenhoven, A., Somerville, S.C., and Schulze-Lefert, P. (2003). SNARE-protein-mediated disease resistance at the plant cell wall. Nature **425**: 973–977.

Colombatti, F., Gonzalez, D.H., and Welchen, E. (2014). Plant mitochondria under pathogen attack: A sigh of relief or a last breath? Mitochondrion **19**: 238–244.

Consonni, C., Humphry, M.E., Hartmann, H.A., Livaja, M., Durner, J., Westphal, L., Vogel, J., Lipka, V., Kemmerling, B., Schulze-Lefert, P., Somerville, S.C., and Panstruga, R. (2006). Conserved requirement for a plant host cell protein in powdery mildew pathogenesis. Nature Genetics **38**: 716–720.

Cornelis, G.R. and Van Gijsegem, F. (2000). Assembly and Function of Type III Secretory Systems. Annual Review of Microbiology **54**: 735–774.

Crouzet, J., Trombik, T., Fraysse, A.S., and Boutry, M. (2006). Organization and function of the plant pleiotropic drug resistance ABC transporter family. FEBS Lett **580**: 1123–1130.

Cui, H., Tsuda, K., and Parker, J.E. (2015). Effector-triggered immunity: from pathogen perception to

robust defense. Annu Rev Plant Biol **66**: 487–511.

Dangl, J.L. and Jones, J.D.G. (2019). A pentangular plant inflammasome. Science **364**: 31–32.
De Zutter, J.K., Levine, K.B., Deng, D., and Carruthers, A. (2013). Sequence determinants of GLUT1 oligomerization: analysis by homology-scanning mutagenesis. J Biol Chem **288**: 20734–20744.

Dempsey, D.A. and Klessig, D.F. (2017). How does the multifaceted plant hormone salicylic acid combat disease in plants and are similar mechanisms utilized in humans? BMC Biology **15**: 23.

Denoux, C., Galletti, R., Mammarella, N., Gopalan, S., Werck, D., De Lorenzo, G., Ferrari, S., Ausubel, F.M., and Dewdney, J. (2008). Activation of Defense Response Pathways by OGs and Flg22 Elicitors in Arabidopsis Seedlings. Molecular Plant **1**: 423–445.

Dettmer, J., Hong-Hermesdorf, A., Stierhof, Y.-D., and Schumacher, K. (2006). Vacuolar H+-ATPase activity is required for endocytic and secretory trafficking in Arabidopsis. Plant Cell **18**: 715–730.
Ding, X., Jimenez-Gongora, T., Krenz, B., and Lozano-Duran, R. (2019). Chloroplast clustering around the nucleus is a general response to pathogen perception in Nicotiana benthamiana. Mol Plant Pathol **20**: 1298–1306.

Dixon, D.P. and Edwards, R. (2010). Glutathione Transferases. Arabidopsis Book **8**.

Dixon, D.P., Hawkins, T., Hussey, P.J., and Edwards, R. (2009). Enzyme activities and subcellular localization of members of the Arabidopsis glutathione transferase superfamily. J Exp Bot **60**: 1207–1218.

Dodds, P.N., Lawrence, G.J., Catanzariti, A.-M., Ayliffe, M.A., and Ellis, J.G. (2004). The Melampsora lini AvrL567 avirulence genes are expressed in haustoria and their products are recognized inside plant cells. Plant Cell **16**: 755–768.

Dodds, P.N., Lawrence, G.J., Catanzariti, A.-M., Teh, T., Wang, C.-I.A., Ayliffe, M.A., Kobe, B., and Ellis, J.G. (2006). Direct protein interaction underlies gene-for-gene specificity and coevolution of the flax resistance genes and flax rust avirulence genes. Proc Natl Acad Sci U S A **103**: 8888–8893.

Dodds, P.N. and Rathjen, J.P. (2010). Plant immunity: towards an integrated view of plant–pathogen interactions. Nature Reviews Genetics **11**: 539–548.

Dombrecht, B., Xue, G.P., Sprague, S.J., Kirkegaard, J.A., Ross, J.J., Reid, J.B., Fitt, G.P., Sewelam, N., Schenk, P.M., Manners, J.M., and Kazan, K. (2007). MYC2 Differentially Modulates Diverse Jasmonate-Dependent Functions in Arabidopsis. The Plant Cell **19**: 2225–2245.

Durrant, W.E. and Dong, X. (2004). Systemic Acquired Resistance. Annual Review of Phytopathology **42**: 185–209.

Duxbury, Z., Ma, Y., Furzer, O.J., Huh, S.U., Cevik, V., Jones, J.D.G., and Sarris, P.F. (2016). Pathogen perception by NLRs in plants and animals: Parallel worlds. Bioessays **38**: 769–781.

Ebine, K. et al. (2011). A membrane trafficking pathway regulated by the plant-specific RAB GTPase ARA6. Nature Cell Biology **13**: 853–859.

Eichmann, R. and Hückelhoven, R. (2008). Accommodation of powdery mildew fungi in intact plant cells. Journal of Plant Physiology **165**: 5–18.

El Zawily, A.M. et al. (2014). FRIENDLY Regulates Mitochondrial Distribution, Fusion, and Quality Control in Arabidopsis1[W][OPEN]. Plant Physiol **166**: 808–828.

Ellinger, D. and Voigt, C.A. (2014). Callose biosynthesis in arabidopsis with a focus on pathogen response: what we have learned within the last decade. Ann Bot **114**: 1349–1358.

Ellis, J. (2006). Insights into Nonhost Disease Resistance: Can They Assist Disease Control in Agriculture? The Plant Cell **18**: 523–528.

Ellis, R.J. (2001). Macromolecular crowding: obvious but underappreciated. Trends in Biochemical Sciences **26**: 597–604.

Engelhardt, S., Boevink, P.C., Armstrong, M.R., Ramos, M.B., Hein, I., and Birch, P.R.J. (2012). Relocalization of Late Blight Resistance Protein R3a to Endosomal Compartments Is Associated with Effector Recognition and Required for the Immune Response. The Plant Cell **24**: 5142–5158.

Erwig, J., Ghareeb, H., Kopischke, M., Hacke, R., Matei, A., Petutschnig, E., and Lipka, V. (2017). Chitin-induced and CHITIN ELICITOR RECEPTOR KINASE1 (CERK1) phosphorylation-dependent endocytosis of Arabidopsis thaliana LYSIN MOTIF-CONTAINING RECEPTOR-LIKE KINASE5 (LYK5). New Phytologist **215**: 382–396.

Fabro, G., Kovács, I., Pavet, V., Szabados, L., and Alvarez, M.E. (2004). Proline Accumulation and AtP5CS2 Gene Activation Are Induced by Plant-Pathogen Incompatible Interactions in Arabidopsis. MPMI **17**: 343–350.

Fan, J., Crooks, C., Creissen, G., Hill, L., Fairhurst, S., Doerner, P., and Lamb, C. (2011). Pseudomonas sax Genes Overcome Aliphatic Isothiocyanate–Mediated Non-Host Resistance in Arabidopsis. Science **331**: 1185–1188.

Fan, L., Li, R., Pan, J., Ding, Z., and Lin, J. (2015). Endocytosis and its regulation in plants. Trends Plant Sci **20**: 388–397.

Faulkner, C., Petutschnig, E., Benitez-Alfonso, Y., Beck, M., Robatzek, S., Lipka, V., and Maule, A.J. (2013). LYM2-dependent chitin perception limits molecular flux via plasmodesmata. PNAS **110**: 9166–9170.

Faustin, B., Lartigue, L., Bruey, J.-M., Luciano, F., Sergienko, E., Bailly-Maitre, B., Volkmann, N., Hanein, D., Rouiller, I., and Reed, J.C. (2007). Reconstituted NALP1 inflammasome reveals two-step mechanism of caspase-1 activation. Mol Cell **25**: 713–724.

Felle, H.H. (2001). pH: Signal and Messenger in Plant Cells. Plant Biology **3**: 577–591.

Felle, H.H., Herrmann, A., Hanstein, S., Hückelhoven, R., and Kogel, K.-H. (2004). Apoplastic pH signaling in barley leaves attacked by the powdery mildew fungus Blumeria graminis f. sp. hordei. Mol Plant Microbe Interact **17**: 118–123.

Ferrari, S., Savatin, D.V., Sicilia, F., Gramegna, G., Cervone, F., and De Lorenzo, G. (2013). Oligogalacturonides: plant damage-associated molecular patterns and regulators of growth and development. Front. Plant Sci. **4**.

Feussner, I. and Wasternack, C. (2002). The lipoxygenase pathway. Annu Rev Plant Biol **53**: 275–297.
Feys, B.J., Wiermer, M., Bhat, R.A., Moisan, L.J., Medina-Escobar, N., Neu, C., Cabral, A., and Parker, J.E. (2005). Arabidopsis SENESCENCE-ASSOCIATED GENE101 stabilizes and signals within an ENHANCED DISEASE SUSCEPTIBILITY1 complex in plant innate immunity. Plant Cell **17**: 2601–2613.

Flor, H.H. (1971). Current Status of the Gene-For-Gene Concept. Annual Review of Phytopathology **9**: 275–296.

Foltz, C., Napolitano, A., Khan, R., Clough, B., Hirst, E.M., and Frickel, E.-M. (2017). TRIM21 is critical for survival of Toxoplasma gondii infection and localises to GBP-positive parasite vacuoles. Scientific Reports **7**: 5209.

Foresti, O. and Denecke, J. (2008). Intermediate organelles of the plant secretory pathway: identity and function. Traffic **9**: 1599–1612.

Foyer, C.H. and Noctor, G. (2005). Redox homeostasis and antioxidant signaling: a metabolic interface between stress perception and physiological responses. Plant Cell **17**: 1866–1875.

Frerigmann, H. and Gigolashvili, T. (2014). MYB34, MYB51, and MYB122 Distinctly Regulate Indolic Glucosinolate Biosynthesis in Arabidopsis thaliana. Molecular Plant **7**: 814–828.

Freytag, S., Arabatzis, N., Hahlbrock, K., and Schmelzer, E. (1994). Reversible cytoplasmic rearrangements precede wall apposition, hypersensitive cell death and defense-related gene activation in potato/ Phytophthora infestans interactions. Planta **194**: 123–135.

Fuchs, R. (2012). Analysen zum subzellulären Lokalisationsverhalten der atypischen Myrosinase PEN2 in Arabidopsis-Mikroben-Interaktionen.

Fuchs, R., Kopischke, M., Klapprodt, C., Hause, G., Meyer, A.J., Schwarzländer, M., Fricker, M.D., and Lipka, V. (2016). Immobilized Subpopulations of Leaf Epidermal Mitochondria Mediate PENETRATION2-Dependent Pathogen Entry Control in Arabidopsis. Plant Cell **28**: 130–145.

Gachon, C.M.M., Langlois-Meurinne, M., Henry, Y., and Saindrenan, P. (2005). Transcriptional co-regulation of secondary metabolism enzymes in Arabidopsis: functional and evolutionary implications. Plant Mol Biol **58**: 229–245.

Gallie, D.R. (2013). The role of l-ascorbic acid recycling in responding to environmental stress and in promoting plant growth. Journal of Experimental Botany **64**: 433–443.

Gao, C., Xing, D., Li, L., and Zhang, L. (2008). Implication of reactive oxygen species and mitochondrial dysfunction in the early stages of plant programmed cell death induced by ultraviolet-C overexposure. Planta **227**: 755–767.

Gao, Q.-M., Zhu, S., Kachroo, P., and Kachroo, A. (2015). Signal regulators of systemic acquired resistance. Front. Plant Sci. **6**.

Geldner, N., Dénervaud-Tendon, V., Hyman, D.L., Mayer, U., Stierhof, Y.-D., and Chory, J. (2009). Rapid, combinatorial analysis of membrane compartments in intact plants with a multicolor marker set. Plant J **59**: 169–178.

Geldner, N., Hyman, D.L., Wang, X., Schumacher, K., and Chory, J. (2007). Endosomal signaling of

plant steroid receptor kinase BRI1. Genes Dev **21**: 1598–1602.

George Thompson, A.M., Iancu, C.V., Neet, K.E., Dean, J.V., and Choe, J. (2017). Differences in salicylic acid glucose conjugations by UGT74F1 and UGT74F2 from Arabidopsis thaliana. Scientific Reports **7**: 46629.

Ghareeb, H., Laukamm, S., and Lipka, V. (2016). COLORFUL-Circuit: A Platform for Rapid Multigene Assembly, Delivery, and Expression in Plants. Front Plant Sci **7**.

Gigolashvili, T., Berger, B., Mock, H.-P., Müller, C., Weisshaar, B., and Flügge, U.-I. (2007). The transcription factor HIG1/MYB51 regulates indolic glucosinolate biosynthesis in Arabidopsis thaliana. The Plant Journal **50**: 886–901.

Glawischnig, E. (2007). Camalexin. Phytochemistry **68**: 401–406.

Goedhart, J., von Stetten, D., Noirclerc-Savoye, M., Lelimousin, M., Joosen, L., Hink, M.A., van Weeren, L., Gadella, T.W.J., and Royant, A. (2012). Structure-guided evolution of cyan fluorescent proteins towards a quantum yield of 93%. Nature Communications **3**: 751.

Goepfert, S., Vidoudez, C., Rezzonico, E., Hiltunen, J.K., and Poirier, Y. (2005). Molecular identification and characterization of the Arabidopsis delta(3,5),delta(2,4)-dienoyl-coenzyme A isomerase, a peroxisomal enzyme participating in the beta-oxidation cycle of unsaturated fatty acids. Plant Physiol **138**: 1947–1956.

Green, J., Carver, T., Gurr, S., Bélanger, R., Bushnell, W., and Dik, A. (2002). The formation and function of infection and feeding structures. undefined.

Grill, E., Löffler, S., Winnacker, E.-L., and Zenk, M.H. (1989). Phytochelatins, the heavy-metal-binding peptides of plants, are synthesized from glutathione by a specific γ-glutamylcysteine dipeptidyl transpeptidase (phytochelatin synthase). Proc Natl Acad Sci U S A **86**: 6838–6842.

Grzam, A., Tennstedt, P., Clemens, S., Hell, R., and Meyer, A.J. (2006). Vacuolar sequestration of glutathione S-conjugates outcompetes a possible degradation of the glutathione moiety by phytochelatin synthase. FEBS Lett **580**: 6384–6390.

Guan, R., Su, J., Meng, X., Li, S., Liu, Y., Xu, J., and Zhang, S. (2015). Multilayered Regulation of Ethylene Induction Plays a Positive Role in Arabidopsis Resistance against Pseudomonas syringae. Plant Physiology **169**: 299–312.

Guigas, G. and Weiss, M. (2016). Effects of protein crowding on membrane systems. Biochimica et Biophysica Acta (BBA) - Biomembranes **1858**: 2441–2450.

Guo, W.-J., Nagy, R., Chen, H.-Y., Pfrunder, S., Yu, Y.-C., Santelia, D., Frommer, W.B., and Martinoia, E. (2014). SWEET17, a Facilitative Transporter, Mediates Fructose Transport across the Tonoplast of Arabidopsis Roots and Leaves. Plant Physiology **164**: 777–789.

Gus-Mayer, S., Naton, B., Hahlbrock, K., and Schmelzer, E. (1998). Local mechanical stimulation induces components of the pathogen defense response in parsley. PNAS **95**: 8398–8403.

Haas, T.J., Sliwinski, M.K., Martínez, D.E., Preuss, M., Ebine, K., Ueda, T., Nielsen, E., Odorizzi, G., and Otegui, M.S. (2007). The Arabidopsis AAA ATPase SKD1 Is Involved in Multivesicular Endosome

Function and Interacts with Its Positive Regulator LYST-INTERACTING PROTEIN5. The Plant Cell **19**: 1295–1312.

Halkier, B.A. and Gershenzon, J. (2006). Biology and biochemistry of glucosinolates. Annu Rev Plant Biol **57**: 303–333.

Hammond-Kosack, K.E. and Parker, J.E. (2003). Deciphering plant-pathogen communication: fresh perspectives for molecular resistance breeding. Curr Opin Biotechnol **14**: 177–193.

Han, L., Li, G.-J., Yang, K.-Y., Mao, G., Wang, R., Liu, Y., and Zhang, S. (2010). Mitogen-activated protein kinase 3 and 6 regulate Botrytis cinerea-induced ethylene production in Arabidopsis. Plant J **64**: 114–127.

Hansen, L.L. and Nielsen, M.E. (2017). Plant exosomes: using an unconventional exit to prevent pathogen entry? J Exp Bot **69**: 59–68.

Hardham, A.R., Takemoto, D., and White, R.G. (2008). Rapid and dynamic subcellular reorganization following mechanical stimulation of Arabidopsisepidermal cells mimics responses to fungal and oomycete attack. BMC Plant Biology **8**: 63.

Hare, P.D. and Cress, W.A. (1997). Metabolic implications of stress-induced proline accumulation in plants. Plant Growth Regulation **21**: 79–102.

Hazen, B.E. and Bushnell, W.R. (1983). Inhibition of the hypersensitive reaction in barley to powdery mildew by heat shock and cytochalasin B. Physiological Plant Pathology **23**: 421–438.

Heath, M.C. (2000). Nonhost resistance and nonspecific plant defenses. Curr Opin Plant Biol **3**: 315–319.

Hebert, D.N. and Carruthers, A. (1991). Cholate-solubilized erythrocyte glucose transporters exist as a mixture of homodimers and homotetramers. Biochemistry **30**: 4654–4658.

Heese, A., Hann, D.R., Gimenez-Ibanez, S., Jones, A.M.E., He, K., Li, J., Schroeder, J.I., Peck, S.C., and Rathjen, J.P. (2007). The receptor-like kinase SERK3/BAK1 is a central regulator of innate immunity in plants. Proc Natl Acad Sci U S A **104**: 12217–12222.

Hématy, K. et al. (2020). Moonlighting Function of Phytochelatin Synthase1 in Extracellular Defense against Fungal Pathogens. Plant Physiology **182**: 1920–1932.

Hiruma, K., Onozawa-Komori, M., Takahashi, F., Asakura, M., Bednarek, P., Okuno, T., Schulze-Lefert, P., and Takano, Y. (2010). Entry mode-dependent function of an indole glucosinolate pathway in Arabidopsis for nonhost resistance against anthracnose pathogens. Plant Cell **22**: 2429–2443.

Hofberger, J.A., Lyons, E., Edger, P.P., Chris Pires, J., and Eric Schranz, M. (2013). Whole genome and tandem duplicate retention facilitated glucosinolate pathway diversification in the mustard family. Genome Biol Evol **5**: 2155–2173.

Holmes, D.R., Grubb, L.E., and Monaghan, J. (2018). The jasmonate receptor COI1 is required for AtPep1-induced immune responses in Arabidopsis thaliana. BMC Res Notes **11**: 555.

Hoorn, R.A.L. van der and Kamoun, S. (2008). From Guard to Decoy: A New Model for Perception of Plant Pathogen Effectors. The Plant Cell **20**: 2009–2017.

Hopkins, R.J., van Dam, N.M., and van Loon, J.J.A. (2009). Role of glucosinolates in insect-plant relationships and multitrophic interactions. Annu Rev Entomol **54**: 57–83.

Horbach, R., Navarro-Quesada, A.R., Knogge, W., and Deising, H.B. (2011). When and how to kill a plant cell: infection strategies of plant pathogenic fungi. J Plant Physiol **168**: 51–62.

Howden, R., Goldsbrough, P.B., Andersen, C.R., and Cobbett, C.S. (1995). Cadmium-sensitive, cad1 mutants of Arabidopsis thaliana are phytochelatin deficient. Plant Physiol **107**: 1059–1066.

Hückelhoven, R. (2005). Powdery mildew susceptibility and biotrophic infection strategies. FEMS Microbiology Letters **245**: 9–17.

Huffaker, A., Pearce, G., and Ryan, C.A. (2006). An endogenous peptide signal in Arabidopsis activates components of the innate immune response. PNAS **103**: 10098–10103.

Humphry, M., Bednarek, P., Kemmerling, B., Koh, S., Stein, M., Göbel, U., Stüber, K., Piślewska-Bednarek, M., Loraine, A., Schulze-Lefert, P., Somerville, S., and Panstruga, R. (2010). A regulon conserved in monocot and dicot plants defines a functional module in antifungal plant immunity. Proc Natl Acad Sci U S A **107**: 21896–21901.

Hunziker, P., Ghareeb, H., Wagenknecht, L., Crocoll, C., Halkier, B.A., Lipka, V., and Schulz, A. (2020). De novo indol-3-ylmethyl glucosinolate biosynthesis, and not long-distance transport, contributes to defence of Arabidopsis against powdery mildew. Plant, Cell & Environment **43**: 1571–1583.

Hunziker, P., Halkier, B.A., and Schulz, A. (2019). Arabidopsis glucosinolate storage cells transform into phloem fibres at late stages of development. J Exp Bot **70**: 4305–4317.

Husebye, H., Chadchawan, S., Winge, P., Thangstad, O.P., and Bones, A.M. (2002). Guard Cell- and Phloem Idioblast-Specific Expression of Thioglucoside Glucohydrolase 1 (Myrosinase) in Arabidopsis. Plant Physiology **128**: 1180–1188.

Huss, M., Ingenhorst, G., König, S., Gassel, M., Dröse, S., Zeeck, A., Altendorf, K., and Wieczorek, H. (2002). Concanamycin A, the specific inhibitor of V-ATPases, binds to the V(o) subunit c. J Biol Chem **277**: 40544–40548.

Irani, N.G. and Russinova, E. (2009). Receptor endocytosis and signaling in plants. Curr Opin Plant Biol **12**: 653–659.

Jaipargas, E.-A., Mathur, N., Bou Daher, F., Wasteneys, G.O., and Mathur, J. (2016). High Light Intensity Leads to Increased Peroxule-Mitochondria Interactions in Plants. Front. Cell Dev. Biol. **4**.

Jarosch, B., Collins, N.C., Zellerhoff, N., and Schaffrath, U. (2005). RAR1, ROR1, and the actin cytoskeleton contribute to basal resistance to Magnaporthe grisea in barley. Mol Plant Microbe Interact **18**: 397–404.

Jeschke, V., Weber, K., Moore, S.S., and Burow, M. (2019). Coordination of Glucosinolate Biosynthesis and Turnover Under Different Nutrient Conditions. Front Plant Sci **10**.

Johansson, O.N., Fantozzi, E., Fahlberg, P., Nilsson, A.K., Buhot, N., Tör, M., and Andersson, M.X.

(2014). Role of the penetration-resistance genes PEN1, PEN2 and PEN3 in the hypersensitive response and race-specific resistance in Arabidopsis thaliana. The Plant Journal **79**: 466–476.

Jones, J.D.G. and Dangl, J.L. (2006). The plant immune system. Nature **444**: 323–329.

Jones, J.D.G., Vance, R.E., and Dangl, J.L. (2016). Intracellular innate immune surveillance devices in plants and animals. Science **354**.

Jørgensen, M.E., Xu, D., Crocoll, C., Ernst, H.A., Ramírez, D., Motawia, M.S., Olsen, C.E., Mirza, O., Nour-Eldin, H.H., and Halkier, B.A. (2017). Origin and evolution of transporter substrate specificity within the NPF family. Elife **6**.

Jubic, L.M., Saile, S., Furzer, O.J., El Kasmi, F., and Dangl, J.L. (2019). Help wanted: helper NLRs and plant immune responses. Curr Opin Plant Biol **50**: 82–94.

Kaever, A., Landesfeind, M., Feussner, K., Mosblech, A., Heilmann, I., Morgenstern, B., Feussner, I., and Meinicke, P. (2015). MarVis-Pathway: integrative and exploratory pathway analysis of non-targeted metabolomics data. Metabolomics **11**: 764–777.

Kanyuka, K. and Rudd, J.J. (2019). Cell surface immune receptors: the guardians of the plant's extracellular spaces. Current Opinion in Plant Biology **50**: 1–8.

Kearse, M. et al. (2012). Geneious Basic: an integrated and extendable desktop software platform for the organization and analysis of sequence data. Bioinformatics **28**: 1647–1649.

Kelly, P.J., Bones, A., and Rossiter, J.T. (1998). Sub-cellular immunolocalization of the glucosinolate sinigrin in seedlings of Brassica juncea. Planta **206**: 370–377.

Kim, B.-H., Shenoy, A.R., Kumar, P., Bradfield, C.J., and MacMicking, J.D. (2012). IFN-inducible GTPases in Host Defense. Cell Host Microbe **12**: 432–444.

Kim, B.-H., Shenoy, A.R., Kumar, P., Das, R., Tiwari, S., and MacMicking, J.D. (2011). A Family of IFN-γ–Inducible 65-kD GTPases Protects Against Bacterial Infection. Science **332**: 717–721.

Kim, C.Y., Liu, Y., Thorne, E.T., Yang, H., Fukushige, H., Gassmann, W., Hildebrand, D., Sharp, R.E., and Zhang, S. (2003). Activation of a Stress-Responsive Mitogen-Activated Protein Kinase Cascade Induces the Biosynthesis of Ethylene in Plants. The Plant Cell **15**: 2707–2718.

Kim, D.-Y., Bovet, L., Maeshima, M., Martinoia, E., and Lee, Y. (2007). The ABC transporter AtPDR8 is a cadmium extrusion pump conferring heavy metal resistance. Plant J **50**: 207–218.

Kissen, R., Rossiter, J.T., and Bones, A.M. (2009). The 'mustard oil bomb': not so easy to assemble?! Localization, expression and distribution of the components of the myrosinase enzyme system. Phytochem Rev **8**: 69–86.

Kittur, F.S., Lalgondar, M., Yu, H.Y., Bevan, D.R., and Esen, A. (2007). Maize beta-glucosidase-aggregating factor is a polyspecific jacalin-related chimeric lectin, and its lectin domain is responsible for beta-glucosidase aggregation. J Biol Chem **282**: 7299–7311.

Kiyosue, T., Abe, H., Yamaguchi-Shinozaki, K., and Shinozaki, K. (1998). ERD6, a cDNA clone for an early dehydration-induced gene of Arabidopsis, encodes a putative sugar transporter1The nucleotide

sequence reported in this paper has been submitted to DDBJ with the accession number of D89051.1. Biochimica et Biophysica Acta (BBA) - Biomembranes **1370**: 187–191.

Kiyosue, T., Yamaguchi-Shinozaki, K., and Shinozaki, K. (1994). Cloning of cDNAs for genes that are early-responsive to dehydration stress (ERDs) inArabidopsis thaliana L.: identification of three ERDs as HSP cognate genes. Plant Mol Biol **25**: 791–798.

Kleinboelting, N., Huep, G., Kloetgen, A., Viehoever, P., and Weisshaar, B. (2012). GABI-Kat SimpleSearch: new features of the Arabidopsis thaliana T-DNA mutant database. Nucleic Acids Res **40**: D1211–D1215.

Klemens, P.A.W., Patzke, K., Trentmann, O., Poschet, G., Büttner, M., Schulz, A., Marten, I., Hedrich, R., and Neuhaus, H.E. (2014). Overexpression of a proton-coupled vacuolar glucose exporter impairs freezing tolerance and seed germination. New Phytol **202**: 188–197.

Kobayashi, I., Kobayashi, Y., and Hardham, A.R. (1994). Dynamic reorganization of microtubules and microfilaments in flax cells during the resistance response to flax rust infection. Planta **195**: 237–247.

Kobayashi, I., Kobayashi, Y., and Hardham, A.R. (1997). Inhibition of rust-induced hypersensitive response in flax cells by the microtubule inhibitor oryzalin. Australian journal of plant physiology.

Kobayashi, I., Kobayashi, Y., Yamaoka, N., and Kunoh, H. (1992). Recognition of a pathogen and a nonpathogen by barley coleoptile cells. III. Responses of microtubules and actin filaments in barley coleoptile cells to penetration attempts. Canadian journal of botany = Journal canadien de botanique.

Koh, S., André, A., Edwards, H., Ehrhardt, D., and Somerville, S. (2005). Arabidopsis thaliana subcellular responses to compatible Erysiphe cichoracearum infections. The Plant Journal **44**: 516–529.

Kohorn, B.D., Hoon, D., Minkoff, B.B., Sussman, M.R., and Kohorn, S.L. (2016). Rapid Oligo-Galacturonide Induced Changes in Protein Phosphorylation in Arabidopsis. Mol Cell Proteomics **15**: 1351–1359.

Koroleva, O.A., Davies, A., Deeken, R., Thorpe, M.R., Tomos, A.D., and Hedrich, R. (2000). Identification of a New Glucosinolate-Rich Cell Type in Arabidopsis Flower Stalk. Plant Physiology **124**: 599–608.

Koroleva, O.A., Gibson, T.M., Cramer, R., and Stain, C. (2010). Glucosinolate-accumulating S-cells in Arabidopsis leaves and flower stalks undergo programmed cell death at early stages of differentiation. Plant J **64**: 456–469.

Kosmacz, M., Gorka, M., Schmidt, S., Luzarowski, M., Moreno, J.C., Szlachetko, J., Leniak, E., Sokolowska, E.M., Sofroni, K., Schnittger, A., and Skirycz, A. (2019). Protein and metabolite composition of Arabidopsis stress granules. New Phytologist **222**: 1420–1433.

Kotzer, A.M., Brandizzi, F., Neumann, U., Paris, N., Moore, I., and Hawes, C. (2004). AtRabF2b (Ara7) acts on the vacuolar trafficking pathway in tobacco leaf epidermal cells. Journal of Cell Science **117**: 6377–6389.

Krogh, A., Larsson, B., von Heijne, G., and Sonnhammer, E.L. (2001). Predicting transmembrane protein topology with a hidden Markov model: application to complete genomes. J Mol Biol **305**:

567–580.

Kuhn, H., Kwaaitaal, M., Kusch, S., Acevedo-Garcia, J., Wu, H., and Panstruga, R. (2016). Biotrophy at Its Best: Novel Findings and Unsolved Mysteries of the Arabidopsis-Powdery Mildew Pathosystem. Arabidopsis Book **14**.

Kumar, A.S., Park, E., Nedo, A., Alqarni, A., Ren, L., Hoban, K., Modla, S., McDonald, J.H., Kambhamettu, C., Dinesh-Kumar, S.P., and Caplan, J.L. (2018). Stromule extension along microtubules coordinated with actin-mediated anchoring guides perinuclear chloroplast movement during innate immunity. eLife **7**: e23625.

Kunoh, H. (1972). Incorporation of Host Mitochondria into the Haustorial Encapsulation of Barley Powdery Mildew (I). Jpn. J. Phytopathol. **38**: 357-358_1.

Kunze, G., Zipfel, C., Robatzek, S., Niehaus, K., Boller, T., and Felix, G. (2004). The N Terminus of Bacterial Elongation Factor Tu Elicits Innate Immunity in Arabidopsis Plants. The Plant Cell **16**: 3496–3507.

Kwon, C. et al. (2008). Co-option of a default secretory pathway for plant immune responses. Nature **451**: 835–840.

Labrou, N.E., Papageorgiou, A.C., Pavli, O., and Flemetakis, E. (2015). Plant GSTome: structure and functional role in xenome network and plant stress response. Curr Opin Biotechnol **32**: 186–194.

Lamb, C.J., Ryals, J.A., Ward, E.R., and Dixon, R.A. (1992). Emerging strategies for enhancing crop resistance to microbial pathogens. Biotechnology (N Y) **10**: 1436–1445.

Lapin, D., Kovacova, V., Sun, X., Dongus, J.A., Bhandari, D., von Born, P., Bautor, J., Guarneri, N., Rzemieniewski, J., Stuttmann, J., Beyer, A., and Parker, J.E. (2019). A Coevolved EDS1-SAG101-NRG1 Module Mediates Cell Death Signaling by TIR-Domain Immune Receptors. Plant Cell **31**: 2430–2455.

Lassowskat, I., Böttcher, C., Eschen-Lippold, L., Scheel, D., and Lee, J. (2014). Sustained mitogen-activated protein kinase activation reprograms defense metabolism and phosphoprotein profile in Arabidopsis thaliana. Front Plant Sci **5**: 554.

Leckie, C.P., And, J. a. C., and Green, J.R. (1995). Reorganization of the endoplasmic reticulum in pea leaf epidermal cells infected by the powdery mildew fungus Erysiphe pisi. New Phytologist **131**: 211–221.

Lee, G.-J., Sohn, E.J., Lee, M.H., and Hwang, I. (2004). The Arabidopsis rab5 homologs rha1 and ara7 localize to the prevacuolar compartment. Plant Cell Physiol **45**: 1211–1220.

Lee, H.-A., Lee, H.-Y., Seo, E., Lee, J., Kim, S.-B., Oh, S., Choi, E., Choi, E., Lee, S.E., and Choi, D. (2016). Current Understandings of Plant Nonhost Resistance. MPMI **30**: 5–15.

Lehmann, S., Funck, D., Szabados, L., and Rentsch, D. (2010). Proline metabolism and transport in plant development. Amino Acids **39**: 949–962.

Levine, A., Tenhaken, R., Dixon, R., and Lamb, C. (1994). H2O2 from the oxidative burst orchestrates the plant hypersensitive disease resistance response. Cell **79**: 583–593.

Li, G., Meng, X., Wang, R., Mao, G., Han, L., Liu, Y., and Zhang, S. (2012). Dual-Level Regulation of ACC Synthase Activity by MPK3/MPK6 Cascade and Its Downstream WRKY Transcription Factor during Ethylene Induction in Arabidopsis. PLOS Genetics **8**: e1002767.

Li, J., Kristiansen, K.A., Hansen, B.G., and Halkier, B.A. (2011). Cellular and subcellular localization of flavin-monooxygenases involved in glucosinolate biosynthesis. Journal of Experimental Botany **62**: 1337–1346.

Li, N., Han, X., Feng, D., Yuan, D., and Huang, L.-J. (2019). Signaling Crosstalk between Salicylic Acid and Ethylene/Jasmonate in Plant Defense: Do We Understand What They Are Whispering? Int J Mol Sci **20**.

Li, X., Bao, H., Wang, Z., Wang, M., Fan, B., Zhu, C., and Chen, Z. (2018). Biogenesis and Function of Multivesicular Bodies in Plant Immunity. Front. Plant Sci. **9**.

Liebe, S. and Quader, H. (1994). Myosin in onion (Allium cepa) bulb scale epidermal cells: involvement in dynamics of organelles and endoplasmic reticulum. Physiologia Plantarum **90**: 114–124.

Liepman, A.H. and Olsen, L.J. (2003). Alanine Aminotransferase Homologs Catalyze the Glutamate:Glyoxylate Aminotransferase Reaction in Peroxisomes of Arabidopsis. Plant Physiol **131**: 215–227.

Liepman, A.H. and Olsen, L.J. (2001). Peroxisomal alanine : glyoxylate aminotransferase (AGT1) is a photorespiratory enzyme with multiple substrates in Arabidopsis thaliana. Plant J **25**: 487–498.

Liesche, J., He, H.-X., Grimm, B., Schulz, A., and Kühn, C. (2010). Recycling of Solanum Sucrose Transporters Expressed in Yeast, Tobacco, and in Mature Phloem Sieve Elements. Molecular Plant **3**: 1064–1074.

Lipka, U., Fuchs, R., Kuhns, C., Petutschnig, E., and Lipka, V. (2010). Live and let die – Arabidopsis nonhost resistance to powdery mildews. European Journal of Cell Biology **89**: 194–199.

Lipka, V. et al. (2005). Pre- and postinvasion defenses both contribute to nonhost resistance in Arabidopsis. Science **310**: 1180–1183.

Lipka, V., Kwon, C., and Panstruga, R. (2007). SNARE-ware: the role of SNARE-domain proteins in plant biology. Annu Rev Cell Dev Biol **23**: 147–174.

Liu, T., Liu, Z., Song, C., Hu, Y., Han, Z., She, J., Fan, F., Wang, J., Jin, C., Chang, J., Zhou, J.-M., and Chai, J. (2012). Chitin-induced dimerization activates a plant immune receptor. Science **336**: 1160–1164.

Liu, Y. and Zhang, S. (2004). Phosphorylation of 1-Aminocyclopropane-1-Carboxylic Acid Synthase by MPK6, a Stress-Responsive Mitogen-Activated Protein Kinase, Induces Ethylene Biosynthesis in Arabidopsis. The Plant Cell **16**: 3386–3399.

Liu, Z., Wu, Y., Yang, F., Zhang, Y., Chen, S., Xie, Q., Tian, X., and Zhou, J.-M. (2013). BIK1 interacts with PEPRs to mediate ethylene-induced immunity. PNAS **110**: 6205–6210.

Lu, D., Wu, S., Gao, X., Zhang, Y., Shan, L., and He, P. (2010). A receptor-like cytoplasmic kinase, BIK1, associates with a flagellin receptor complex to initiate plant innate immunity. PNAS **107**: 496–

501.

Lu, H., Liu, Y., and Greenberg, J.T. (2005). Structure-function analysis of the plasma membrane- localized Arabidopsis defense component ACD6. Plant J **44**: 798–809.

Lu, H., Rate, D.N., Song, J.T., and Greenberg, J.T. (2003). ACD6, a Novel Ankyrin Protein, Is a Regulator and an Effector of Salicylic Acid Signaling in the Arabidopsis Defense Response. Plant Cell **15**: 2408–2420.

Lu, X., Dittgen, J., Piślewska-Bednarek, M., Molina, A., Schneider, B., Svatoš, A., Doubský, J., Schneeberger, K., Weigel, D., Bednarek, P., and Schulze-Lefert, P. (2015). Mutant Allele-Specific Uncoupling of PENETRATION3 Functions Reveals Engagement of the ATP-Binding Cassette Transporter in Distinct Tryptophan Metabolic Pathways. Plant Physiol **168**: 814–827.

Macho, A.P. and Zipfel, C. (2014). Plant PRRs and the activation of innate immune signaling. Mol Cell **54**: 263–272.

Macho, A.P. and Zipfel, C. (2015). Targeting of plant pattern recognition receptor-triggered immunity by bacterial type-III secretion system effectors. Curr Opin Microbiol **23**: 14–22.

Madsen, S.R., Kunert, G., Reichelt, M., Gershenzon, J., and Halkier, B.A. (2015). Feeding on Leaves of the Glucosinolate Transporter Mutant gtr1gtr2 Reduces Fitness of Myzus persicae. J Chem Ecol **41**: 975–984.

Madsen, S.R., Olsen, C.E., Nour-Eldin, H.H., and Halkier, B.A. (2014). Elucidating the Role of Transport Processes in Leaf Glucosinolate Distribution. Plant Physiology **166**: 1450–1462.

Maeda, K., Houjyou, Y., Komatsu, T., Hori, H., Kodaira, T., and Ishikawa, A. (2009). AGB1 and PMR5 Contribute to PEN2-Mediated Preinvasion Resistance to Magnaporthe oryzae in Arabidopsis thaliana. MPMI **22**: 1331–1340.

Makarov, M.V., Trammell, S.A.J., and Migaud, M.E. (2019). The chemistry of the vitamin B3 metabolome. Biochem Soc Trans **47**: 131–147.

Maleck, K., Levine, A., Eulgem, T., Morgan, A., Schmid, J., Lawton, K.A., Dangl, J.L., and Dietrich, R.A. (2000). The transcriptome of Arabidopsis thaliana during systemic acquired resistance. Nature Genetics **26**: 403–410.

Malka, S.K. and Cheng, Y. (2017). Possible Interactions between the Biosynthetic Pathways of Indole Glucosinolate and Auxin. Front. Plant Sci. **8**.

Mao, H., Aryal, B., Langenecker, T., Hagmann, J., Geisler, M., and Grebe, M. (2017). Arabidopsis BTB/POZ protein-dependent PENETRATION3 trafficking and disease susceptibility. Nature Plants **3**: 854–858.

Maqbool, A., Saitoh, H., Franceschetti, M., Stevenson, C., Uemura, A., Kanzaki, H., Kamoun, S., Terauchi, R., and Banfield, M. (2015). Structural basis of pathogen recognition by an integrated HMA domain in a plant NLR immune receptor. eLife **4**: e08709.

Maróti, G., Kereszt, A., Kondorosi, E., and Mergaert, P. (2011). Natural roles of antimicrobial peptides in microbes, plants and animals. Res Microbiol **162**: 363–374.

Martinoia, E., Massonneau, A., and Frangne, N. (2000). Transport Processes of Solutes across the Vacuolar Membrane of Higher Plants. Plant and Cell Physiology **41**: 1175–1186.

Matern, A., Böttcher, C., Eschen-Lippold, L., Westermann, B., Smolka, U., Döll, S., Trempel, F., Aryal, B., Scheel, D., Geisler, M., and Rosahl, S. (2019). A substrate of the ABC transporter PEN3 stimulates bacterial flagellin (flg22)-induced callose deposition in Arabidopsis thaliana. Journal of Biological Chemistry **294**: 6857–6870.

Matsushima, R., Kondo, M., Nishimura, M., and Hara-Nishimura, I. (2003). A novel ER-derived compartment, the ER body, selectively accumulates a beta-glucosidase with an ER-retention signal in Arabidopsis. Plant J **33**: 493–502.

McMahon, H.T. and Boucrot, E. (2011). Molecular mechanism and physiological functions of clathrin-mediated endocytosis. Nature Reviews Molecular Cell Biology **12**: 517–533.

Mélida, H., Sopeña-Torres, S., Bacete, L., Garrido-Arandia, M., Jordá, L., López, G., Muñoz-Barrios, A., Pacios, L.F., and Molina, A. (2018). Non-branched β-1,3-glucan oligosaccharides trigger immune responses in Arabidopsis. Plant J **93**: 34–49.

Mellersh, D.G., Foulds, I.V., Higgins, V.J., and Heath, M.C. (2002). H2O2 plays different roles in determining penetration failure in three diverse plant-fungal interactions. Plant J **29**: 257–268.

Méresse, S., Steele-Mortimer, O., Moreno, E., Desjardins, M., Finlay, B., and Gorvel, J.-P. (1999). Controlling the maturation of pathogen-containing vacuoles: a matter of life and death. Nature Cell Biology **1**: E183–E188.

Meyer, D., Pajonk, S., Micali, C., O'Connell, R., and Schulze-Lefert, P. (2009). Extracellular transport and integration of plant secretory proteins into pathogen-induced cell wall compartments. Plant J **57**: 986–999.

Micali, C., Göllner, K., Humphry, M., Consonni, C., and Panstruga, R. (2008). The Powdery Mildew Disease of Arabidopsis: A Paradigm for the Interaction between Plants and Biotrophic Fungi. Arabidopsis Book **6**.

Mine, A., Seyfferth, C., Kracher, B., Berens, M.L., Becker, D., and Tsuda, K. (2018). The Defense Phytohormone Signaling Network Enables Rapid, High-Amplitude Transcriptional Reprogramming during Effector-Triggered Immunity. The Plant Cell **30**: 1199–1219.

Mittler, R., Vanderauwera, S., Gollery, M., and Van Breusegem, F. (2004). Reactive oxygen gene network of plants. Trends in Plant Science **9**: 490–498.

Miya, A., Albert, P., Shinya, T., Desaki, Y., Ichimura, K., Shirasu, K., Narusaka, Y., Kawakami, N., Kaku, H., and Shibuya, N. (2007). CERK1, a LysM receptor kinase, is essential for chitin elicitor signaling in Arabidopsis. Proc Natl Acad Sci U S A **104**: 19613–19618.

Modiano, N., Lu, Y.E., and Cresswell, P. (2005). Golgi targeting of human guanylate-binding protein-1 requires nucleotide binding, isoprenylation, and an IFN-gamma-inducible cofactor. Proc Natl Acad Sci U S A **102**: 8680–8685.

Morant, A.V., Jørgensen, K., Jørgensen, C., Paquette, S.M., Sánchez-Pérez, R., Møller, B.L., and Bak,

S. (2008). beta-Glucosidases as detonators of plant chemical defense. Phytochemistry **69**: 1795–1813.

Müller, R., de Vos, M., Sun, J.Y., Sønderby, I.E., Halkier, B.A., Wittstock, U., and Jander, G. (2010). Differential Effects of Indole and Aliphatic Glucosinolates on Lepidopteran Herbivores. J Chem Ecol **36**: 905–913.

Mur, L.A.J., Kenton, P., Lloyd, A.J., Ougham, H., and Prats, E. (2008). The hypersensitive response; the centenary is upon us but how much do we know? Journal of Experimental Botany **59**: 501–520.

Muroi, A., Ishihara, A., Tanaka, C., Ishizuka, A., Takabayashi, J., Miyoshi, H., and Nishioka, T. (2009). Accumulation of hydroxycinnamic acid amides induced by pathogen infection and identification of agmatine coumaroyltransferase in Arabidopsis thaliana. Planta **230**: 517.

Musiani, F. and Giorgetti, A. (2017). Chapter Two - Protein Aggregation and Molecular Crowding: Perspectives From Multiscale Simulations. In International Review of Cell and Molecular Biology, M. Sandal, ed, Early Stage Protein Misfolding and Amyloid Aggregation. (Academic Press), pp. 49–77.

Nakano, R.T., Piślewska-Bednarek, M., Yamada, K., Edger, P.P., Miyahara, M., Kondo, M., Böttcher, C., Mori, M., Nishimura, M., Schulze-Lefert, P., Hara-Nishimura, I., and Bednarek, P. (2017). PYK10 myrosinase reveals a functional coordination between endoplasmic reticulum bodies and glucosinolates in Arabidopsis thaliana. Plant J **89**: 204–220.

Naur, P., Petersen, B.L., Mikkelsen, M.D., Bak, S., Rasmussen, H., Olsen, C.E., and Halkier, B.A. (2003). CYP83A1 and CYP83B1, Two Nonredundant Cytochrome P450 Enzymes Metabolizing Oximes in the Biosynthesis of Glucosinolates in Arabidopsis. Plant Physiology **133**: 63–72.

Návarová, H., Bernsdorff, F., Döring, A.-C., and Zeier, J. (2012). Pipecolic Acid, an Endogenous Mediator of Defense Amplification and Priming, Is a Critical Regulator of Inducible Plant Immunity[W]. Plant Cell **24**: 5123–5141.

Nawrath, C. and Métraux, J.P. (1999). Salicylic acid induction-deficient mutants of Arabidopsis express PR-2 and PR-5 and accumulate high levels of camalexin after pathogen inoculation. Plant Cell **11**: 1393–1404.

Ng, S., De Clercq, I., Van Aken, O., Law, S.R., Ivanova, A., Willems, P., Giraud, E., Van Breusegem, F., and Whelan, J. (2014). Anterograde and Retrograde Regulation of Nuclear Genes Encoding Mitochondrial Proteins during Growth, Development, and Stress. Molecular Plant **7**: 1075–1093.

Ngou, B.P.M., Ahn, H.-K., Ding, P., and Jones, J.D. (2020). Mutual Potentiation of Plant Immunity by Cell-surface and Intracellular Receptors. bioRxiv: 2020.04.10.034173.

Nielsen, M.E., Feechan, A., Böhlenius, H., Ueda, T., and Thordal-Christensen, H. (2012). Arabidopsis ARF-GTP exchange factor, GNOM, mediates transport required for innate immunity and focal accumulation of syntaxin PEN1. Proc Natl Acad Sci U S A **109**: 11443–11448.

Nielsen, M.E., Jürgens, G., and Thordal-Christensen, H. (2017). VPS9a Activates the Rab5 GTPase ARA7 to Confer Distinct Pre- and Postinvasive Plant Innate Immunity. The Plant Cell **29**: 1927–1937.

Nielsen, M.E. and Thordal-Christensen, H. (2013). Transcytosis shuts the door for an unwanted guest. Trends Plant Sci **18**: 611–616.

Nintemann, S.J., Hunziker, P., Andersen, T.G., Schulz, A., Burow, M., and Halkier, B.A. (2018). Localization of the glucosinolate biosynthetic enzymes reveals distinct spatial patterns for the biosynthesis of indole and aliphatic glucosinolates. Physiol Plant **163**: 138–154.

Noctor, G., Queval, G., and Gakière, B. (2006). NAD(P) synthesis and pyridine nucleotide cycling in plants and their potential importance in stress conditions*. Journal of Experimental Botany **57**: 1603–1620.

Noctor, G., Veljovic-Jovanovic, S., and Foyer, C.H. (2000). Peroxide processing in photosynthesis: antioxidant coupling and redox signalling. Philos Trans R Soc Lond B Biol Sci **355**: 1465–1475.

Nomura, H. et al. (2012). Chloroplast-mediated activation of plant immune signalling in Arabidopsis. Nat Commun **3**: 926.

Nour-Eldin, H.H., Andersen, T.G., Burow, M., Madsen, S.R., Jørgensen, M.E., Olsen, C.E., Dreyer, I., Hedrich, R., Geiger, D., and Halkier, B.A. (2012). NRT/PTR transporters are essential for translocation of glucosinolate defence compounds to seeds. Nature **488**: 531–534.

Nürnberger, T. and Lipka, V. (2005). Non-host resistance in plants: new insights into an old phenomenon. Mol Plant Pathol **6**: 335–345.

O'Connell, R.J. and Panstruga, R. (2006). Tête à tête inside a plant cell: establishing compatibility between plants and biotrophic fungi and oomycetes. New Phytologist **171**: 699–718.

Oome, S., Raaymakers, T.M., Cabral, A., Samwel, S., Böhm, H., Albert, I., Nürnberger, T., and Ackerveken, G.V. den (2014). Nep1-like proteins from three kingdoms of life act as a microbe-associated molecular pattern in Arabidopsis. PNAS **111**: 16955–16960.

Oome, S. and Van den Ackerveken, G. (2014). Comparative and functional analysis of the widely occurring family of Nep1-like proteins. Mol Plant Microbe Interact **27**: 1081–1094.

Ortiz, D., Guillen, K. de, Cesari, S., Chalvon, V., Gracy, J., Padilla, A., and Kroj, T. (2017). Recognition of the Magnaporthe oryzae Effector AVR-Pia by the Decoy Domain of the Rice NLR Immune Receptor RGA5. The Plant Cell **29**: 156–168.

Otegui, M.S. (2018). ESCRT-mediated sorting and intralumenal vesicle concatenation in plants. Biochem Soc Trans **46**: 537–545.

Padmanabhan, M.S. and Dinesh-Kumar, S.P. (2010). All hands on deck—the role of chloroplasts, endoplasmic reticulum, and the nucleus in driving plant innate immunity. Mol Plant Microbe Interact **23**: 1368–1380.

Pagni, M., Ioannidis, V., Cerutti, L., Zahn-Zabal, M., Jongeneel, C.V., and Falquet, L. (2004). MyHits: a new interactive resource for protein annotation and domain identification. Nucleic Acids Res **32**: W332-335.

Pan, R., Liu, J., Wang, S., and Hu, J. (2020). Peroxisomes: versatile organelles with diverse roles in plants. New Phytologist **225**: 1410–1427.

Panstruga, R. and Moscou, M.J. (2020). What is the Molecular Basis of Nonhost Resistance? MPMI

33: 1253–1264.

Park, Y.-G., Mun, B.-G., Kang, S.-M., Hussain, A., Shahzad, R., Seo, C.-W., Kim, A.-Y., Lee, S.-U., Oh, K.Y., Lee, D.Y., Lee, I.-J., and Yun, B.-W. (2017). Bacillus aryabhattai SRB02 tolerates oxidative and nitrosative stress and promotes the growth of soybean by modulating the production of phytohormones. PLOS ONE **12**: e0173203.

Pedras, M.S.C. and Ahiahonu, P.W.K. (2002). Probing the phytopathogenic stem rot fungus with phytoalexins and analogues: unprecedented glucosylation of camalexin and 6-methoxycamalexin. Bioorg Med Chem **10**: 3307–3312.

Pedras, M.S.C., Yaya, E.E., and Glawischnig, E. (2011). The phytoalexins from cultivated and wild crucifers: chemistry and biology. Nat Prod Rep **28**: 1381–1405.

Pedrazzini, E., Komarova, N.Y., Rentsch, D., and Vitale, A. (2013). Traffic Routes and Signals for the Tonoplast. Traffic **14**: 622–628.

Pessino, A., Hebert, D.N., Woon, C.W., Harrison, S.A., Clancy, B.M., Buxton, J.M., Carruthers, A., and Czech, M.P. (1991). Evidence that functional erythrocyte-type glucose transporters are oligomers. Journal of Biological Chemistry **266**: 20213–20217.

Petre, B. and Kamoun, S. (2014). How Do Filamentous Pathogens Deliver Effector Proteins into Plant Cells? PLoS Biol **12**.

Petutschnig, E.K., Jones, A.M.E., Serazetdinova, L., Lipka, U., and Lipka, V. (2010). The Lysin Motif Receptor-like Kinase (LysM-RLK) CERK1 Is a Major Chitin-binding Protein in Arabidopsis thaliana and Subject to Chitin-induced Phosphorylation. J Biol Chem **285**: 28902–28911.

Pfalz, M., Mikkelsen, M.D., Bednarek, P., Olsen, C.E., Halkier, B.A., and Kroymann, J. (2011). Metabolic Engineering in Nicotiana benthamiana Reveals Key Enzyme Functions in Arabidopsis Indole Glucosinolate Modification. The Plant Cell **23**: 716–729.

Pfalz, M., Vogel, H., and Kroymann, J. (2009). The Gene Controlling the Indole Glucosinolate Modifier1 Quantitative Trait Locus Alters Indole Glucosinolate Structures and Aphid Resistance in Arabidopsis. Plant Cell **21**: 985–999.

Piasecka, A., Jedrzejczak-Rey, N., and Bednarek, P. (2015). Secondary metabolites in plant innate immunity: conserved function of divergent chemicals. New Phytologist **206**: 948–964.

Piślewska-Bednarek, M., Nakano, R.T., Hiruma, K., Pastorczyk, M., Sanchez-Vallet, A., Singkaravanit-Ogawa, S., Ciesiołka, D., Takano, Y., Molina, A., Schulze-Lefert, P., and Bednarek, P. (2018). Glutathione Transferase U13 Functions in Pathogen-Triggered Glucosinolate Metabolism. Plant Physiology **176**: 538–551.

Pogorelko, G.V., Kambakam, S., Nolan, T., Foudree, A., Zabotina, O.A., and Rodermel, S.R. (2016). Impaired Chloroplast Biogenesis in Immutans, an Arabidopsis Variegation Mutant, Modifies Developmental Programming, Cell Wall Composition and Resistance to Pseudomonas syringae. PLOS ONE **11**: e0150983.

Poschet, G., Hannich, B., Raab, S., Jungkunz, I., Klemens, P.A.W., Krueger, S., Wic, S., Neuhaus, H.E., and Büttner, M. (2011). A Novel Arabidopsis Vacuolar Glucose Exporter Is Involved in Cellular Sugar

Homeostasis and Affects the Composition of Seed Storage Compounds. Plant Physiology **157**: 1664–1676.

Postel, S. and Kemmerling, B. (2009). Plant systems for recognition of pathogen-associated molecular patterns. Semin Cell Dev Biol **20**: 1025–1031.

Postma, J., Liebrand, T.W.H., Bi, G., Evrard, A., Bye, R.R., Mbengue, M., Kuhn, H., Joosten, M.H.A.J., and Robatzek, S. (2016). Avr4 promotes Cf-4 receptor-like protein association with the BAK1/SERK3 receptor-like kinase to initiate receptor endocytosis and plant immunity. New Phytologist **210**: 627–642.

Protter, D.S.W. and Parker, R. (2016). Principles and Properties of Stress Granules. Trends Cell Biol **26**: 668–679.

Pruitt, R.N. et al. (2020). Arabidopsis cell surface LRR immune receptor signaling through the EDS1-PAD4-ADR1 node. bioRxiv: 2020.11.23.391516.

Pryce-jones, E., Carver, T., and Gurr, S.J. (1999). The roles of cellulase enzymes and mechanical force in host penetration by Erysiphe graminis f.sp.hordei. Physiological and Molecular Plant Pathology **55**: 175–182.

Raiborg, C. and Stenmark, H. (2009). The ESCRT machinery in endosomal sorting of ubiquitylated membrane proteins. Nature **458**: 445–452.

Ramonell, K., Berrocal-Lobo, M., Koh, S., Wan, J., Edwards, H., Stacey, G., and Somerville, S. (2005). Loss-of-Function Mutations in Chitin Responsive Genes Show Increased Susceptibility to the Powdery Mildew Pathogen Erysiphe cichoracearum. Plant Physiol **138**: 1027–1036.

Rappsilber, J., Ishihama, Y., and Mann, M. (2003). Stop and go extraction tips for matrix-assisted laser desorption/ionization, nanoelectrospray, and LC/MS sample pretreatment in proteomics. Anal Chem **75**: 663–670.

Rappsilber, J., Mann, M., and Ishihama, Y. (2007). Protocol for micro-purification, enrichment, pre-fractionation and storage of peptides for proteomics using StageTips. Nat Protoc **2**: 1896–1906.

Rate, D.N., Cuenca, J.V., Bowman, G.R., Guttman, D.S., and Greenberg, J.T. (1999). The Gain-of-Function Arabidopsis acd6 Mutant Reveals Novel Regulation and Function of the Salicylic Acid Signaling Pathway in Controlling Cell Death, Defenses, and Cell Growth. The Plant Cell **11**: 1695–1708.

Rausch, T. (1991). The hexose transporters at the plasma membrane and the tonoplast of higher plants. Physiologia Plantarum **82**: 134–142.

Rea, P.A. (2006). Phytochelatin synthase, papain's cousin, in stereo. Proc Natl Acad Sci U S A **103**: 507–508.

del Río, L.A., Corpas, F.J., Sandalio, L.M., Palma, J.M., Gómez, M., and Barroso, J.B. (2002). Reactive oxygen species, antioxidant systems and nitric oxide in peroxisomes. J Exp Bot **53**: 1255–1272.

Robatzek, S., Chinchilla, D., and Boller, T. (2006). Ligand-induced endocytosis of the pattern recognition receptor FLS2 in Arabidopsis. Genes Dev **20**: 537–542.

Robinson, D.G., Jiang, L., and Schumacher, K. (2008). The Endosomal System of Plants: Charting New and Familiar Territories. Plant Physiology **147**: 1482–1492.

Ross, A.F. (1961). Systemic acquired resistance induced by localized virus infections in plants. Virology **14**: 340–358.

Rosso, M.G., Li, Y., Strizhov, N., Reiss, B., Dekker, K., and Weisshaar, B. (2003). An Arabidopsis thaliana T-DNA mutagenized population (GABI-Kat) for flanking sequence tag-based reverse genetics. Plant Mol Biol **53**: 247–259.

Rost, S., Frank, C., and Beck, E. (1996). The chloroplast envelope is permeable for maltose but not for maltodextrins. Biochimica et Biophysica Acta (BBA) - General Subjects **1291**: 221–227.

Roux, M., Schwessinger, B., Albrecht, C., Chinchilla, D., Jones, A., Holton, N., Malinovsky, F.G., Tör, M., de Vries, S., and Zipfel, C. (2011). The Arabidopsis leucine-rich repeat receptor-like kinases BAK1/SERK3 and BKK1/SERK4 are required for innate immunity to hemibiotrophic and biotrophic pathogens. Plant Cell **23**: 2440–2455.

Ruano, G. and Scheuring, D. (2020). Plant Cells under Attack: Unconventional Endomembrane Trafficking during Plant Defense. Plants (Basel) **9**.

Rutter, B.D. and Innes, R.W. (2017). Extracellular Vesicles Isolated from the Leaf Apoplast Carry Stress-Response Proteins. Plant Physiology **173**: 728–741.

Saenz, G.S. and Taylor, J.W. (2011). Phylogeny of the Erysiphales (powdery mildews) inferred from internal transcribed spacer ribosomal DNA sequences. Canadian Journal of Botany.

Sanchez-Vallet, A., Ramos, B., Bednarek, P., López, G., Piślewska-Bednarek, M., Schulze-Lefert, P., and Molina, A. (2010). Tryptophan-derived secondary metabolites in Arabidopsis thaliana confer non-host resistance to necrotrophic Plectosphaerella cucumerina fungi. Plant J **63**: 115–127.

Santos, J.C., Dick, M.S., Lagrange, B., Degrandi, D., Pfeffer, K., Yamamoto, M., Meunier, E., Pelczar, P., Henry, T., and Broz, P. (2018). LPS targets host guanylate-binding proteins to the bacterial outer membrane for non-canonical inflammasome activation. EMBO J **37**.

Schäfer, G., Heber, U., and Heldt, H.W. (1977). Glucose Transport into Spinach Chloroplasts. Plant Physiology **60**: 286–289.

Schäfer, P. and Eichmann, R. (2012). The endoplasmic reticulum in plant immunity and cell death. Front. Plant Sci. **3**.

Schindelin, J. et al. (2012). Fiji: an open-source platform for biological-image analysis. Nat Methods **9**: 676–682.

Schmelzer, E. (2002). Cell polarization, a crucial process in fungal defence. Trends in Plant Science **7**: 411–415.

Schneider, K., Kienow, L., Schmelzer, E., Colby, T., Bartsch, M., Miersch, O., Wasternack, C., Kombrink, E., and Stuible, H.-P. (2005). A new type of peroxisomal acyl-coenzyme A synthetase from Arabidopsis thaliana has the catalytic capacity to activate biosynthetic precursors of jasmonic acid. J Biol Chem **280**: 13962–13972.

Schuhegger, R., Nafisi, M., Mansourova, M., Petersen, B.L., Olsen, C.E., Svatoš, A., Halkier, B.A., and Glawischnig, E. (2006). CYP71B15 (PAD3) Catalyzes the Final Step in Camalexin Biosynthesis. Plant Physiol **141**: 1248–1254.

Schulze, B., Mentzel, T., Jehle, A.K., Mueller, K., Beeler, S., Boller, T., Felix, G., and Chinchilla, D. (2010). Rapid heteromerization and phosphorylation of ligand-activated plant transmembrane receptors and their associated kinase BAK1. J Biol Chem **285**: 9444–9451.

Schwarzländer, M. and Finkemeier, I. (2013). Mitochondrial Energy and Redox Signaling in Plants. Antioxid Redox Signal **18**: 2122–2144.

Schwarzländer, M., Fricker, M.D., Müller, C., Marty, L., Brach, T., Novak, J., Sweetlove, L.J., Hell, R., and Meyer, A.J. (2008). Confocal imaging of glutathione redox potential in living plant cells. J Microsc **231**: 299–316.

Schweizer, F., Fernández-Calvo, P., Zander, M., Diez-Diaz, M., Fonseca, S., Glauser, G., Lewsey, M.G., Ecker, J.R., Solano, R., and Reymond, P. (2013). Arabidopsis Basic Helix-Loop-Helix Transcription Factors MYC2, MYC3, and MYC4 Regulate Glucosinolate Biosynthesis, Insect Performance, and Feeding Behavior[W][OPEN]. Plant Cell **25**: 3117–3132.

Scott, I. and Logan, D.C. (2008). Mitochondrial morphology transition is an early indicator of subsequent cell death in Arabidopsis. New Phytol **177**: 90–101.

Selin, C., de Kievit, T.R., Belmonte, M.F., and Fernando, W.G.D. (2016). Elucidating the Role of Effectors in Plant-Fungal Interactions: Progress and Challenges. Front. Microbiol. **7**.

Shao, Z.-Q., Xue, J.-Y., Wu, P., Zhang, Y.-M., Wu, Y., Hang, Y.-Y., Wang, B., and Chen, J.-Q. (2016). Large-Scale Analyses of Angiosperm Nucleotide-Binding Site-Leucine-Rich Repeat Genes Reveal Three Anciently Diverged Classes with Distinct Evolutionary Patterns. Plant Physiology **170**: 2095–2109.

Shen, J., Zeng, Y., Zhuang, X., Sun, L., Yao, X., Pimpl, P., and Jiang, L. (2013). Organelle pH in the Arabidopsis Endomembrane System. Molecular Plant **6**: 1419–1437.

Shenoy, A.R., Wellington, D.A., Kumar, P., Kassa, H., Booth, C.J., Cresswell, P., and MacMicking, J.D. (2012). GBP5 promotes NLRP3 inflammasome assembly and immunity in mammals. Science **336**: 481–485.

Sinclair, A.M., Trobacher, C.P., Mathur, N., Greenwood, J.S., and Mathur, J. (2009). Peroxule extension over ER-defined paths constitutes a rapid subcellular response to hydroxyl stress. Plant J **59**: 231–242.

Skalamera, D. and Heath, M.C. (1998). Changes in the cytoskeleton accompanying infection-induced nuclear movements and the hypersensitive response in plant cells invaded by rust fungi. Plant J **16**: 191–200.

Smirnoff, N. (2000). Ascorbic acid: metabolism and functions of a multi-facetted molecule. Current Opinion in Plant Biology **3**: 229–235.

Sohn, E.J., Kim, E.S., Zhao, M., Kim, S.J., Kim, H., Kim, Y.-W., Lee, Y.J., Hillmer, S., Sohn, U., Jiang, L., and Hwang, I. (2003). Rha1, an Arabidopsis Rab5 Homolog, Plays a Critical Role in the Vacuolar Traf-

ficking of Soluble Cargo Proteins. Plant Cell **15**: 1057–1070.

Sønderby, I.E., Geu-Flores, F., and Halkier, B.A. (2010). Biosynthesis of glucosinolates – gene discovery and beyond. Trends in Plant Science **15**: 283–290.

Souza, C. de A., Li, S., Lin, A.Z., Boutrot, F., Grossmann, G., Zipfel, C., and Somerville, S.C. (2017). Cellulose-Derived Oligomers Act as Damage-Associated Molecular Patterns and Trigger Defense-Like Responses. Plant Physiology **173**: 2383–2398.

Sowden, R.G., Watson, S.J., and Jarvis, P. (2018). The role of chloroplasts in plant pathology. Essays Biochem **62**: 21–39.

Stahl, E., Bellwon, P., Huber, S., Schlaeppi, K., Bernsdorff, F., Vallat-Michel, A., Mauch, F., and Zeier, J. (2016). Regulatory and Functional Aspects of Indolic Metabolism in Plant Systemic Acquired Resistance. Molecular Plant **9**: 662–681.

Stein, M., Dittgen, J., Sánchez-Rodríguez, C., Hou, B.-H., Molina, A., Schulze-Lefert, P., Lipka, V., and Somerville, S. (2006). Arabidopsis PEN3/PDR8, an ATP binding cassette transporter, contributes to nonhost resistance to inappropriate pathogens that enter by direct penetration. Plant Cell **18**: 731–746.

Stoddard, A. and Rolland, V. (2019). I see the light! Fluorescent proteins suitable for cell wall/apoplast targeting in Nicotiana benthamiana leaves. Plant Direct **3**: e00112.

Stotz, H.U., Sawada, Y., Shimada, Y., Hirai, M.Y., Sasaki, E., Krischke, M., Brown, P.D., Saito, K., and Kamiya, Y. (2011). Role of camalexin, indole glucosinolates, and side chain modification of glucosinolate-derived isothiocyanates in defense of Arabidopsis against Sclerotinia sclerotiorum. Plant J **67**: 81–93.

Strader, L.C. and Bartel, B. (2009). The Arabidopsis PLEIOTROPIC DRUG RESISTANCE8/ABCG36 ATP binding cassette transporter modulates sensitivity to the auxin precursor indole-3-butyric acid. Plant Cell **21**: 1992–2007.

Su, T., Li, W., Wang, P., and Ma, C. (2019). Dynamics of Peroxisome Homeostasis and Its Role in Stress Response and Signaling in Plants. Front. Plant Sci. **10**.

Sugiyama, R. and Hirai, M.Y. (2019). Atypical Myrosinase as a Mediator of Glucosinolate Functions in Plants. Front Plant Sci **10**.

Sukarta, O.C.A., Slootweg, E.J., and Goverse, A. (2016). Structure-informed insights for NLR functioning in plant immunity. Semin Cell Dev Biol **56**: 134–149.

Sun, T., Nitta, Y., Zhang, Q., Wu, D., Tian, H., Lee, J.S., and Zhang, Y. (2018). Antagonistic interactions between two MAP kinase cascades in plant development and immune signaling. EMBO reports **19**: e45324.

Sweetlove, L.J. and Fernie, A.R. (2013). The Spatial Organization of Metabolism Within the Plant Cell. Annual Review of Plant Biology **64**: 723–746.

Szabados, L. and Savouré, A. (2010). Proline: a multifunctional amino acid. Trends in Plant Science **15**: 89–97.

Takáč, T., Pechan, T., Šamajová, O., Ovečka, M., Richter, H., Eck, C., Niehaus, K., and Šamaj, J. (2012). Wortmannin Treatment Induces Changes in Arabidopsis Root Proteome and Post-Golgi Compartments. J. Proteome Res. **11**: 3127–3142.

Takemoto, D., Jones, D.A., and Hardham, A.R. (2003). GFP-tagging of cell components reveals the dynamics of subcellular re-organization in response to infection of Arabidopsis by oomycete pathogens. Plant J **33**: 775–792.

Takken, F.L.W. and Tameling, W.I.L. (2009). To nibble at plant resistance proteins. Science **324**: 744–746.

Tang, D., Wang, G., and Zhou, J.-M. (2017). Receptor Kinases in Plant-Pathogen Interactions: More Than Pattern Recognition. Plant Cell **29**: 618–637.

Tao, Y., Xie, Z., Chen, W., Glazebrook, J., Chang, H.-S., Han, B., Zhu, T., Zou, G., and Katagiri, F. (2003). Quantitative Nature of Arabidopsis Responses during Compatible and Incompatible Interactions with the Bacterial Pathogen Pseudomonas syringae. The Plant Cell **15**: 317–330.

Thomma, B.P., Nelissen, I., Eggermont, K., and Broekaert, W.F. (1999). Deficiency in phytoalexin production causes enhanced susceptibility of Arabidopsis thaliana to the fungus Alternaria brassicicola. Plant J **19**: 163–171.

Thomma, B.P.H.J., Nürnberger, T., and Joosten, M.H.A.J. (2011). Of PAMPs and effectors: the blurred PTI-ETI dichotomy. Plant Cell **23**: 4–15.

Thordal-Christensen, H. (2020). A holistic view on plant effector-triggered immunity presented as an iceberg model. Cell Mol Life Sci **77**: 3963–3976.

Thulasi Devendrakumar, K., Li, X., and Zhang, Y. (2018). MAP kinase signalling: interplays between plant PAMP- and effector-triggered immunity. Cell. Mol. Life Sci. **75**: 2981–2989.

Tomiyama, K., Sato, K., and Doke, N. (1982). Effect of cytochalasin b and colchicine on hypersensitive death of potato cells infected by incompatible race of phytophthora infestans. Jpn. J. Phytopathol. **48**: 228–230.

Torres, M.A. and Dangl, J.L. (2005). Functions of the respiratory burst oxidase in biotic interactions, abiotic stress and development. Curr Opin Plant Biol **8**: 397–403.

de Torres Zabala, M. et al. (2015). Chloroplasts play a central role in plant defence and are targeted by pathogen effectors. Nat Plants **1**: 15074.

Tretina, K., Park, E.-S., Maminska, A., and MacMicking, J.D. (2019). Interferon-induced guanylate-binding proteins: Guardians of host defense in health and disease. J Exp Med **216**: 482–500.

Tsuda, K., Sato, M., Stoddard, T., Glazebrook, J., and Katagiri, F. (2009). Network Properties of Robust Immunity in Plants. PLOS Genetics **5**: e1000772.

Tsuji, J., Jackson, E.P., Gage, D.A., Hammerschmidt, R., and Somerville, S.C. (1992). Phytoalexin Accumulation in Arabidopsis thaliana during the Hypersensitive Reaction to Pseudomonas syringae pv syringae. Plant Physiology **98**: 1304–1309.

Tucker, S.L. and Talbot, N.J. (2001). Surface Attachment and Pre-Penetration Stage Development by Plant Pathogenic Fungi. Annual Review of Phytopathology **39**: 385–417.

Ueda, T., Yamaguchi, M., Uchimiya, H., and Nakano, A. (2001). Ara6, a plant-unique novel type Rab GTPase, functions in the endocytic pathway of Arabidopsis thaliana. EMBO J **20**: 4730–4741.

Ülker, B., Peiter, E., Dixon, D.P., Moffat, C., Capper, R., Bouché, N., Edwards, R., Sanders, D., Knight, H., and Knight, M.R. (2008). Getting the most out of publicly available T-DNA insertion lines. The Plant Journal **56**: 665–677.

Underwood, W. (2012). The Plant Cell Wall: A Dynamic Barrier Against Pathogen Invasion. Front. Plant Sci. **3**.

Underwood, W., Ryan, A., and Somerville, S.C. (2017). An Arabidopsis Lipid Flippase Is Required for Timely Recruitment of Defenses to the Host–Pathogen Interface at the Plant Cell Surface. Molecular Plant **10**: 805–820.

Underwood, W. and Somerville, S.C. (2013). Perception of conserved pathogen elicitors at the plasma membrane leads to relocalization of the Arabidopsis PEN3 transporter. PNAS **110**: 12492–12497.

Van Gestel, K., Köhler, R.H., and Verbelen, J. (2002). Plant mitochondria move on F-actin, but their positioning in the cortical cytoplasm depends on both F-actin and microtubules. Journal of Experimental Botany **53**: 659–667.

Vanacker, H., Lu, H., Rate, D.N., and Greenberg, J.T. (2001). A role for salicylic acid and NPR1 in regulating cell growth in Arabidopsis. Plant J **28**: 209–216.

VanEtten, H.D., Mansfield, J.W., Bailey, J.A., and Farmer, E.E. (1994). Two Classes of Plant Antibiotics: Phytoalexins versus “Phytoanticipins.” The Plant Cell **6**: 1191–1192.

Vellosillo, T., Aguilera, V., Marcos, R., Bartsch, M., Vicente, J., Cascón, T., Hamberg, M., and Castresana, C. (2013). Defense Activated by 9-Lipoxygenase-Derived Oxylipins Requires Specific Mitochondrial Proteins1[W]. Plant Physiol **161**: 617–627.

Voigt, C.A. (2014). Callose-mediated resistance to pathogenic intruders in plant defense-related papillae. Front Plant Sci **5**: 168.

Wada, M. and Suetsugu, N. (2004). Plant organelle positioning. Curr Opin Plant Biol **7**: 626–631.

Wagner, S., Stuttmann, J., Rietz, S., Guerois, R., Brunstein, E., Bautor, J., Niefind, K., and Parker, J.E. (2013). Structural basis for signaling by exclusive EDS1 heteromeric complexes with SAG101 or PAD4 in plant innate immunity. Cell Host Microbe **14**: 619–630.

Wagner, U., Edwards, R., Dixon, D.P., and Mauch, F. (2002). Probing the diversity of the Arabidopsis glutathione S-transferase gene family. Plant Mol Biol **49**: 515–532.

Wan, J., Tanaka, K., Zhang, X.-C., Son, G.H., Brechenmacher, L., Nguyen, T.H.N., and Stacey, G. (2012). LYK4, a lysin motif receptor-like kinase, is important for chitin signaling and plant innate immunity in Arabidopsis. Plant Physiol **160**: 396–406.

Wan, W.-L., Fröhlich, K., Pruitt, R.N., Nürnberger, T., and Zhang, L. (2019). Plant cell surface immune receptor complex signaling. Curr Opin Plant Biol **50**: 18–28.

Wang, J., Cai, Y., Miao, Y., Lam, S.K., and Jiang, L. (2009). Wortmannin induces homotypic fusion of plant prevacuolar compartments*. Journal of Experimental Botany **60**: 3075–3083.

Wang, J., Hu, M., Wang, J., Qi, J., Han, Z., Wang, G., Qi, Y., Wang, H.-W., Zhou, J.-M., and Chai, J. (2019a). Reconstitution and structure of a plant NLR resistosome conferring immunity. Science **364**.

Wang, J., Wang, J., Hu, M., Wu, S., Qi, J., Wang, G., Han, Z., Qi, Y., Gao, N., Wang, H.-W., Zhou, J.-M., and Chai, J. (2019b). Ligand-triggered allosteric ADP release primes a plant NLR complex. Science **364**.

Wang, R. and Brattain, M.G. (2007). The maximal size of protein to diffuse through the nuclear pore is larger than 60kDa. FEBS Letters **581**: 3164–3170.

Wang, W., Feng, B., Zhou, J.-M., and Tang, D. (2020). Plant immune signaling: Advancing on two frontiers. Journal of Integrative Plant Biology **62**: 2–24.

Wang, Y.-Y. and Tsay, Y.-F. (2011). Arabidopsis Nitrate Transporter NRT1.9 Is Important in Phloem Nitrate Transport[W][OA]. Plant Cell **23**: 1945–1957.

Weng, J.-K., Philippe, R.N., and Noel, J.P. (2012). The rise of chemodiversity in plants. Science **336**: 1667–1670.

Wiermer, M., Feys, B.J., and Parker, J.E. (2005). Plant immunity: the EDS1 regulatory node. Curr Opin Plant Biol **8**: 383–389.

Wildermuth, M.C., Dewdney, J., Wu, G., and Ausubel, F.M. (2001). Isochorismate synthase is required to synthesize salicylic acid for plant defence. Nature **414**: 562–565.

Wilhelm, L.P., Wendling, C., Védie, B., Kobayashi, T., Chenard, M.-P., Tomasetto, C., Drin, G., and Alpy, F. (2017). STARD3 mediates endoplasmic reticulum-to-endosome cholesterol transport at membrane contact sites. The EMBO Journal **36**: 1412–1433.

Willmann, R. et al. (2011). Arabidopsis lysin-motif proteins LYM1 LYM3 CERK1 mediate bacterial peptidoglycan sensing and immunity to bacterial infection. PNAS **108**: 19824–19829.

Wilson, R.A., Fernandez, J., Rocha, R.O., Marroquin-Guzman, M., and Wright, J.D. (2019). Genetic evidence for Magnaporthe oryzae vitamin B3 acquisition from rice cells. Microbiology (Reading) **165**: 1198–1202.

Win, J., Chaparro-Garcia, A., Belhaj, K., Saunders, D.G.O., Yoshida, K., Dong, S., Schornack, S., Zipfel, C., Robatzek, S., Hogenhout, S.A., and Kamoun, S. (2012). Effector Biology of Plant-Associated Organisms: Concepts and Perspectives. Cold Spring Harb Symp Quant Biol **77**: 235–247.

Winter, D., Vinegar, B., Nahal, H., Ammar, R., Wilson, G.V., and Provart, N.J. (2007). An "Electronic Fluorescent Pictograph" browser for exploring and analyzing large-scale biological data sets. PLoS One **2**: e718.

Wittstock, U. and Halkier, B.A. (2002). Glucosinolate research in the Arabidopsis era. Trends in Plant Science **7**: 263–270.

Wollert, T. and Hurley, J.H. (2010). Molecular Mechanism of Multivesicular Body Biogenesis by ESCRT Complexes. Nature **464**: 864–869.

Wu, C.-H., Derevnina, L., and Kamoun, S. (2018). Receptor networks underpin plant immunity. Science **360**: 1300–1301.

Wu, Z., Li, M., Dong, O.X., Xia, S., Liang, W., Bao, Y., Wasteneys, G., and Li, X. (2019). Differential regulation of TNL-mediated immune signaling by redundant helper CNLs. New Phytol **222**: 938–953.

Xiao, S., Calis, O., Patrick, E., Zhang, G., Charoenwattana, P., Muskett, P., Parker, J.E., and Turner, J.G. (2005). The atypical resistance gene, RPW8, recruits components of basal defence for powdery mildew resistance in Arabidopsis. Plant J **42**: 95–110.

Xu, D., Hanschen, F.S., Witzel, K., Nintemann, S.J., Nour-Eldin, H.H., Schreiner, M., and Halkier, B.A. (2017). Rhizosecretion of stele-synthesized glucosinolates and their catabolites requires GTR-mediated import in Arabidopsis. J Exp Bot **68**: 3205–3214.

Xu, J., Meng, J., Meng, X., Zhao, Y., Liu, J., Sun, T., Liu, Y., Wang, Q., and Zhang, S. (2016). Pathogen-Responsive MPK3 and MPK6 Reprogram the Biosynthesis of Indole Glucosinolates and Their Derivatives in Arabidopsis Immunity. The Plant Cell **28**: 1144–1162.

Xu, Y., Berkowitz, O., Narsai, R., Clercq, I.D., Hooi, M., Bulone, V., Breusegem, F.V., Whelan, J., and Wang, Y. (2019). Mitochondrial function modulates touch signalling in Arabidopsis thaliana. The Plant Journal **97**: 623–645.

Xu, Z., Escamilla-Treviño, L., Zeng, L., Lalgondar, M., Bevan, D., Winkel, B., Mohamed, A., Cheng, C.-L., Shih, M.-C., Poulton, J., and Esen, A. (2004). Functional genomic analysis of Arabidopsis thaliana glycoside hydrolase family 1. Plant Mol Biol **55**: 343–367.

Yamada, K., Osakabe, Y., Mizoi, J., Nakashima, K., Fujita, Y., Shinozaki, K., and Yamaguchi-Shinozaki, K. (2010). Functional Analysis of an Arabidopsis thaliana Abiotic Stress-inducible Facilitated Diffusion Transporter for Monosaccharides. J Biol Chem **285**: 1138–1146.

Yamada, K., Yamashita-Yamada, M., Hirase, T., Fujiwara, T., Tsuda, K., Hiruma, K., and Saijo, Y. (2016). Danger peptide receptor signaling in plants ensures basal immunity upon pathogen-induced depletion of BAK1. EMBO J **35**: 46–61.

Yang, L., Qin, L., Liu, G., Peremyslov, V.V., Dolja, V.V., and Wei, Y. (2014). Myosins XI modulate host cellular responses and penetration resistance to fungal pathogens. PNAS **111**: 13996–14001.

Yuan, M., Jiang, Z., Bi, G., Nomura, K., Liu, M., He, S.Y., Zhou, J.-M., and Xin, X.-F. (2020). Pattern-recognition receptors are required for NLR-mediated plant immunity. bioRxiv: 2020.04.10.031294.

Yun, B.-W., Atkinson, H.A., Gaborit, C., Greenland, A., Read, N.D., Pallas, J.A., and Loake, G.J. (2003). Loss of actin cytoskeletal function and EDS1 activity, in combination, severely compromises non-host resistance in Arabidopsis against wheat powdery mildew. Plant J **34**: 768–777.

Zeyen, R.J., Kruger, W.M., Lyngkjær, M.F., and Carver, T.L.W. (2002). Differential effects of D -mannose and 2-deoxy- D -glucose on attempted powdery mildew fungal infection of inappropriate and appropriate G ramineae. Physiological and Molecular Plant Pathology **61**: 315–323.

Zhang, J. et al. (2010). Receptor-like cytoplasmic kinases integrate signaling from multiple plant immune receptors and are targeted by a Pseudomonas syringae effector. Cell Host Microbe **7**: 290–301.

Zhang, L. and Xing, D. (2008). Methyl jasmonate induces production of reactive oxygen species and alterations in mitochondrial dynamics that precede photosynthetic dysfunction and subsequent cell death. Plant Cell Physiol **49**: 1092–1111.

Zhang, X., Dodds, P.N., and Bernoux, M. (2017a). What Do We Know About NOD-Like Receptors in Plant Immunity? Annu Rev Phytopathol **55**: 205–229.

Zhang, Z., Shrestha, J., Tateda, C., and Greenberg, J.T. (2014). Salicylic acid signaling controls the maturation and localization of the arabidopsis defense protein ACCELERATED CELL DEATH6. Mol Plant **7**: 1365–1383.

Zhang, Z., Tateda, C., Jiang, S.-C., Shrestha, J., Jelenska, J., Speed, D.J., and Greenberg, J.T. (2017b). A Suite of Receptor-Like Kinases and a Putative Mechano-Sensitive Channel Are Involved in Autoimmunity and Plasma Membrane–Based Defenses in Arabidopsis. MPMI **30**: 150–160.

Zhou, Y., Qu, H., Dibley, K.E., Offler, C.E., and Patrick, J.W. (2007). A suite of sucrose transporters expressed in coats of developing legume seeds includes novel pH-independent facilitators. Plant J **49**: 750–764.

Zimorski, V., Ku, C., Martin, W.F., and Gould, S.B. (2014). Endosymbiotic theory for organelle origins. Curr Opin Microbiol **22**: 38–48.

Zipfel, C., Kunze, G., Chinchilla, D., Caniard, A., Jones, J.D.G., Boller, T., and Felix, G. (2006). Perception of the Bacterial PAMP EF-Tu by the Receptor EFR Restricts Agrobacterium-Mediated Transformation. Cell **125**: 749–760.

Zipfel, C., Robatzek, S., Navarro, L., Oakeley, E.J., Jones, J.D.G., Felix, G., and Boller, T. (2004). Bacterial disease resistance in Arabidopsis through flagellin perception. Nature **428**: 764–767.

Zolman, B.K., Monroe-Augustus, M., Thompson, B., Hawes, J.W., Krukenberg, K.A., Matsuda, S.P., and Bartel, B. (2001). chy1, an Arabidopsis mutant with impaired beta-oxidation, is defective in a peroxisomal beta-hydroxyisobutyryl-CoA hydrolase. J Biol Chem **276**: 31037–31046.

6 Supplemental material

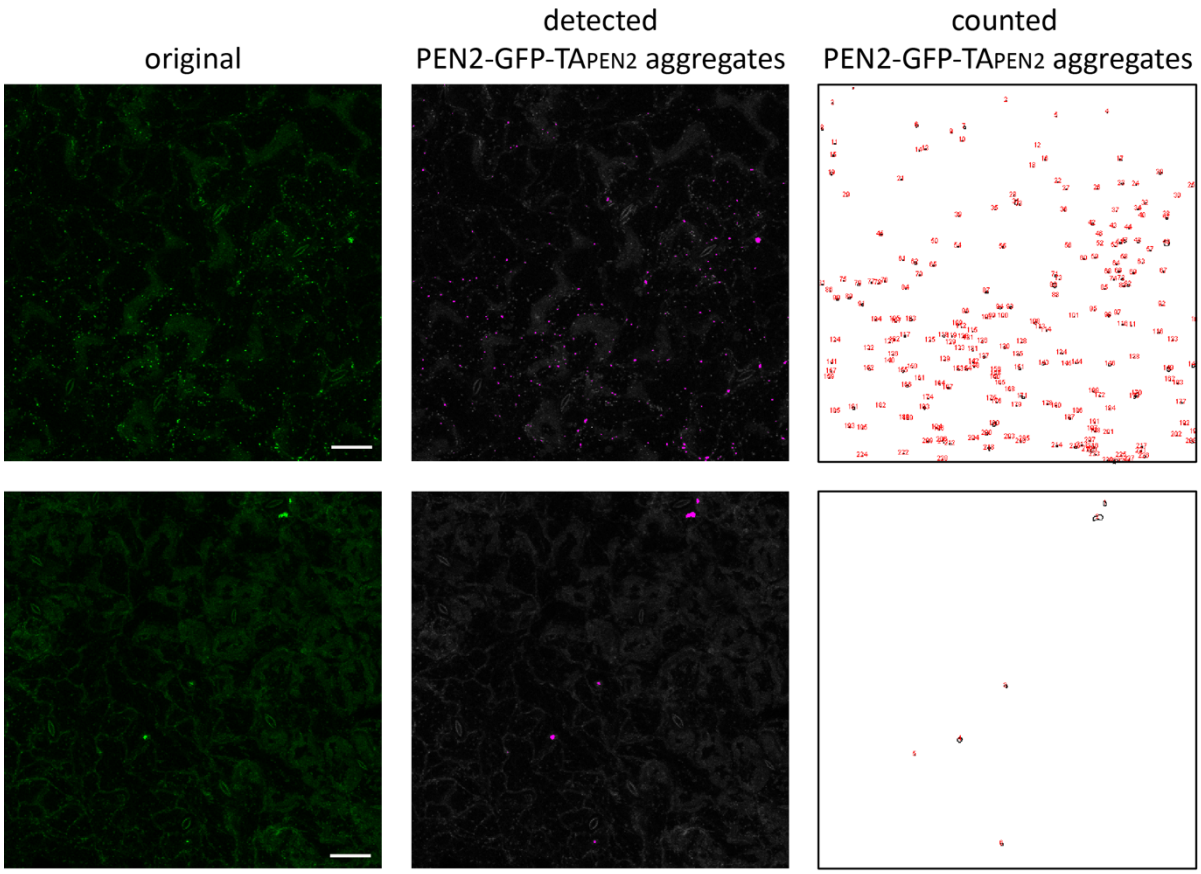

Figure S1. PEN2-GFP-TAPEN2 aggregate quantification. Illustration of PEN2-GFP-TA$_{PEN2}$ aggregate quantification from samples 20 hours after chitin vacuum infiltration. Original CLSM images are maximum z-projections with a size of 11 µm. Punctate structures with high contrast to the background were identified and marked as objects of interest in magenta. Detected PEN2-GFP-TA$_{PEN2}$ aggregates were enumerated and counted. Scale bar = 20 µm.

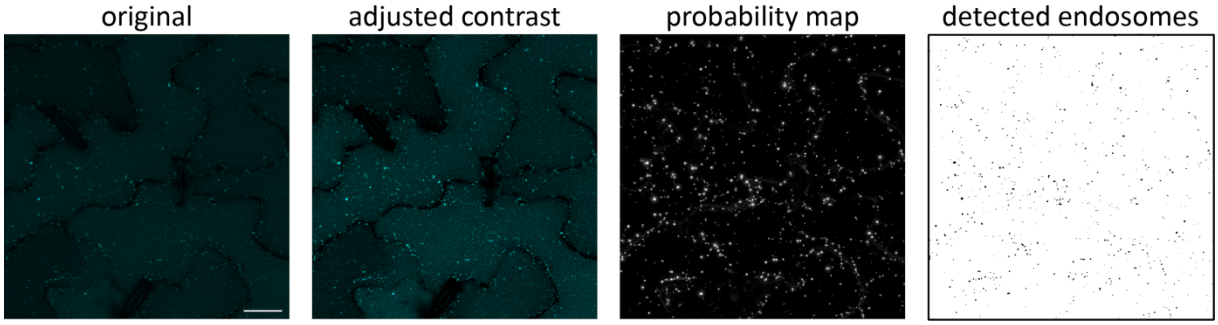

Figure S2: ERD6-mTurquoise2 endosome quantification. Visual representation of ERD6-mTurquoise2 vesicle quantification from an untreated sample. Original CLSM images are maximum z-projections with a size of 13 µm. Contrast was adjusted and followed by Trainable WEKA Segmentation. A trained classifier was applied to generate probability maps. Individual punctate structures were detected and counted. Scale bar = 20 µm.

A

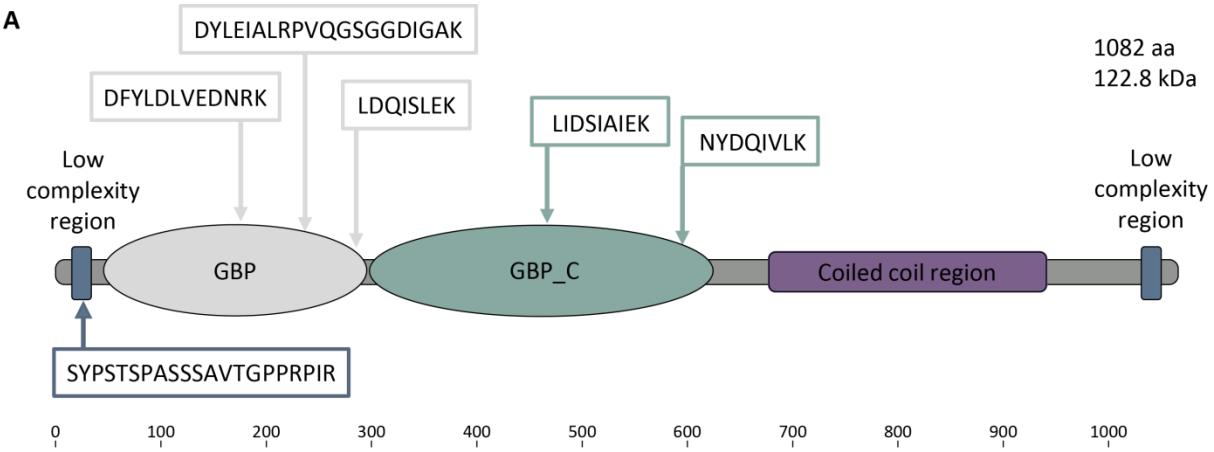

B

Experiment	Sample	Protein Unique Peptides	Coverage [%]
1	PEN2-GFP-TA$_{PEN2\Delta TM}$ chitin	1	2
1	PEN2-GFP-TA$_{PEN2}$ chitin	4	4
2	PEN2-GFP-TA$_{PEN2\Delta TM}$ chitin	2	3
2	PEN2-GFP-TA$_{PEN2}$ chitin	5	6
3	PEN2-GFP-TA$_{PEN2\Delta TM}$ chitin	1	2
3	PEN2-GFP-TA$_{PEN2}$ chitin	1	2

Figure S3. GBPL3 protein unique peptides identified by mass spectrometry. (A) Schematic illustration of the predicted protein domain organization of GBPL3. The predicted Guanylate-binding protein N-terminal domain (GBP) is indicated in light grey, the predicted Guanylate-binding protein C-terminal domain (GBP_C) is illustrated in green, the coiled-coil region in purple and the regions of low complexity in blue. Identified protein unique peptide sequences are illustrated. **(B)** Number of GBPL3 protein unique peptides and percentage of GBPL3 protein sequence covered by identified peptides in PEN2-GFP-TA$_{PEN2\Delta TM}$ and PEN2-GFP-TA$_{PEN2}$ samples 3 hours after chitin infiltration in 3 independent biological replicates.

Table S1: Macros used for PEN2-GFP-TA$_{PEN2}$ aggregate image quantification

Scripts for Quantification

LIF Projector[1]

```
// Get the folder name
DIR_PATH=getDirectory("Select a directory");
print("\\Clear");
print("DIR_PATH :"+DIR_PATH);
// Get all file names
ALL_NAMES=getFileList(DIR_PATH);
ALL_EXT=newArray(ALL_NAMES.length);
// Create extensions array
for (i=0; i<ALL_NAMES.length; i++) {
        LENGTH=lengthOf(ALL_NAMES[i]);
        ALL_EXT[i]=substring(ALL_NAMES[i],LENGTH-4,LENGTH);}
```

```
// Initialize choices variables
BACK_ARRAY = newArray("None", "25", "50", "100", "200", "500");
FILT_ARRAY = newArray("None", "Median", "Mean", "Gaussian", "Sigma");
PROJ_ARRAY = newArray("Max Intensity", "Average Intensity", "Sum Slices");
SAVE_ARRAY = newArray("No, thanks", "In the source folder", "In a subfolder of the source folder", "In a folder next to
the source folder", "In a custom folder");
// Creation of the dialog box
Dialog.create("Leica Projector");
Dialog.addMessage("\n");
Dialog.addChoice("Substract background before projection", BACK_ARRAY, "None");
Dialog.addChoice("Filter before projection",FILT_ARRAY,"None");
Dialog.addChoice("Projection Type",PROJ_ARRAY,"None");
Dialog.addCheckbox("Reset spatial scales for projections ?", false);
Dialog.addChoice("Save Projections ?", SAVE_ARRAY, "In a subfolder of the source folder");
Dialog.addCheckbox("Close results images (if saved)", false);
Dialog.show();
// Feeding variables from dialog choices
BACK_TYPE=Dialog.getChoice();
FILT_TYPE=Dialog.getChoice();
PROJ_TYPE=Dialog.getChoice();
RESET_SCALE=Dialog.getCheckbox();
SAVE_TYPE=Dialog.getChoice();
CLOSE_CHOICE=Dialog.getCheckbox();
setBatchMode(true);
// Loop on all .lei and .lif extensions
for (n=0; n<ALL_EXT.length; n++) {
if (ALL_EXT[n]==".lei" || ALL_EXT[n]==".lif") {
        // Get the file path
        FILE_PATH=DIR_PATH+ALL_NAMES[n];
        // Store components of the file name
        FILE_NAME=File.getName(FILE_PATH);
        FILE_PATH_LENGTH=lengthOf(FILE_PATH);
        FILE_NAME_LENGTH=lengthOf(FILE_NAME);
        FILE_DIR=substring(FILE_PATH,0,FILE_PATH_LENGTH-FILE_NAME_LENGTH);
        FILE_EXT=substring(FILE_NAME,FILE_NAME_LENGTH-4,FILE_NAME_LENGTH);
        FILE_SHORTNAME=substring(FILE_NAME,0,FILE_NAME_LENGTH-4);
print("");
print("FILE_PATH:", FILE_PATH);
print("FILE_NAME:", FILE_NAME);
print("FILE_DIR:", FILE_DIR);
print("FILE_EXT:", FILE_EXT);
print("FILE_SHORTNAME:", FILE_SHORTNAME);
        // Localize or create the output folder
        OUTPUT_DIR="Void";
        if (SAVE_TYPE=="In the source folder") {
                OUTPUT_DIR=FILE_DIR;}
        if (SAVE_TYPE=="In a subfolder of the source folder") {
                OUTPUT_DIR=FILE_DIR+FILE_SHORTNAME+"_ZProj"+File.separator;
                File.makeDirectory(OUTPUT_DIR);}
        if (SAVE_TYPE=="In a folder next to the source folder") {
                OUTPUT_DIR=File.getParent(FILE_PATH);
                OUTPUT_DIR=OUTPUT_DIR+"_"+FILE_SHORTNAME+"_ZProj"+File.separator;
                File.makeDirectory(OUTPUT_DIR);}
        if (SAVE_TYPE=="In a custom folder") {
```

```
		OUTPUT_DIR=getDirectory("Choose the save folder");}
print("OUTPUT_DIR: "+OUTPUT_DIR);
print("");
	// Start BioFormats and get series number in file.
	run("Bio-Formats Macro Extensions");
	Ext.setId(FILE_PATH);
	Ext.getSeriesCount(SERIES_COUNT);
	SERIES_NAMES=newArray(SERIES_COUNT);
print("SERIES_COUNT: "+SERIES_COUNT);
	// Loop on all series in the file
	for (i=0; i<SERIES_COUNT; i++) {
		// Get serie name and channels count
		Ext.setSeries(i);
		Ext.getEffectiveSizeC(CHANNEL_COUNT);
		SERIES_NAMES[i]="";
		Ext.getSeriesName(SERIES_NAMES[i]);
		TEMP_NAME=toLowerCase(SERIES_NAMES[i]);
print("SERIES_NAMES["+i+"]: "+ SERIES_NAMES[i] + " (TEMP_NAME: " + TEMP_NAME +")");
		// Import the serie (split channels)
//		run("Bio-Formats Importer", "open=["+ FILE_PATH + "] " + "view=[Standard ImageJ]" + "
stack_order=Default split_channels " + TEMP_NAME);
//		print("Bio-Formats Importer", "open=["+ FILE_PATH + "] " + "split_channels view=[Standard ImageJ]"
+ " stack_order=Default " + "series_"+d2s(i+1,0));
		run("Bio-Formats Importer", "open=["+ FILE_PATH + "] " + "split_channels view=[Standard ImageJ]" +
" stack_order=Default " + "series_"+d2s(i+1,0));
		// Loop on each channel (each opened window)
		for(j=0; j<CHANNEL_COUNT; j++) {
			// Construct window name
			TEMP_CHANNEL=d2s(j,0);
			// Windows has Series Name in title only if more than one Serie
			if(SERIES_COUNT==1) {
				SOURCE_WINDOW_NAME=FILE_NAME+ " - C="+TEMP_CHANNEL;}
			 else {SOURCE_WINDOW_NAME=FILE_NAME+" - "+SERIES_NAMES[i]+" -
			 C="+TEMP_CHANNEL;}
			TYPE="";
			//Select source image and filter if asked
			selectWindow(SOURCE_WINDOW_NAME);
// print("SOURCE_WINDOW_NAME: "+SOURCE_WINDOW_NAME);
			if (BACK_TYPE!="None") {
				run("Subtract Background...", "rolling="+BACK_TYPE+" sliding disable stack");
				TYPE=TYPE+" - "+"BG";}
			if (FILT_TYPE=="Median") {
				run("Median...", "radius=1 stack");}
			if (FILT_TYPE=="Mean") {run("Mean...", "radius=1 stack");}
			if (FILT_TYPE=="Gaussian") {
				run("Gaussian Blur...", "radius=1 stack");}
			if (FILT_TYPE=="Sigma") {
				run("Sigma Filter Plus", "radius=2 use=2 minimum=0.2 outlier stack");}
			if (FILT_TYPE!="None") {
				TYPE=TYPE+" - "+substring(FILT_TYPE,0,3)+"Filt";}
			// Project source stack or duplicate it if no projection
			if (nSlices!=1 && PROJ_TYPE!="None") {
				run("Z Project...", "projection=["+PROJ_TYPE+"]");
				TYPE=TYPE+" - "+substring(PROJ_TYPE,0,3)+"Proj";}
```

```
                        else {
                                run("Duplicate...", "title="+SOURCE_WINDOW_NAME+"-1");}
                        // Reset spatial scale of the projection if the option is chosen
                        if (RESET_SCALE==true) {
                                run("Set Scale...", "distance=0 known=1 pixel=1 unit=pixel"); }

                        // Rename output image and close source image
                         NEW_WINDOW_NAME=FILE_NAME+" - "+SERIES_NAMES[i]+" -
                         C="+TEMP_CHANNEL+TYPE;
                        rename(NEW_WINDOW_NAME);
                        selectWindow(SOURCE_WINDOW_NAME);
                        close();
                        selectWindow(NEW_WINDOW_NAME);
print("NEW_WINDOW_NAME: "+NEW_WINDOW_NAME);
                        // Create output file path and save the output image
                        OUTPUT_PATH="Void";
                        if (SAVE_TYPE!="No, thanks") {
                                OUTPUT_PATH=OUTPUT_DIR+NEW_WINDOW_NAME+".tif";
                                save(OUTPUT_PATH);}
// print("OUTPUT_PATH :"+OUTPUT_PATH);
                        // Close output image if asked
                        if (SAVE_TYPE!="No, thanks" && CLOSE_CHOICE==true) {
                                close();
// end of IF loop on lei and lif extensions
// end of FOR loop on n extensions
setBatchMode("exit and display");
showStatus("finished");
run("Close All");
// end of macro
```

PEN2 Particle Counter[2]

```
dir1 = getDirectory("Choose Source Directory ");
dir2 = getDirectory("Choose Destination Directory ");
list = getFileList(dir1);
setBatchMode(true);
for (i=0; i<list.length; i++) {
showProgress(i+1, list.length);
filename = dir1 + list[i];
if (endsWith(filename, "tif")) {
open(filename);
run("8-bit");
idOrig = getImageID();
run("Duplicate...", "duplicate");
idDuplicate = getImageID();
run("RGB Color");
run("8-bit");
run("Unsharp Mask...", "radius=3 mask=0.3");
run("Gaussian Blur...", "sigma=0.9");
run("Subtract Background...", "rolling=1.1 sliding");
setMinAndMax(40, 255);
call("ij.ImagePlus.setDefault16bitRange", 8);
run("Apply LUT");
run("Auto Threshold", "method=MaxEntropy white");
run("Set Scale...", "distance=1 global");
run("Set Measurements...", "area display redirect=None decimal=2");
run("Analyze Particles...", "display summarize");
run("Magenta");
run("Duplicate...", "title=[My subtracted image]");
```

```
selectImage(idOrig);
run("Add Image...", "image=[My subtracted image] x=0 y=0 opacity=100 zero");
saveAs("PNG", dir2+list[i]);
run("Close All");
}
}
selectWindow("Results");
saveAs("Results", dir2+"Individual measurements.xls");
selectWindow("Summary");
saveAs("Results", dir2+"Summary.xls");
```

PEN2 Particle Number[2]

```
setBatchMode(true);
function action(dir1, dir2, filename) {
                        open(dir1 + filename);
run("8-bit");
idOrig = getImageID();
run("Duplicate...", "duplicate");
idDuplicate = getImageID();
run("RGB Color");
run("8-bit");
run("Unsharp Mask...", "radius=3 mask=0.3");
run("Gaussian Blur...", "sigma=0.9");
run("Subtract Background...", "rolling=1.1 sliding");
setMinAndMax(40, 255);
call("ij.ImagePlus.setDefault16bitRange", 8);
run("Apply LUT");
run("Auto Threshold", "method=MaxEntropy white");
run("Set Scale...", "distance=1 global");
run("Set Measurements...", "area redirect=None decimal=2");
run("Analyze Particles...", "  show=Outlines");
saveAs("PNG", dir2+list[i]);
getImageID();
run("Add Image...", "idOrig x=0 y=0 opacity=100 zero");
saveAs("Results", dir2+filename+"results.xls" );
run("Clear Results");
close();
}
dir1 = getDirectory("Choose Source Directory ");
dir2 = getDirectory("Choose Destination Directory ");
list = getFileList(dir1);
for (i = 0; i < list.length; i++)
                        action(dir1, dir2, list[i]);
setBatchMode(false);
```

[1] https://biii.eu/lif-projector

[2] developed by Dr. Hassan Ghareeb

Table S2. All proteins identified by LC-MS/MS proteomic analysis from *pen2-1*, PEN2-GFP-TA$_{PEN2\Delta TM}$, PEN2-GFP-TA$_{PEN2}$ plants untreated or 3 hours post chitin vacuum infiltration in 3 independent biological experiments.

Accession	Name	Peptide-Spectrum matching score (PSM)												sum of PSMs
		Experiment 1				Experiment 2				Experiment 3				
		pen2-1		PEN2-GFP-TAPEN2ΔTM		PEN2-GFP-TA$_{PEN2}$		*pen2-1*		PEN2-GFP-TA$_{PEN2\Delta TM}$		PEN2-GFP-TA$_{PEN2}$		
		untreated	chitin	untreated	chitin	untreated	chitin	untreated	chitin	untreated	chitin	untreated	chitin	
AT2G44490	Glycosyl hydrolase superfamily protein (PEN2)	10	2	340	302	221	258	0	275	282	201	213	0	300	371	224	257	3256
AT5G15520	Ribosomal protein S19e family protein	0	0	0	10	0	6	0	0	16	12	0	0	0	0	0	26	70
AT3G21370	beta glucosidase 19	0	0	3	7	0	4	0	5	10	0	4	0	0	2	0	0	35
AT5G46070	Guanylate-binding family protein	0	0	0	2	0	8	0	0	0	0	12	0	0	2	0	2	30
AT3G04770	40s ribosomal protein SA B	0	0	0	4	0	0	0	0	4	0	4	0	6	0	0	6	24
AT4G24780	Pectin lyase-like superfamily protein	0	0	0	1	0	5	0	0	0	0	6	0	0	4	4	0	20
AT2G44470	beta glucosidase 29	0	0	2	2	1	3	0	1	1	0	0	0	2	2	0	3	17
AT1G58290	Glutamyl-tRNA reductase family protein	0	0	0	4	0	4	0	0	2	2	0	0	2	0	2	0	16
AT3G26400	eukaryotic translation initiation factor 4B1	0	0	0	0	0	6	0	0	0	0	6	0	0	0	0	2	14
AT3G05910	Pectinacetylesterase family protein	0	0	0	0	0	2	0	2	0	0	4	0	0	6	0	0	14
AT1G67680	SRP72 RNA-binding domain-containing protein	0	0	0	2	0	0	0	0	2	0	2	0	2	2	2	4	14
AT5G27120	NOP56-like pre RNA processing ribonucleoprotein	0	0	0	0	0	2	0	0	0	0	2	0	0	8	0	1	13
AT3G12670	CTP synthase family protein	0	0	4	0	0	0	0	4	0	0	2	0	0	3	0	0	13
AT5G47690	binding protein	0	0	0	0	0	4	0	0	0	0	4	0	0	4	0	0	12
AT2G25840	Nucleotidyl transferase superfamily protein	0	0	0	0	0	2	0	2	2	2	2	0	0	2	0	0	12
AT1G76810	eukaryotic translation initiation factor 2 (eIF-2) family protein	0	0	0	1	0	6	0	0	2	0	0	0	0	2	0	2	11
AT3G54660	glutathione reductase	0	0	0	0	0	2	0	3	0	0	4	0	0	2	0	0	11
AT3G13570	SC35-like splicing factor 30A	0	0	0	0	0	2	0	0	0	0	2	0	0	2	2	2	10
AT2G30000	PHF5-like protein	0	0	2	2	0	2	0	0	0	0	2	0	0	0	0	2	10
AT5G18620	chromatin remodeling factor17	0	0	0	0	0	2	0	0	0	0	4	0	0	0	2	0	10
AT1G77180	chromatin protein family	0	0	0	0	0	2	0	0	2	0	4	0	0	2	0	0	10
AT5G25220	homeobox protein knotted-1-like 3	0	0	0	0	0	4	0	0	0	0	2	0	0	0	2	0	8
AT4G34660	SH3 domain-containing protein	0	0	0	0	0	4	0	0	0	0	2	0	2	2	0	0	8
AT4G38740	rotamase CYP 1	0	0	0	0	0	2	0	0	0	0	1	0	0	0	0	5	8
AT1G18450	actin-related protein 4	0	0	0	0	0	2	0	0	2	0	2	0	0	2	0	0	8
AT4G31780	monogalactosyl diacylglycerol synthase 1	0	0	0	0	0	2	0	0	0	0	2	0	2	2	0	0	8
AT4G12780	Chaperone DnaJ-domain superfamily protein	0	0	0	0	0	1	0	0	0	0	2	0	0	2	2	0	7
AT2G16710	Iron-sulfur cluster biosynthesis family protein	0	0	0	0	2	0	0	2	0	0	0	0	1	0	0	2	7
AT1G72930	toll/interleukin-1 receptor-like protein	0	0	0	0	4	0	0	0	0	1	0	0	0	2	0	0	7
AT5G06530	ABC-2 type transporter family protein	0	0	0	0	0	2	0	0	0	0	2	0	0	0	0	2	6
AT1G25350	glutamine-tRNA ligase 2C	0	0	0	1	0	0	0	0	2	0	0	0	0	0	0	2	5
AT5G13530	protein kinases3B; ubiquitin-protein ligase	0	0	2	0	0	0	0	0	1	0	0	0	2	0	0	0	5

List of figures

List of tables

List of supplemental figures and tables

List of supplemental figures

List of supplemental tables

Danksagung

An dieser Stelle möchte ich mich ganz herzlich bei allen Personen bedanken, die mich während meiner Promotion unterstützt und begleitet haben.

Zuerst möchte ich mich bei Prof. Dr. Volker Lipka bedanken, der mir die Möglichkeit gab an diesem spannenden und vielfältigen Projekt zu arbeiten. Außerdem möchte ich mich für die vielen Diskussionen und die konstruktive Kritik bedanken, die nicht nur das Projekt vorangebracht haben, sondern auch mich motivierten und mir erlaubten an meinen Aufgaben zu wachsen. Des Weitern möchte ich mich für seine Begeisterung für die Wissenschaft bedanken, mit der er mir das Feld der pflanzlichen Zellbiologie nähergebracht hat. Außerdem möchte ich ihm für seine Funktion als Erstprüfer und die Begutachtung dieser Arbeit danken.

Ein weiterer Dank gilt Prof. Ivo Feußner für die Übernahme des Zweitgutachtens, sowie die stets weiterführende Unterstützung und die vielen Ratschläge während meiner Progress Reports, die zum Gelingen dieser Arbeit beigetragen haben.

Bei PD Dr. Thomas Teichmann, Dr. Marcel Wiermer, Prof. Dr. Andrea Polle, und PD Dr. Till Ischebeck möchte ich mich bedanken, dass Sie zusammen mit meinem Betreuungsausschuss meine Prüfungskommission bilden.

Ein großes Dankeschön gilt Dr. Elena Petutschnig für die Hilfe bei der Durchführung von Experimenten und den vielen spontanen Ideen im Laboralltag. Danke für die Unterstützung während der Schreibphase, ganz besonders für deine kritischen Kommentare und die hilfreichen Diskussionen. Vielen Dank für das Korrekturlesen meiner Arbeit.

PD Dr. Thomas Teichmann danke ich für seine Ratschläge und große Hilfsbereitschaft während der Promotion. Ganz besonders möchte ich mich für die Unterstützung und Hilfe bedanken, wenn sich mal wieder mein Rechner oder die Freezer selbständig gemacht haben.

Ein weiteres Dankeschön geht an Dr. Hassan Gharreb für die Unterstützung im Laboralltag, die mir den Anfang in der Abteilung erheblich erleichtert hat. Ganz besonders möchte ich mich für seine Hilfe bei aller Art Mikrokopieproblemen, sowie der Unterstützung bei der PEN2-Aggregat-Quantifizierung bedanken.

Vielen Dank auch an Dr. Kirstin Feußner für die Metaboliten-Analyse, sowie die hilfreiche Kommunikation.

Ganz herzlich möchte ich mich auch bei Gaby, Melanie, Sabine und Ludmilla bedanken. Danke für eure Zuverlässigkeit und ständige Hilfsbereitschaft bei Experimenten, das Bereitstellen von Materialien, schöne Gespräche, das offene Ohr bei allen möglichen Problemen und die Beantwortung all meiner Fragen. Ein riesiges Dankeschön geht dabei an Gaby für deine alltägliche Hilfe und Übernahme von kleinen und großen Aufgaben, sowie die angenehme und lustige Atmosphäre bei uns im Labor. Feli und Susanne möchte ich für das Bereitstellen von unzähligen Schalen mit gestopften Töpfen, das Pikieren von Pflanzen, das Sieben von Saatgut und viele herzliche Gespräche danken. Ein weiterer großer Dank geht an unsere Sekretärin Anja für die Unterstützung bei allen bürokratischen und organisatorischen Angelegenheiten. Danke für deine Ratschläge und viele lustige Plaudereien zwischendurch. Ohne euch alle wäre diese Arbeit nicht möglich gewesen.

Danke auch an Julia Reißmann die ihm Rahmen ihres Bachelorstudiums einen Teil des Projekts vorangebracht hat.

Außerdem danke ich meinen Dotorandenkolleg:innen Chrissi, Sina, Julia, Andrea, Mo, Mascha, Leonie, Mohamed, Konrad, Denise, Daniel, Qiqi und Philipp, sowie Josy, Leon und Jan für das gemeinsame Unterstützen, Lachen, Aufregen und Aufmuntern.

Ein großes Dankeschön gilt Chrissi, Ronja, Sina, Julia und Josy für die gute Atmosphäre bei uns im Büro. Danke für aufbauende und motivierende Gespräche, sowie für die vielen lustigen und wundervollen Momente. Chrissi, die Zeit mit dir in Marburg und Göttingen hat dich für mich nicht nur zu einer Kollegin, sondern auch zu einer Freundin gemacht. Danke, dass du nicht nur den Büroplatz mit mir geteilt hast, sondern auch viele Erinnerungen an Marburg. Danke für die stetige Hilfsbereitschaft und die vielen Diskussionen bei experimentellen Fragen während der letzten Jahre und ganz besonders für deine Unterstützung während der Schreibphase. Ronja, danke für die schöne Zeit, deine Unterstützung, die wertvollen Ratschläge und dein „Gut gemacht“. Danke liebe Sina für deine Hilfsbereitschaft und das Teilen deiner lebensrettenden Schoki-Vorräte. Danke, dass ihr die Zeit für mich in Göttingen unvergesslich gemacht habt.

Ein Dankeschön geht auch an Chrissi, Ronja, Anja, Tobi, Melanie, Josy, Leon und Jan für die schönen Mittagspausen im Seminarraum, auf der Dachterrasse oder der wackeligen Bank, immer mit viel lustigem Gesprächsstoff.

Des Weiteren möchte ich mich bei allen aktuellen und ehemaligen Mitgliedern der Arbeitsgruppe für die angenehme Atmosphäre und die vielen Geburtstags- und Weihnachtsfeiern, sowie das unterhaltsame Weihnachtskegeln bedanken.

Danke auch an Phil, Anna, Luce und Laura für die gemeinsame Zeit in Göttingen mit leckerem Essen und vielen lustigen Momenten. Danke für die schönen Erinnerungen - es war „el cubo perfecto“.
Ein Dankeschön gilt auch Miri, Tram, Lea und Niko fürs Ablenken, Mitfühlen, Zuhören und die entspannten Pausen bei uns im Garten.

Katha, Hanna, Resi, Lotte, Kate, Hanadi, Nissrin, Eli, Tabea und Anne danke ich für schöne Momente und Erinnerungen, die Reisen, viele Gespräche und eure Freundschaft. Danke, dass Ihr trotz der Entfernung immer da seid.

Meinem Freund Tobi möchte ich von ganzem Herzen danken, dass er immer an mich glaubt und mich ermutigt. Danke für deine Geduld und Unterstützung in den letzten Jahren. Ohne dich wäre ich bestimmt nicht so weit gekommen.

Zuletzt möchte ich mich bei meiner Familie bedanken. Ganz besonders möchte ich mich bei meinen Eltern dafür bedanken, dass sie mir immer unterstützend und liebevoll zu Seite stehen. Danke für alles!